



VNIVERSITAT  
DE VALÈNCIA

1

2     **Search for associated production of a Higgs**  
3     **boson and a single top quark in  $2\ell + \tau_{had}$**   
4     **final state using proton-proton collisions**  
5     **at  $\sqrt{s} = 13$  TeV with the ATLAS detector**

6

PhD Thesis

7

**Pablo Martínez Agulló**

8

Instituto de Física Corpuscular (IFIC)

9

Departament de Física Atòmica, Molecular i Nuclear

10

Programa de Doctorat en Física

11

Under the supervision of

12

**Carlos Escobar Ibáñez**

13

and

14

**Susana Cabrera Urbán**

15

València, 18th September 2022



<sup>16</sup> **Carlos Escobar Ibáñez,**  
<sup>17</sup> investigador científico del Consejo Superior de Investigaciones Científicas, y  
<sup>18</sup>

<sup>19</sup> **Susana Cabrera Urbán,**  
<sup>20</sup> científica titular del Consejo Superior de Investigaciones Científicas,

<sup>21</sup> **Certifican:**

<sup>22</sup> Que la presente memoria, **Search for associated production of a**  
**Higgs boson and a single top quark in  $2\ell + \tau_{had}$  final state**  
**using proton-proton collisions at  $\sqrt{s} = 13$  TeV with the ATLAS**  
**detector**, ha sido realizada bajo su dirección en el Instituto de Física  
Corpuscular, centro mixto de la Universitat de València y del CSIC, por  
**Pablo Martínez Agulló**, y constituye su Tesis para optar al grado de  
Doctor en Física.

<sup>29</sup> Y para que así conste, en cumplimiento de la legislación vigente, presenta  
<sup>30</sup> en el Departamento de Física Atómica, Molecular y Nuclear de la Univer-  
<sup>31</sup> sidad de Valencia la referida Tesis Doctoral, y firman el presente certificado.

<sup>32</sup>

<sup>33</sup> València, a DD de MES de 2022,

<sup>34</sup>

<sup>35</sup> Carlos Escobar Ibáñez

Susana Cabrera Urbán



36

37

38

39

*C'est quoi ce bordel ???*

—DANIEL BOSSON,



# <sup>40</sup> Preface

<sup>41</sup> The Standard Model (SM) of particle physics is both incredibly suc-  
<sup>42</sup> cessful and glaringly incomplete theory. It brings together all elementary  
<sup>43</sup> particles that make up the known universe in a single theory. Among these,  
<sup>44</sup> the top quark and the Higgs boson are of special interest because they can  
<sup>45</sup> help to answer some of the open questions. The object of study of this thesis  
<sup>46</sup> focusses in these two singular particles and its interplay. This is done through  
<sup>47</sup> two different analysis. On one hand the measurement of the top-quark po-  
<sup>48</sup> larisation and, on the other hand, the search of the associated production  
<sup>49</sup> of a Higgs boson and a single-top quark.

<sup>50</sup> The two studies presented at this dissertation have been carried using an  
<sup>51</sup> integrated luminosity of  $139 \text{ fb}^{-1}$  of proton-proton collision data at centre-  
<sup>52</sup> of-mass energy of 13 TeV collected by the ATLAS detector during the Large  
<sup>53</sup> Hadron Collider (LHC) Run 2. Located at the European Organization for  
<sup>54</sup> Nuclear Research (CERN), the LHC is the most powerful particle acceler-  
<sup>55</sup> ator in the world and ATLAS its largest detector. The experimental setup  
<sup>56</sup> in which this work is contextualised is described in Chapter 2. The data  
<sup>57</sup> and generation of Monte Carlo (MC) simulations within ATLAS is described  
<sup>58</sup> in Chapter 3. The reconstruction and identification of physical objects is  
<sup>59</sup> explained in Chapter 4.

## <sup>60</sup> Measurement of the top-quark polarisation

<sup>61</sup> The top quark is the heaviest elementary particle discovered so far, with a  
<sup>62</sup> mass of  $cd m_{top} = 172.76 \pm 0.30 \text{ GeV}$  [1]. Due to its large mass, it presents  
<sup>63</sup> some unique features. Being one of the most relevant the fact that it is the  
<sup>64</sup> only quark that decays before hadronising. This allows to measure its prop-  
<sup>65</sup> erties through its decay products. At LHC the top quark can be produced  
<sup>66</sup> either via the strong interaction, resulting in quark-antiquark pairs ( $t\bar{t}$ ), or  
<sup>67</sup> by the electroweak interaction, which produces them singly. In the second  
<sup>68</sup> scenario, the single-top quarks are created with their spin aligned in a par-  
<sup>69</sup> ticular direction. My contribution to the measurement of the polarisation  
<sup>70</sup> observables is presented in Chapter 5. The result of this work is presented  
<sup>71</sup> in reference [2].

72 **Search for associated production of a Higgs boson and a single top  
73 quark**

74 The discovery of a Higgs boson by the ATLAS and CMS experiments in  
75 2012 opened a new field for exploration in the realm of particle physics. In  
76 order to better understand SM, it is of prominent interest to determine the  
77 Yukawa coupling of the Higgs boson to the top quark ( $y_t$ ), being the latter  
78 the most massive fundamental particle and, consequently, the one with the  
79 largest coupling to the Higgs boson.

80 The direct measurement of  $y_t$  is only possible at the LHC via two asso-  
81 ciated Higgs productions: with a top-quark-antiquark pair ( $t\bar{t}H$ ) and with  
82 a single-top quark ( $tHq$ ). While the  $t\bar{t}H$  just permits the determination  
83 of the magnitude of  $y_t$ , the only way of simultaneously measuring its sign  
84 and magnitude is through the  $tHq$  production. The possible observation of  
85 an excess of signal events with respect to the SM prediction, would be an  
86 evidence of new physics in terms of CP-violating  $y_t$  coupling.

87 In this work it is presented a search for the  $tHq$  production in a final  
88 state with two light-flavoured-charged leptons (electrons or muons) and one  
89 hadronically-decaying tau lepton (named  $2\ell + 1\tau_{\text{had}}$  channel). This search  
90 is exceptionally challenging due to the extremely small cross-section of the  
91  $tHq$  process (70 fb), and of the  $2\ell + 1\tau_{\text{had}}$  final-state channel, in particular,  
92 which only accounts for a 3.5% of the total  $tHq$  production.

93 Therefore, to distinguish the  $tHq$  signal events from background events,  
94 machine-learning techniques are used. Particularly, boosted-decision trees  
95 (BDTs) are employed to define signal-enriched regions as well as control  
96 regions that constrain the most important background processes. The most  
97 relevant backgrounds are those related to top-quark-antiquark-pair produc-  
98 tion without and with an additional boson ( $t\bar{t}$ ,  $t\bar{t}H$ ,  $t\bar{t}W$  and  $t\bar{t}Z$ ) and  $Z$   
99 boson plus jets.

100 Additionally, to help identifying signal events within the data, the re-  
101 construction of the event plays an important role. Different tools are used  
102 to retrieve the four momentum of the top quark and Higgs boson from the  
103 reconstructed objects. This information can be later used to build variables  
104 that help separating the signal events from the processes that mimic the  
105  $2\ell + 1\tau_{\text{had}}$  signature. The reconstruction of the events is also enhanced by  
106 similar machine-learning methods since in the scenario in which the light-  
107 flavour leptons have the same sign, a priori, it is not possible to determine  
108 which lepton is originated from the Higgs boson and which from the top  
109 quark.

110 Significant suppression of the background events with jets wrongly selec-  
111 ted as leptons or non-prompt leptons originating from heavy-flavour decays

112 is achieved by demanding electrons and muons to pass strict identification  
113 and isolation requirements. Simultaneously, hadronic- $\tau$  leptons are deman-  
114 ded to pass the requirement of a recurrent-neural-network-based discrimin-  
115 ator to reduce misidentifications from jets.

116 The tools and methods developed for the associated  $tHq$  production  
117 search are described in Chapter 6.



# <sup>118</sup> Acknowledgements

<sup>119</sup> This work would not have been possible without the invaluable help of a  
<sup>120</sup> large number of people, whom I have been fortunate to meet, and to whom  
<sup>121</sup> I would like to thank and dedicate this thesis.

<sup>122</sup> Special mention to you, Stack Overflow, this thesis is as much yours as  
<sup>123</sup> it is mine. Thanks.

<sup>124</sup> Gracias gracias



# <sup>125</sup> Contents

<sup>126</sup>	<b>Preface</b>	v
<sup>127</sup>	<b>Acknowledgements</b>	ix
<sup>128</sup>	<b>1 Theoretical Framework</b>	1
<sup>129</sup>	1.1 The Standard Model of particle physics . . . . .	1
<sup>130</sup>	1.1.1 Introduction to the SM and its elementary particles . . . . .	2
<sup>131</sup>	1.1.2 Quantum electrodynamics . . . . .	6
<sup>132</sup>	1.1.3 Electroweak interactions . . . . .	8
<sup>133</sup>	1.1.4 Quantum chromodynamics . . . . .	15
<sup>134</sup>	1.1.5 Particle masses . . . . .	19
<sup>135</sup>	1.1.6 Charge-Parity . . . . .	26
<sup>136</sup>	1.1.7 Wrap up . . . . .	26
<sup>137</sup>	1.2 Top quark . . . . .	32
<sup>138</sup>	1.2.1 Top quark discovery . . . . .	34
<sup>139</sup>	1.2.2 Top quark production at LHC . . . . .	35
<sup>140</sup>	1.2.3 Top quark decay . . . . .	42
<sup>141</sup>	1.2.4 Top quark polarisation . . . . .	44
<sup>142</sup>	1.2.5 Top quark physics . . . . .	45
<sup>143</sup>	1.3 Higgs boson . . . . .	46
<sup>144</sup>	1.3.1 Higgs boson discovery . . . . .	46
<sup>145</sup>	1.3.2 Higgs boson production at LHC . . . . .	46

146	1.3.3 Higgs boson decay . . . . .	48
147	1.3.4 Higgs boson physics . . . . .	49
148	1.4 Top quark and Higgs boson interplay . . . . .	50
149	1.4.1 $t\bar{t}H$ . . . . .	51
150	1.4.2 $tHq$ . . . . .	52
151	<b>2 The ATLAS experiment at the Large Hadron Collider of CERN laboratory</b>	<b>57</b>
152		
153	2.1 CERN . . . . .	57
154	2.2 Large Hadron Collider . . . . .	59
155	2.2.1 Machine design . . . . .	59
156	2.2.2 Accelerator complex . . . . .	63
157	2.2.3 LHC Experiments . . . . .	64
158	2.2.4 LHC Computing grid . . . . .	67
159	2.2.5 Energy, Luminosity and Cross-section . . . . .	69
160	2.2.6 The Pile-up effect . . . . .	74
161	2.2.7 Phenomenology of proton-proton collisions . . . . .	75
162	2.3 ATLAS . . . . .	79
163	2.3.1 Coordinate system . . . . .	82
164	2.3.2 Inner Detector . . . . .	83
165	2.3.3 Calorimeters . . . . .	88
166	2.3.4 Muon Spectrometer . . . . .	93
167	2.3.5 Magnet system . . . . .	95
168	2.3.6 Trigger and Data Acquisition System . . . . .	98
169	2.3.7 ATLAS upgrade towards HL-LHC . . . . .	99
170	2.4 Alignment of the inner detector . . . . .	104
171	2.4.1 Alignment requirements . . . . .	104
172	2.4.2 Track based alignment . . . . .	104
173	2.4.3 Alignment results during Run-2 . . . . .	104
174	2.4.4 Alignment towards Run-3 . . . . .	104

175	<b>3 Recording data and simulating events in ATLAS</b>	<b>105</b>
176	<b>3.1 Data</b> . . . . .	105
177	<b>3.2 Monte Carlo</b> . . . . .	105
178	<b>3.2.1 MC simulations</b> . . . . .	106
179	<b>3.2.2 MC generators</b> . . . . .	106
180	<b>4 Object reconstruction and identification</b>	<b>107</b>
181	<b>4.1 Tracking</b> . . . . .	107
182	<b>4.1.1 Sagitta method</b> . . . . .	108
183	<b>4.2 Vertices</b> . . . . .	108
184	<b>4.3 Electrons and photons</b> . . . . .	108
185	<b>4.4 Muons</b> . . . . .	108
186	<b>4.5 Jets</b> . . . . .	108
187	<b>4.5.1 Jet energy calibration and resolution</b> . . . . .	109
188	<b>4.5.2 Bottom quark induced jets</b> . . . . .	109
189	<b>4.6 Missing transverse energy</b> . . . . .	110
190	<b>4.7 Overlap removal</b> . . . . .	110
191	<b>5 Probing the top-quark polarisation in the single-top <math>t</math>-channel production</b>	<b>111</b>
192	<b>5.1 Introduction</b> . . . . .	111
193	<b>5.2 Top quark polarisation observables</b> . . . . .	112
194	<b>5.3 Simulated event samples</b> . . . . .	112
195	<b>5.4 Object reconstruction</b> . . . . .	112
196	<b>5.5 Trigger requirements and event preselection</b> . . . . .	112
197	<b>5.6 Top quark reconstruction</b> . . . . .	112
198	<b>6 Search for rare associate <math>tHq</math> production</b>	<b>113</b>
199	<b>6.1 Introduction</b> . . . . .	113
200	<b>6.2 Data and simulated events</b> . . . . .	114
201	<b>6.3 Object definition and reconstruction</b> . . . . .	115

203	6.4 Signal . . . . .	115
204	6.4.1 Signal generation and validation . . . . .	115
205	6.4.2 Parton-level truth validation . . . . .	115
206	6.4.3 Lepton assignment . . . . .	115
207	6.4.4 Top quark and Higgs boson reconstruction . . . . .	120
208	6.5 Background estimation . . . . .	120
209	6.5.1 Fakes estimation . . . . .	120
210	6.5.2 Prompt backgrounds . . . . .	122
211	6.6 Event selection . . . . .	122
212	6.6.1 Preselection . . . . .	122
213	6.6.2 BDT . . . . .	122
214	6.6.3 Signal Region . . . . .	123
215	6.6.4 Control Regions . . . . .	123
216	6.7 Systematic uncertainties . . . . .	124
217	6.7.1 Theoretical uncertainties . . . . .	125
218	6.7.2 Modelling uncertainties . . . . .	125
219	6.7.3 Experimental uncertainties . . . . .	125
220	6.8 Fit results . . . . .	125
221	6.8.1 Likelihood fit . . . . .	125
222	6.8.2 Strategy . . . . .	127
223	6.8.3 Fit with Asimov data . . . . .	127
224	6.8.4 Fit to data . . . . .	127
225	6.8.5 Results . . . . .	127
226	6.8.6 Data fit . . . . .	127
227	6.9 Combination results . . . . .	127
228	6.10 Conclusions . . . . .	127
229	<b>7 Conclusion</b>	<b>129</b>
230	<b>A Effect of negative weights</b>	<b>131</b>

231	A.1 Negative weights uncertainties . . . . .	131
232	A.2 Statistical uncertainty of negative weights . . . . .	131
233	A.2.1 Errors in binned histograms . . . . .	133
234	A.3 Negative weights in MVA methods . . . . .	134
235	<b>Appendices</b>	<b>130</b>
236	<b>B Boosted Decision Trees</b>	<b>135</b>
237	B.1 How does a BDT work? . . . . .	135
238	B.1.1 Training . . . . .	136
239	B.1.2 Evaluation / Validation . . . . .	139
240	B.1.3 Application . . . . .	139
241	B.2 Treatment of negative weights . . . . .	139
242	B.3 Cross validation and $k$ -folding . . . . .	139
243	<b>Abbreviations</b>	<b>142</b>
244	<b>Bibliography</b>	<b>145</b>
245	<b>Summary of the results</b>	<b>159</b>
246	<b>Resum de la tesi</b>	<b>161</b>
247	1 Marc teòric . . . . .	161
248	1.1 El Model Estàndard . . . . .	161
249	1.2 La física del quark top . . . . .	161
250	1.3 La física del bosó de Higgs . . . . .	161
251	2 Dispositiu experimental . . . . .	161
252	3 L'experiment ATLAS del LHC al CERN . . . . .	162
253	3.1 El gran col·lisionador d'hadrons . . . . .	162
254	3.2 El detector ATLAS . . . . .	162
255	4 Mesura de la polarització del quark top al canal- $t$ . . . . .	162

---

256	4.1	Selecció d'esdeveniments	162
257	4.2	Estimació del fons	162
258	4.3	Fonts d'incertesa	162
259	4.4	Resultats	162
260	5	Recerca de processos $tH$ amb un estat final $2\ell + 1\tau_{\text{had}}$	162
261	5.1	Selecció d'esdeveniments	162
262	5.2	Estimació del fons	162
263	5.3	Fonts d'incertesa	162
264	5.4	Resultats	162
265	6	Conclusions	162

# <sup>266</sup> Chapter 1

## <sup>267</sup> Theoretical Framework

### <sup>268</sup> 1.1 The Standard Model of particle physics

<sup>269</sup> Since the very first moment of our history, the humankind has pursued  
<sup>270</sup> the knowledge of nature, has tried to understand and describe how the  
<sup>271</sup> universe works at a fundamental level. In fact, the word physics comes  
<sup>272</sup> from the Greek “*φυσική*” which means “nature” [3][4]. Most of the enquires  
<sup>273</sup> regarding this, can be boiled down to two basic questions: What are the  
<sup>274</sup> ultimate building blocks of reality? and which are the rules that govern  
<sup>275</sup> them?

<sup>276</sup> In the 7<sup>th</sup> century BCE, the pre-Socratic philosopher Thales of Miletus  
<sup>277</sup> already proclaimed that every event had a natural cause [5]. Later, to un-  
<sup>278</sup> derstand how the basic components of the matter were formed, the ancient  
<sup>279</sup> Indian philosophers such as Kanada and Dignaga on the 6<sup>th</sup> century BCE  
<sup>280</sup> and Greeks Democritus and Leucippus on the 5<sup>th</sup> century BCE, developed  
<sup>281</sup> the atomism, which comes from “*ατομον*” meaning uncuttable or indivisible  
<sup>282</sup> [6][7].

<sup>283</sup> From then to our days, the search for the minute fragments that comprise  
<sup>284</sup> the matter and its interactions has led us to the Standard Model (SM) of  
<sup>285</sup> particle physics, one of the most successful scientific theories cultivated  
<sup>286</sup> so far. This understanding of the universe can explain phenomena from  
<sup>287</sup> behaviour of atoms to how stars burn.

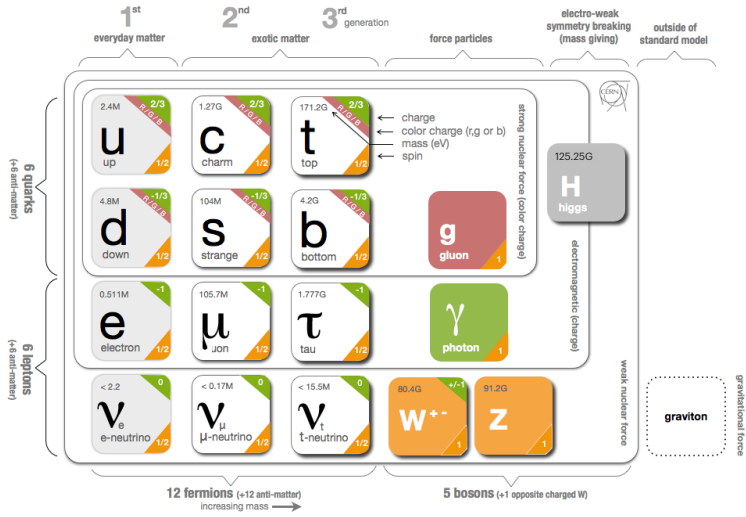


**Figure 1.1:** Fundamental particles of the Standard Model (image modified from [8]).

### 288    1.1.1 Introduction to the SM and its elementary 289    particles

290    Based on Quantum Field Theory (QFT), the SM of particle physics  
291    provides the theoretical framework that constitutes what is currently ac-  
292    cepted as the best description of particles physics. It aims to explain both  
293    all particles of matter and their interactions. The completion of the SM  
294    was a collaborative effort of several scientists during the second half of the  
295    20<sup>th</sup>, being the current formulation finalised in the decade of 1970. A rep-  
296    resentation of the fundamental particles, i.e. particles that are not made  
297    of anything else, that compose the SM is presented in Figure 1.1. Most of  
298    these particles are unstable and decay to lighter particles within fractions  
299    of a second. As the scheme in Figure 1.1 indicates, the 12 fermions have  
300    their corresponding 12 anti-fermions and the quarks and gluons carry colour  
301    charge.

302    The SM is a gauge theory based on the symmetry group  
303     $SU(3)_C \otimes SU(2)_L \otimes U(1)_Y$ , which describes all fundamental interactions  
304    except from the gravitational force<sup>1</sup>. This theory provides an explana-  
305    tion to strong, weak and electromagnetic interactions via the exchange of  
306    the corresponding vector<sup>2</sup> bosons (spin-1 gauge fields). The mediation for  
307    the electromagnetic interaction (explicated in 1.1.2) is done by one mass-  
308    less photon ( $\gamma$ ), this force is invariant under the  $U(1)$  symmetry group.

<sup>1</sup>The gravitational interaction is described by Einstein's General Relativity (GR) [9].

<sup>2</sup>“Vector bosons” refer to all bosons that have spin 1 in contrast to the “scalar boson’s” which have spin 0.

Interaction	Theory	Mediator	Relative strength	Range (m)
Strong	QCD	$g$	1	$10^{-15}$
Electromagnetic	QED/EW	$\gamma$	$1/137$	$\infty$
Weak	EW	$W^\pm, Z$	$10^{-6}$	$10^{18}$
Gravitational	GR	-	$6 \times 10^{-39}$	$\infty$

**Table 1.1:** Typical strength of the fundamental interactions with respect to the strong interaction. Here the strength is understood as the coupling constant. In GR the gravitational interaction is not a force but the effect of the four-dimensional spacetime curvature and, hence, it has no mediator in this formalism.

309 While for the weak interactions, guided by  $SU(2)$ , three massive bosons,  
 310  $W^+$ ,  $W^-$  and  $Z$ , act as mediators ( $m_{W^\pm} = 80.385 \pm 0.015$  GeV and  
 311  $m_Z = 91.1876 \pm 0.02$  GeV). Although the electromagnetic and weak in-  
 312 teractions seem completely different at low energies, they are two aspects of  
 313 the same force and can be described simultaneously by the  $SU(2)_L \otimes U(1)_Y$   
 314 symmetry group, which represents the so called Electro-Weak (EW) sector  
 315 (detailed in Section 1.1.3). The strong force, with its 8 massless gluons  
 316 ( $g$ ), is described by the  $SU(3)_C$  colour group (see Section 1.1.4). All these  
 317 interactions differ in their magnitude, range and the physical phenomena  
 318 that describe. These features are summarised in Table 1.1, where not only  
 319 the interactions of the SM are included but the gravitation is as well.

320 Apart from the vector bosons, there is one massive scalar boson, the  
 321 Higgs boson ( $m_H = 125.25 \pm 0.17$  GeV). Through the interaction with this  
 322 particle, all massive particles of Figure 1.1 gain their mass via the EW  
 323 spontaneous symmetry breaking. This mechanism is described in Section  
 324 1.1.5.1.

325 Before describing the fundamental interactions of the SM in the QFT  
 326 formalism, let's introduce the main two types of particles according to their  
 327 spin, i.e. intrinsic angular momentum: fermions and bosons.

### 328 Fermions

329 The fermions are the particles that follow the Fermi-Dirac statistics, i.e.  
 330 obey the Pauli exclusion principle [10], resulting in a distribution of particles  
 331 over energy levels in which two elements with the same quantum numbers  
 332 cannot occupy the same states. The fermions include all particles with half-  
 333 integer spin: quarks, leptons and baryons. A baryon is a non-fundamental  
 334 particle composed of an odd number of valence quarks<sup>3</sup> (consequently hav-

<sup>3</sup>The hadrons (baryons are mesons) are understood as a sea of partons being the valence quarks those which are more probable to be found in the hadron according to the parton distribution functions.

335 ing half-integer spin) and nearly all matter that may be encountered or  
 336 experienced in everyday life is baryonic matter. Some examples of baryons  
 337 are<sup>4</sup> the proton ( $u\ u\ d$ ), the neutron ( $d\ d\ u$ ),  $\Lambda$  ( $u\ d\ s$ ),  $\Lambda_c^+$  ( $u\ d\ c$ ) and  $\Sigma^+$   
 338 ( $u\ u\ s$ ). Apart from the 3-quark baryons, an exotic pentaquark state has  
 339 been observed at LHCb experiment of the LHC [11].

340 The fundamental fermionic matter (Table 1.2) is organised in the three  
 341 families of leptons and quarks:

$$342 \quad \begin{bmatrix} \nu_e & u \\ e^- & d \end{bmatrix}, \begin{bmatrix} \nu_\mu & c \\ \mu^- & s \end{bmatrix}, \begin{bmatrix} \nu_\tau & t \\ \tau^- & b \end{bmatrix}$$

343 .

344 These three generations, which are defined as the columns in Figure 1.1,  
 345 exhibit the same kind of gauge interactions and they only differ in their  
 346 mass [12]. According to the EW symmetry, each family can be classified as:

$$347 \quad \begin{bmatrix} \nu_\ell & q_u \\ \ell^- & q_d \end{bmatrix} \equiv \begin{pmatrix} \nu_\ell \\ \ell^- \end{pmatrix}_L, \begin{pmatrix} q_u \\ q_d \end{pmatrix}_L, \ell^-_R, q_{uR}, q_{dR}$$

348 (plus the corresponding antiparticles) where the subindices  $L$  and  $R$  stand  
 349 from left and right handed particles respectively. This structure responds to  
 350 the fact that left-handed particles convert different than right-handed ones  
 351 under  $SU(2)$  transformations. The left-handed fields are  $SU(2)_L$  doublets  
 352 and the right-handed ones  $SU(2)_R$  singlets. This difference is explained  
 353 with more detail in Section 1.1.3.

354 The fundamental representation of  $SU(3)$  is a triplet, this is why each  
 355 quark can appear in three different colours, whereas each antiquark can  
 356 exhibit one of the corresponding “anticolours”.

357 The SM fermions properties are summarised in Table 1.2. As can be seen  
 358 in its last rows, the neutrino flavour states do no correspond to the mass  
 359 states ( $\nu_1, \nu_2, \nu_3$ ). What happens is that each flavour state is a quantum  
 360 mechanical combination of neutrinos of different masses and viceversa. More  
 361 details about the neutrino masses can be found in a dedicated text in Section  
 362 1.1.7.2

363 The fundamental fermions are usually understood as the fundamental  
 364 building blocks of matter. However, while the building blocks are important,  
 365 there is a point that also has to be taken into account, the force. Without  
 366 force these fermions would not interact which each other. The particles that  
 367 mediate these interactions are the gauge bosons.

---

<sup>4</sup>Between round brackets, the valence quarks are shown.

Family	Name	Mass	Q
Quarks	Up ( $u$ )	$2.16^{+0.49}_{-0.26}$ MeV	2/3
	Down ( $d$ )	$4.67^{+0.48}_{-0.17}$ MeV	-1/3
	Charm ( $c$ )	$1.27 \pm 0.02$ GeV	2/3
	Strange ( $s$ )	$93^{+11}_{-5}$ MeV	-1/3
	Top ( $t$ )	$172.76 \pm 0.30$ GeV	2/3
	Bottom ( $b$ )	$4.18^{+0.03}_{-0.02}$ GeV	-1/3
Leptons	Electron ( $e^-$ )	$0.5109989461 \pm 0.0000000031$ MeV	-1
	Muon ( $\mu$ )	$105.6583745 \pm 0.0000024$ MeV	-1
	Tau ( $\tau$ )	$776.86 \pm 0.12$ MeV	-1
	Electron neutrino ( $\nu_e$ )	$\nu_e, \nu_\mu, \nu_e$	0
	Muon neutrino ( $\nu_\mu$ )	$\neq$	0
	Tau neutrino ( $\nu_\tau$ )	$\nu_1, \nu_2, \nu_3$	0

**Table 1.2:** Properties of the quarks and leptons. The electric charge is represented here by Q. The  $\nu_1, \nu_2, \nu_3$  are the neutrino mass eigenstates.

### 368    **Bosons**

369    Bosons differ from fermions by obeying the Bose-Einstein statistics, thus,  
 370    bosons are not limited to single occupancy for a determined state. In other  
 371    words, the Pauli exclusion principle is not applied. All particles with integer  
 372    spin are bosons; from the particles shown on the right columns of Figure 1.1  
 373    to the mesons. Mesons, along with baryons, are part of the hadron family,  
 374    i.e. particles composed of quarks (see Section 1.1.4). The particularity  
 375    of mesons is that they are formed from an equal number of quarks and  
 376    antiquarks (usually one of each) bound together by strong interactions.  
 377    Some examples of mesons are  $\pi^+$  ( $u \bar{d}$ ),  $\pi^0$  ( $\frac{u\bar{u}-d\bar{d}}{\sqrt{2}}$ ),  $K^+$  ( $u \bar{s}$ ) and  $J/\psi$   
 378    ( $c \bar{c}$ ).

379    The elementary vector bosons are the force carriers and presented in  
 380    Table 1.1 while Higgs boson is a fundamental particle as well.

### 381    **Gauge Invariance**

382    Constituting one of the most successful theories of Physics, the SM is able  
 383    to provide an elegant mathematical framework to describe the experimental  
 384    physics results with great precision. Another key element to understand the  
 385    SM is the concept of gauge invariance. As it is illustrated during the rest of  
 386    the Section 1.1, by demanding that the Lagrangian remains invariant under  
 387    local gauge transformations, the existence of the SM force-carrier bosons  
 388    ( $\gamma, W^+, W^-, Z$  and  $g$ ).

<sup>389</sup> **1.1.2 Quantum electrodynamics**

<sup>390</sup> The gauge invariance refers to the invariance of a theory under trans-  
<sup>391</sup> formations which the theory is said to posses internal symmetry. The trans-  
<sup>392</sup> formations which are applied in all space-time locations simultaneously are  
<sup>393</sup> known as “global” transformations while the ones that vary from one point  
<sup>394</sup> to another are “local”. Each local symmetry is the basis of a gauge theory  
<sup>395</sup> and requires the introduction of its own gauge bosons as it is discussed in  
<sup>396</sup> the following pages.

In QFT, particles are described as excitations of quantum fields that satisfy the corresponding mechanical field equations. The Lagrangians in QFT are used analogous to those of classical mechanics, where the equation of motion can be derived from the Lagrangian density function ( $\mathcal{L}$ ) and the Euler-Lagrange equations for fields:

$$\frac{\partial \mathcal{L}}{\partial \phi} - \partial_\mu \frac{\partial \mathcal{L}}{\partial (\partial_\mu \phi)} = 0$$

<sup>397</sup>, where  $\partial_\mu = \frac{\partial}{\partial x^\mu}$  denotes the partial derivatives with respect to the four-  
<sup>398</sup> vector  $x^\mu$  and  $\phi = \phi(\vec{x}, t)$  is the quantum field of a fermion or boson. The  
<sup>399</sup> Lagrangian density (or just Lagrangian, for simplicity) is used to express  
<sup>400</sup> the dynamics of the quantum field. In QFT, Noether’s theorem [13] relates  
<sup>401</sup> a symmetry in the  $\mathcal{L}$  to a conserved current.

<sup>402</sup> The Dirac equation,  $(i\gamma^\mu \partial_\mu - m)\Psi(x) = 0$ , is one of the simplest relativistic field equations. Its Lagrangian describes a free Dirac fermion:

$$\mathcal{L}_0 = i\bar{\Psi}(x)\gamma^\mu \partial_\mu \Psi(x) - m\bar{\Psi}(x)\Psi(x) \quad (1.1)$$

<sup>404</sup>, being  $\Psi$  the wave function (spinor represented by four complex-valued  
<sup>405</sup> components) of the particle,  $\gamma^\mu$  are the Dirac or gamma matrices,  
<sup>406</sup>  $\{\gamma^0, \gamma^1, \gamma^2, \gamma^3\}$ ,  $m$  the mass of the fermion and  $\bar{\Psi} = \Psi^\dagger \gamma^0$ , the hermitic  
<sup>407</sup> conjugate of the wave function. The gamma matrices build a set of ortho-  
<sup>408</sup> gonal basis vectors for covariant vectors in a Minkowski space. The first  
<sup>409</sup> term of  $\mathcal{L}_0$  is the kinetic term while the second is the mass term.

This Lagrangian is invariant under  $U(1)$  global transformations such as:

$$\Psi(x) \xrightarrow{U(1)} \Psi'(x) \equiv \exp\{iQ\theta\}\Psi(x) \quad (1.2)$$

<sup>410</sup>, where  $Q\theta$  is a real constant. The phase of  $\Psi(x)$  is a pure convention-  
<sup>411</sup> dependent quantity without a physical meaning since the observables de-  
<sup>412</sup> pend on  $|\Psi(x)|^2$ .

However, if  $\theta$  was  $x$  dependent, the transformation 1.2 would be:

$$\Psi(x) \xrightarrow{U(1)} \Psi'(x) \equiv \exp\{iQ\theta(x)\}\Psi(x) \quad (1.3)$$

, which is not longer a global transformation but a local transformation instead. The transformation in 1.3 would not let the  $\mathcal{L}_0$  in 1.1 invariant because the derivative in the kinetic term would go as:

$$\partial_\mu \Psi(x) \xrightarrow{U(1)} \exp\{iQ\theta\}(\partial_\mu + iQ\partial_\mu\theta)\Psi(x) \quad (1.4)$$

413 .

The gauge principle is the requirement that the  $U(1)$  phase invariance should hold locally. In order to do so, it is necessary to introduce an additional term to the Lagrangian so that when one applies  $\Psi'(x) \equiv \exp\{iQ\theta(x)\}\Psi(x)$ , the  $\partial_\mu\theta$  term is canceled in 1.4. To achieve this invariance, a term with the vector gauge field  $A_\mu$  is inserted. This field transforms as

$$A_\mu(x) \xrightarrow{U(1)} A'_\mu(x) \equiv A_\mu(x) + \frac{1}{e}\partial_\mu\theta \quad (1.5)$$

with a new covariant derivative:

$$D_\mu\Psi(x) \equiv [\partial_\mu + ieQA_\mu(x)]\Psi(x) \quad (1.6)$$

which transforms like the field:

$$D_\mu\Psi(x) \xrightarrow{U(1)} (D_\mu\Psi)'(x) \equiv \exp\{iQ\theta\}D_\mu\Psi(x)$$

414 .

The Lagrangian density can be defined by replacing the partial derivatives in  $\mathcal{L}_0$  (1.1) by the covariant derivative in 1.6:

$$\begin{aligned} \mathcal{L}_{QED} &\equiv i\bar{\Psi}(x)\gamma^\mu D_\mu\Psi(x) - m\bar{\Psi}(x)\Psi(x) \\ &= i\bar{\Psi}(x)\gamma^\mu[\partial_\mu + ieQA_\mu(x)]\Psi(x) - m\bar{\Psi}(x)\Psi(x) \\ &= i\bar{\Psi}(x)\gamma^\mu\partial_\mu\Psi(x) - \bar{\Psi}(x)\gamma^\mu eQA_\mu\Psi(x) - m\bar{\Psi}(x)\Psi(x) \\ &= \mathcal{L}_0 - eQA_\mu\bar{\Psi}(x)\gamma^\mu\Psi(x) \end{aligned} \quad (1.7)$$

415 .

416 The resulting Lagrangian is invariant under  $U(1)$  local transformation.  
 417 When the conversions 1.3 and 1.5 take place, the effects of the transformation  
 418 are canceled out. Along with the original Lagrangian ( $\mathcal{L}_0$ ), the  $\mathcal{L}_{QED}$   
 419 has an additional term describing the interaction between the fermion  $\Psi$   
 420 and the gauge field  $A_\mu$  with a strength proportional to the charge  $eQ$ . This  
 421 term,  $eQA_\mu\bar{\Psi}\gamma^\mu\Psi$ , that has been generated only by demanding the gauge  
 422 invariance under  $U(1)$ , is not other than the vertex of Quantum Electrodynamics  
 423 (QED) (Figure 1.2).

This new  $A_\mu$  term is the electromagnetic field and its quanta is the photon. A mass term containing  $A^\mu A_\mu$  is forbidden because it would violate

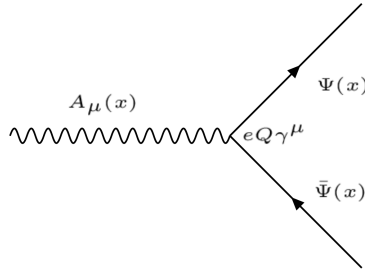


**Figure 1.2:** Three-point interaction vertex of QED.

the  $U(1)$  local invariance. In consequence, the mediator of the new  $A_\mu$  field, the photon, is predicted to be a massless particle. To make  $A_\mu$  a propagating field it is necessary to add the kinetic term of the field  $A_\mu$ :

$$\mathcal{L}_{kin} \equiv -\frac{1}{4} F_{\mu\nu}(x) F^{\mu\nu}(x) \quad (1.8)$$

, where  $F^{\mu\nu} \equiv \partial_\mu A_\nu - \partial_\nu A_\mu$ . The kinetic term  $F_{\mu\nu} F_{\mu\nu} F^{\mu\nu}$  is already invariant under local  $U(1)$  phase transformations. From the QED Lagrangian in 1.7 and the kinetic term in 1.8, the Maxwell equations can be derived to describe electromagnetism, the infinite range<sup>5</sup> interaction that occurs between particles with electrical charge. The  $\mathcal{L}_{QED}$  with this kinetic term is written as:

$$\mathcal{L}_{QED} = \bar{\Psi}(x)(i\gamma^\mu \partial_\mu - m)\Psi(x) - eQ\bar{\Psi}(x)\gamma^\mu A_\mu\Psi(x) - \frac{1}{4}F_{\mu\nu}(x)F^{\mu\nu}(x) \quad (1.9)$$

### 424 1.1.3 Electroweak interactions

#### 425 1.1.3.1 Weak interactions and Symmetries

426 The weak interaction is mediated by the  $W^+$ ,  $W^-$  and  $Z$  massive gauge  
 427 bosons. Due their large mass ( $m_{W^\pm} = 80.4$  GeV and  $m_Z = 91.2$  GeV), the  
 428 range of the interactions is restricted to  $\sim 10^{-18}$  m. It is responsible for  
 429 radioactive decays, nuclear fusions and flavour changing<sup>6</sup> decays of fermions  
 430 such as the decay of the muon ( $\mu^- \rightarrow e^- \bar{\nu}_e \nu_\mu$ ).

431 Another particularity of this interaction is that it is the only interaction  
 432 that violates several fundamental symmetries. There is a relation between  
 433 symmetries and conservations laws which is known as Noether's theorem.  
 434 Classical physics examples of how the symmetries leads to conserved quant-  
 435 ities are:

<sup>5</sup>Since the photon is (predicted to be) massless, the electromagnetic interaction has an infinite range.

<sup>6</sup>The leptonic charges are conserved.

- 436    • Invariance under change of time → Conservation of energy  
437    • Invariance under translation in space → Conservation of momentum  
438    • Invariance under rotation → Conservation of angular momentum

439    The three discrete symmetries that are fundamental for the SM formulation and are always hold for electromagnetic and strong interactions are:

- **Charge conjugation ( $\mathcal{C}$ ):** Replace positive quantum charges by negative charges and vice versa. It does not affect mass, energy, momentum or spin. Essentially, it is a transformation that switches all particles with their corresponding antiparticles.

$$\mathcal{C}\Psi(\vec{r}, t) = \bar{\Psi}(\vec{r}, t)$$

- **Parity ( $\mathcal{P}$ ):** Parity involves a transformation that changes the algebraic sign of the spatial coordinate system. It does not reverse time, mass, energy or other scalar quantities.

$$\mathcal{P} : \begin{pmatrix} x \\ y \\ z \end{pmatrix} \rightarrow \begin{pmatrix} -x \\ -y \\ -z \end{pmatrix} \quad \mathcal{P}\Psi(\vec{r}, t) = \Psi(-\vec{r}, t)$$

- **Time reversal ( $\mathcal{T}$ ):** Consists in flipping the sign of the time

$$\mathcal{T} : t \rightarrow -t \quad \mathcal{T}\Psi(\vec{r}, t) = \Psi(\vec{r}, -t)$$

441    The simultaneous combination of this three symmetries mentioned above  
442 results in the  $\mathcal{CPT}$  symmetry, a profound symmetry of QFT which is  
443 consistent through all experimental observations [14]. Meanwhile, the  $\mathcal{P}$ -  
444 symmetry and the  $\mathcal{C}$ -symmetry can be combined to create the  $\mathcal{CP}$ -symmetry,  
445 the product of the two transformations. The weak interaction violates  $\mathcal{P}$   
446 and  $\mathcal{C}$  symmetries. It also violates the combined  $\mathcal{CP}$ -symmetry. Therefore,  
447 through the CPT theorem [15], if the  $\mathcal{CP}$  is violated,  $\mathcal{T}$  is violated as well  
448 to preserve the  $\mathcal{CPT}$  invariance [16].

#### 449 **Parity and Charge conjugation violation**

450 Previously theorised by Lee and Yang [17], the confirmation of the non-  
451 conservation of  $\mathcal{P}$  in weak interactions arrived with the Wu experiment in  
452 1957 [18]. Studying the beta decay of the Cobalt-60, Wu and collaborators  
453 found that the neutrino and the antineutrino have the relative orientations  
454 of spin and linear momentum fixed. The neutrino spin is always opposite

455 to the linear momentum, this is called left-handed particles. Meanwhile, for  
 456 the antineutrinos, the momentum is always aligned in the same direction as  
 457 the spin (right-handed particles). This causes the weak interactions which  
 458 emit neutrinos or antineutrinos to violate the conservation of parity.

Only left-handed particles and right-handed antiparticles are sensitive to the weak force. Dirac fermion fields,  $\psi$ , exhibit chiral symmetry and the right and left handed chiral states can be expressed as:

$$\psi_L(x) = \frac{1}{2}(1 - \gamma_5)\psi(x) \equiv P_L\psi(x) \quad (1.10)$$

$$\psi_R(x) = \frac{1}{2}(1 + \gamma_5)\psi(x) \equiv P_R\psi(x) \quad (1.11)$$

with

$$\gamma^5 \equiv \gamma_5 \equiv \gamma^0\gamma^1\gamma^2\gamma^3 = \begin{pmatrix} 1 & 0 \\ 0 & 1 \end{pmatrix}$$

459 where  $P_L$  and  $P_R$  are known as projection operators. The last equality is  
 460 valid in the Dirac representation.

461 In the same year, the  $\mathcal{C}$  violation was found too [19]. **Describe how**  
 462 **the  $\mathcal{C}$  violation was discovered**

### 463 $\mathcal{CP}$ violation

464 While  $\mathcal{P}$  and  $\mathcal{C}$  are violated in a maximal way by the weak interactions,  
 465 the product of these two discrete transformations,  $\mathcal{CP}$ , is still a good sym-  
 466 metry (left-handed fermions  $\leftrightarrow$  right-handed fermions). Experiences such  
 467 as the Wu experiment respect the  $\mathcal{CP}$  symmetry and, in fact, in the  $\mathcal{CP}$  is a  
 468 symmetry of nearly all the observed phenomena. However, in 1964 Cronin  
 469 and Fitch discovered a slight (2%) violation of the  $\mathcal{CP}$  symmetry in the  
 470 decays of neutral kaons [20]. The  $\mathcal{CP}$  violation plays a fundamental role to  
 471 explain the dominance of matter over antimatter in the present universe.  
 472 More information about the matter-antimatter asymmetry can be found in  
 473 the dedicated text in Section 1.1.7.2.

474 Direct  $\mathcal{CP}$  violation is allowed in the SM if a complex phase is present  
 475 in the CKM matrix (described below). The “direct”  $\mathcal{CP}$  violation is a phe-  
 476 nomenon where the same decay process has a different probability for a  
 477 particle than for an antiparticle. An example of strong global  $\mathcal{CP}$  asym-  
 478 metry observed corresponds to the decay into two kaons and one pion. The  
 479 probability of  $B^+ \rightarrow \pi^+ K^+ K^-$  is 20% higher than for  $B^- \rightarrow \pi^- K^+ K^-$ .

### CKM matrix

The eigenstates that interact through weak interactions, known as “weak

eigenstates” ( $d'$ ,  $s'$ ,  $u'$ ), are different from the the physically observed mass eigenstates ( $d$ ,  $s$ ,  $u$ ). This make possible the charged-flavour-changing-weak decays trough the Cabibbo-Kobayashi-Maskawa (CKM) matrix. The CKM matrix,  $V_{CKM}$ , describes the mixing between the three generations of quarks in the SM. The coupling of two quarks  $i$  and  $j$  to a  $W$  boson is proportional to the CKM matrix element  $V_{ij}$ .

$$\begin{pmatrix} d' \\ s' \\ u' \end{pmatrix} = \begin{pmatrix} V_{ud} & V_{us} & V_{ub} \\ V_{cd} & V_{cs} & V_{cb} \\ V_{td} & V_{ts} & V_{tb} \end{pmatrix} \begin{pmatrix} d \\ s \\ u \end{pmatrix} \quad (1.12)$$

It is a  $3 \times 3$  unitary matrix described by four independent parameters: three angles ( $\theta_{ij}$ ) and one phase ( $\delta_{13}$ ). Different equivalent representations of the CKM matrix can be found in literature but the Particle Data Group recommends the standard CKM parameterisation:

$$V_{CKM} = \begin{pmatrix} c_{12}c_{13} & -s_{12}c_{13} & s_{13}e^{-i\delta_{13}} \\ -s_{12}c_{23} - c_{12}s_{23}s_{13}e^{i\delta_{13}} & -c_{12}c_{23} - s_{12}s_{23}s_{13}e^{i\delta_{13}} & s_{23}c_{13} \\ s_{12}s_{23} - c_{12}c_{23}s_{13}e^{i\delta_{13}} & -c_{12}s_{23} - s_{12}c_{23}s_{13}e^{i\delta_{13}} & c_{23}c_{13} \end{pmatrix} \quad (1.13)$$

where  $c_{ij} \equiv \cos \theta_{ij}$  and  $s_{ij} \equiv \sin \theta_{ij}$ , with  $i$  and  $j$  labelling the generations ( $i, j \in \{1, 2, 3\}$ ). The angles  $\theta_{12}$ ,  $\theta_{23}$  and  $\theta_{13}$  are known as Euler angles. The complex phase  $\delta_{13}$  allows the  $\mathcal{CP}$  violation [21]. There are other popular parameterisations such as the Kobayashi-Maskawa one or the Wolfenstein one.

The different elements of the CKM matrix are determined experimentally and are summarised in Table 1.3. As can be seen in this table, the largest values correspond to the diagonal elements of the CKM matrix. This implies that the processes that do not change the flavour are strongly preferred over the family-changing charged currents. For instance, for the top quark, the decay to any of the three down-type quarks is allowed but only  $|V_{td}|^2 \times 100\% = 0.0064\%$  of times will decay to a down quark and  $|V_{ts}|^2 \times 100\% = 0.14\%$  to a strange quark.

**check:** [23]

### 1.1.3.2 Electroweak unification

At energies above the scale of the mass of the weak vector bosons ( $E_{EW} \sim m_Z \sim m_W \sim 100 \text{ GeV}$ ), the electromagnetic and weak interactions are unified into the Electroweak (EW) force. In other words, electromagnetism and weak interactions are simultaneously described by the symmetry

CKM element	Value
$V_{ud}$	$0.97370 \pm 0.00014$
$V_{us}$	$0.2245 \pm 0.0008$
$V_{cd}$	$0.221 \pm 0.004$
$V_{cs}$	$0.984 \pm 0.011$
$V_{cb}$	$0.0410 \pm 0.0014$
$V_{ub}$	$0.0038 \pm 0.00024$
$V_{td}$	$0.0080 \pm 0.0003$
$V_{ts}$	$0.0380 \pm 0.0011$
$V_{tb}$	$1.013 \pm 0.030$

**Table 1.3:** Magnitude of the nine elements of the CKM matrix. The mean for the different measurements has been done by [22].

group  $SU(2)_L \times U(1)_Y$ . The subindex  $L$  refers to left-handed fields and  $Y$  to the weak hypercharge. In contrast, at low energies, these interactions are treated as independent phenomena, the electromagnetism is described QED and the weak interaction by Fermi's theory.

In the EW model (Glashow-Salam-Weinberg model), two new quantum numbers are assigned to the particles of the SM: the weak isospin ( $\vec{T}$ ) and  $Y$ . Here, the left-handed chiral states of fermions form isospin doublets ( $\chi_L$ ) with  $T_3 = \pm 1/2$  and the right-handed form chiral states are composed of isospin singlets ( $\chi_R$ ) with  $T_3 = 0$ . For a particle,  $T_3$  is the third component of the  $\vec{T}$ , which is related to the electric charge ( $Q$ ) and the  $U(1)$  hypercharge by Gell-Mann-Nishijima relation:

$$Q = T_3 + \frac{1}{2}Y \quad (1.14)$$

With this expression, the electromagnetic coupling and the electroweak couplings are connected. Having  $\chi_L$  with  $T_3 = \pm 1/2$  and  $\chi_R$  with  $T_3 = 0$  implies that a  $SU(2)$  weak interaction can rotate left-handed particles (i.e. convert a left-handed  $e^-$  into a left-handed  $\nu_e$  emitting a  $W^-$ ) but cannot do the same with right-handed.

Using the gauge invariance principle it is possible to find the QED and QCD Lagrangians, as it is described in Sections 1.1.2 and 1.1.4 respectively.

The free Lagrangian, as in the case of QED and QCD is:

$$\begin{aligned} \mathcal{L} &= i \sum_{j=1}^3 \bar{\Psi}(x) \gamma^\mu \partial_\mu \Psi(x) \\ &= i \sum_{j=1}^3 \bar{\chi}_L(x) \gamma^\mu \partial_\mu \chi_L(x) + i \sum_{k=1}^3 \bar{\chi}_R(x) \gamma^\mu \partial_\mu \chi_R(x) \end{aligned} \quad (1.15)$$

where the wave function  $\Psi$  has been spited into the left isospin doublets  $\chi_L$  and and right isospin singlets  $\chi_R$ . The indices  $j$  and  $k$  run over the three generations of the SM. This Lagrangian should be invariant when a gauge transformation under the  $SU(2)_L \times U(1)_Y$  symmetry group in the flavour space is applied:

$$\chi_L(x) \xrightarrow{SU(2)_L \times U(1)_Y} \chi'_L(x) = \exp\{i\alpha^n \tau_n\} \exp\{i\beta y\} \chi_L(x) \quad (1.16)$$

$$\chi_R(x) \xrightarrow{SU(2)_L \times U(1)_Y} \chi'_R(x) = \exp\{i\beta y\} \chi_R(x) \quad (1.17)$$

with  $\alpha, \beta \in \mathbb{R}$  and  $n \in \{1, 2, 3\}$ . This transformation is given by the generators of  $SU(2)_L \times U(1)_Y$ , i.e. the Pauli matrices  $(\tau_n)$  and the weak hypercharge  $y$ . Note that  $SU(2)_L$  transformation,  $\exp\{i\alpha^n \tau_{nu}\}$ , only acts on the doublet fields. This term containing the Pauli matrices is non-abelian like in QCD and, like in QCD, this leads to self-interacting terms.

To ensure invariance under  $SU(2)_L \times U(1)_Y$ , four different gauge fields have to be added (three from  $SU(2)$  and one from  $U(1)$ ). Four is also the correct number of gauge bosons needed to describe EW interactions:  $W^+$ ,  $W^-$ ,  $Z$  and Pgamma. While the three week isospin currents couple to the triplet of vector bosons  $W_\mu^n$  with  $n \in \{1, 2, 3\}$ , the weak hypercharge couples to an isosinglet  $B_\mu$ . The fields  $W_\mu^1$  and  $W_\mu^2$  are electrically charged whereas  $W_\mu^3$  and  $B_\mu$  are neutral fields. The EW covariant derivative is defined as:

$$D^\mu \chi_{L_j}(x) = [\partial_\mu - ig \frac{\tau_i}{2} W_\mu^i(x) - ig' \frac{y_j}{2} B_\mu(x)] \chi_{L_j}(x) \quad i \in [1, 2, 3] \quad (1.18)$$

$$D^\mu \chi_{R_j}(x) = [\partial_\mu - ig' \frac{y_j}{2} B_\mu(x)] \chi_{R_j}(x) \quad (1.19)$$

where  $g$  and  $g'$  are the interaction couplings to  $W_\mu^i$  isotriplet and the  $B_\mu$  isosinglet.

Using the derivatives in equations 1.18 and 1.19, the Lagrangian in 1.20 is already invariant under local  $SU(2)_L \times U(1)_Y$  transformations:

$$\mathcal{L} = i \sum_{j=1}^3 \bar{\chi}_L^j(x) \gamma^\mu D_\mu \chi_L^j(x) + i \sum_{k=1}^3 \bar{\chi}_R^k(x) \gamma^\mu D_\mu \chi_R^k(x) \quad (1.20)$$

Finally, if kinetic terms for the gauge bosons are included in 1.20, the EW SM Lagrangian is obtained:

$$\begin{aligned} \mathcal{L}_{EW} = & i \sum_{j=1}^3 \bar{\chi}_L^j(x) \gamma^\mu D_\mu \chi_L^j(x) + i \sum_{k=1}^3 \bar{\chi}_R^k(x) \gamma^\mu D_\mu \chi_R^k(x) \\ & - \frac{1}{4} W_{\mu\nu}^n(x) W_n^{\mu\nu}(x) - \frac{1}{4} B_{\mu\nu}(x) B^{\mu\nu}(x) \end{aligned} \quad (1.21)$$

521 Where the addition of kinetic terms gives rise to cubic and quadratic self-  
 522 interactions among the gauge fields. Note that the mass terms of the fields  
 523 are forbidden in order to ensure local gauge invariance and since the physical  
 524  $W^+$ ,  $W^-$  and  $Z$  bosons have a mass different from zero, for the moment  
 525 let's assume that something breaks the symmetry generating the observed  
 526 masses.

527 The in  $\mathcal{L}_{EW}$  in 1.21 can be divided in two different parts according to  
 528 the charge of the bosons: charged currents and neutral currents. Relating  
 529 the charged currents ( $W_\mu^1$  and  $W_\mu^2$ ) to the  $W^+$  and  $W^-$  bosons of the SM  
 530 and the neutral ( $W_\mu^3$  and  $B_\mu$ ) ones with the  $Z$  and  $\gamma$ , it is possible to build  
 531 linear combinations fo the original gauge fields that define the SM bosons.

Therefore, from the charged-current interactions, the  $W^+$  and  $W^-$  bosons are:

$$W^\pm \equiv \frac{1}{\sqrt{2}}(W_\mu^1 \mp i W_\mu^2) \quad (1.22)$$

While for the neutral-current these combinations can be defined as a rotation of the so called Weinberg (or weak mixing) angle  $\theta_W$ :

$$\begin{pmatrix} W_\mu^3 \\ B_\mu \end{pmatrix} \equiv \begin{pmatrix} \cos \theta_W & \sin \theta_W \\ -\sin \theta_W & \cos \theta_W \end{pmatrix} \begin{pmatrix} Z_\mu \\ A_\mu \end{pmatrix}$$

Rewriting this equation, the photon and  $Z$ -boson fields are

$$A_\mu = B_\mu \cos \theta_W + W_\mu^3 \sin \theta_W Z_\mu \quad = -B_\mu \cos \theta_W + W_\mu^3 \sin \theta_W \quad (1.23)$$

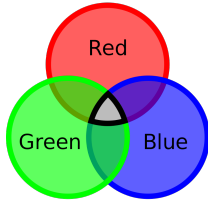
In order to ensure that this  $A_\mu$  is the one of QED, apart from the Gell-Mann-Nishijima relation (equation 1.14), it is requiered that the couplings of the  $\gamma$ ,  $W$  and  $Z$  satisfy the relation:

$$g \sin \theta_W = g' \cos \theta_W = e \quad (1.24)$$

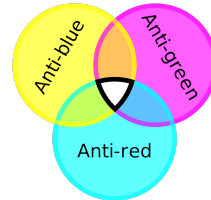
532 .

533 Within the unified EW model, once  $\theta_W$  is known, the properties of  
 534  $Z$  are specified. Current measurements of  $\theta_W$  give a value of  $\sin^2 \theta_W =$   
 535  $0.2310 \pm 0.0005$  [24].

536 There is no mass term for the bosons in the EW Lagrangian that has  
 537 been obtained in 1.21 by demanding the  $SU(2)_L \times U(1)_Y$  local invariance,  
 538 which enters in contradiction with the experimental observations for the  
 539  $W$  and  $Z$  bosons ( $m_{Z,W} \sim 80$  GeV). The introduction of such a mass term  
 540 would break the symmetry, however, the it is possible to add the mass for  
 541 the  $W$  and  $Z$  bosons without loosing the properties of the symmetry. The  
 542 method to do so is known as Englert–Brout–Higgs–Guralnik–Hagen–Kibble  
 543 mechanism or, more commonly, just as Higgs mechanism. This mechanism  
 544 is described in Section 1.1.5.



(a) Quark colours combine to be colourless.



(b) Antiquark colours also combine to be colourless.

**Figure 1.3:** Colour charge combinations for quarks and antiquarks

#### **545 1.1.4 Quantum chromodynamics**

##### **546 1.1.4.1 Quarks and colour**

547        Quantum chromodynamics (QCD) is QFT-based theory for describing  
 548        the strong interactions between quarks and gluons (partons). This type of  
 549        interaction is the responsible of the nuclear force, the one that acts between  
 550        the protons and neutrons of atoms binding them together. Without the  
 551        strong force, the protons inside the nucleus would push each other apart  
 552        due to the electromagnetic repulsion. It also holds the quarks within a  
 553        hadron together.

QCD is based in the  $SU(3)$  symmetry group and its name derives from the “colour” charge, an analogous to the electric charge of QED but for strong interactions. The colour charge was introduced in 1964 [25] to explain how quarks could coexist within some hadrons apparently having the same quantum state without violating the Pauli exclusion principle. To satisfy the Fermi-Dirac statistics it is necessary to add an additional quantum number, the colour, to the theory. Each species of quark ( $q$ ) may have three different colours ( $q^\alpha$ ,  $\alpha = 1, 2, 3$ ): red, green, blue. Baryons and mesons are described then by the colour singlet combinations:

$$B = \frac{1}{\sqrt{6}} \epsilon^{\alpha\beta\gamma} |q_\alpha q_\beta q_\gamma\rangle \quad M = \frac{1}{\sqrt{3}} \epsilon^{\alpha\beta} |q_\alpha \bar{q}_\beta\rangle$$

554 .

555        Additionally, it is postulated that all hadrons must have a global neut-  
 556        ral colour charge, i.e. the hadrons must be “colourless”. This assumption  
 557        is known as confinement hypothesis and it is made to avoid the existence  
 558        of non-observed extra states with non-zero colour. It is called colour con-  
 559        finement because it implies that it is not possible to observe free quarks  
 560        since they carry colour charge and, hence, they have to be confined within  
 561        colour-singlet combinations. Figure 1.3 depicts how different colours and  
 562        anticolours combine to create the “colourless” state.

563 **1.1.4.2 Gauge invariance for  $SU(3)$**

The dynamics of the quarks and gluons are controlled by the QCD Lagrangian. Using the power of the gauge invariance principle it is possible to deduce  $\mathcal{L}_{QCD}$  similarly to the reasoning developed in Section 1.1.2. Firstly, let's denote a quark field of colour  $\alpha$  and flavour  $f$  by  $q_f^\alpha$ . The vector  $q_f^T \equiv (q_f^1, q_f^2, q_f^3)$  is defined under the  $SU(3)$  colour space, meaning that each dimension corresponds to a colour. The Lagrangian

$$\mathcal{L}_0 = \sum_f \bar{q}_f (i\gamma^\mu \partial_\mu - m_f) q_f \quad (1.25)$$

is invariant under global  $SU(3)$  transformation in the colour space,

$$q_f^\alpha \rightarrow (q_f^\alpha)' = U_\beta^\alpha q_\alpha^\beta, \quad UU^\dagger = U^\dagger U = 1, \quad \det U = 1 \quad (1.26)$$

564 .

In the  $SU(N)$  algebra,  $SU(N)$  is the group of  $N \times N$  unitary matrices ( $U$ ) which can be written in the form  $U = \exp\{i(\lambda^a/2)\theta_a\}$  with  $a = 1, 2, \dots, N^2 - 1$ . Therefore, the  $SU(3)$  matrices can be written as

$$U = \exp\left\{i\frac{\lambda^a}{2}\theta_a\right\} \quad (1.27)$$

where the index  $a$  goes from 1 to 8 for the arbitrary parameter  $\theta_a$  and  $\frac{\lambda^a}{2}$ , which denotes the fundamental representation of the  $SU(3)$  algebra. The Einstein notation for summation over repeated indices is implied. The matrices  $\lambda^a$  are traceless and satisfy the commutation relations [12]:

$$\left[\frac{\lambda^a}{2}, \frac{\lambda^b}{2}\right] = if^{abc}\frac{\lambda^c}{2} \quad (1.28)$$

565 , being  $f^{abc}$  the  $SU(3)_C$  structure constants, which are real and totally 566 antisymmetric.

To satisfy the gauge invariance requirement, the Lagrangian has to be invariant under  $SU(3)$  local transformations, i.e, transformations in which the phase is dependent of the space-time location,  $\theta_a = \theta_a(x)$ . To fulfil the condition, the quark derivatives in the Lagrangian in 1.25 have to be substituted by covariant objects. Since there are eight independent gauge parameters, eight different gauge bosons  $G_a^\mu(x)$  are needed<sup>7</sup>. These bosons are the eight gluons and the new covariant objects are:

$$D^\mu q_f \equiv \left[ \partial_\mu + ig_s \frac{\lambda^a}{2} G_a^\mu(x) \right] q_f \equiv [\partial_\mu + ig_s G^\mu(x)] q_f$$

---

<sup>7</sup>The eightfold multiplicity of gluons is labeled by a combination of color and anticolor charge (e.g. red–antigreen)

- 567 The compact matrix notation is used  $[G^\mu(x)]_{\alpha\beta} \equiv \left(\frac{\lambda^a}{2}\right)_{\alpha\beta} G_a^\mu(x)$ .

To ensure that the covariant derivative  $(D^\mu q_f)$  transforms like the  $q_f$ , the transformation of the gauge fields are:

$$D^\mu \rightarrow (D^\mu)' = UD^\mu U^\dagger \quad G^\mu \rightarrow (G^\mu)' = UG^\mu U^\dagger + \frac{i}{g_s}(\partial_\mu U)U^\dagger \quad (1.29)$$

. The quark and gluon fields transform under an infinitesimal local transformation, i.e.  $\theta_a(x) = \delta\theta_a(x) \approx 0$ , the  $SU(3)_C$  unitary matrices (eq. 1.27) can be expressed as their first order expansion:

$$U = \exp\left\{i\frac{\lambda^a}{2}\theta_a(x)\right\} \approx 1 + i\left(\frac{\lambda^a}{2}\right)\delta\theta_a(x)$$

and, consequently, the transformations for the colour-vector field (eq. 1.26) and gluon field (eq. 1.29) become:

$$\begin{aligned} q_f^\alpha &\rightarrow (q_f^\alpha)' = q_f^\alpha + \left(\frac{\lambda^a}{2}\right)_{\alpha\beta}\delta\theta_a q_f^\beta \\ G_a^\mu &\rightarrow (G_a^\mu)' = G_a^\mu - i\frac{i}{g_s}\partial_\mu(\delta\theta_a) - f^{abc}\delta\theta_b G_c^\mu \end{aligned}$$

568 .

569 In contrast to the transformation for the photon field in QED (equation 1.5), the non-commutativity<sup>8</sup> of the  $SU(3)_C$  matrices give rise to an  
 570 additional term involving the gluon fields themselves  $(-f^{abc}\delta\theta_b G_c^\mu)$ , as the  
 571 relation 1.28 expresses. For constant  $\delta\theta_a$ , the transformation rule for the  
 572 gauge fields is expressed in terms of the structure constants  $f^{abc}$ ; thus, the  
 573 gluon fields belong to the adjoint representation for the colour group. There  
 574 is a unique coupling at  $SU(3)_C$ ,  $g_s$ . All the colour-triplet flavours couple to  
 575 the gluon fields with exactly the same interaction strength.

It is necessary to introduce the corresponding fields strengths to build a gauge-invariant kinetic terms for the gluon fields.

$$\begin{aligned} G^{\mu\nu} &\equiv -i\frac{-i}{g_s}[D^\mu, D^\nu] = \partial_\mu G^\nu - \partial_\nu G^\mu + ig_s[G^\mu, G^\nu] \equiv \frac{\lambda^a}{2}G_a^{\mu\nu}(x) \\ G_a^{\mu\nu} &\equiv \partial_\mu G_a^\nu - \partial_\nu G_a^\mu - g_s f^{abc}G_b^\mu G_c^\nu \end{aligned}$$

Under a  $SU(3)_C$  transformation,

$$G^{\mu\nu} \rightarrow (G^{\mu\nu})' = UG^{\mu\nu}U^\dagger \quad (1.30)$$

---

<sup>8</sup>Because the generators of  $SU(3)$  do not commute, QCD is known as non-Abelian gauge theory.

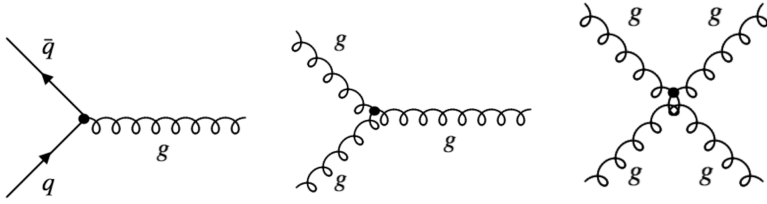


**Figure 1.4:** The predicted QCD interaction vertices arising from the requirement of  $SU(3)_C$  local gauge invariance. The presence of the triples and quadruple gluon vertices is possible to the Non-Abelian nature of  $SU(3)_C$ .

and the colour trace  $\text{Tr}(G^{\mu\nu}G_{\mu\nu}) = \frac{1}{2}G^{\mu\nu}G_{\mu\nu}$  remains invariant. Normalising the gluon kinetic term, the  $SU(3)_C$  invariant QCD Lagrangian is obtained:

$$\mathcal{L}_{QCD} \equiv -\frac{1}{4}G_a^{\mu\nu}G_{\mu\nu}^a + \sum_f \bar{q}_f(i\gamma^\mu D_\mu - m_f)q_f \quad (1.31)$$

577 Note how the gluon-gluon vertex is find by demanding the gauge invari-  
 578 ance under local  $SU(3)_C$  transformation. A mass term is forbidden for the  
 579 gluon fields by the  $SU(3)_C$  gauge symmetry because a something of the form  
 580  $\frac{1}{2}m_G^2 G_a^\mu G_\mu^a$  would not be invariant under the transformation in 1.29. The  
 581 gluons are, then, predicted by the theory to be spin-1 massless particles.

582 Thanks to the colour symmetry properties, this Lagrangian looks very  
 583 simple and all its interactions depend on the strong coupling constant,  $g_s$ .  
 584 In contrast to the Lagrangian derived for QED (eq 1.7), in  $\mathcal{L}_{QCD}$  the boson  
 585 field have a self-interacting term. This gluon self-interactions give rise to the  
 586 triple and quadratic gluon vertex (center and right diagrams in Figure 1.4).  
 587 This self-interactions among the gluon fields can explain features the asymp-  
 588 totic freedom and confinement, properties that were not present in QED.  
 589 The asymptotic freedom causes interactions between particles to become  
 590 asymptotically weaker as the energy scale increases and the corresponding  
 591 length scale decreases. The confinement implies that the strong forces in-  
 592 crease with the distance, therefore, as two colour charges are separated,  
 593 at some point it becomes energetically favorable for a new quark-antiquark  
 594 pair to appear rather than keep getting further. This new quarks bond with  
 595 the previous two, preventing single quarks to be isolated. This mechanism,  
 596 depicted in Figure 1.5, explains why the strong interaction is responsable  
 597 for keeping the quarks together forming hadrons.

598 **Maybe, expand the QCD Lagrangian in 1.31 and explain its  
 599 different elements.**



**Figure 1.5:** The QCD colour confinement explains the inseparability of quarks inside a hadron in spite of investing ever more energy. In this example, the mechanism is shown for a meson.

### 600 1.1.5 Particle masses

For the QED Lagrangian,  $\mathcal{L}_{QED}$  (eq. 1.9), it is clear how the mass of the photon must be zero in order to satisfy the  $U(1)$  local gauge symmetry because, if a mass term for the vector gauge field  $A_\mu$  is included, the  $\mathcal{L}_{QED}$  would be:

$$\mathcal{L}_{QED} = \bar{\Psi}(x)(i\gamma^\mu\partial_\mu - m)\Psi(x) - eQ\bar{\Psi}(x)\gamma^\mu A_\mu\Psi(x) - \frac{1}{4}F_{\mu\nu}(x)F^{\mu\nu}(x) + \frac{1}{2}m_\gamma^2 A_\mu A^\mu$$

and, with the  $U(1)$  transformation in equation 1.5, the new mass term becomes:

$$\frac{1}{2}m_\gamma^2 A_\mu A^\mu \rightarrow \frac{1}{2}m_\gamma^2 (A_\mu + \frac{1}{e}\partial_\mu\theta)(A^\mu + \frac{1}{e}\partial^\mu\theta) \neq \frac{1}{2}m_\gamma^2 A_\mu A^\mu$$

601 Confirming that the photon mass term is not invariant under local  $U(1)$   
 602 and, consequently, that the photon must be massless to satisfy the gauge  
 603 invariance. Experimental efforts to measure the mass of the photon have  
 604 set an upper limit of  $m_\gamma \leq 1 \times 10^{-18}$  eV [26].

605 With the Lagrangian of QCD in equation 1.31 happens the same, the  
 606 mass term for the gluon fields are forbidden by the  $SU(3)_C$  gauge symmetry.  
 607 Therefore, the mediating bosons for the strong interactions are massless as  
 608 well (experimentally, a mass as large as upper limits of a few MeV have  
 609 been seted, see [27]).

610 While the prohibition of mass terms for the bosons of QED and QCD is  
 611 not a problem, this requirement also applies to the  $SU(2)_L$ . This condition  
 612 enters into open contradiction with the measurements of large masses for  
 613 the  $W$  ( $m_W = 80.370 \pm 0.007$  (stat.)  $\pm 0.017$  (syst.) MeV[28]) and  $Z$  ( $m_Z =$   
 614  $91.1852 \pm 0.0030$  GeV [29]) bosons of weak interactions. **<- to do: Aquí  
 615 no estoy utilizando las mismas medidas de la masa de  $m_W$  y  $m_Z$   
 616 que antes. He de escoger una and stick to it.**

617 For weak interactions, the problem of massless particles do not only  
 618 affect the bosons. Since under the  $SU(2)_L$  transformations left-handed  
 619 particles transform as weak isospin doubles and right-handed particles as

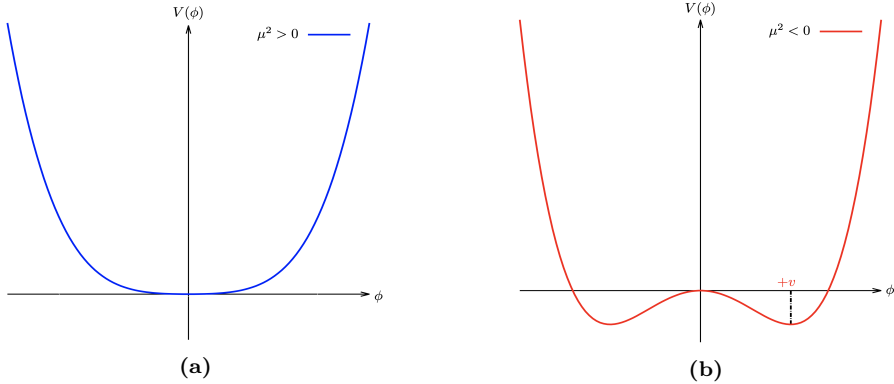


**Figure 1.6:** The potential  $V(\phi)$  of Lagrangian 1.32 for (a)  $\mu^2$  positive and (b) negative.

620 isospin singlets, the mass term of a spinor field  $\Psi$  written as chiral states  
 621 also breaks the required gauge invariance:  $-m\bar{\Psi}(x)\Psi(x) = -m\bar{\Psi}(x)(P_R +$   
 622  $P_L)\Psi(x) = -m(\bar{\Psi}_R(x)\Psi_L(x) + \bar{\Psi}_L(x)\Psi_R(x))$

623 The Higgs mechanism describes how both the  $W$  and  $Z$  bosons and the  
 624 fermions acquire mass without breaking the local gauge symmetry of the  
 625 SM.

#### 626 1.1.5.1 The Higgs mechanism

##### Goldstone theorem and spontaneous symmetry breaking

For a scalar field  $\phi$  with a Lagrangian of the form:

$$\mathcal{L} = \frac{1}{2}\partial_\mu\phi_i\partial^\mu\phi_i - V(\phi) \text{ where } V(\phi) = \frac{1}{2}\mu^2\phi_i\phi_i + \frac{1}{4}\lambda(\phi_i\phi_i)^2 \quad (1.32)$$

This Lagrangian is invariant under  $\phi_i \rightarrow \phi'_i = R_{ij}\phi_j$ , where  $R_{ij}$  are rotational matrices in 4-dimensions. The mass term is the one with  $\phi_i\phi_i$  and the parameter  $\lambda$  has to be positive for  $\mathcal{L}$  to describe a physical system, if  $\lambda < 0$  the potential is unbounded from below. Contrary, the parameter  $\mu^2$  can be either positive or negative. As depicted in Figure 1.6a, if  $\mu^2 > 0$ , the vacuum expectation value (i.e. minimum of potential) is located at the origin  $\phi_0$  and this  $\mathcal{L}$  would describe a spin-0 particle of mass  $\mu$ . However, if  $\mu^2 < 0$ , the potential  $V(\phi)$  has the form of Figure 1.6a and  $\mathcal{L}$  would not represent anymore the Lagrangian of a particle of mass  $\mu$ . The vacuum expectation value is now multivalued:

$$\phi_0 = \pm\sqrt{-\frac{\mu^2}{\lambda}} \equiv \pm v$$

Expanding the field around the minima at  $\phi_i = (0, 0, 0, v)$ , the  $\mathcal{L}$  becomes:

$$\begin{aligned}\mathcal{L} = & \frac{1}{2} \partial_\mu \sigma \partial^\mu \sigma + \mu^2 \sigma^2 - \sqrt{\mu^2 \lambda} \sigma^3 - \frac{1}{4} \lambda^4 \\ & + \frac{1}{2} \partial_\mu \pi_i \partial^\mu \pi_i - \frac{1}{4} \lambda (\pi_i \pi_i)^4 - \lambda v \pi_i \pi_i \sigma - \frac{1}{2} \pi_i \pi_i \sigma^2\end{aligned}\quad (1.33)$$

where  $i$  runs from 1 to 3. Here  $\sigma = \phi_4 - v$  and  $\pi_i = \phi_i$  are new boson fields, being the latter massless and the with a mass of  $m_\sigma^2 = -2\mu^2$ . The new terms break the original symmetry because the symmetry of the Lagrangian is not longer a symmetry of the vacuum, it has been spontaneously broken. One massive  $\sigma$  boson and three massless  $\pi_i$  bosons with a residual  $O(3)$  symmetry have appeared. This is a consequence of the Goldstone theorem which states that “for a continuous symmetry group  $\mathcal{G}$  spontaneously broken down to a subgroup  $\mathcal{H}$ , the number of broken generators is equal to the number of massless scalars that appear in the theory” [30]. Therefore, since the  $O(N)$  group has  $N(N-1)/2$  generators, the  $O(N-1)$  has  $(N-1)(N-2)/2$  and, hence,  $N-1$  Goldstone bosons appear. The example shown is for  $N=4$ .

### The Higgs mechanism in the SM - Bosons

To apply this mechanism to the SM, it is necessary to generate mass for the  $W^+$ ,  $W^-$  and  $Z$  bosons while keeping the photon massless. In order to do so, the EW symmetry group  $SU(2)_L \times U(1)_Y$  has to be broken into a  $U(1)$  subgroup describing electromagnetism. A gauge-invariant interaction that gives masses to fermions without mixing chiral components is introduced by defining a  $SU(2)$  isospin doublet of complex scalar field with hypercharge  $Y=1$ :

$$\Phi = \begin{pmatrix} \phi^+ \\ \phi_0 \end{pmatrix}$$

Being  $\phi^+$  positively charged and  $\phi^0$  neutral. The Lagrangian  $\mathcal{L}_{Higgs}$  has to be added to the  $\mathcal{L}_{EW}$  in 1.21.

$$\mathcal{L}_{Higgs} = (D_\mu \Phi)^\dagger (D^\mu \Phi) - V(\Phi) \text{ where } V(\Phi) = \mu^2 \Phi^\dagger \Phi + \lambda (\Phi^\dagger \Phi)^2$$

with  $\lambda > 0$  required for vacuum stability. When  $\mu^2 > 0$ , the minimum of the potential occurs when both fields ( $\phi^+$  and  $\phi^0$ ) are at zero. If  $\mu^2 < 0$ , the minimum of the potential has an infinite number of degenerate states that satisfy  $\Phi^\dagger \Phi = \mu^2 / 2\lambda$  and the physical vacuum state will correspond to any particular point on the circle of Figure 1.7. Having to chose a particular point breaks the global  $U(1)$  symmetry of the Lagrangian. Without loss of generality, in this scenario, the ground state  $\Phi_0$  can be chosen to be:

$$\Phi_0 = \frac{1}{\sqrt{2}} \begin{pmatrix} 0 \\ v \end{pmatrix} \text{ where } v = 2\sqrt{\frac{\mu^2}{\lambda}}$$

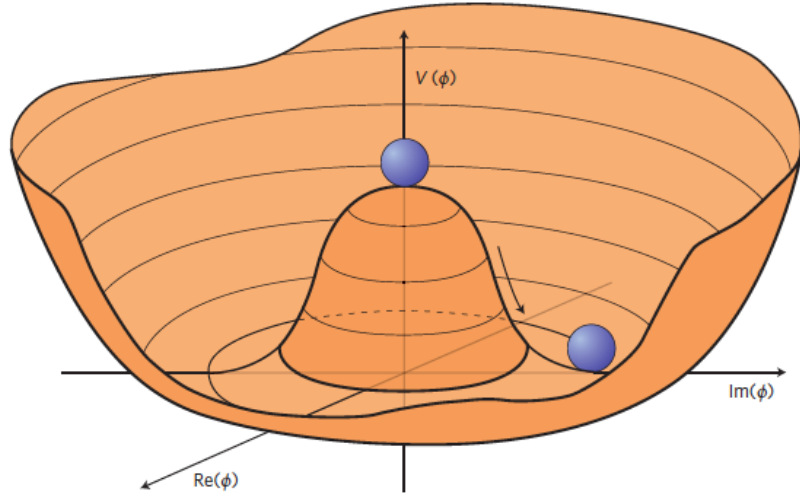


**Figure 1.7:** An illustration of the Higgs potential  $V(\Phi)$  in the case of  $\mu^2 < 0$ . Choosing any particular point in the circle defined by  $v$  spontaneously breaks the  $U(1)$  rotational symmetry. This type of potential is frequently called “Mexican hat”.

638 being  $v$  the vacuum expectation value. This defines the already mentioned  
639 circle in the minimum of  $V(\Phi)$  in the  $\mu^2 < 0$  scenario.

The Lagrangian density must be formulated in terms of deviations from one of these ground states. This can be done by introducing an excitation,  $h(x)$ , that can be understood as a small deviation of the field from the ground state. Accordingly, the fields can be expanded around the minimum as:

$$\Phi = \frac{1}{\sqrt{2}} \begin{pmatrix} 0 \\ v + h(x) \end{pmatrix} \exp\{i\chi(x)\}$$

The new field  $\chi(x)$  can be set to zero in the so called “unitary gauge”.

$$\Phi = \frac{1}{\sqrt{2}} \begin{pmatrix} 0 \\ v + h(x) \end{pmatrix} \quad (1.34)$$

Expanding the covariant derivative of the  $\mathcal{L}_{Higgs}$ :

$$\begin{aligned} (D_\mu \Phi)^\dagger (D^\mu \Phi) &= \left| \left( \partial_\mu + ig \frac{\tau^k}{2} W_\mu^k(x) + ig' \frac{y}{2} B_\mu \right) \right|^2 \\ &= \frac{1}{2} \begin{vmatrix} \left( \partial_\mu + i \frac{1}{2} (g W_\mu^3 + g' \frac{y}{2} B_\mu) \right) & \left( i \frac{g}{2} (W_\mu^1 - i W_\mu^2) \right) \\ \left( i \frac{g}{2} (W_\mu^1 - i W_\mu^2) \right) & \left( \partial_\mu - i \frac{1}{2} (g W_\mu^3 - g' \frac{y}{2} B_\mu) \right) \end{vmatrix} \begin{pmatrix} 0 \\ v + h \end{pmatrix}^2 \\ &= \frac{1}{2} (\partial_\mu h)^2 + \frac{1}{8} (v + h)^2 |W_\mu^1 - i W_\mu^2|^2 \\ &\quad + \frac{1}{8} (v + h)^2 |g W_\mu^3 - g' B_\mu|^2 + (\text{interaction terms}) \end{aligned}$$

Where the  $\tau_k$  with  $k = 1, 2, 3$  are the Pauli Matrices. In this equation there are terms mixing the  $W^3$  and the  $B_\mu$  fields that, by using the physical fields defined in equation 1.1.3.2, should disappear since the physical bosons do not mix. Applying the relation 1.1.3.2 into the covariant derivative,

$$(D_\mu \Phi)^\dagger (D^\mu \Phi) = \frac{1}{2} + \frac{g^2 v^2}{4} W_\mu^+ W^{-\mu} + \frac{g^2 v^2}{8 \cos^2 \theta_W} Z_\mu Z^\mu + 0 A_\mu A^\mu$$

, the  $W^+$ ,  $W^-$  and  $Z$  bosons have finally acquired mass. Through the Higgs mechanism, their masses within the SM are:

$$M_W = \frac{1}{2} g v \quad M_Z = \frac{1}{2} \frac{g v}{\cos \theta_W}$$

640 Additionally, a new scalar field  $h(x)$  has appeared with its correspondent  
 641 mass term, the Higgs field. Note that the  $h(x)$  was introduced as a perturba-  
 642 tion from the ground state of the Higgs potential  $V(\Phi)$ , so the Higgs boson  
 643 can be understood as an excitation of the Higgs potential. Apart from cou-  
 644 pings to the electroweak gauge fields, the Higgs field has also self-interaction  
 645 vertices. The mass of this boson is  $m_H = \sqrt{2}\mu$ .

With this covariant term, the Higgs Lagrangian density of the system is obtained:

$$\begin{aligned} \mathcal{L}_{Higgs} = & \frac{1}{2} (\partial_\mu h) (\partial^\mu h) + \frac{g}{4} (v + h)^4 W_\mu W^\mu + \frac{g^2}{8 \cos^2 \theta_W} (v + h)^2 Z_\mu Z^\mu \\ & + \frac{\mu^2}{2} (v + h)^2 - \frac{\lambda}{16} (v + h)^4 \end{aligned}$$

and expressing it in terms of the boson masses and coupling parameters, it can be written as:

$$\begin{aligned} \mathcal{L}_{Higgs} = & \frac{1}{2} (\partial_\mu h) (\partial^\mu h) - \frac{1}{2} m_H^2 h^2 + \frac{1}{2} m_W W_\mu W^\mu + \frac{1}{2} m_Z Z_\mu Z^\mu + g m_W h W_\mu W^\mu \\ & + \frac{g^2}{4} W_\mu W^\mu + g \frac{m_Z}{2 \cos \theta_W} h Z_\mu Z^\mu - g^2 \frac{1}{4 \cos^2 \theta_W} h^2 Z_\mu Z^\mu - g \frac{m_H^2}{4 m_W} h^3 \\ & - g^2 \frac{m_H^2}{32 m_W^2} h^4 + \text{const.} \end{aligned} \tag{1.35}$$

646 As can be seen in the Lagrangian 1.35, the coupling strengths of the  $W$  and  
 647  $Z$  fields to the Higgs are proportional to  $m_W$  and  $m_Z$  respectively. This  
 648 is why it is said that the more a fundamental particle interacts with the Higgs  
 649 boson, the more massive it is.

### The Higgs mechanism in the SM - Fermions

The Higgs mechanism for spontaneous symmetry breaking of the  $SU(2)_L \times U(1)_Y$  gauge group of the SM generates the masses of the  $W^\pm$  and  $Z$  bosons. For originating the mass of the fermions without violating the EW gauge symmetry a similar procedure is carried but taking into account that the left-handed particles transform different than the right-handed. To do so, additional terms including the Yukawa couplings are added into the Lagrangian. These terms are of the form:

$$-y_f(\bar{\chi}_L^f \Phi \chi_R^f + \bar{\chi}_R^f \Phi^\dagger \chi_L^f)$$

where the  $f$  superindex runs over all quarks and charged leptons. It is usual to express the second part of the sum just as “plus hermitic conjugate” (“+ h.c.”). Note that the hermitic conjugate part is necessary to ensure that expression fulfills the requirement for a hermitian operator to be self-adjoint in a complex Hilbert space. The different  $y_f$  constants are known as Yukawa couplings of the particle  $f$  to the Higgs field. The Higgs doublet is denoted by  $\Phi$ . For the electron  $SU(2)$  doublet, the element with this coupling can be written as:

$$\mathcal{L}_e = -y_e \left[ (\bar{\nu}_e \bar{e})_L \begin{pmatrix} \phi^+ \\ \phi^0 \end{pmatrix} e_R + \bar{e}_R (\phi^{+*} \phi^{0*}) \begin{pmatrix} \nu_e \\ e \end{pmatrix}_L \right] \quad (1.36)$$

Here,  $y_e$  is the Yukawa coupling of the electron to the Higgs boson. After spontaneously breaking the symmetry as it is done in eq. 1.34, the Lagrangian in 1.36 becomes:

$$\mathcal{L}_e = \frac{-y_e}{\sqrt{2}} v (\bar{e}_L e_R + \bar{e}_R e_L) + \frac{-y_e}{\sqrt{2}} h (\bar{e}_L e_R + \bar{e}_R e_L) \quad (1.37)$$

The  $y_e$  is not predicted by the Higgs mechanism, but can be chosen to be consistent with the observed electron mass ( $m_e$ ) so that  $y_e = \sqrt{2} m_e / v$ . Using this relation, the Lagrangian in 1.37 becomes:

$$\mathcal{L}_e = -m_e \bar{e} e - \frac{m_e}{v} \bar{e} e h \quad (1.38)$$

650 The first element of the Lagrangian in 1.38 gives mass to the electron and  
 651 gives rise to the coupling of the electron to the Higgs fields in its non-  
 652 zero vacuum expectation. The second term represents the coupling of the  
 653 electron and the Higgs boson itself.

654 The non-zero vacuum expectation value occurs only in the neutral part  
 655 of the Higgs doublet (the lower in  $\Phi = \begin{pmatrix} \phi^+ \\ \phi^0 \end{pmatrix}$ ) due to the form in the  
 656 ground state in 1.34. This implies that the combination  $\bar{\chi}_L^f \Phi \chi_R^f + \bar{\chi}_R^f \Phi^\dagger \chi_L^f$

657 can only generate masses for the fermions in the lower component of an  
 658  $SU(2)$  doublet, i.e. the charged leptons and the down type quarks. Putting  
 659 aside the procedure to give mass to the up-type quarks, this explains why  
 660 the neutrinos do not get mass through the Higgs mechanism.

For the up-type quarks, a gauge invariant term can be constructed from  $\bar{\chi}_L^f \Phi_c \chi_R^f + \bar{\chi}_R^f \Phi_c^\dagger \chi_L^f$ :

$$\mathcal{L}_u = y_u (\bar{u} \bar{d})_L \begin{pmatrix} -\phi^{0*} \\ \phi^- \end{pmatrix} u_R + \text{h.c.}$$

Applying the symmetry breaking:

$$\mathcal{L}_u = \frac{-y_u}{\sqrt{2}} v (\bar{u}_L u_R + \bar{u}_R u_L) + \frac{-y_u}{\sqrt{2}} h (\bar{u}_L u_R + \bar{u}_R u_L)$$

with a Yukawa coupling between the up quark and the boson  $y_u = \sqrt{2} m_u/v$ , resulting in:

$$\mathcal{L}_u = -m_u \bar{u} u - \frac{m_u}{v} \bar{u} u h$$

661 .

Therefore, for Dirac fermions, mass terms that let the Lagrangian invariant under local gauge transformations can be constructed from

$$\mathcal{L} = -y_f [\bar{\chi}_L^f \Phi \chi_R^f + (\bar{\chi}_R^f \Phi \chi_L^f)^\dagger] \quad \text{or} \quad \mathcal{L} = y_f [\bar{\chi}_L^f \Phi_c \chi_R^f + (\bar{\chi}_R^f \Phi_c^\dagger \chi_L^f)^\dagger]$$

. The left Lagrangian is used for the leptons and down-type quarks, while the right one is used for the up-type quarks. These elements give rise not only to the mass of the fermions but also to the interaction strengths between these fermions and the Higgs boson. The Yukawa coupling of the fermions to the Higgs field is given by:

$$y_f = \sqrt{2} \frac{m_f}{v} \tag{1.39}$$

662 where the Higgs vacuum expectation value is fixed by the Fermi coupling  
 663  $G_F$  and is measured to be  $v = \sqrt{2} G_F \approx 246.22 \text{ GeV}$ . The  $G_F$  is measured  
 664 from the  $\mu^+$  lifetime [31]. The  $G_F$  is also used to determine the magnitude  
 665 of the elements in the CKM matrix.

666 The value of fermionic masses is not predicted by the SM but obtained  
 667 through experimental observations. Given the  $m_{top} = 172.76 \pm 0.30 \text{ GeV}$ ,  
 668 it is of particular interest the Yukawa coupling of the top quark to the  
 669 Higgs field,  $y_t$ , which is almost exactly equal to one. It is important to  
 670 verify this because deviation of the measured  $y_t$  from the SM prediction  
 671 would be a proof of new phenomena beyond the SM that could provide an  
 672 answer to several open questions concerning the fundamental interactions  
 673 of elementary particles.

674 **1.1.6 Charge-Parity**675 **Probably, this section is gonna be absorbed by 1.1.3**676 **1.1.7 Wrap up**

677 Perhaps the ultimate and definitive (if talking about definitive makes  
 678 any sense) theory of particle physics is a simple equation with a small num-  
 679 ber of free parameters. Meanwhile, the SM is here, and while it is not  
 680 the ultimate theory, it is unquestionably one of modern physics' greatest  
 681 successes. Despite its achievements, many questions remain unsolved.

682 **1.1.7.1 The parameters of the Standard Model**

The SM contains 25 free parameters that must be determined through observation and experimentation. These are the masses of the twelve fermions (assuming color variations and antiparticles are not viewed as separate fermions) or, more precisely, the twelve Yukawa couplings to the Higgs field:

$$m_{\nu_1}, m_{\nu_2}, m_{\nu_3}, m_e, m_\mu, m_\tau, m_u, m_d, m_c, m_s, m_t \text{ and } m_b$$

The three coupling constants of describing the strength of the gauge interactions

$$g, g' \text{ and } g_s$$

the two parameters describing the Higgs potential ( $\mu$  and  $\lambda$ ) or, equivalently, its vacuum expectation value and the Higgs mass

$$v \text{ and } m_h$$

The three mixing angles and the complex phase of the CKM matrix and the four of the PMNS matrix (the Pontecorvo–Maki–Nakagawa–Sakata matrix is similar to the CKM matrix but for the mixing of neutrino-mass eigenstates with neutrino-falvour eigenstates):

$$\theta_{12}, \theta_{13}, \theta_{23}, \rho_{13}, \theta'_a, \theta'_b, \theta'_c \text{ and } \theta'_d$$

683 From the 25 free parameters of the SM, 14 are associated to the Higgs  
 684 field, eight with the flavour sector and only three with the gauge interac-  
 685 tions.

---

### 686 1.1.7.2 Problems with the Standard Model

687 While the SM is very good theory that has passed rigorous testing, this  
 688 is not the ending of the story, there are several limitations of the SM and  
 689 a variety phenomena that it does not explain. The SM does not cover all  
 690 questions in the universe and, hence, physicist continue looking for better  
 691 theories to explain more. There is a long list of small and minor issues with  
 692 the SM in the following pages only the most relevant ones are described.

693 **Gravity**

694 Gravity is the first force that any person learns about and the one known  
 695 by the humankind for the most time. The SM describes all the other funda-  
 696 mental interactions but this one. In the Table 1.1, the four forces are  
 697 presented along with the theories to describe them. While QCD, QED and  
 698 EW interactions are part of the SM, the GR is not. GR is a geometric the-  
 699 ory that currently describes the gravitation in modern physics. Some of the  
 700 suggested solutions to integrate gravitational interactions in the SM consist  
 701 in postulating a new force carrier particle, the “graviton”, that mediates  
 702 this interaction in a similar way to how the gauge bosons were proposed.  
 703 Other explanations state that the gravity can only be described by a deeper  
 704 theory in which the time-space structure is not flat like it is in the SM but  
 705 dynamic.

706 **Neutrino masses**

707 According to the SM the neutrinos are massless, nevertheless, many ex-  
 708 periments confirm that this is not true [32]. This is due to a property of  
 709 neutrinos that allows them to change their flavour while traveling through  
 710 the space, this feature is known as “neutrino oscillations”. Each of the  
 711 three neutrino flavours ( $\nu_e$ ,  $\nu_\mu$ ,  $\nu_\tau$ ) is a linear combination of three dis-  
 712 crete neutrino-mass eigenstates ( $\nu_i$  with  $i \in \{1, 2, 3\}$ ) with mass eigenvalues  
 713 ( $m_i$ ). While the neutrino oscillation experiments could probe the squared  
 714 neutrino-mass eigenvalues ( $\Delta m_{ij}^2$ ), both the total scale of the masses and the  
 715 sign of  $\Delta m_{ij}$  remains as some the most relevant open questions in particle  
 716 physics. Regarding to the sign of  $\Delta m_{ij}$ , it is known that the mass of  $\nu_2$   
 717 is slightly higher than  $\nu_1$  ( $\Delta m_{21}^2 \equiv m_2^2 - m_1^2 \sim 10^{-4}$  eV) but for the third  
 718 mass eigenstate it has not been measured yet whether it is greater (normal  
 719 ordering) or lower (inverted ordering) than the other two. This is referred  
 720 as “hierarchy problem” and is depicted in Figure 1.8. Nevertheless, the  
 721 absolute square difference is known ( $\Delta m_{31}^2 \equiv |m_3^2 - m_1^2| \sim 10^{-3}$  eV).

722 Non-zero neutrino masses opened an interesting portal on beyond SM  
 723 physics and, even though neutrinos are very elusive when it comes to detect

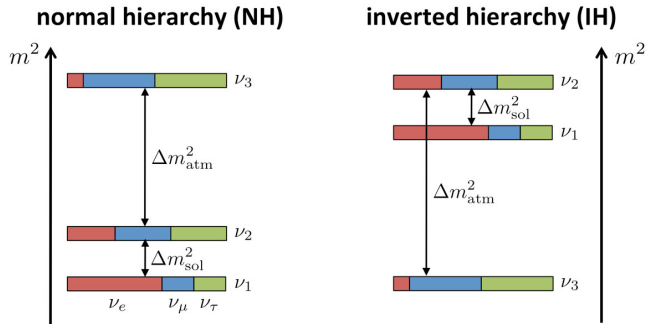


**Figure 1.8:** Two potential mass orderings of neutrinos are the normal ordering (normal hierarchy) and the inverted ordering (inverted hierarchy)

them, some next-generation experiments such as Dune are very promising when it comes to set competitive and model independent limits on neutrino masses.

Regarding to the nature of this mass, one could add mass terms to the SM as it is done in Section 1.1.5.1 for the up-type quarks but the origin of the neutrino masses is still not known. It is possible that this mass comes from the Higgs mechanism, however, this is not clear. Also, if neutrinos gained mass through Yukawa interaction, it would imply the presence of right-handed neutrinos, which has not been observed.

### 733 Matter-antimatter asymmetry

In principle, the Big Bang should have produced an equal amount of matter and antimatter which would all have then annihilated, leaving behind an empty Universe filled with EM radiation. However, everything we see now is essentially totally constituted of matter, from the tiniest life forms on Earth to the greatest celestial objects. In comparison, there isn't a lot of antimatter around.

By looking at the CMB radiation, which contain the residual photons of the Big Bang, researchers have determined that there was a symmetry between the matter and antimatter content in the early universe. For every  $3 \times 10^9$  antimatter particles, there were  $3 \times 10^9$  and 1 matter particles. The matter and antimatter annihilate and produced the CMB and the remaining 1 part turned into all the stars and galaxies that are seen. The field of cosmology that studies the processes that produced an asymmetry between leptons and antileptons in the very early universe is called leptogenesis.

Researches carried during the last few decades have revealed that the laws of nature do not equally apply to matter and antimatter. So far, the

750 only non-trivial difference between matter and antimatter found is the  $\mathcal{CP}$   
 751 asymmetry (or  $\mathcal{CP}$  violation, which has been introduced in Section 1.1.3).  
 752 Alas, the quantity of  $\mathcal{CP}$  asymmetry included in the SM is insufficient to  
 753 explain the composition of the observable universe and, hence, extensive  
 754 searches of new sources of  $\mathcal{CP}$  violation are being carried.

755 In this context, the studies described in this thesis are part of the seek  
 756 of new  $\mathcal{CP}$ -violation sources. As Section 1.4.2 details, the observation of a that  
 757 cross-section greater than the one predicted by the SM would imply a that  
 758 Higgs-single-top-quark associated production does not conserve  $\mathcal{CP}$ .

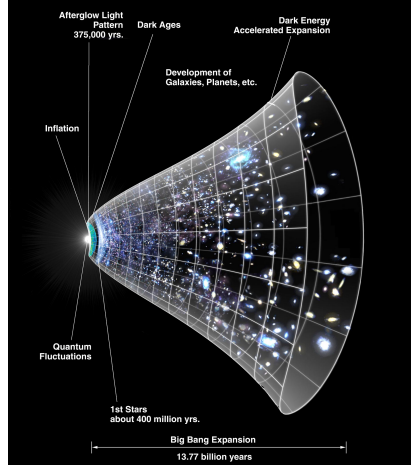
### 759 Strong $\mathcal{CP}$ problem

760

## 761 Dark energy

762 According to cosmological observations, the matter described by the SM  
 763 only makes up around 5% of the universe. It turns out that roughly 68% of  
 764 the universe is dark energy, which is not considered by the SM.

765 Dark energy is an unknown  
 766 type of energy postulated to ex-  
 767 plain the observed accelerated ex-  
 768 pansion of the universe. This ex-  
 769 pansion is dominated by a spa-  
 770 tially smooth component with neg-  
 771 ative pressure called dark energy.  
 772 Modern cosmological measurements  
 773 are based in supernovae, cosmic  
 774 microwave background fluctuations,  
 775 galaxy clustering and weak gravita-  
 776 tional lensing, and methods agree  
 777 with a spatially flat universe with  
 778 about 30% matter (visible and  
 779 dark) and 70% dark energy [33].



## 780 Dark matter

781 The rest of the energy content in the universe is the matter. Dark matter  
 782 (DM) adds up for approximately 85% of all matter and 27% of all energy.  
 783 This matter is called dark because it does not interact with the electromag-  
 784 netic field, so maybe a name such us invisible matter would have been more  
 785 appropriate since rather than being dark it just does not emit or reflect  
 786 light. The only way to interact with DM is via gravitational interaction,

which is about 25 orders of magnitude weaker than the weak force (as Table 1.1 shows). This is why DM is so difficult to detect. The SM does not provide a proper explanation but searches are being carried and candidates such as weakly interacting massive particles (WIMPs) or axions have been proposed.

The existence of DM has been inferred through gravitational effects in astrophysical and cosmological observations. The rotational speed of the galaxies[34], the gravitational lensing[35] and the CMB angular spectrum[36] are some examples of phenomena that cannot be explained with general relativity unless there is more present matter than what is seen.

Although the vast majority of scientific community accepts dark matter existence, alternative explanations for the observed phenomena have suggested. Most of these models consist in modifications of GR. The search of DM at particle colliders, which is focused on large missing transverse energy signatures, have not resulted in any observation. Nevertheless, the existence of a particle is never discarded, only its presence within the detector sensitivity limits.

#### 804 **Unification of the strong interaction**

There are unification attempts to treat all interactions as one, with the same coupling constant and the same symmetry group<sup>9</sup>. In the same way the EW unifies QED and Weak forces, the grand unified theories (GUT) unifies all three interactions (QED, Weak and QCD) of the SM at high energies, where the coupling constants approach each other. Note that gravity is still left out, because it is much weaker than the other interactions.

#### 811 **Supersymmetry**

Originally motivated by the hierarchy problem, supersymmetry (SUSY) is an extension to the SM. In SUSY the equations for force and the equations for matter are identical and each SM particle has its supersymmetric partner “sparticle” from which differs by half spin unit. Therefore, for each SM fermion, the corresponding sfermion is a spin-0 scalar and hence a boson. Identically, there is a super-partner for each of the SM bosons. The gluons have the spin-half gauginos. The Higgs have a weak isospin doublet or spin-half Higgsinos ( $\tilde{H}_{1,2}^0$  and  $\tilde{H}^\pm$ ). The new particles interact through the forces of the SM but would have different masses

SUSY is not a theory but a principle and any theory with that property is said to be supersymmetric. So, there are not one but dozens of supersymmetric theories. A lot of focus has been put searching for supersymmetric

---

<sup>9</sup>The most popular symmetry group for unification is  $SU(5)$ .

824 particles but so far the supersymmetric partners have not been found, which  
825 is a good reason to be skeptical about SUSY. **maybe cite here some AT-**  
826 **LAS SUSY searches**

827 **Others**

828 The different problems mentioned hitherto are just some of the most relevant  
829 open questions that fundamental physics has not being able to answer yet.  
830 Nonetheless, there are many other issues whose discussion would need many  
831 pages and are outside the scope of this work. Even so, it won't harm to list  
832 a few of them:

- 833 • Hierarchy problem: It is caused by the enormous distance between  
834 two fundamental physics scales: the EW scale ( $\sim 10^2$  GeV) and the  
835 Planck scale ( $\sim 10^{19}$  GeV).
- 836 • Strong  $\mathcal{CP}$  problem: It refers to the fact that, while QCD does not  
837 explicitly prohibit  $\mathcal{CP}$  violation in strong interactions, it has yet to be  
838 observed in experiments.
- 839 • Naturalness: It is the property that the dimensionless ratios between  
840 free parameters or physical constants appearing in a physical theory  
841 should take values of order unity. By looking at the parameters of the  
842 SM described in Section 1.1.7.1, it can be seen that the naturalness  
843 principle is not satisfied. For instance, the masses of the first  
844 generation of fermions are in the range of 1 MeV while the top quark has  
845 a mass of 173 GeV. Though this is not a flaw in the theory itself, it is  
846 frequently seen as a sign of undiscovered principles hidden behind a  
847 more comprehensive theory.
- 848 • Composite Higgs models:
- 849 • Majorana neutrinos: It is not clear yet if neutrinos are Majorana  
850 particles, i.e. they are their own antiparticles ( $\nu = \bar{\nu} = \nu_M$ ). Current  
851 experiments trying to solve this question are focused on neutrino-  
852 less double- $\beta$  decay, which can occur only if neutrinos are Majorana  
853 particles.
- 854 • String theory: It is theoretical framework in which fundamental point-  
855 like particles are understood as vibrational states of a more basic  
856 object, the so called “string”. A string is a one-dimensional entity  
857 that can be either be open (forming a segment with two endpoints) or  
858 close (forming a loop) and may have other special properties. Despite  
859 being in development since the late 1970s, it has not been accepted  
860 nor discarded yet.

Most of theoretical concepts of the SM were in place by the end of the 1960s. With the discovery of the  $W$  and  $Z$  bosons at CERN in the mid 1980s and the Higgs boson in 2012, the SM has established itself as one of the major pillars of modern physics. The understanding of the universe at the most fundamental level is based in this theory, which has been tried to be summarised through the entire Section 1.1.

Despite its brilliance and success, the SM is not the ending of the story. As exposed above, there are far too many unanswered questions and loose ends. The HL-LHC (see Section ??) and the next generation of experiments will look for evidence of physics outside the SM in the next years.

Among the open questions, unresolved concerns and measurements to be completed, this research is focused on the top quark<sup>10</sup>. On one hand, contributions to the measurement of the polarisation of this quark are presented and, on the other hand, the study of the associated production of a single-top quark with a Higgs boson is present as well. Now that the basics of the SM have been settled, in the sections to come, the context of these two topics is being discussed.

## 1.2 Top quark

The top quark ( $t$ ) or, for simplicity, just top is the up-type quark of the third generation of fermions. Sometimes called truth quark, its most distinctive feature is its huge mass, which is the largest among all fundamental particle particles. The left-handed top is the  $Q = 2/3$  and  $T_3 = +1/2$  member of the weak isospin doublet that also contains the bottom quark. The right-handed top quark is the  $SU(2)_L$  weak isospin singlet ( $Q = 2/3$  and  $T_3 = 0$ ). Its phenomenology is driven by its large mass. The top quark is often regarded as a window for new physics since it provides a unique laboratory where to test the understanding of the SM.

Due to being so massive, its life time is very short ( $\tau_t = 5 \times 10^{-25}$  s [35]). Actually, it is shorter than the hadronisation time (cite), this represents a unique opportunity to study quarks in free state, something that is very rare due to colour confinement, as explained in Section 1.1.4. In fact, the top quark is the only quark that can be investigated in isolation. Some of its properties, such as the spin information, can be accessed through its decay products and, consequently, be measured. This is the base to study its polarisation, a work that is contextualised in Section 1.2.4 and described in Chapter 5).

---

<sup>10</sup>Here and in the following, the usage of the term top quark includes the top antiquark.

Another consequence of its large mass is that the top quark is the only quark with a Yukawa coupling ( $y_t$ ) to the Higgs boson on the order of one; hence, a thorough understanding of its properties (mass, couplings, decay branching ratios, production cross section, etc.) can reveal crucial information on basic interactions at the electroweak symmetry-breaking scale and beyond. The main objective of this thesis is, precisely, the study of the top quark and Higgs boson interplay to, ultimately, help to determine if the  $y_t$  is that predicted by the SM or there is some  $\mathcal{CP}$ -violating phase that would affect the sign of the Higgs-top Yukawa coupling. The theoretical base for the understanding the associated production of a top quark and a Higgs boson given in Section 1.4 and the analysis investigating this matter is presented in Chapter 6.

## Top quark mass

-> Latest results (june 2022) <https://cds.cern.ch/record/2811385?>

-> Top quark mass defines the stability of the EW vacuum. It is a key factor to test the internal consistency of the SM.

->  $m_{top}$  s a free parameter of the SM. It has to be determined experimentally.

As discussed in Section 1.1.7.1,  $m_{top}$  is a free parameter of the SM. The theory does not predict its value, hence it must be determined experimentally. To derive the  $m_{top}$  from hadron collision data, two approaches are explored:

- Direct measurements (also known as template methods) [37]: The  $m_{top}$  is determined by reconstructing (fully or partially) the decay products of one or more top quarks in a  $t\bar{t}$  or single-top event<sup>11</sup>. A comparison of the detector-level distribution with templates created with a MC generator is used to determine the mass. Analysing  $t\bar{t}$  events with lepton-plus-jets and dilepton topologies provides the most precise results. →  $m_t^{MC}$  with  $O(480 \text{ MeV})$  precision.
- Indirect measurements[37]: Performed from measurements of cross-section. These methods rely on the dependence on the value of the  $m_{top}$  for the total or differential production cross sections for processes involving top quarks. →  $m_t^{pole}$  with  $O(1 \text{ GeV})$  precision

The most precisely studied property of the top quark is its mass. The most recent results for the top quark mass measurements result in  $m_{top} =$

---

<sup>11</sup>In particle physics, an event is the result of a collision, as recorded by the experiment.

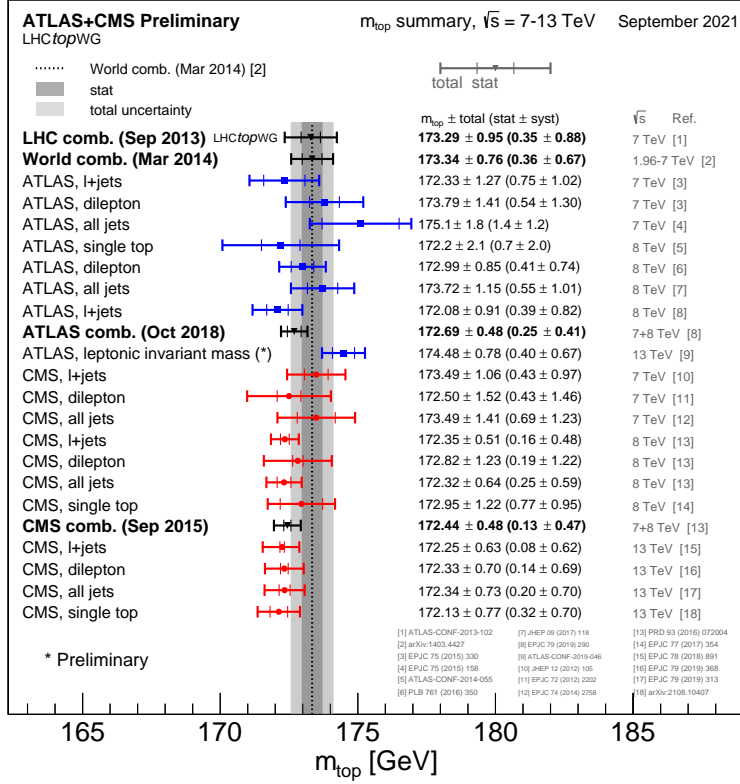


**Figure 1.9:** Summary of the ATLAS and CMS measurements from top quark decay. Results compared to LHC  $m_{top}$  combination.

933 172.76  $\pm$  0.30 GeV [1]. This number is an average of the measurements at  
934 LHC with ATLAS (172.69  $\pm$  66 GeV [38]) and CMS (172.6  $\pm$  3.5 GeV at CMS  
935 [39]) and at Tevatron with CDF and D $\emptyset$  (combined result: 174.30  $\pm$  0.89 GeV  
936 [40]). These values are measured from the kinematics of  $t\bar{t}$  events<sup>12</sup>.

937 Figure 1.9 summarises the measurements of ATLAS and CMS for  $m_{top}$   
938 from direct top quark decay.

### 939 1.2.1 Top quark discovery

940 In 1973, Kobayashi and Maskawa postulated the possibility of a third  
941 generation of quarks to explain  $\mathcal{CP}$  violations in kaon decays[41]. To match  
942 the names of the up and down quarks, the new generation's quarks were  
943 given the names top and bottom. The GIM mechanism, which predicted  
944 the existence of the yet-to-be-discovered charm quark, was used to make  
945 this prediction. When the charm was observed [42], the GIM was integ-

<sup>12</sup>This  $m_{top}$  results are sensitive to the top quark mass used in the MC generator that is usually interpreted as the pole mass.

946 rated into the SM and the postulation of the third family, and thus the top  
947 quark, gained acceptance. Shortly after the charm, the bottom quark was  
948 discovered in the E288 experiment at Fermilab [43], reinforcing the idea of  
949 the existence of the top quark. However, due to its large mass, it took 18  
950 years to confirm the existence of the top.

951 The top quark was observed for the first time at Tevatron with the  
952 CDF [44] and D $\emptyset$  [45] detectors via flavour-conserving strong interaction  
953 in 1995. Back then and until the start of LHC Run-1, Tevatron was the  
954 only accelerator powerful enough to produce top quarks.

### 955 1.2.2 Top quark production at LHC

956 The LHC is sometimes referred as a top quark factory due to its ability  
957 to produce such particles. In this collider, at  $pp$  collisions, the top quark  
958 is mainly produced via two mechanisms: through QCD in top and anti-top  
959 pairs ( $t\bar{t}$ ), and by means of the  $Wtb$  vertex of EW in single-top quarks  
960 associated with other particles. Apart from the  $t\bar{t}$  (Section 1.2.2.1) and  
961 single-top (Section 1.2.2.2) productions, the associated  $t\bar{t} + X$  and four-top-  
962 quark productions (Sections 1.2.2.3 and 1.2.2.4 respectively) are presented  
963 as well.

964 Since the top quark production is so relevant at LHC, the top quarks  
965 often constitute a main background in other physics analysis and, as a result,  
966 a better understanding of this particle's properties will directly translate  
967 into improvements in those searches.

#### 968 1.2.2.1 Top pairs

969 The production top and anti-top pair of quarks is the largest source of  
970 production of top quarks in hadron collisions. This process is one of the  
971 most important at LHC because it allows to precisely study the properties  
972 of the top quark. Additionally, due to the dominance of this production  
973 mode, the top-quark-pair production is also a major background in many  
974 searches for rare processes.

975 For the  $p\bar{p}$  collisions at Tevatron or  $pp$  at LHC, the  $t\bar{t}$  production is  
976 described by perturbative QCD. In this approach, a hard scattering process  
977 between the two hadrons is the result of an interaction between the quarks  
978 and gluons that constitute these hadrons. This model is described with  
979 detail in Section 2.2.7.

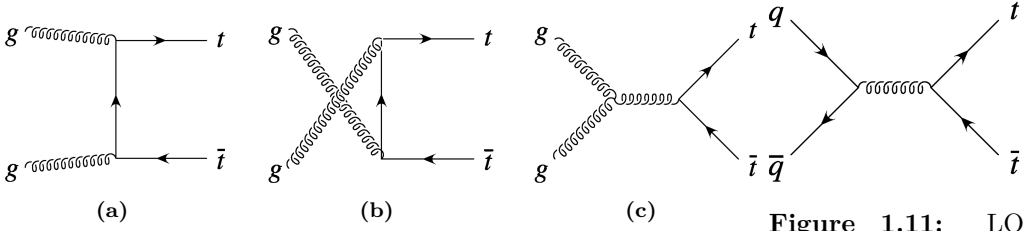


**Figure 1.10:** Representative Feynman diagrams of the LO processes contributing to the  $t\bar{t}$  production through gluon fusion at LHC.

**Figure 1.11:** LO Feynman diagram for  $t\bar{t}$  production via quark and anti-quark annihilation.

At LHC, the gluon fusion (Figure 1.10) dominates with a 90% of the  $t\bar{t}$  production. It is followed by the quark and anti-quark annihilation (Figure 1.11), which accounts for a 10% of the total top-quark-pair production. Due to its primordial importance for the physics programme of LHC, the theoretical calculations for the  $t\bar{t}$  production are done to an accuracy of next-to-next-to-leading order (NNLO) in QCD [46] and measured by ATLAS and CMS. Figure 1.12 shows the measurements for the  $t\bar{t}$  production cross section ( $\sigma_{t\bar{t}}$ ) at  $\sqrt{s} = 13$  TeV. The measurements and the theory calculations are quoted at  $m_{top} = 172.5$  GeV.

### 1.2.2.2 Single top

In addition to the top-quark-antiquark-pair production, the single-top-quark processes are of great importance to the study of the top quark properties at the LHC. This mechanism has a cross section three times smaller than that of  $t\bar{t}$  and are almost exclusively produced through the electroweak  $Wtb$  vertex. This is precisely the reason why single-top-quark production is essential to gather information the  $Wtb$  interaction and to directly measure  $|V_{tb}|$  at hadron colliders. The reason to decay and be produced from the bottom quark and not from strange or down quarks is because the CKM elements  $V_{ts}$  and  $V_{td}$  are much more smaller than  $V_{tb}$  being  $|V_{tb}| = 0.99915$ ,  $|V_{ts}| = 0.0403$  and  $|V_{td}| = 0.00875$ .

At LO, there are three production modes for single top, being the  $t$ -channel the dominant mechanism at the LHC with, approximately 70% of the single top quark cross section ( $\sigma_{Single-t}$ ) at a  $\sqrt{s} = 13$  TeV. The other processes are the  $s$ -channel and the associated production  $tW$  production. Only  $t$ -channel and  $tW$  productions are relevant to the electroweak single top production at LHC.

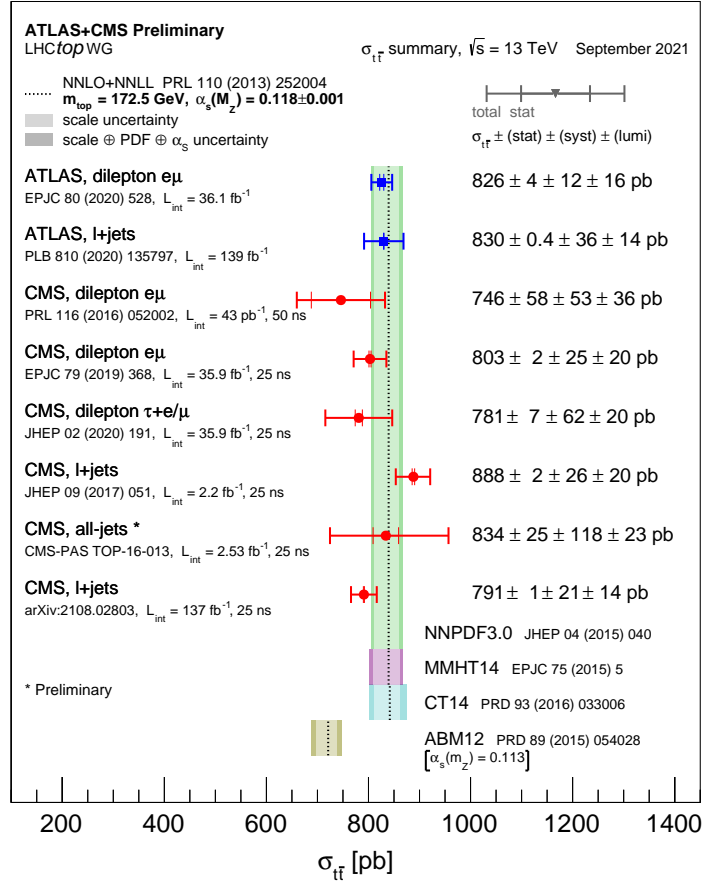


**Figure 1.12:** Summary of measurements  $\sigma_{t\bar{t}}$  at 13 TeV compared to the exact NNLO QCD calculation complemented with NNLL resummation.

### 1006 **$t$ -channel**

1007 This production mode, involves the scattering of a light quark and a gluon  
 1008 from the proton sea as shown in Figure 1.13. Note that additional dia-  
 1009 grams to those in Figure 1.13 are obtained by either replacing the  $u$  and  $d$   
 1010 by a  $c$  and  $s$  quarks or by switching the light quarks in the fermion line.  
 1011 The diagrams for antitop production are the charge conjugate of the ones  
 1012 presented.

The measurements cross sections at 13 TeV for single-top ( $\sigma_{t-channel,t}$ ) and single-anti-top ( $\sigma_{t-channel,\bar{t}}$ ) quarks in the  $t$ -channel production are shown in Figure 1.14. The theoretical calculations at NLO for  $\sigma_{t-channel,t+\bar{t}}$

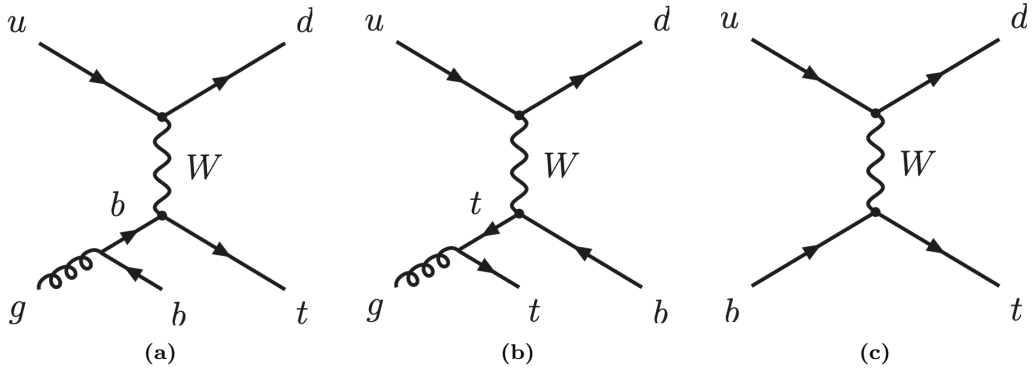


**Figure 1.13:** Representative Feynman diagrams for the single-top-quark production in the  $t$ -channel process.

at 13 TeV are:

$$\begin{aligned}\sigma_{t\text{-channel}, t} &= 136^{+4.1}_{-2.9}(\text{scale}) \pm 3.5(\text{PDF} + \alpha_s) \text{ pb}, \\ \sigma_{t\text{-channel}, \bar{t}} &= 81.0^{+2.5}_{-1.7}(\text{scale}) \pm 3.2(\text{PDF} + \alpha_s) \text{ pb}, \\ \sigma_{t\text{-channel}, t+\bar{t}} &= 217^{+6.6}_{-4.6}(\text{scale}) \pm 6.5(\text{PDF} + \alpha_s) \text{ pb}.\end{aligned}$$

<sup>1013</sup> These numbers have been obtained using HATHOR 2.1 [47][48].

<sup>1014</sup> The dominant process in the SM is the one in diagram 1.13a, while  
<sup>1015</sup> the one in 1.13b is included in order to form a gauge invariant set but its  
<sup>1016</sup> contribution is not very significative since for the gluon is easier to decay to  
<sup>1017</sup>  $b\bar{b}$  pair than to a  $t\bar{t}$  pair. These two  $3 \rightarrow 2$  production modes are known as  
<sup>1018</sup> 4 Flavour Scheme (FS) because the proton is considered to be composed by  
<sup>1019</sup> five quark flavours ( $u, d, c$  and  $s$ ) and is characterised by having a  $b$  quark  
<sup>1020</sup> in the final state. This final state  $b$  quark is sometimes referred as second  
<sup>1021</sup>  $b$  and it has a transverse momentum ( $p_T$ ) distribution peaking around 2 or  
<sup>1022</sup> 3 GeV as can be seen in Figure 1.15. This is the reason why the final  $b$   
<sup>1023</sup> quark from the gluon splitting frequently goes undetected, because it does  
<sup>1024</sup> not pass the  $p_T$  threshold of the detector.

<sup>1025</sup> The  $2 \rightarrow 2$  process in 1.13c is known as 5FS because the proton is  
<sup>1026</sup> considered to be composed by five flavours of quarks ( $u, d, c$  and  $s$ ) and it  
<sup>1027</sup> is characterised by having a  $b$  quark in the initial state. The simulations for  
<sup>1028</sup> the 4FS and 5FS diagrams are produced separately and merged afterwards.  
<sup>1029</sup> When adding the two contributions, some double-counting may appear due  
<sup>1030</sup> to the overlap in the phase space so one has to be careful.

### <sup>1031</sup> **s-channel**

<sup>1032</sup> The  $s$ -channel process for single-top is the one with less impact among  
<sup>1033</sup> single-top production channels. It is depicted in Figure 1.16. This produc-

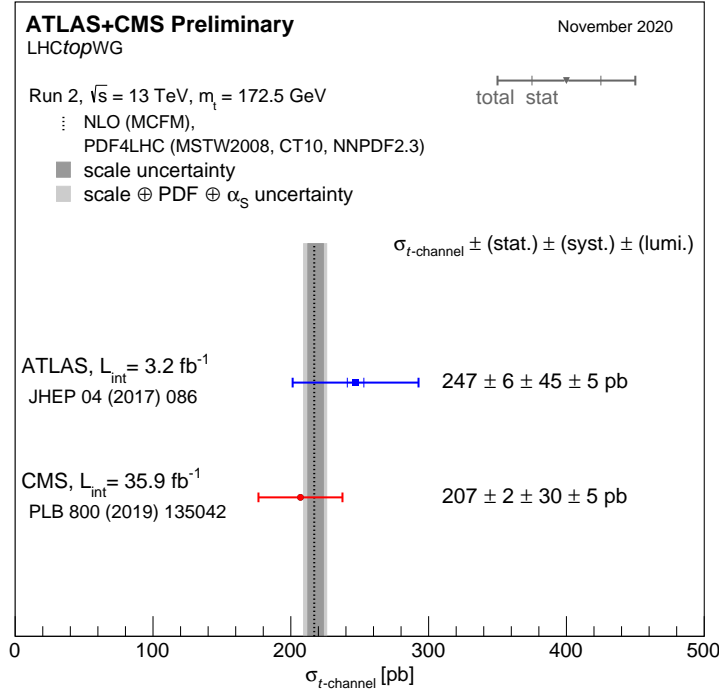


**Figure 1.14:** Summary of the ATLAS and CMS Collaboration measurements of the single top production cross-sections in the  $t$ -channel at 13 TeV.

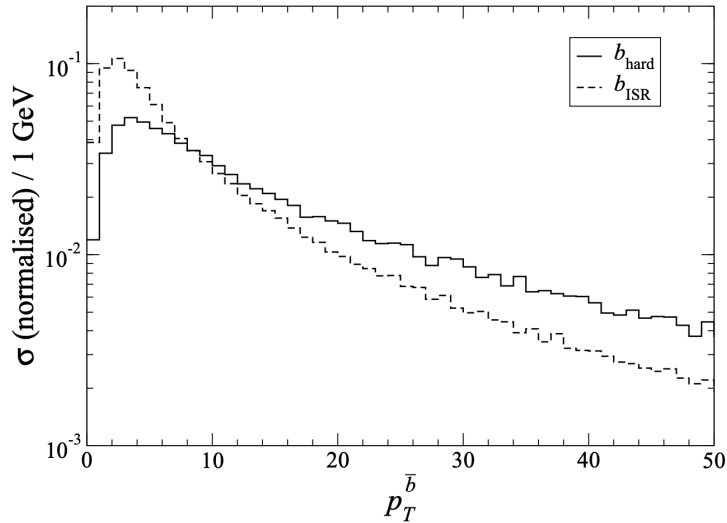


**Figure 1.15:** Normalised  $p_T$  distribution of the second  $b$  quark in the  $t$ -channel process, generated by Monte Carlo (MC) simulation [49].

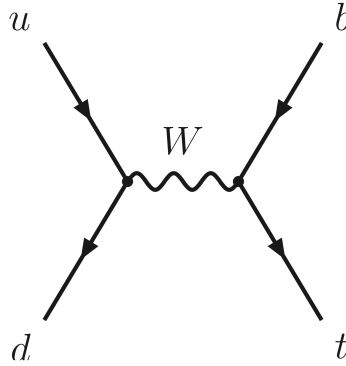


**Figure 1.16:** Representative Feynman diagram for the single-top-quark production in the  $s$ -channel.

tion mode is also referred as the quark-antiquark annihilation or  $W^*$  process and it is very similar to the Drell-Yann.

According to the LHC cross section group, at 13 TeV of center-of-mass energy, the cross sections for the single top and single anti-top production in the  $s$ -channel ( $\sigma_{s\text{-channel}}$ ) are:

$$\begin{aligned}\sigma_{s\text{-channel},t} &= 6.35^{+0.18}_{-0.15}(\text{scale}) \pm 0.9(\text{PDF} + \alpha_s) \text{ pb}, \\ \sigma_{s\text{-channel},\bar{t}} &= 3.97^{+0.11}_{-0.09}(\text{scale}) \pm 0.15(\text{PDF} + \alpha_s) \text{ pb}, \\ \sigma_{s\text{-channel},t+\bar{t}} &= 10.32^{+0.29}_{-0.34}(\text{scale}) \pm 0.27(\text{PDF} + \alpha_s) \text{ pb}.\end{aligned}$$

Note that while at LHC the  $s$ -channel production has not been observed at LHC, for Tevatron it was a significant part of the total single-top cross-section.

### Associated $tW$

Finally, the associated production of a single top quark with a  $W$  boson (sometimes referred as  $tW$ -channel) is represented by two the Feynman diagrams in Figure 1.18. To these two diagrams, the charge conjugate processes could be added to complete the  $tW$  mechanisms. The cross section for the associated  $tW$  is:

$$\sigma_{tW,t+\bar{t}} = 71.7 \pm 1.80(\text{scale}) \pm 3.40(\text{PDF} + \alpha_s) \text{ pb}.$$

This and all  $\sigma$  in the section are calculated for a top mass of  $m_{top} = 172.5$  GeV and NLO in QCD with HATHOR v.2.1. The PDF and  $\alpha_s$  uncertainties are calculated using the PDF4LHC prescription [50] with the MSTW2008 68% CL NLO [51][52], CT10 NLO [53] and NNPDF2.3 [54] PDF sets, added in quadrature to the scale uncertainty.

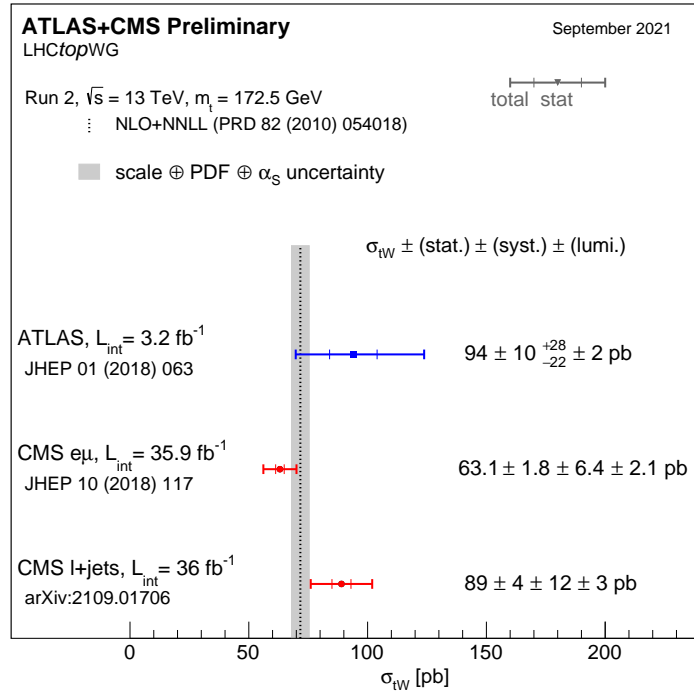


**Figure 1.17:** Cross-section measurements for the associated  $tW$  production boson performed by ATLAS and CMS at 13 TeV, and combined result compared with the NLO+NNLL prediction.

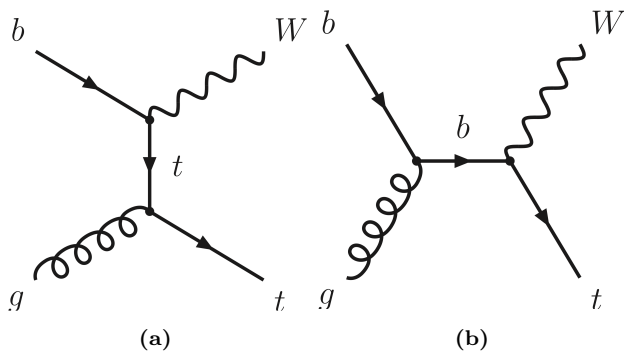


**Figure 1.18:** Representative Feynman diagrams for the single-top-quark production in association with a  $W$  boson.

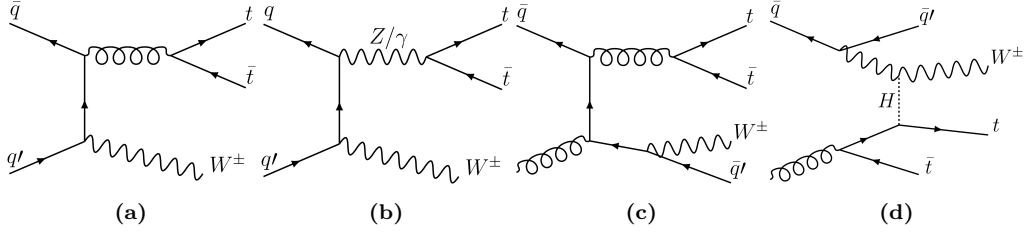


**Figure 1.19:** Representative Feynman diagrams for  $t\bar{t}W$  production. Left diagrams show the  $\bar{q}\bar{q}' \rightarrow t\bar{t}W$  processes and right ones the  $\bar{q}\bar{q} \rightarrow t\bar{t}Wq'$  production.

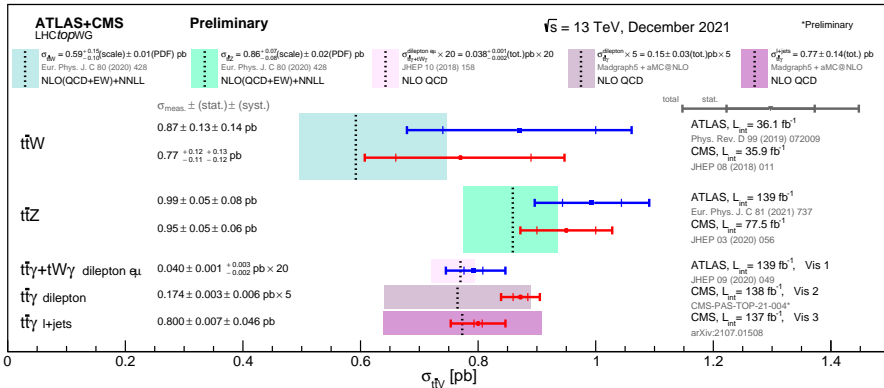


**Figure 1.20:** Summary of the ATLAS and CMS measurements of the  $t\bar{t} + X$  production cross-sections at 13 TeV. Here  $X = W, Z$  and  $\gamma$ .

### 1.2.2.3 Associated $t\bar{t} + X$ production

### 1.2.2.4 Four tops

Figure 1.22

### 1.2.3 Top quark decay

As advanced in the Section 1.2.2.2, due to the large  $V_{tb}$  element of the CKM matrix, the top quark decays almost entirely ( $\sim 99.8\%$ ) through the medium of the  $Wtb$  vertex to a  $b$  quark and a  $W$  boson. The final state decay is classified according to the subsequent decay of the  $W$  boson. As  $W$  are massive vector bosons, its lifetime is very short ( $\tau_W \approx 3 \times 10^{-25}$  s).

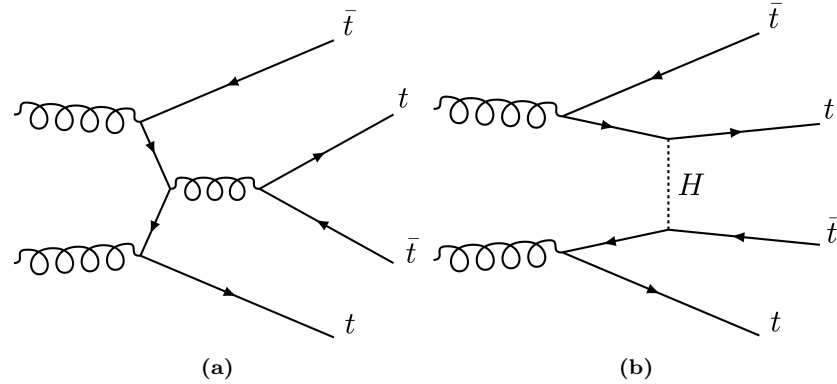


**Figure 1.21:** Representative Feynman diagrams for the  $gg \rightarrow t\bar{t}t\bar{t}$  production.

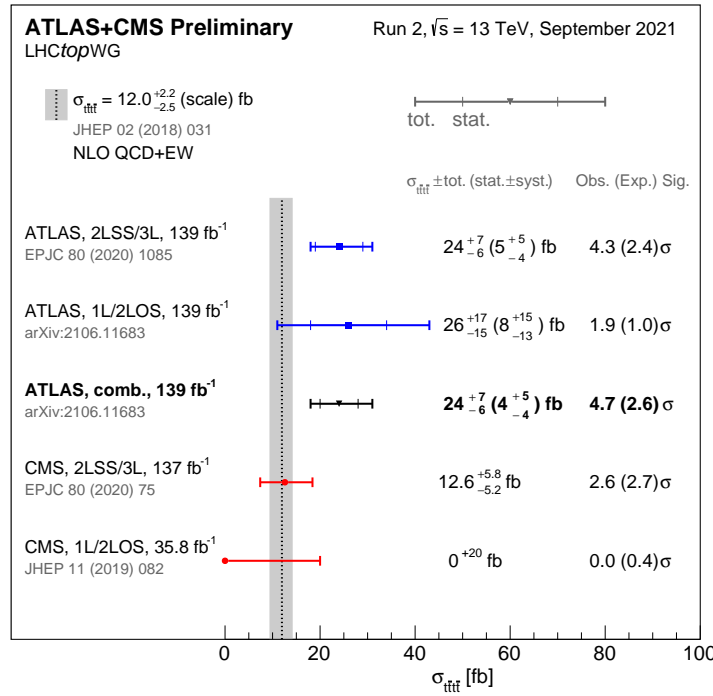


**Figure 1.22:** Summary of the ATLAS and CMS measurements of the  $t\bar{t} t\bar{t}$  production cross-sections at 13 TeV in various channels

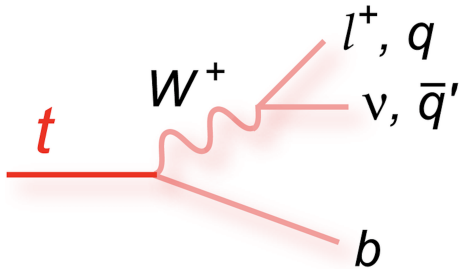


**Figure 1.23:** Decay of a top quark to a  $b$  quark and a  $W$  boson. The  $W$  boson can decay either leptонically to a neutrino and a lepton or hadronically to a pair of quarks. In the hadronic  $W$  decay, a jet triplet is formed along with the  $b$  quark.

For the  $W^+$ , the decay modes are:

$W^+ \rightarrow e^+ \nu_e$	( $10.71 \pm 0.16$ )%
$W^+ \rightarrow \mu^+ \nu_\mu$	( $10.63 \pm 0.15$ )%
$W^+ \rightarrow \tau^+ \nu_\tau$	( $11.38 \pm 0.21$ )%
$W^+ \rightarrow q\bar{q}$ (hadrons)	( $67.41 \pm 0.27$ )%
$W^+ \rightarrow$ invisible	( $1.4 \pm 2.9$ )%

1048 For the conjugate processes involving the  $W^-$ , the branching ratios (BR)  
 1049 are the same. Therefore, the  $W$  decay and consequently the  $t$  decay can be  
 1050 classified either as leptonic or hadronic. The decay chain of the top quark is  
 1051 represented in Figure 1.23. Due to its large mass, the  $W$  can decay to any  
 1052 quark except the top quark. For a certain decay mode, the BR is defined  
 1053 as the fraction times that the particle decays in that particular mode with  
 1054 respect to total possible decays.

## 1055 1.2.4 Top quark polarisation

1056 Angular measurements in ATLAS:

- 1057 • Top polarisation: how the top is produced
- 1058 • Helicity fractions: how the top decays
- 1059 • Spin correlation: information between produced top-quarks. Provides  
 1060 information about quantum entanglement.

1061 For polarisation: Top polarised in direction of spectator quark Define 3  
 1062 Polarisation directions:  $\{P_{xt}, P_{xy}, P_{zt}, \}$  Lepton direction used as spin ana-  
 1063 lyser ( $\alpha_l$ )

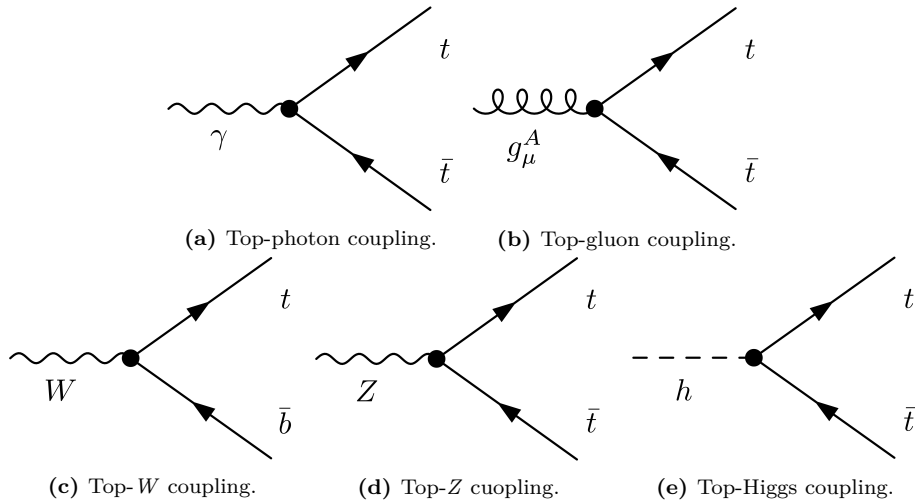


**Figure 1.24:** Top quark coupling to SM bosons.

1064 In the single top  $t$ -channel production, the top quark is polarised due  
 1065 to left-handed  $W$ -coupling. Top-quark spin points in the direction of the  
 1066 spectator-quark( $q'$ )

### 1067 1.2.5 Top quark physics

1068 **Probably this section is not necessary since the physics are**  
 1069 **mostly explained above.** The top quark couples directly to all SM vector  
 1070 ( $\gamma$ ,  $W^+$ ,  $W^-$ ,  $Z$ ,  $g$ ) and scalar ( $H$ ) bosons. For both photons and gluons,  
 1071 the interaction is described by a vectorial fermion-gauge coupling  $\bar{\Psi}\Psi A_\mu$ .  
 1072 From boson-fermion interacting term of the  $\mathcal{L}_{QED}$  in 1.9, the coupling of  
 1073 the top quark to photons (Figure 1.24a) has a strength of  $eQ\gamma^\mu = \frac{2}{3}e\gamma^\mu$ .  
 1074 Meanwhile, for the top-gluon coupling (Figure 1.24b), the expanded form  
 1075 of the gluon-fermion term in the  $\mathcal{L}_{QCD}$  of 1.31 gives the  $g_s \frac{\lambda_a}{2} \gamma^\mu$ .

1076 For the charged weak current only the only the left-handed top couples  
 1077 to the  $W^\pm$  with coupling. This is done via the  $Wtb$  vertex with a strength  
 1078 of  $g\gamma^\mu(1 - \gamma^5)V_{tb}$  (Figures 1.23 and 1.24c). The value of  $V_{tb}$  is given in Table  
 1079 1.3. The top couples to the  $Z$  bosons (Figure 1.24d) with unequal left and  
 1080 right-handed components,  $\frac{ig}{2\cos\theta_W}\gamma^\mu(v_t - a_t\gamma^5)$ . Being  $v_t = 1/2 - 2Q_t\sin^2\theta_W$   
 1081 and  $a_t = 1/2$ . Finally, for the Higgs boson (Figure 1.24e), the top quark  
 1082 couples with a Yukawa type interaction  $\bar{\Psi}\Psi\phi$  with a strength  $y_t = \frac{\sqrt{2}m_{top}}{v}$ ,  
 1083 as equation 1.39 states. All of these couplings are flavour-conserving, with  
 1084 the exception of the charged-current interaction with the  $W$  bosons.

---

## 1085 1.3 Higgs boson

1086 Following the top quark, the Englert-Brout-Higgs-Guralnik-Hagen-  
 1087 Kibble-Higgs boson or, for simplicity, Higgs boson ( $H$ ) or just Higgs is  
 1088 the most massive particle in the SM with a mass of  $m_H = 125.25 \pm 0.17$   
 1089 GeV [55]. The value provided by [55] is an average of the ATLAS com-  
 1090 bined measurement ( $m_H = 124.86 \pm 0.27$  GeV [56]) and the CMS results  
 1091 ( $m_H = 125.46 \pm 0.16$  [57]).

1092 The Higgs boson was the final piece in the SM puzzle. Its existence  
 1093 was theorised in 1964 by three independent groups: Englert-Brout [58],  
 1094 Higgs [59] and Guralnik-Hagen-Kibble [60], and its discovery meant one of  
 1095 the greatest successes of the SM. This theory was not only able to calculate  
 1096 with great precision the physics but also predicted the existence of a particle  
 1097 that was found later (see 1.3.1).

1098 In the SM, fundamental particles acquire mass through their interactions  
 1099 with the Higgs fields. It is important to note that not all mass is related to  
 1100 the Higgs mechanism. For instance, the mass of the proton does not come  
 1101 from the interaction of its components with the Higgs but from the kinetic  
 1102 energy of the particles that compose the proton.

### 1103 1.3.1 Higgs boson discovery

1104 Any particle physicist enthusiast remembers July 4th of 2012 pretty  
 1105 well, it was LHC experiments ATLAS [61] and CMS [62] who announced  
 1106 the discovery of a massive state  $H$  with the properties expected for the  
 1107 Higgs boson.

1108 Both the ATLAS and CMS Collaborations reported excesses of events  
 1109 for 2011 ( $\sqrt{s} = 7$  TeV and  $\mathcal{L} = 4.8 \text{ fb}^{-1}$ ) and 2012 ( $\sqrt{s} = 8$  TeV and  $\mathcal{L} = 458 \text{ fb}^{-1}$ )  
 1110 datasets of proton-proton collisions. This surplus of events was compatible  
 1111 in its production and decay with the SM Higgs boson in the mass region  
 1112  $m_H \in [124, 135]$  GeV with significances of  $2.9\sigma$  for ATLAS and  $3.1\sigma$  for  
 1113 CMS. At Tevatron (circular proton-antiproton collider at Fermilab), the  
 1114 experiments CDF [63] and D $\emptyset$  [64] also reported an excess in the mass  
 1115 region  $m_H \in [120, 135]$  GeV.

### 1116 1.3.2 Higgs boson production at LHC

1117 One of the reasons why the Higgs boson was found the latest among  
 1118 SM fundamental particles is because it is a fairly heavy particle and, hence,

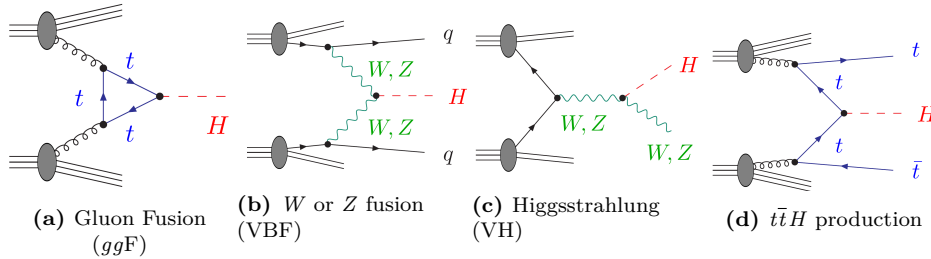


**Figure 1.25:** Lowest-order Feynman diagrams for the dominant production mechanisms of a Higgs boson at hadron colliders.

it was necessary a lot of energy to produce it. Even though that colliders such us SLAC or LEP had enough energy, they were colliding electrons and positrons and, since the coupling of the Higgs to fermions is proportional to the fermions mass, the process  $e^- e^+ \rightarrow H$  processes is highly suppressed<sup>13</sup> and, for this reason, there were not enough statistics of events with a Higgs boson. The most favoured way of producing a Higgs boson is trough the mediation of the heaviest fundamental particles in the SM because these have the strongest couplings with the Higgs and, consequently, the greater cross section.

The four most dominant processes for Higgs boson production at LHC are summarised in Figure 1.25:

- **Gluon Fusion (ggF):** This channel is depicted in Figure 1.25a and, as the diagram shows, the process  $gg \rightarrow H$  has to be mediated by a massive fermion loop. This due to the fact that there is no direct gluon-Higgs coupling within the SM. Although in principle all quarks should be included in the loop, in practise it is the top quark the one doing so because its coupling to the Higgs boson is 35 times stronger than the next-heaviest fermion, the bottom quark.

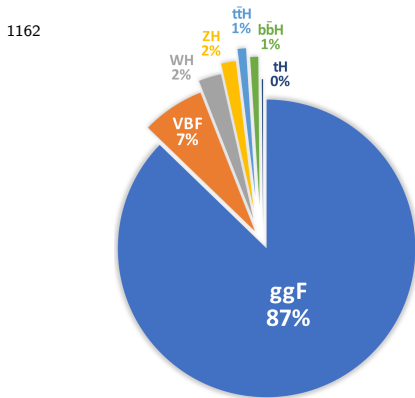
Due to the abundance of gluons in  $pp$  collisions, the ggF is very favoured at LHC.

- **Vector Boson Fusion (VBF):** The second most important is the radiation by the incoming quarks of a  $W$  or  $Z$  vector bosons that fuse to from a Higgs as Figure 1.25b illustrates. The vector bosons of the process  $V\bar{V} \rightarrow H$  are originated from initial state quarks which scatter thorough the final state (changing its flavours in the case of  $W$  fusion) producing two forward jets.

<sup>13</sup>The dominant Higgs production in  $e^- e^+$  annihilation is the so called Higgsstrahlung, an  $s$ -channel process in which the  $H$  is produced in association to a  $Z$  boson similarly to Figure 1.25c.

- **Higgsstrahlung (VH)**: There is another significant contribution involving the  $W$  or  $Z$  bosons, the Higgsstrahlung or associated  $WH$  or  $ZH$  production. Here, a, off-shell  $W$  or  $Z$  (formed from the annihilation of two quarks) radiate a Higgs boson via  $V^* \rightarrow VH$ . Figure 1.25c depicts the VH associated production.
- **Quark-pair associated production ( $q\bar{q}H$ )**: In this mode, the Higgs is produced from a  $q\bar{q}$  pair via  $q\bar{q} \rightarrow H$  with a  $q\bar{q}H$  final state. Typically, the involved quark pair is either a  $b\bar{b}$  or  $t\bar{t}$ . In the case of  $t\bar{t}$  (Figure 1.25d), the top quarks decay before hadronising, leading to a high multiplicity final state.
- **Associated Higgs boson and single-top quark ( $tHX$ )**: This sub-dominant contribution can be either a  $tHq$  or a  $tWH$ .

The cross section of the different procedures for Higgs boson production at  $\sqrt{s} = 13$  TeV are shown in Figure 1.26 as a function of  $m_H$ . For Figure 1.26a, the  $\sigma_{tH}$  accounts for the  $t$ -channel and  $s$ -channel but not the  $tW$ -channel. Assuming a  $m_H = 125.2$  GeV, the cross-sections for Higgs production are [65]:



$$\begin{aligned}\sigma_{ggF} &= 48.5^{+2.2}_{-3.3} \text{ pb} \\ \sigma_{VBF} &= 3.78 \pm 0.05 \text{ pb} \\ \sigma_{WH} &= 1.37 \pm 0.03 \text{ pb} \\ \sigma_{ZH} &= 0.89^{+0.04}_{-0.03} \text{ pb} \\ \sigma_{t\bar{t}H} &= 0.5^{+0.03}_{-0.05} \text{ pb} \\ \sigma_{b\bar{b}H} &= 0.49^{+0.10}_{-0.11} \text{ pb} \\ \sigma_{tHX} &= 0.09 \pm 0.01 \text{ pb}\end{aligned}$$

### 1.3.3 Higgs boson decay

The Higgs boson has a very short lifetime ( $\tau_H = 1.6 \times 10^{-22}$  s [65]) and, hence, is always detected through its decay products. Despite the expected large Yukawa coupling between the Higgs boson and the top quark, the  $H \rightarrow t\bar{t}$  is forbidden because the  $m_H < 2m_{top}$ . Consequently, the most prominent decay mode is the  $H \rightarrow b\bar{b}$  followed by the  $H \rightarrow W^+ W^-$ . For the rest fermionic decays, the decay rates are ordered by the fermion mass. Regardless of the expected large coupling between the weak force bosons and the Higgs, the  $H \rightarrow VV^*$  is suppressed due to the requirement that one vector boson has to be produced off-shell.

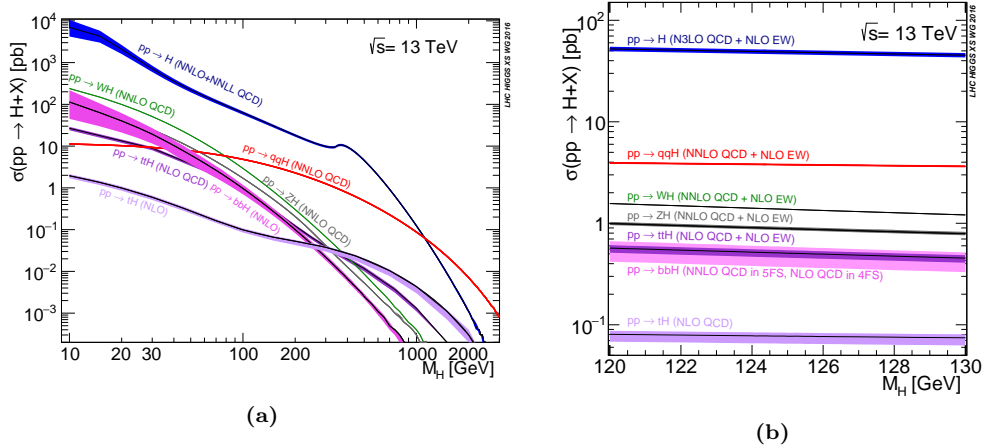
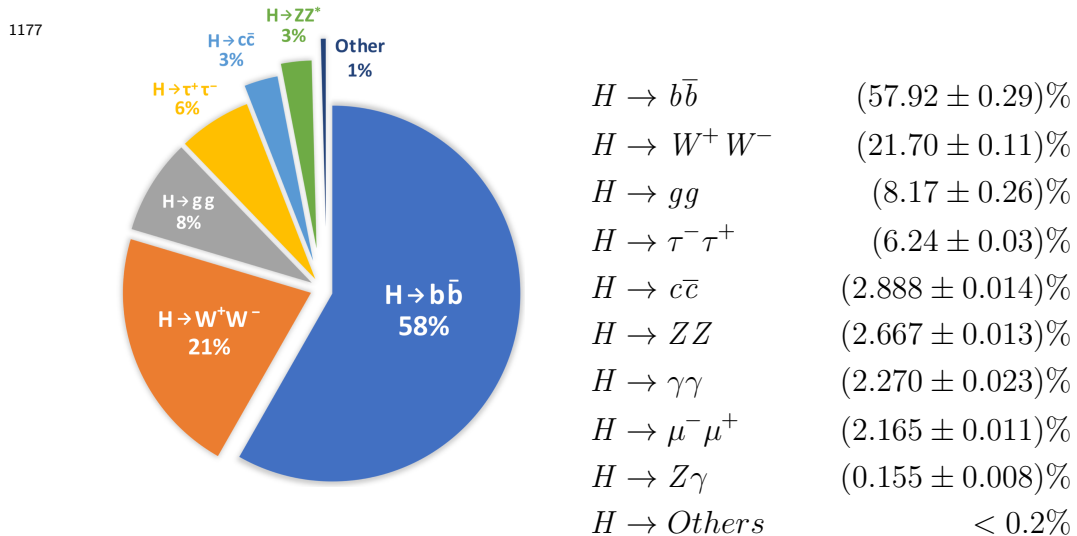


**Figure 1.26:** Higgs boson production cross sections as function of  $m_H$  at  $\sqrt{s} = 13$  TeV [65].

### Add some diagrams of the Higgs decay modes

For the analysis carried in this thesis, are of particular the decays  $H \rightarrow W^+ W^-$ ,  $H \rightarrow ZZ$  and  $H \rightarrow \tau^- \tau^+$ . Sorted by its importance and assuming a  $m_H = 125.2$  GeV, the BR for the Higgs are [66]:



### 1.3.4 Higgs boson physics

#### Work in progress

The gauge symmetry is broken is broken by the vacuum, triggering the EW Spontaneous Symmetry Breaking (SSB). This means that the symmetry group of the EW sector,  $U(2)_L \otimes U(1)_Y$ .

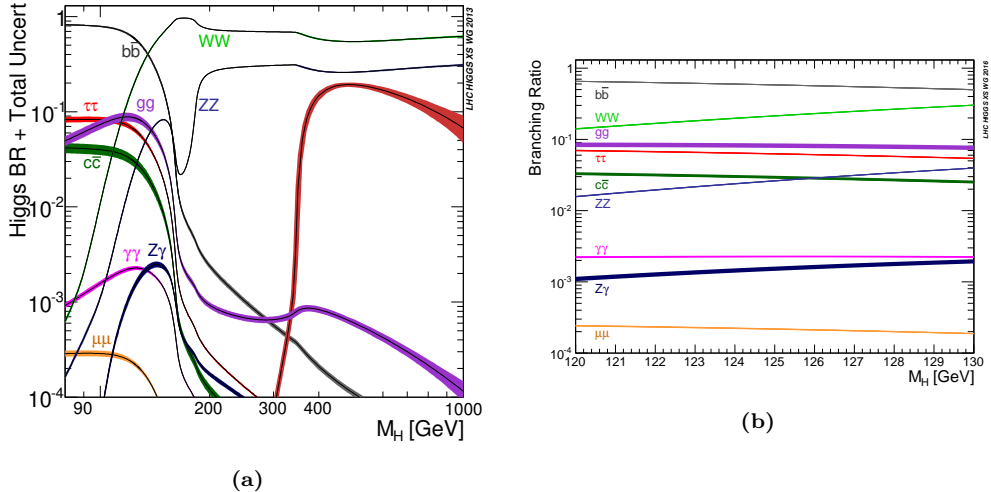


**Figure 1.27:** Standard Model Higgs boson decay branching ratios as function of  $m_H$  at  $\sqrt{s} = 13$  TeV citeLHCIGGSSWG2013.

$$SU(3)_C \otimes SU(2)_L \otimes U(1)_Y \xrightarrow{\text{SSB}} SU(3)_C \otimes U(1)_{QED}$$

Production and decay rates, constrains on its couplings: <https://arxiv.org/abs/1606.02266>

The Higgs mass is given by  $m_H = \sqrt{\lambda/2v}$ , being  $v$  the vacuum expectation value of the Higgs field and  $\lambda$  the Higgs self-coupling.

Electro weak symmetry breaking [67]: <https://arxiv.org/pdf/1512.08749.pdf> In this paper the Yukawa coupling of the top is introduced, link it with the tHq paper.

### 1191 Work in progress

## 1192 1.4 Top quark and Higgs boson interplay

1193 So far, the couplings of the Higgs boson to the SM particles have been  
 1194 found to be proportional to the mass of these particles. Since the top quark  
 1195 is the most massive particle and the coupling of Higgs to SM particles is  
 1196 uniquely determined by the mass of these particles, the Yukawa coupling  
 1197 between the top quark and the Higgs boson ( $y_t$ ) is expected to be the  
 1198 greatest among all fermions and, hence, its study is of crucial importance,  
 1199 as it is discussed in references [68][69] and developed in the succeeding  
 1200 sections.

1201 The production of a pair or top quarks along with a Higgs boson ( $t\bar{t}H$ )  
 1202 it is possible to measure the absolute value of  $y_t$ . This process has the

1203 advantage of being the leading mechanism to produce the Higgs together  
 1204 with the quark top. At  $\sqrt{s} = 13$  TeV it has a cross section of **poner cálculos**  
 1205 **del SM para  $\sigma_{t\bar{t}H}$**  (the definition of cross section can be found in Section  
 1206 2.2.5).

1207 Despite having a very much lower cross section than  $t\bar{t}H$  (**poner**  
 1208 **números**), the Higgs boson production alongside a single top quark ( $tHq$  or  
 1209  $tH$ ) brings valuable information, specially regarding the sign of the Yukawa  
 1210 coupling. Note that the sign of  $y_t$  is not physical by itself but the relative  
 1211 sign compared to the coupling of the Higgs to weak<sup>14</sup> boson is, in deed,  
 1212 physical [68]. This is explored with more detail in 1.4.2.

1213 A change in the Yukawa sign and/or absolute value with respect to its  
 1214 SM value would signal an origin of the fermion masses different from the  
 1215 described by the EWSB because the relative sign of the Higgs coupling to  
 1216 fermions and gauge vector bosons is crucial for recovering the unitarity and  
 1217 renormalizability of the theory s[70].

### 1218     **All section 1.4 is work in progress**

1219     →  $\mathcal{CP}$  Properties of Higgs Boson Interactions with Top Quarks in the  
 1220  $tH$  and  $t\bar{t}H$  processes at ATLAS: <https://inspirehep.net/literature/1790698>

1222  
 1223 Only 1% of all Higgs bosons are produced in association with top quarks,  
 1224 the observation of such processes is very challenging. Notably, it is a immensely  
 1225 ambitious task to measure the associated production of a Higgs  
 1226 with a single top which has an extremely low cross section as can be seen  
 1227 in Figure 1.26b.

## 1228     1.4.1     $t\bar{t}H$

1229 The first associated production of a Higgs boson with a pair of top  
 1230 quarks was observed in 2008 by ATLAS [71] and CMS [72]. This process  
 1231 marked a significant milestone for the field of high-energy physics because  
 1232 it helped establishing the first direct measurement of the tree-level coupling  
 1233 of the Higgs boson to the top quark, which interacted with the predicted  
 1234 strength.

1235 The associated production of  $H$  with top quark pair has been studied by  
 1236 ATLAS and CMS previously during Run-1 at  $\sqrt{s} = 7$  TeV and 8 TeV [73]  
 1237 [74] and Run-2 [**buscar  $t\bar{t}H$  en Run-2**]

---

<sup>14</sup>The coupling of the Higgs to the gauge bosons is taken as positive.

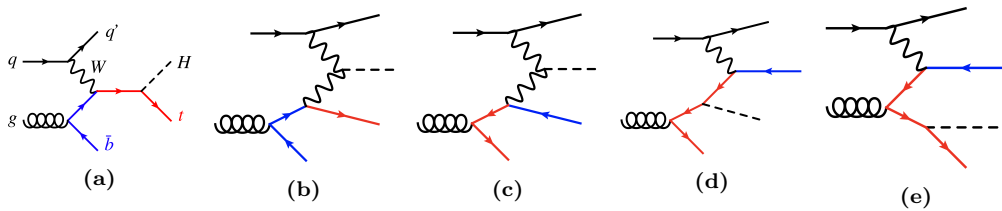


**Figure 1.28:** LO Feynman diagrams for  $t$ -channel  $tH$  production in the 4FS.

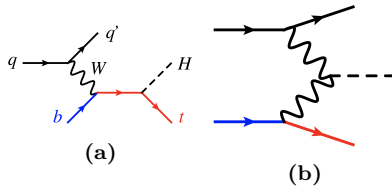


**Figure 1.29:** LO Feynman diagrams for  $t$ -channel  $tH$  production in the 5FS.

#### 1238 1.4.1.1 $t\bar{t}H$ Standard Model

#### 1239 1.4.1.2 $t\bar{t}H$ Charge-Parity

#### 1240 1.4.2 $tHq$

1241 The  $tH$  production is divided in  $tHq$  and  $tWH$ .

#### 1242 $tHq$ production modes

1243 At LO, the production of a Higgs boson in association with a single top  
 1244 quark ( $tHq$ ) in  $pp$  collisions is classified in three groups according to the  
 1245 virtuality of the  $W$  boson. These groups are:  $t$ -channel production,  $s$ -  
 1246 channel production and associated production with an on-shell  $W$  boson.  
 1247 This categorisation is the same as for the single-top-quark (Section 1.2.2.2),  
 1248 which makes sense since the  $tH$  associated production is, basically, a single-  
 1249 top-quark process in which a Higgs boson is radiated either from the  $W$  or  
 1250 the top.

1251 In the  $t$ -channel production modes are classified in 4FS and 5FS as it  
 1252 is done for the single-top case. The 4FS and the 5FS modes are shown in  
 1253 Figures 1.28 and 1.29 respectively. For the 4FS modes, the diagrams in  
 1254 which the gluon decays to a top pair (1.28c, 1.28d and 1.28e) contribute  
 1255 less than the ones in which it does to a  $b\bar{b}$  (1.28a and 1.28b).

1256 **Poner las tablas para las cross section de Demartin [75] para**  
 1257  **$t$ -channel y  $s$ -channel**

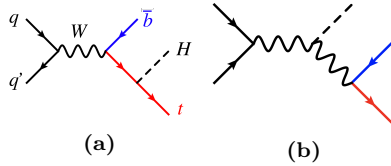


**Figure 1.30:** LO Feynman diagrams for  $s$ -channel  $tH$  production in the 5FS.

1258 Since the  $s$ -channel contribution is so small to the total cross section of  
 1259 the  $tHq$  process,

1260 For  $tH$  and single-top-quark production at colliders, the 5FS calculations  
 1261 are easier than the 4FS due to the lesser final state-multiplicity and simpler  
 1262 phase space. This is why in the 5FS the single-top production is known  
 1263 at NNLO while the 4FS this is done only for NLO. Another advantage of  
 1264 the 5FS is that the  $t$ -channel,  $s$ -channel and associated  $tWH$  production do  
 1265 not interfere until NNLO. Contrary, the in 4FS, the  $t$ -channel at NLO and  
 1266  $s$ -channel at NNLO can interfere. Nevertheless, this interferences are very  
 1267 small and can be neglected [75].

1268 **Poner algo in información del  $tWH$ production mode para  $tH$**   
 1269 **y** The  $tWH$ production is a background in the  $tHq$  analysis.

1270 In reference 1.31 is shown that the shapes of the distributions of most  
 1271 observables in the  $s$ -channel differ significantly from those of the  $t$ -channel.  
 1272 So, even though the total cross section of the  $tHq$  production with the  $s$ -  
 1273 channel is much more smaller than the one for  $t$ -channel, one could think  
 1274 that including the  $s$ -channel in the analysis would increase the precision.  
 1275 This is not the case because the LHC is not sensible for to the  $tHq$  produc-  
 1276 tion via  $s$ -channel. In fact, not event the  $s$ -channel-single-top production  
 1277 (without any associated Higgs boson) has been found at LHC.

1278 **Summarise production modes described in [75]**

### **$tHq$ sensibility to $y_t$**

As already commented in the introduction of the Section 1.4, the main interest of the  $tHq$  process is that it is among the few processes in the LHC that are sensible to the relative size and phase between the couplings of the Higgs top and the Higgs to the gauge bosons. The other mechanisms to determine this relative sign are  $H \rightarrow \gamma\gamma$  and  $gg \rightarrow ZZ$ . This is due to the fact that in the SM the  $tHq$  production of the where the  $H$  couples to the  $W$  (Figure 1.31 right) interfere destructively with those in which the  $H$  is radiated from the top (Figure 1.31 left). As it is later explained in Section 2.2.5, the cross section is proportional to the square of the matrix element,  $\mathcal{M}$  and if there are several diagrams for a same process, the matrix elements

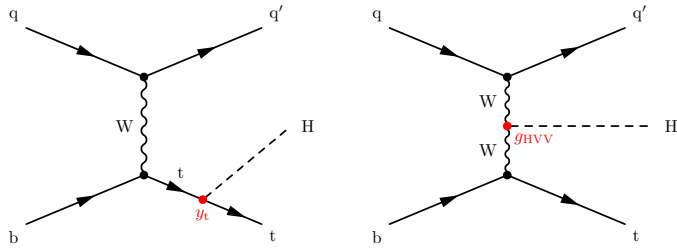


**Figure 1.31:** Representative LO Feynman diagrams for the  $t$ -channel  $tHq$  associated production, where the Higgs boson couples either to the top quark (left) or the  $W$  boson (right)

have to be summed before squaring leading to interference terms. For the  $tHq$  production

$$\sigma_{tHq} \propto |\mathcal{M}_{qq \rightarrow tHq}|^2 = |\mathcal{M}_{qq \rightarrow tHq_{WH}} + \mathcal{M}_{qq \rightarrow tHq_{tH}}|^2 \quad (1.40)$$

When squaring the scattering amplitude, the destructive interference<sup>15</sup> term decreases the  $\sigma_{tHq}$ . This behaviour makes the  $tHq$  cross section exceptionally sensible to the departures of  $y_t$  from the SM predictions. Typically, the destructive interference yields a reduction in the rate as compared to the contribution from each individual diagram by about an order of magnitude [76]. Therefore, in the presence of non-SM new physics, a positive relative sign between the  $tH$  and the  $WH$  couplings would imply that the amount of  $tHq$  events recorded should increase a factor of  $\sim 13$  over the SM expectations, surpassing the  $t\bar{t}H$  production [77].

The  $tHq$  production has been studied at LHC Run-1 by CMS [78]

**Usar los papers the  $tHq$  de CMS la sección 5 de Demartin [75]**

#### 1.4.2.1 $tH$ Standard Model

#### 1.4.2.2 $tH$ Charge-Parity

#### 1.4.2.3 ATLAS and CMS results

In order to gather the necessary information, the widest possible campaign of measurements has to be undertaken, including all the different Higgs decay modes. In this context, the scope of this thesis is the study of the production  $tH$  with a final state characterised by two light leptons ( $\ell$ ), i.e. electrons ( $e^\pm$ ) or muons ( $\mu^\pm$ ), and one hadronically decaying tau lepton

<sup>15</sup>By destructive interference is meant that the relative sign between  $\mathcal{M}_{qq \rightarrow tHq_{WH}}$  and  $\mathcal{M}_{qq \rightarrow tHq_{tH}}$  is negative.

<sub>1298</sub> ( $\tau_{\text{had}}$ ). This signature is usually referred as dileptau or lep-had channel and  
<sub>1299</sub> is denoted by  $2\ell + 1\tau_{\text{had}}$ .



<sub>1300</sub> **Chapter 2**

<sub>1301</sub> **The ATLAS experiment at the  
1302 Large Hadron Collider of  
1303 CERN laboratory**

<sub>1304</sub> The work developed in this thesis is framed in the context of the ATLAS  
<sub>1305</sub> detector, a general-purpose particle physics detector registering the events  
<sub>1306</sub> originated from the collisions produced by the largest and most powerful  
<sub>1307</sub> particle accelerator built up to this date, the LHC. This experimental setup  
<sub>1308</sub> is located in one of the largest and most renowned centres for scientific  
<sub>1309</sub> research in the world, the CERN.

<sub>1310</sub> This chapter is devoted to the introduction of the CERN laboratory and  
<sub>1311</sub> a description of the technical design of LHC and ATLAS. The CERN or-  
<sub>1312</sub> ganisation is presented through an overview of its history, its achievements  
<sub>1313</sub> and some of the most relevant research projects carried out currently. The  
<sub>1314</sub> essential technical aspects of the LHC machine design are covered. The  
<sub>1315</sub> distribution and functioning of the accelerator complex and the main exper-  
<sub>1316</sub> iments conducted at LHC are summarised as well. Finally, a full overview  
<sub>1317</sub> of the different components of the ATLAS detector is exposed, presenting  
<sub>1318</sub> the specific features of each of its parts.

<sub>1319</sub> **2.1 CERN**

<sub>1320</sub> The European Organization for Nuclear Research, known as CERN, is  
<sub>1321</sub> the largest particle physics laboratory in the world. The convention estab-  
<sub>1322</sub> lishing CERN was ratified in 1954. Its name is derived from the French  
<sub>1323</sub> acronym *Conseil Européen pour la Recherche Nucléaire*, which was the pro-  
<sub>1324</sub> visional body designated in 1952 to foster the fundamental physics research

in Europe, and the acronym has been maintained until CERN’s foundation.  
Initially formed by 12 member states, now it has 23 member states and  
many non-European countries involved in different ways such as associate  
members, partners and observers [79].

The main site of the laboratory is located at Meyrin, a municipality of  
the Canton of Geneva (Switzerland), at the Franco–Swiss border. There  
are other sites in the vicinity of the Meyrin site, being the most relevant the  
Prévessin Site, the CERN’s second-largest site, straddling the communes of  
Prévessin-Moën (France).

Since its beginning, CERN’s objective has been helping to uncover what  
the universe is made of and how it works. CERN started its first accelerator,  
the Synchrocyclotron, on 1957 and rapidly observed the electron decay of  
the pion for the very first time [80]. Thereafter, the laboratory has con-  
tinued contributing to not only particle and nuclear physics but also more  
technical fields. For instance, one of the most important achievements made  
through CERN experiments is the discovery in 1973 of neutral currents in  
the Gargamelle bubble chamber installed in the Proton Synchrotron (PS)  
[81]. This observation was an indirect evidence for the existence of the  $Z$   
boson and ten years later, in 1983, CERN announced the discovery of the  
 $Z$  and  $W$  bosons [82]. This finding was done at the UA1 and UA2 ex-  
periments, located within the Super Proton Synchrotron (SPS), and it was  
awarded with the laboratory first Nobel Prize in 1984. Other major suc-  
cesses of CERN were the determination of the number of light neutrino  
families at the Large Electron-Positron Collider (LEP) on 1995 [83] and the  
creation for the very first time of antihydrogen atoms in 1995 at the PS210  
experiment [84]. More crucial accomplishment followed such as the discov-  
ery during the 1990’s of  $\mathcal{CP}$  violation by NA31 [85] and NA48 experiments  
[86]. And, in 2012, the Higgs boson discovery by ATLAS and CMS [61] [62],  
a fundamental test for the robustness of the SM as described in Section  
[1.3.1](#). More recently, in 2015, a state consistent with a pentaquark was  
observed at LHCb [87].

Currently, a wide diversity of projects are carried at CERN being the  
most renowned of them the LHC and its experiments which are described in  
more detail in Section [2.2](#). In addition, fixed-target experiments, antimatter  
experiments and experimental facilities make use of the LHC injector chain.  
The main fixed-target experiments at CERN are the Antiproton Decelerator  
(AD) [88] for slowing antiprotons for the antimatter factory [89] and the  
On-Line Isotope Mass Separator (ISOLDE) facility for short-lived ions [90].  
The world’s first proton-driven plasma wakefield acceleration experiment is  
also at CERN, the Advanced Proton Driven Plasma Wakefield Acceleration  
Experiment (AWAKE) [91]. In the International Space Station (ISS), the

1366    Alpha Magnetic Spectrometer (AMS) tries to observe dark matter [92].  
1367    The research programme at CERN covers topics from the basic structure  
1368    of matter to cosmic rays, and from the Standard Model to supersymmetry.

1369    Important breakthroughs and advances have been done by CERN on  
1370    three main technical fields: accelerators, detectors and computing. Behind  
1371    these three areas of technology, lies a great number of topics of expertise:  
1372    cryogenics, ultra-high vacuums, particle tracking, radiation monitoring, su-  
1373    perconductivity, plasma-physics and many more. Probably, the most popu-  
1374    lar of the contributions is the invention of the World Wide Web (WWW) in  
1375    1989 at CERN facilities [93]. All of this proves the versatility and capability  
1376    of CERN as a contributor to science, technology and society.

## 1377    2.2 Large Hadron Collider

1378    In the mid of the decade of 1980, the plans for building the Large Hadron  
1379    Collider (LHC) were started. At several high-energy physics workshops  
1380    and conferences, the idea of assembling a machine able to reach multi-TeV  
1381    energies was discussed. This instrument would allow physicists to search for  
1382    the Higgs boson at all possible masses. In 1991 the Long-Range Planning  
1383    Committee of CERN proposed the construction of the LHC as the best step  
1384    forward in CERN's future [94]. The approval of the LHC project arrived in  
1385    1994 and in 1995 the Conceptual Design Report was published [95]. Finally,  
1386    on 10 September 2008, a beam of protons was successfully directed into the  
1387    LHC pipes for the first time.

1388    A summary of the main parameters of LHC for  $p p$  collisions is pre-  
1389    sented in Table 2.1. These parameters are shown for how the machine was  
1390    designed, for Run-1 (2011-2012) and Run-2 (2015-2018) as well as the ex-  
1391    pected parameters for Run-3 (2025-2027). The forecasted values for the  
1392    High Luminosity (HL) LHC upgrade (after 2027) are exposed too.

### 1393    2.2.1 Machine design

1394    The LHC is a circular hadron accelerator with a circumference of 27 km.  
1395    Located where once was the LEP collider, the accelerator used by CERN  
1396    from 1999 to 2000 [96], the LHC tunnels are almost entirely outside the  
1397    main site, being mainly on french territory. An overall schematic view of  
1398    the LHC is shown in Figure 2.1.

1399    The LHC has two rings with ultra-high vacuum (to prevent collisions  
1400    with gas molecules while moving through the accelerator) inside of which

Parameter	Design	Run-1	Run-2	Run-3	HL-LHC
Beam energy	7	3.5 - 4	6.5	7	7
Center-of-mass energy ( $\sqrt{s}$ ) [TeV]	14	7 - 8	13	14	14
Bunch spacing [ns]	25	50	25	25	25
Bunch Intensity [ $10^{11}$ ppb]	1.15	1.6	1.2	up to 1.8	2.2
Number of bunches ( $n_b$ )	2800	1400	2500	2800	2800
Transverse emittance ( $\epsilon$ ) [ $\mu\text{m}$ ]	3.5	2.2	2.2	2.5	2.5
Amplitude function at the interaction point ( $\beta^*$ ) [cm]	55	80	30→25	30→25	down to 15
Crossing angle [ $\mu\text{rad}$ ]	285	-	300→260	300→260	TBD
Peak Luminosity [ $10^{34} \text{ cm}^2 \text{ s}^{-1}$ ]	1.0	0.8	2.0	2.0	5.0
Peak pileup	25	45	60	55	150
Nominal magnetic field ( $B$ ) [T]	8.73	4.16 - 7.76	7.73	8.73	8.73
Injection energy [GeV]				450	
Circumference length [km]				26.7	
Radius [km]				4.24	
Number of dipole magnets				1232	
Length of dipole magnets [m]				14.3	
Number of quadrupole magnets				395	
Total mass [tons]				27.5	

**Table 2.1:** Summary of main accelerator parameters for the LHC, showing the design values, and those used during Run-1 and Run-2, as well as the expected parameters for Run-3 and the HL-LHC.

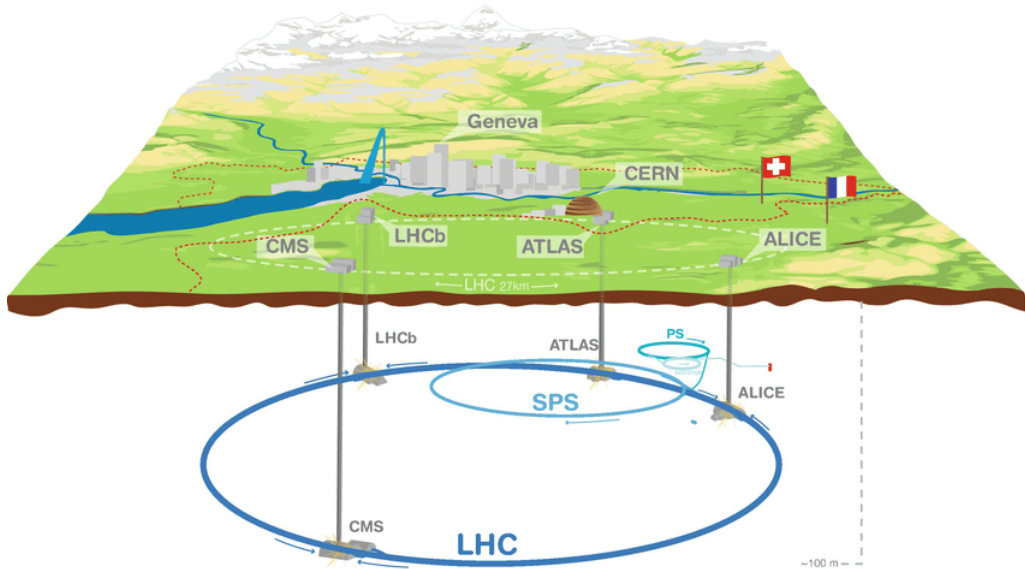


**Figure 2.1:** Overall view of the LHC including the ATLAS, CMS, ALICE and LHCb experiments.

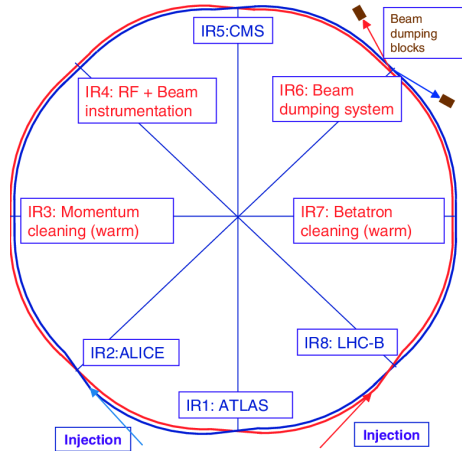


**Figure 2.2:** Schematic layout of the LHC (Beam 1 clockwise, Beam 2 anti-clockwise).



**Figure 2.3:** LHC dipole cross section.

1401 particle beams travel in opposite directions. It was designed to accelerate  
 1402 and collide proton beams with a center-of-mass energy ( $\sqrt{s}$ ) up to 14 TeV  
 1403 at a luminosity ( $\mathcal{L}$ ) of  $10^{34} \text{ cm}^2 \text{ s}^{-1}$  (see Section 2.2.5 for details about  
 1404 luminosity). As well as protons, it can collide heavy ions, in particular  
 1405 lead nuclei, at  $\sqrt{s} = 2.3 \text{ TeV}$  per nucleon and a peak luminosity of  $\mathcal{L} = 10^{27}$   
 1406  $\text{cm}^2 \text{ s}^{-1}$  [97]. These specifications make the LHC the accelerator with higher  
 1407 collision energy [98].

1408 The beams in the LHC are made up of bunches of protons that are  
 1409 spaced 7 m apart and collide every 25 ns. Each bunch contains  $1.1 \times 10^{11}$   
 1410 hadrons, being 2556 the maximum possible number of bunches that can be  
 1411 reached with the beam preparation method currently used [99]. The size of  
 1412 each bunch is 25 cm [100].

1413 The LEP tunnel lies between 45 m and 170 m below the surface on a  
 1414 plane inclined at 1.4% sloping towards the Léman lake. The underground  
 1415 construction adds some shielding from outside interferences that could  
 1416 interact with the detectors and cause anomalous readings. Even 100 m under-  
 1417 ground, the cosmic rays can reach the detectors, so these are used to help to  
 1418 calibrate them. The tunnel has an internal diameter of 3.7 m, which makes  
 1419 it extremely difficult to install two completely separate proton rings [101]  
 1420 as in the Superconducting Super Collider (SSC). Therefore, the counter-  
 1421 rotating rings are built under the *two-in-one* twin-bore superconducting  
 1422 magnet design. These twin bore configurations have the disadvantage of  
 1423 having the rings magnetically coupled, which adversely affects flexibility  
 1424 [102]. Figure 2.3 shows an example of the LHC twin-bore dipole magnet.

The LHC is not a perfect circle. Approximately 22 km of the LHC ring consists of 8 curved sections. The remaining 5 km of the tunnel are made of 8 straight sections, denominated insertion regions (IR), that provide space for the experiments. Figure 2.2 shows the distribution of IR and crossing points for the LHC. This layout follows that of the LEP tunnel. The number of crossing points where the beams pass from one ring to the other for colliding was decreased from the original 8 at LEP to 4 in the LHC in order to reduce costs and optimise the utility insertions containing Radio Frequency (RF), the collimation and the beam dump systems [95].

The arcs contain the dipole bending magnets, which are shown in Section 2.3. The 1232 twin-bore magnets curve the trajectory of the particle beam that would, otherwise, follow a straight line. Dipoles are also equipped with additional multipole lattice magnets (sextupole, octupole and decapole), which correct for small imperfections in the magnetic field at the extremities of the dipoles.

Each of the 8 straight sections is approximately 528 m long. The RF cavities delivering 2 MV (an accelerating field of 5 MV/m) at 400 MHz are located in the IR4. The 16 RF cavities compensate the synchrotron radiation losses (the electromagnetic radiation emitted when charged particles travel in curved paths) that take place at the arcs of LHC. The energy radiated per particle by synchrotron radiation is proportional to the inverse of the mass of the particle:  $\Delta E \propto 1/m^4$ . This radiation is, thus, smaller for protons than for electrons. That is why the LHC machine has much less synchrotron radiation losses than LEP and its design would ideally have longer arcs and shorter straight sections for the same circumference. But using the tunnel as built for LEP was the cost-effective solution. During the 20 minutes that are needed to reach the beams maximum energy, the bunches have passed the RF cavities more than 10 million times [95].

The RF cavities (also known as resonators) are metallic chambers spaced at intervals along the accelerator shaped to resonate at specific frequencies, allowing radio waves to interact with passing particle bunches. The main role of the RF cavities is to keep the proton bunches tightly packed to ensure the required luminosity at the interaction point. They also transfer RF power to the beam to accelerate it to the top energy [103].

At the insertion of the arc and straight sections, quadrupole magnets are installed to suppress the dispersion of particles. Acting as focal lenses, quadrupole magnets gather the particles together. This system not only cancels the horizontal dispersion arising in the arc but also adapts the LHC reference orbit to the geometry of the LEP tunnel. Before entering the detectors, the inner triplets (which are made mostly from quadrupoles)

<sup>1465</sup> tighten the beam, from  $0.2 \times 10^{-3}$  m down to  $16 \times 10^{-6}$  m. These are known  
<sup>1466</sup> as insertion magnets.

<sup>1467</sup> In total there are more than 9000 magnets all over the LHC and more  
<sup>1468</sup> than 50 types of magnets are needed to make the particles circulate in  
<sup>1469</sup> their path without losing speed. The coils are made of niobium-titanium  
<sup>1470</sup> (NbTi) which is cooled to less than 2 K with superfluid helium to reach  
<sup>1471</sup> superconductivity.

Of course, only stable charge particles<sup>1</sup> such as electrons, positrons, protons, antiprotons and some ions, can be accelerated by the magnetic fields described. The force that experiments a charged particle with charge  $q$  moving under a magnetic field  $B$  at a speed  $v$  is given by Lorentz law

$$\vec{F} = q \vec{v} \times \vec{B} \quad (2.1)$$

<sup>1472</sup> and, since  $\vec{B}$  is perpendicular to  $\vec{v}$ , this force is always directed to the  
<sup>1473</sup> center of the circle of radius  $r$ :  $F = Bqv = m\frac{v^2}{r}$ .

## <sup>1474</sup> 2.2.2 Accelerator complex

<sup>1475</sup> To accelerate the proton beams, the existing CERN accelerator complex  
<sup>1476</sup> is used. These accelerators were, back in the day, the state of the art  
<sup>1477</sup> colliders and now they serve as injection system for the LHC. The path  
<sup>1478</sup> followed by the particle beams is presented in Figure 2.4. The accelerator  
<sup>1479</sup> complex consists in several machines interconnected with higher and higher  
<sup>1480</sup> capabilities, i.e. the beams are injected from one accelerator to the next in  
<sup>1481</sup> sequence, boosting the particles to higher energies in each step until they  
<sup>1482</sup> enter into the LHC.

<sup>1483</sup> The proton bunches are produced ionising a gas of hydrogen atoms and  
<sup>1484</sup> then they are accelerated to a momentum of 50 MeV by the linear accelerator  
<sup>1485</sup> (LINAC2). Starting from Run-3, the LINAC2 is being replaced by the  
<sup>1486</sup> LINAC4. After being produced, the beams enter into the first circular  
<sup>1487</sup> accelerator, the Proton Synchrotron Booster (PSB) which has 630 m radius  
<sup>1488</sup> and increases the energy of the protons until 1.4 GeV.

<sup>1489</sup> The main advantage of circular accelerators compared to linear ones is  
<sup>1490</sup> that they can speed up particles with much less physical space. Circular  
<sup>1491</sup> accelerators ramp up two different beams with opposite charges at the same  
<sup>1492</sup> time with a single magnetic field. The maximum energy transferred to the  
<sup>1493</sup> beams in a circular accelerator is given by  $p_T$  [GeV] =  $0.3qB[T]r[m]$ , being

---

<sup>1</sup>Long-lived particles such as the muon ( $\tau \approx 2 \times 10^{-6}$  s) are discussed to be used on a muon collider [104].

1494  $p_T$  the transverse momentum of the particles,  $q$  the charge of the particles  
1495 ( $q = 1$  for protons),  $B$  the magnetic field applied and  $r$  the radius of the  
1496 circular accelerator.

1497 Right after the PSB, the Proton Synchrotron brings the particles 25 GeV.  
1498 The next step in the chain raises the energy to 450 GeV. This is done by the  
1499 SPS, which is 6.9 km long. Once the protons have 450 GeV, the minimum  
1500 energy at which the LHC can maintain a stable beam, they are injected  
1501 into the LHC by two different 2 km-long Transfer Injection (TI) lines [105].  
1502 Protons will circulate in the LHC for 20 minutes until reaching the maximum  
1503 speed and energy (650 GeV per beam) [102].

1504 Heavy-ion collisions were included in the conceptual design of the LHC  
1505 from an early stage. Lead ions for the LHC are extracted from a source  
1506 of vaporised lead and enter LINAC3 before being collected and accelerated  
1507 in the Low Energy Ion Ring (LEIR). They, then, follow the same route to  
1508 maximum acceleration as the protons [102].

### 1509 **2.2.3 LHC Experiments**

1510 In the LHC four major experiments are carried, each of them with its own  
1511 detector (Figure 2.5). These particle detectors measure particles produced  
1512 as debris from the  $pp$  collisions through the interaction with the material  
1513 of the sub-detectors. Distributed along the collider as is shown in Figures  
1514 2.1, 2.2 and 2.4, these highly sophisticated experiments are:

- 1515 • **A Toroidal LHC ApparatuS (ATLAS)** [106]: Located in the IR1,  
1516 it is a generic multi-purpose experiment for high luminosity (up to  $\mathcal{L}$   
1517  $= 10^{34} \text{ cm}^2 \text{ s}^{-1}$ ). It studies proton-proton collisions and investigates  
1518 a wide range of physics, from the search for extra dimensions to dark  
1519 matter. It has the dimensions of a cylinder, 46 m long, 25 m in dia-  
1520 meter. The ATLAS detector weighs  $7 \times 10^3$  tonnes. The design of the  
1521 ATLAS detector features excellent jet and  $E_T^{\text{miss}}$  resolution, particle  
1522 identification and flavour tagging and standalone muon measurements.  
1523 ATLAS will be covered in detail in Section 2.3.
- 1524 • **Compact Muon Solenoid (CMS)** [107]: Built inside the IR5, it's  
1525 the other general-purpose experiment for high luminosity (same  $\mathcal{L}$  as  
1526 ATLAS). CMS has the same objectives and goals as ATLAS but both  
1527 its hardware and software designs are different. Even though CMS is  
1528 smaller than ATLAS (21 m long, 15 m in diameter) it is much heavier,  
1529 weighting  $14 \times 10^3$  tonnes. The bulk of its weight is the steel yoke that  
1530 confines the 4 T magnetic field of its superconducting solenoid. The

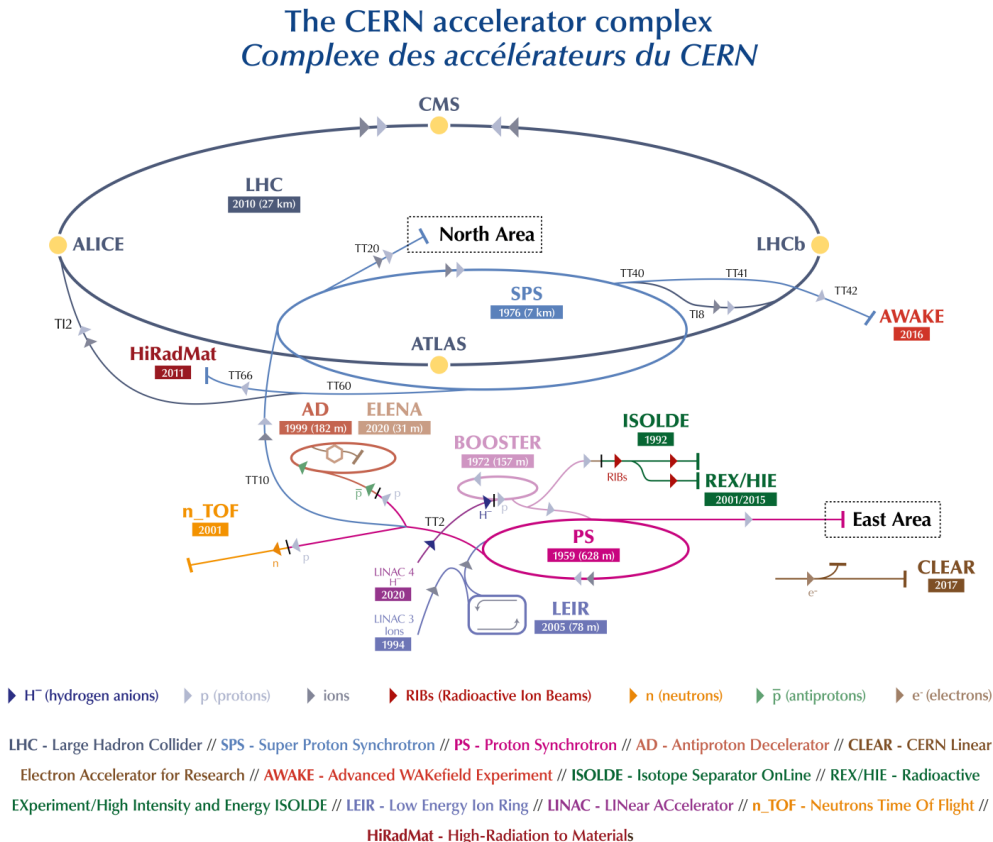


**Figure 2.4:** Scheme of CERN accelerator complex. Protons are injected from the LINAC2 into the PS Booster, then the PS, followed by the SPS, before finally reaching the LHC.

design of CMS emphasises magnificent electron/photon energy and momentum resolution. The role of coexistence of CMS and ATLAS is fundamental so that one can verify and confirm the experiments of the other independently.

- **Large Hadron Collider beauty (LHCb) [108]:** Hosted at IR2, it is a lower luminosity experiment designed to study the small asymmetries between matter and antimatter through  $\mathcal{CP}$  violation using rare decays of  $b$ -quark based hadrons. The detector is arranged as a succession of planar sub-detectors since most of the  $b$ -flavoured mesons follow the beam pipe direction when created in the proton-proton collision. LHCb delivers remarkable low-momentum track reconstruction and particle identification.
- **A Large Ion Collider Experiment (ALICE) [109]:** It is a low luminosity experiment in IR8 that focuses on QCD, the strong-

1545 interaction sector of the SM. The main feature of ALICE is a general-  
 1546 purpose detector that it uses heavy-ion collisions to study matter in-  
 1547 teracting at extreme densities and temperatures, thus reproducing the  
 1548 quark-gluon plasma. This detector provides highly efficient track re-  
 1549 construction in an environment full of heavy ions. Besides running  
 1550 with Pb ions, the physics programme includes collisions with lighter  
 1551 ions, lower energy collisions and a dedicated proton-nucleus run.

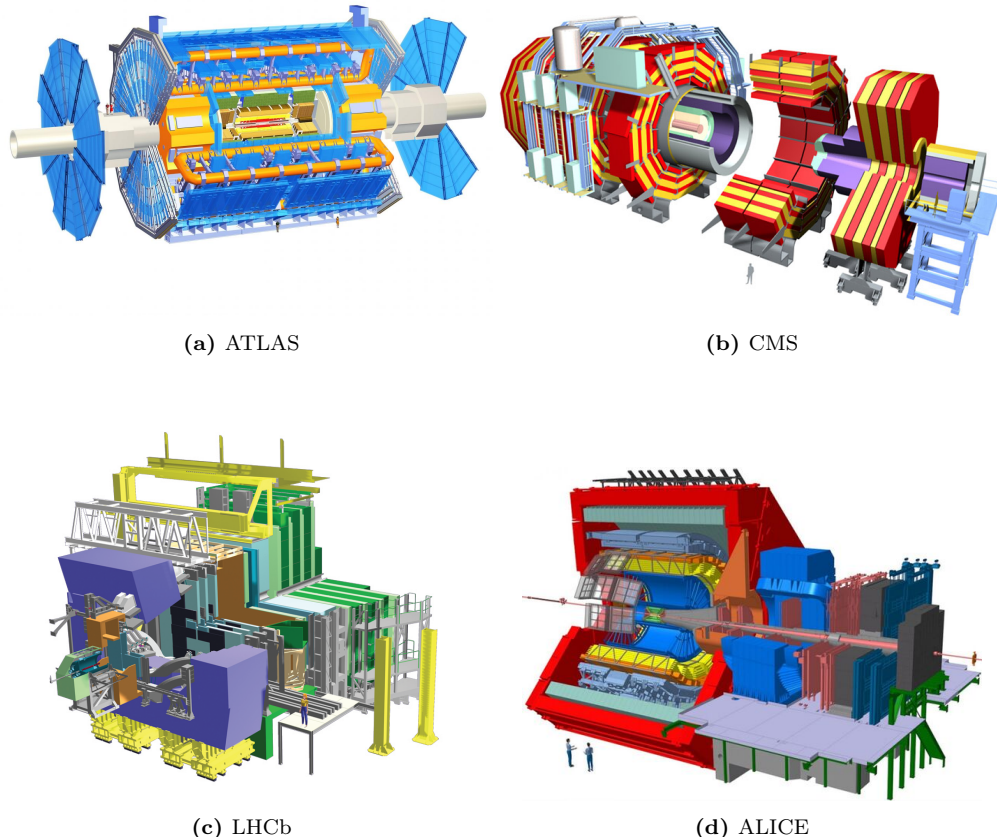


**Figure 2.5:** Scheme of LHC main experiments. Note that the images are not equally scaled.

1552 Along the LHC machine, there are other experiments much more smaller  
 1553 than ATLAS, CMS, LHCb and ALICE, typically sharing the cavern with  
 1554 the major projects. The most relevant among the minor experiments are:

- 1555 • **The Large Hadron Collider forward (LHCf)** [110]: Uses  
 1556 particles thrown forward by collisions in the Large Hadron Collider  
 1557 as a source to simulate cosmic rays in laboratory conditions. It shares  
 1558 its cavern with the ATLAS detector [111].

- 1559     • **The Massive Timing Hodoscope for Ultra Stable neutrAL**  
1560     **pArticles (MATHUSLA)** [112]: Is dedicated large-volume dis-  
1561     placed vertex detector for the HL-LHC on the surface above ATLAS  
1562     or CMS for the search for neutral long-lived particles.
  
- 1563     • **MilliQan** [113][114]: Consists on a small-scale detector experiment  
1564     aiming to detect millicharged particles, i.e., particles with charges  
1565     much smaller than that of the electron.
  
- 1566     • **Monopole and exotic particle detector at the LHC**  
1567     (**MoEDAL**) [115]: Deployed at LHCb cavern, it is optimised to de-  
1568     tect highly ionising particles such as magnetic monopoles, dyons and  
1569     multiple-electrically charged stable massive particles predicted in a  
1570     number of theoretical scenarios.
  
- 1571     • **TOTEM** [116]: Aims to measure the total cross-section of  $pp$  inter-  
1572     action using a luminosity-independent method and study elastic and  
1573     diffractive scattering at the LHC. As CERN longest experiment, TO-  
1574     TEM detectors are spread across almost half a kilometre around the  
1575     CMS interaction point.
  
- 1576     • **ForwArd Search ExpeRiment (FASER)** [117][118]: Designed to  
1577     search for new, yet undiscovered, light and weakly-interacting particles  
1578     and study the interactions of high-energy neutrinos.

#### 1579     2.2.4 LHC Computing grid

1580     The data collected by the different LHC experiments is stored, processed  
1581     and, then, made available for all the researchers of each collaboration<sup>2</sup>. This  
1582     is possible thanks to the last piece of the LHC, its computing model and  
1583     infrastructure: the LHC Computing Grid (LCG). It consists of several com-  
1584     puting farms distributed around the world and interconnected. Figure 2.6  
1585     shows the geographical distribution of the different facilities that comprise  
1586     the LCG. Just as the WWW enables access to information, the Grid en-  
1587     ables access to computer resources. Employing a grid certificate, is possible  
1588     for any user to run jobs on the grid and to access the data stored. The  
1589     implementation of the grid model implies an effective coordination among  
1590     all LHC collaboration centres [119].

1591     Different types of computing centres have been defined and classified in  
1592     Tiers [121]:

---

<sup>2</sup>Within the grid context, each collaboration is known as Virtual Organisation (VO).



**Figure 2.6:** Worldwide LHC Computing Grid geolocalisation of sites [120].

- **Tier-0:** This facility is located at CERN and it is responsible for archiving (first copy) and distributing the raw data received from the Event Filter, i.e., the data emerging from the Data Acquisition systems (DAQ) after the trigger. It provides prompt reconstruction and distributes a copy of the raw data to the Tier-1 centres.
- **Tier-1:** These facilities archive the raw data permanently and provide the computational capacity for reprocessing and for physical analysis. It also stores the simulated and reprocessed data. Currently, there are thirteen large computer centres serving as Tier-1 (see Figure 2.7). These make data available to their Tier-2 centres [122].
- **Tier-2:** Typically located at universities and other scientific institutes, there are more than 150 Tier-2 sites. The derived datasets produced by the physics groups are copied to the Tier-2 facilities for further analysis. The MC simulations for event production are executed at this level.
- **Tier-3:** The local computing resources, from local clusters to even just an individual PC are referred to as Tier-3. There is no formal engagement between worldwide LCG and the Tier-3.

This system provides near real-time access to LHC data. The LCG collaboration spreads out over 42 countries with 170 computing centres and 1 million computer cores, being the world's largest computer grid. It deals with over two million tasks daily. These specifications make the LCG the most sophisticated system for data taking and analysis ever built for science.

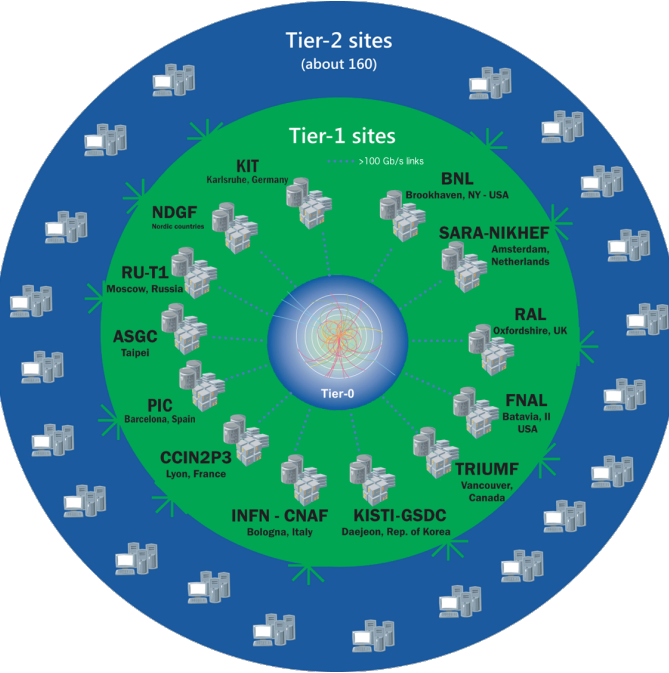


**Figure 2.7:** LCG Tiers [122].

### 1616 2.2.5 Energy, Luminosity and Cross-section

#### 1617 Energy

1618 Another name to refer to the field of Particle Physics is “high energy phys-  
 1619 ics”. Particles such as the Higgs boson or the top quark are more than 100  
 1620 times heavier than the proton so, in order to produce them, huge energies  
 1621 are required. The energy of the interaction,  $\sqrt{s}$ , allows the production of  
 1622 physical effects. The greater the energy is, the bigger is the range of the  
 1623 different processes that can be produced by the accelerator.

The four-vector,  $\mathbf{p} = (E, \vec{p})$ , of a particle of mass  $m$  describes its kinematics with its energy  $E$  and  $\vec{p}$ . The square of the four-vector,  $\mathbf{p}^2$ , corresponds to the particle mass:

$$\mathbf{p}^2 = E^2 - \vec{p}^2 = m^2 \quad (2.2)$$

When two particles of mass  $m_1$  and  $m_2$  and momenta  $\vec{p}_1$  and  $\vec{p}_2$  respectively collide, the center of mass energy,  $\sqrt{s}$ , can be expressed as:

$$s = E_{CM}^2 = (\mathbf{p}_1 + \mathbf{p}_2)^2 = (E_1 + E_2)^2 - (\vec{p}_1 + \vec{p}_2)^2 \quad (2.3)$$

For symmetric colliding beams, such those of LHC, the collision point is at rest in the laboratory frame ( $\vec{p}_1 = -\vec{p}_2$ ) and, hence, the energy is

$$s = E_{CM}^2 = (E_1 + E_2)^2 \quad (2.4)$$

1624 Since the energy of each beam is 650 GeV during Run-2, the center of mass  
1625 energy of LHC collisions is

$$\sqrt{s} = E_{CM} = (E_{beam1} + E_{beam2}) = 650 \text{ GeV} + 650 \text{ GeV} = 13 \text{ TeV} \quad (2.5)$$

When LHC is used for fix target experiments, one of the particles in the collision is at rest ( $\vec{p}_2 = 0$ ) and the equation 2.3 writes as:

$$E_{CM}^2 = (m_1^2 + m_2^2 + 2m_2 E_{1,lab}) \quad (2.6)$$

Then, the energy for a proton-proton fix target collision with one beam at 650 GeV is

$$\begin{aligned} E_{CM}^2 &= (m_p^2 + m_p^2 + 2m_p E_{beam}) \\ &= 2(0.938 \text{ GeV})^2 + 2 \cdot 0.938 \text{ GeV} \cdot 650 \text{ GeV} = 1221.2 \text{ GeV}^2 \\ E_{CM} &= 34.9 \text{ GeV} \end{aligned} \quad (2.7)$$

1626 This shows why colliding beams are essential to achieve high center of mass  
1627 energies.

1628 **Luminosity**

1629 Besides  $\sqrt{s}$ , the luminosity is the most relevant parameter in an experiment,  
1630 especially in searches for events with small cross-section. It measures the  
1631 ability of the particle accelerator to produce enough events of the desired  
1632 type.

The luminosity,  $\mathcal{L}$ , is the ratio of events detected in a certain period of time for a given cross-section ( $\sigma$ ):

$$\mathcal{L} = \frac{1}{\sigma} \frac{dN}{dt} = \frac{1}{\sigma} R \quad (2.8)$$

1633 where  $N$  is the number of the events and  $t$  the time.  $R = \frac{dN}{dt}$  is known as  
1634 reaction rate. It can be understood as number of particle collision per unit  
1635 area (typically expressed in  $\text{cm}^2$ ) and per second, therefore it is measured in  
1636  $\text{cm}^2 \text{s}^{-1}$  [123]. For instance, for LEP was  $\mathcal{L}_{LEP} = 1.0 \times 10^{32} \text{ cm}^2 \text{s}^{-1}$  and  
1637 the LHC is designed to achieve  $\mathcal{L}_{LHC_{pp}} = 2.1 \times 10^{34} \text{ cm}^2 \text{s}^{-1}$  in  $pp$  collisions  
1638 and  $\mathcal{L}_{LHC_{PbPb}} = 6.1 \times 10^{27} \text{ cm}^2 \text{s}^{-1}$  for heavy ion collisions.

For two beams colliding, the instantaneous luminosity is proportional to the number of bunches per beam ( $n_1$  and  $n_2$ ), the revolution frequency ( $f$ ) with which the bunches are crossing and the number of proton bunches in

the machine ( $n_b$ ), and it is and inversely proportional to the beams effective transverse area in which the collision takes places (Area =  $4\pi\sigma_x\sigma_y$ )

$$\mathcal{L} = f \cdot \frac{n_1 n_2 n_b}{4\pi\sigma_x\sigma_y} \cdot F(\theta_c, \sigma_x, \sigma_z) \quad (2.9)$$

where  $F(\theta_c, \sigma_x, \sigma_z)$  is a factor accounting for the luminosity reduction due to the beam crossing angle ( $\theta_c$ ). At the LHC, assuming that the particles travel at the speed of light, for its 27 km, the bunch crossing frequency is  $f = 11245.5$  Hz. The maximum number of proton bunches in the machine with 25 ns slots is<sup>3</sup>  $n_b = 2808$ . In each bunch there are  $n_1 \approx n_2 \approx 1.15 \times 10^{11}$  particles. Finally, characterising the optics of the collision at the interaction point (IP), the RMS transverse beam width in the horizontal and vertical directions are  $\sigma_x \approx \sigma_y \approx 12, \dots, 50 \mu m$ . The expression 2.9 assumes that the particles in the beam are Gaussian distributed. According to equation 2.9 the instantaneous luminosity only depends on the machine and its beam parameters [124][125].

The integrated luminosity over time is given by

$$L = \int \mathcal{L} dt \quad (2.10)$$

and it is used to determine the number of events,  $N$ , that have taken place during that time:  $N = \sigma \times L$ . The ability to observe low cross-section events is

$$N_{events}^{obs} = \sigma_{process} \times \text{efficiency} \times L \quad (2.11)$$

, where the efficiency of the detection is to be optimised by the experimental physicist, the integrated luminosity ( $L$ ) is delivered by LHC and the cross-section of the process ( $\sigma_{process}$ ) is given by nature.

On one hand, several factors can limit the maximum luminosity that can be achieved at LHC [123]:

- **Beam-beam effect:** The bunches of two beams or the particles in the same bunch can interact electromagnetically, this leads to distortions from the orbit and results in an increase of the emittance,  $\epsilon$ .
- **Crossing angle:** Often used to avoid unwanted collisions in machines with many bunches, due to the crossing angle  $\theta_c$ , the luminosity is reduced by a factor  $F(\theta_c, \sigma_x, \sigma_z) = \sqrt{1 + (\theta_c \sigma_z / 2\sigma x)^2}$ .
- **Beam offset:** Originated from the beam-beam effects or misalignments in the quadrupole magnets, the beams can collide with small

---

<sup>3</sup>The theoretical maximum of 3564 bunches cannot be reached due to space needed between bunch trains and for the beam dump kicker magnets.

Year	2015	2016	2017	2018
Peak instantaneous luminosity ( $\times 10^{33} \text{ cm}^2 \text{ s}^{-1}$ )	5	13	16	19
Total delivered integrated luminosity ( $\text{fb}^{-1}$ )	4.0	38.5	50.2	63.4

**Table 2.2:** Peak luminosity and total integrated luminosity delivered by the LHC at  $\sqrt{s} = 13 \text{ TeV}$  in Run-2 per year [127].

1663 transverse offset. Such beams' offsets induce a loss of  $\mathcal{L}$  at the inter-  
 1664 action point.

- 1665 • **Hourglass effect:** Appears when beams collide in a point away from  
 1666 the IP.

1667 On the other hand, there are diverse strategies to maximise the lumin-  
 1668 osity delivered by a machine [124]:

- 1669 • **Maximise the total beam current:** Improvements in beam col-  
 1670 limitation, cryogenics vacuum and background protection could extend  
 1671 the limit on the maximum beam current.
- 1672 • **Compensate reduction factor:** The hourglass effect may be re-  
 1673duced by shorter bunches at the expense of a higher longitudinal pileup  
 1674 density (see Section 2.2.6).

1675 The cumulative luminosity delivered by LHC to ATLAS during the Run-  
 1676 2 per year is shown in Figure 2.8. In Figure 2.9, the total Run-2 cumulative  
 1677 luminosity is presented differentiating between the delivered and recorded  
 1678 luminosity and showing that almost all delivered events are considered to  
 1679 be good data quality. The delivered luminosity accounts for the luminosity  
 1680 given from the start of stable beams until the LHC requests ATLAS to  
 1681 put the detector in a safe standby mode to allow a beam dump or beam  
 1682 studies. The recorded luminosity reflects the DAQ inefficiency, as well as  
 1683 the inefficiency of the so-called “warm start”: when the stable beam flag is  
 1684 raised, the tracking detectors undergo a ramp of the high-voltage and, for  
 1685 the pixel system, turning on the preamplifiers. The All Good Data Quality  
 1686 criteria require all reconstructed physics objects to be of good data quality  
 1687 [126].

### 1688 Cross-section

1689 The cross-section is a metric of the likely is a particular reaction to occur.  
 1690 The higher the cross section is for a process, the more probable is for it to  
 1691 take place. Denoted by  $\sigma$ , it is measured in units of area named barns: 1  
 1692 barn =  $b = 10^{-24} \text{ cm}^2$ . For instance, for the LHC energy:

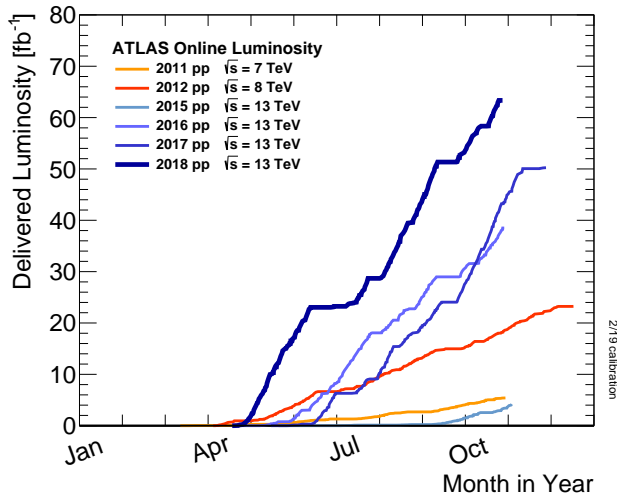


**Figure 2.8:** Cumulative luminosity versus day delivered to ATLAS during stable beams and for high energy  $pp$  collisions **Maybe it is not a good idea to put an ATLAS plot before introducing ATLAS. Move figure to section 3.2.1.5.**

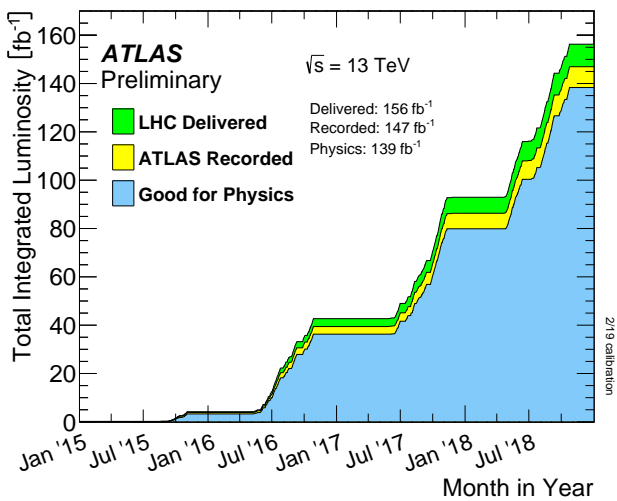


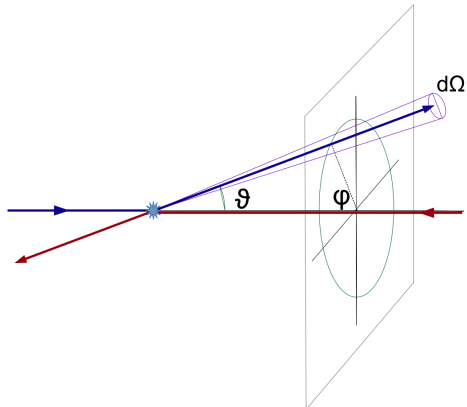
**Figure 2.9:** Total cumulative luminosity versus time delivered to ATLAS (green), recorded by ATLAS (yellow) and certified to be good quality data (blue) during stable beams for  $pp$  collisions at  $\sqrt{s} = 13 \text{ TeV}$ .

- 1693 •  $\sigma(pp \rightarrow X) \approx 0.1 \text{ b}$
- 1694 •  $\sigma(pp \rightarrow X + H) \approx 1 \times 10^{-11} \text{ b}$
- 1695 •  $\sigma(pp \rightarrow X + H; H \rightarrow \gamma\gamma) \approx 50 \times 10^{-15} \text{ b}$

1696 In experiments with rotational symmetry, such as ATLAS, it is usual to  
1697 define the differential cross-section ( $\frac{d\sigma}{d\Omega}$ ) as the cross-section per solid angle.  
1698 If the differential cross-section is integrated over corresponding the angular  
1699 range, the cross-section for a specific region ( $\sigma_\vartheta$ ) is obtained:

$$1700 \quad \sigma_\vartheta = \int_0^\vartheta \int_0^{2\pi} \frac{d\sigma}{d\Omega} \sin(\vartheta) d\phi d\vartheta$$

1701 with  $\vartheta \in [0, \pi]$  is the coverage of  
1702 the scattering angle.



The total cross-section is determined by the matrix element  $\mathcal{M}$ , which is independent of the experimental setup. The  $\mathcal{M}$ , also known as scattering amplitude, relates the initial state and the final state of a physical system undergoing a scattering process. Using  $\mathcal{M}$ , the total cross-section for a process is determined by:

$$\sigma_{tot} = \int \frac{d\sigma}{d\Omega} d\Omega = \int \frac{1}{\Phi} |\mathcal{M}|^2 dQ$$

1701 being  $\Phi$  the incident particle flux in the process and the parameter  $dQ$   
1702 describes the kinematic phase space.

## 1703 2.2.6 The Pile-up effect

1704 Pile-up is a challenging matter among detectors and for the acquisition  
1705 and analysis of the data. In particle physics, pile-up is called to the situation  
1706 where the detector is being affected by several events at the same time.

1707 Even though the bunches are composed by  $\sim 10^{11}$  protons, there are  
1708 only around 30 collisions per crossing with nominal beam currents. The  
1709 mean number of interactions per bunch crossing is presented in Figure 2.10  
1710 for each year of Run-2. The data shown in Figure 2.10 is recorded by AT-  
1711 LAS during stable beams at  $\sqrt{s} = 13 \text{ TeV}$ . The mean number of interactions

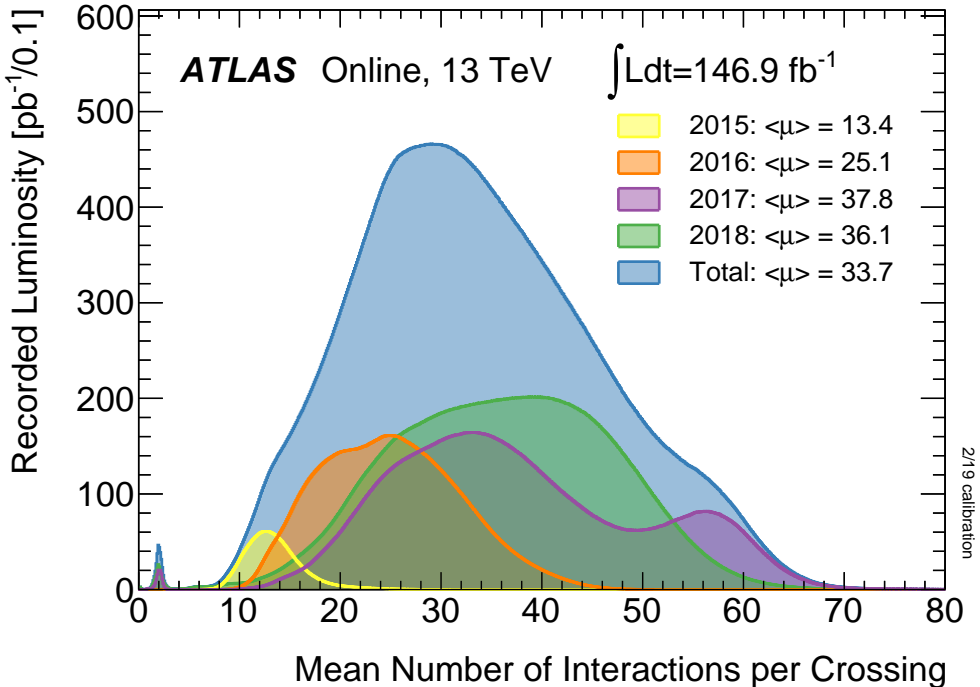


**Figure 2.10:** Luminosity-weighted distribution of the mean number of interactions per crossing  $\langle \mu \rangle$  for Run-2 with  $pp$  collisions data.

per crossing corresponds to the mean of the poisson distribution of the number of interactions per crossing calculated for each bunch. It is calculated from the instantaneous per bunch luminosity as  $\langle \mu \rangle = \mathcal{L}_{bunch} \times \sigma_{inel}/f_r$  where  $\mathcal{L}_{bunch}$  is the instantaneous luminosity per bunch,  $\sigma_{inel} = 80$  mb is the inelastic cross section of  $pp$  collisions at 13 TeV and  $f_r = 11.245$  kHz is the LHC revolution frequency.

#### 1718 Work in progress

### 1719 2.2.7 Phenomenology of proton-proton collisions

1720 During LHC Run-2 data taking period, the protons were colliding at a  
 1721 center-of-mass energy of  $\sqrt{s} = 13$  TeV. The  $pp$  total cross-section at this  
 1722 energy is measured to be  $\sigma_{tot} = (110.6 \pm 3.4)$  mb [128]. The luminosity-  
 1723 independent method used to measure  $\sigma_{tot}$  allows to split the cross-section  
 1724 into elastic and inelastic cross-sections,  $\sigma_{el} = (31.9 \pm 1.7)$  mb and  $\sigma_{inel} =$   
 1725  $(79.5 \pm 1.8)$  mb respectively. However, only inelastic scattering generates  
 1726 particles with an sufficient angle with respect to the beam axis so that  
 1727 these particles enter into the geometrical acceptance of the detector. Figure  
 1728 2.11 shows the cross-section (elastic, inelastic and total) for  $pp$  collisions

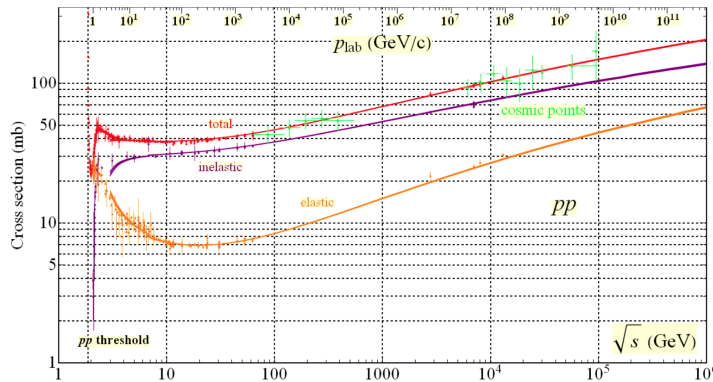


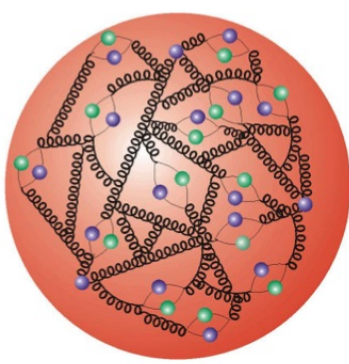
**Figure 2.11:** Total and elastic cross-section for  $pp$  collisions as a function of the laboratory momentum and the  $\sqrt{s}$  [129].

1729 depending on  $\sqrt{s}$  ([Why the values of the Figure 2.11 do not match the:  \$\sigma\_{tot} = \(110.6 \pm 3.4\)\$ ,  \$\sigma\_{el} = \(31.9 \pm 1.7\)\$  and  \$\sigma\_{inel} = \(79.5 \pm 1.8\$ \)](#)).  
 1730 The shown cross-section can be computed as the convolution of parton  
 1731 density functions (PDF) with the parton scattering matrix element  $\mathcal{M}$ .  
 1732

1733 Unlike leptons, protons are composite objects since they are made of  
 1734 quarks and gluons. Therefore and specially at LHC energy regime, the  $pp$   
 1735 collisions cannot be described as a point-like interactions, here is where the  
 1736 PDFs come into play. The PDFs are functions containing the long distance  
 1737 structure of the hadron in terms of valence and sea quarks and gluons.  
 1738 This description is known as “parton model”.

### 1739 2.2.7.1 Proton structure and parton model for collisions

1740



The parton model for hadrons describes these non-fundamental particles as a composite of a number of point-like constituents named partons. The proton is not only simply made of three quarks ( $uud$ , the so called “valence” quarks) but also, there is a “sea” of gluons and short-lived quark and anti-quark pairs. The partons in the sea are continuously interacting with each other and can have any flavour.

1741 The PDFs describe the distribution of the hadron’s momentum among  
 1742 its constituents. The PDFs are essential to describe the  $pp$  interactions be-  
 1743 cause these collisions cannot be understood as point-like particles crashing.  
 1744 Instead, all the constituents of the protons are taken into account [50].

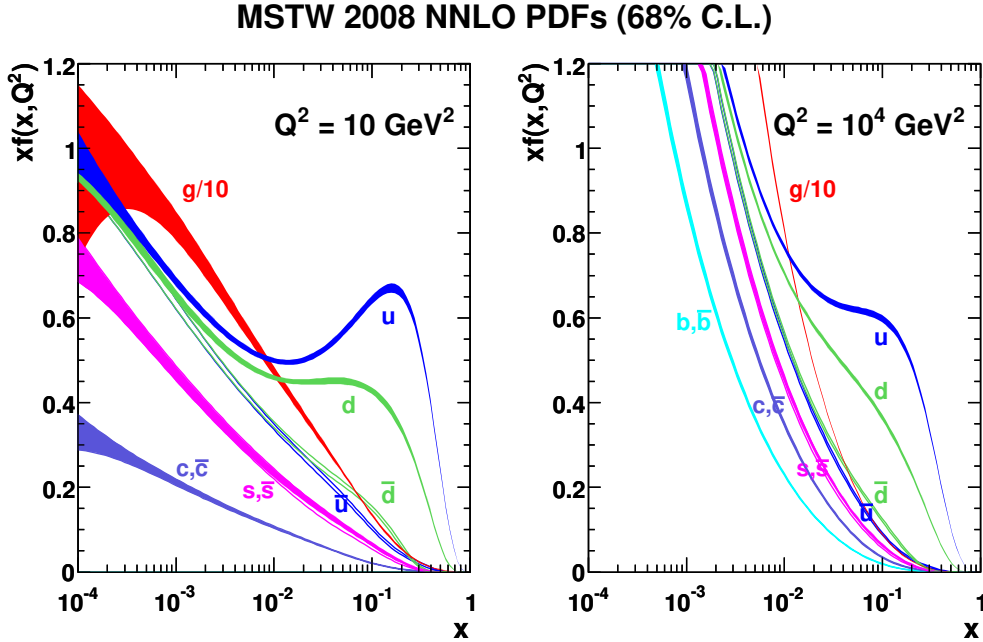


**Figure 2.12:** Parton distribution functions  $xf(x, q^2)$  plotted against  $x$  for gluons different quark flavours at  $Q^2 = 10 \text{ GeV}^2$  and  $Q^2 = 10^4 \text{ GeV}^2$  using MSTW 2008 NNLO [51].

1745 Due to the fact that inside of hadrons the quarks are continuously interacting  
 1746 with each other via the exchange of gluons, it is not possible to calculate PDFs using non-perturbative QCD.  
 1747 Instead, the momentum distribution function of the partons within the proton is obtained by a fit on  
 1748 a large number of cross-section data points over a grid of  $x$  and  $Q^2$  values  
 1749 obtained from many experiments (deep inelastic scattering, Drell-Yan and jet measurements).  
 1750 There are various global fitting collaborations (ABM, CT, MMHT, NNPDF, MSTW, CTEQ), each taking different approaches  
 1751 to this fitting procedure. These fits are later extrapolated to new energy scales.  
 1752

1753 Formally, the PDF  $f_{a/A}(x, Q^2)$  is defined as the probability of finding  
 1754 a parton  $a$  within the hadron  $A$  carrying a fraction  $x = p_a/p_A$  of its momentum at  $Q^2$  energy scale.  
 1755 The energy scale  $Q$  characterises the hard scattering and typically corresponds to the momentum transfer in the given process.  
 1756 As an example, several PDFs at two different scale energies are presented in Figure 2.12 as a function of  $x$ .  
 1757

1758 The momentum of the proton is distributed among its constituents and,  
 1759 while at lower energies ( $Q \sim 1 \text{ GeV}$ ) it is shared mainly between the valence quarks,  
 1760 at higher energies ( $1 < Q \lesssim 1 \text{ GeV}$ ) the emission of gluons carrying some of the initial momentum of the quark is more probable. Within the

1765 QCD theory, these interactions can be classified in two main groups: “hard”  
 1766 and “soft”. The hard processes are those involving large momentum trans-  
 1767 fer. This type of processes are well understood and their cross-section can  
 1768 be predicted with good precision using perturbation theory. In contrast,  
 1769 the low momentum transfer of soft interactions leads to a much more dom-  
 1770 inant impact of non-perturbative QCD, which makes much more difficult to  
 1771 calculate the cross-section.

1772 When two protons ( $A$  and  $B$ ) collide, what actually happens is that the  
 1773 partons of one proton can interact with partons of the other via a hard  
 1774 scattering process. Each of the interactions between the partons pairs (let  $a$   
 1775 be a parton from  $A$  interacting with  $b$ , a parton from  $B$ ) is independent from  
 1776 the interactions of other partons. The remaining partons also contribute to  
 1777 the final state as “underlaying events”.

In a  $pp$  or, more generally, in a hadron-hadron ( $A$  and  $B$ ) hard scattering process, the total cross section is given by:

$$\sigma_{AB \rightarrow X} = \sum_{a,b} \iint dx_a dx_b f_a(x_a, Q^2) f_b(x_b, Q^2) \times \hat{\sigma}_{ab \rightarrow X} \quad (2.12)$$

1778 where  $a$  and  $b$  denote the parton constituents of the hadrons  $A$  and  $B$   
 1779 respectively and  $f_i(x_i, Q^2)$  their PDF. Here, the  $Q$  is chosen to be the fac-  
 1780 torisation scale ( $\mu_F$ ). The contributions of the individual partons  $a$  and  $b$  is  
 1781 denoted by  $\hat{\sigma}_{ab \rightarrow X}$ . With this equation, all process in  $pp$  collisions can can  
 1782 be computed.

Depending on the order achieved in perturbation theory (LO, NLO, NNLO, ...), the cross-section of the individual partons to give the final state of instest ( $ab \rightarrow X$ ) is calculated as

$$\begin{aligned} \hat{\sigma}_{ab \rightarrow X} &= \sum_{i=0}^{\infty} \alpha_s^i(\mu_R) \sigma_n(x_a, x_b, \mu_F^2) \\ &= [\sigma_{LO}(x_a, x_b, \mu_F^2) + \alpha_s(\mu_R) \sigma_{NLO}(x_a, x_b, \mu_F^2) \\ &\quad + \alpha_s(\mu_R)^2 \sigma_{NNLO}(x_a, x_b, \mu_F^2) + \dots]_{ab \rightarrow X} \end{aligned}$$

1783 where  $\alpha_s^i(\mu_R)$  is the coupling constant derived for a specific renormalization  
 1784 scale ( $\mu_R$ ).

1785 **Work in progress**

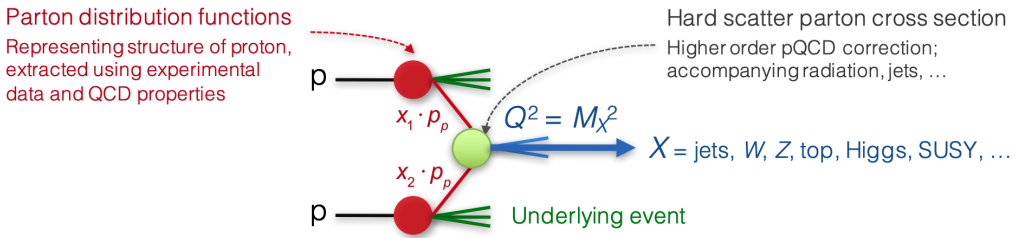


**Figure 2.13:** Simplified view of a  $pp$  collision [124].

### 1786 2.2.7.2 Underlaying event

## 1787 2.3 ATLAS

1788 Installed in its experimental cavern at point 1, ATLAS is the largest de-  
 1789 tector ever constructed for a particle collider with its 46 m long and 25 m in  
 1790 diameter. It is designed to record events of high-energy colliding particles  
 1791 at high luminosities. The thousands of millions of interactions that take  
 1792 place at the centre of the ATLAS detector are recorded and processed by  
 1793 the different sub-detectors, which are composed by more than 100 million  
 1794 sensitive electronic channels. Each ATLAS sub-detector is sensible to a dif-  
 1795 ferent type of particle and to different properties. Therefore, the layered  
 1796 structure allows for effective particle identification, as well as enables accu-  
 1797 rate measurements of energy and momentum. Figure 2.14 shows an overall  
 1798 layout of the ATLAS detector and identifies its different sub-detectors. In  
 1799 the picture can be appreciated that the cylindrical shape of ATLAS is di-  
 1800 vided into two parts: the “barrel” (curved parts) and the two “end-caps”  
 1801 (bases). In the barrel region, the sub-detectors are built as coaxial layers  
 1802 around the beam pipe (see memo 2.15). As one moves away from the axis,  
 1803 it finds the Inner Detector (ID), the solenoid magnet, the Electromagnetic  
 1804 (ECAL) and Hadronic (HCAL) Calorimeters, and the Muon Spectrometer  
 1805 (MS) in the outermost layer. The technical details of these sub-detectors  
 1806 are presented in the coming sections.

1807 ATLAS is able to explore a wide range of phenomena with high pre-  
 1808 cision, including new physics events. Even though it is a general-purpose  
 1809 experiment, it was designed taking into account the Higgs searches that  
 1810 were carried out at LHC. This is why, since the mass of the Higgs was not  
 1811 known at that time, its performance requirements cover a large mass range  
 1812 for the Higgs decay products.

1813 The stone for the foundations of ATLAS was laid in March 1992 at  
 1814 the critical ‘Towards the LHC Experimental Programme’ meeting, where  
 1815 physicists proposed several possible experiments for the LHC [131]. Two

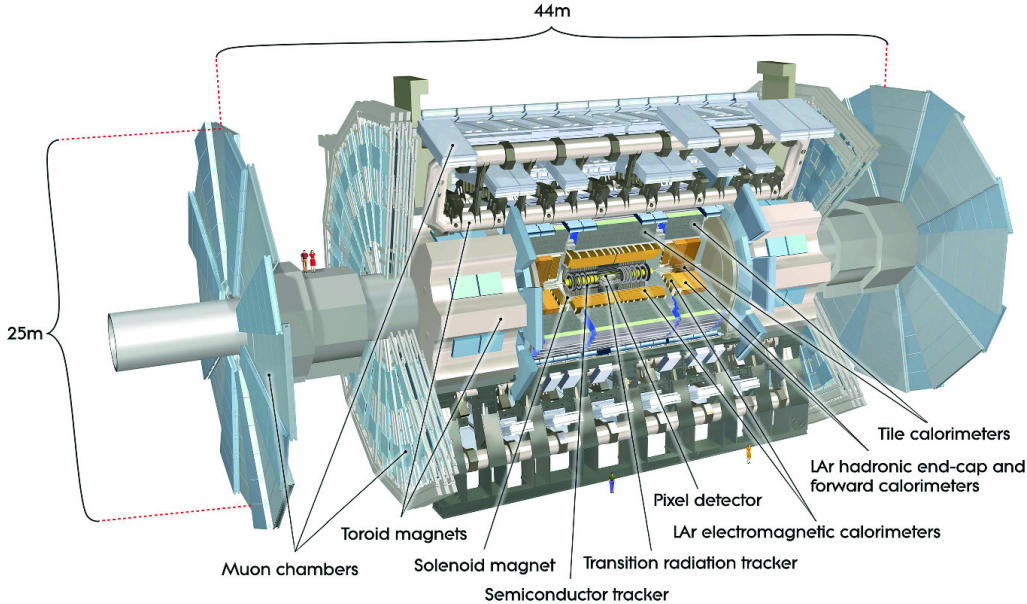


**Figure 2.14:** Simulated schematic view of the ATLAS detector.

1816 projects based on large toroidal magnet systems were proposed EAGLE  
 1817 and ASCOT. By the summer of that year, both experiments merged into  
 1818 ATLAS. In October 1992, the letter of intent of the ATLAS Collaboration  
 1819 was sent to the LHC Experiments committee and, in 1994, the technical  
 1820 proposal [132]. In 1997 the formal approval of the ATLAS experiment  
 1821 arrived and one year later the excavation on the cavern began. The cavern  
 1822 was inaugurated five years later and the construction of the ATLAS detector  
 1823 ended in 2008. Later, in 2009, at  $\sqrt{s} = 2.36$  TeV, ATLAS records its first  
 1824 collisions [133].

1825 One of the most important milestones for ATLAS (and for all science in  
 1826 the last decades) was the observation of a particle consistent with the Higgs  
 1827 boson in July 2012 (see 1.3.1). In 2016, the combination of ATLAS and  
 1828 CMS measurements for Higgs boson production on decay rates with Run-  
 1829 1 data was published [134]. After that, the physics programme at 13 TeV  
 1830 allowed precision studies of the Higgs boson and other SM particles, as well  
 1831 as the search for new particles with higher masses.

1832 Other relevant items in ATLAS timeline are the observation and rate  
 1833 measurement of  $t\bar{t}$  events [135] or the evidence for rare electroweak  $W^\pm W^\pm$   
 1834 production [136]. The first evidence of light-by-light scattering at high  
 1835 energy was also found with ATLAS [137]. The first  $t\bar{t}H$  associate production  
 1836 [138] and  $H \rightarrow b\bar{b}$  decays [139] were observed for first time by ATLAS too.

1837 The physics programme of ATLAS include precise measurements of the  
 1838 SM [140], super-symmetry studies [141], sources of  $\mathcal{CP}$ -violation [142], large

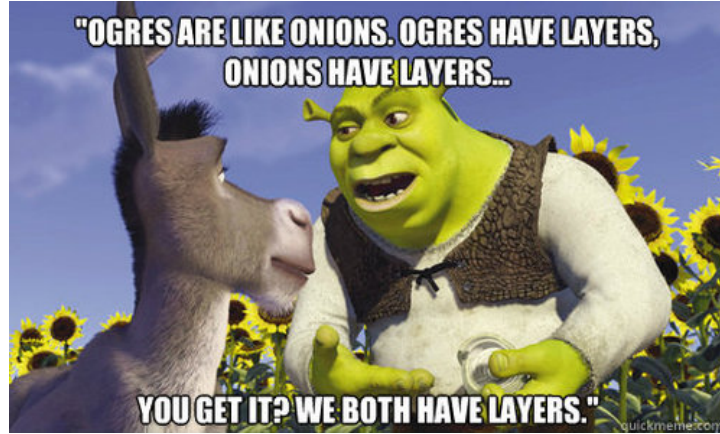


**Figure 2.15:** Due to its coaxial-layered structure ATLAS can be understood as cylindric onion: “*ATLAS have layers, onions have layers*” [130].

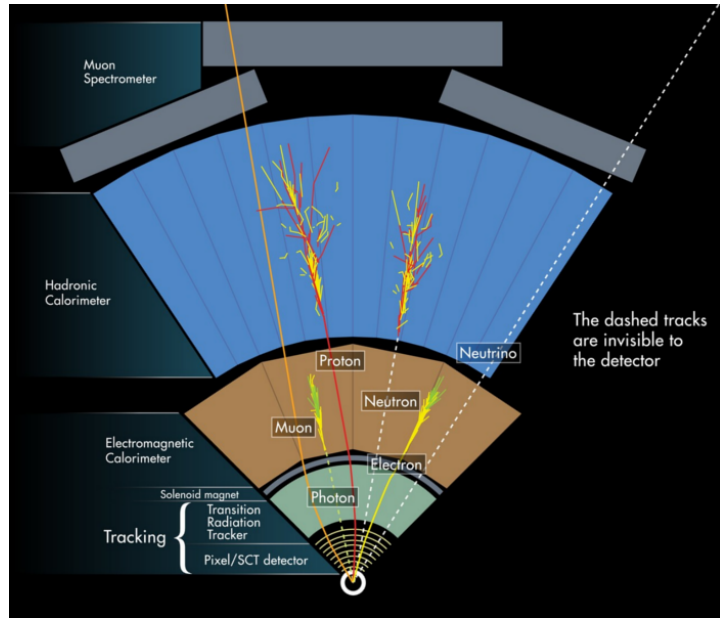


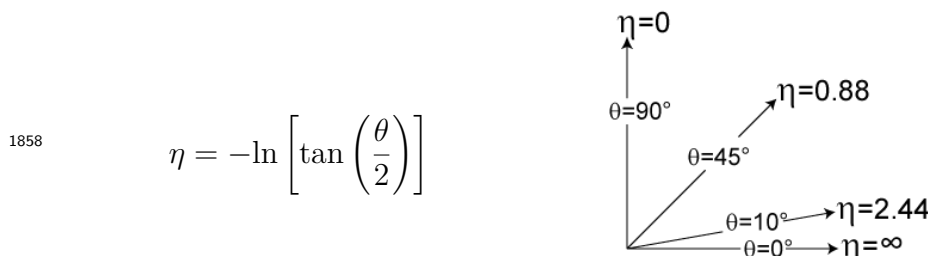
**Figure 2.16:** Fraction of the transversal plane of ATLAS. Each particle leaves a different signature in each layer. By signature is meant the particular distribution of energy deposition. This scheme is fundamental to understand the object reconstruction in the next chapter.

<sup>1839</sup>  $E_T^{\text{miss}}$  dark matter searches [143], astroparticle physics [144], extra dimensions [145] and others.

<sup>1841</sup> ATLAS is not only a detector but also a collaboration of people composed of more than 5000 members including physicists, engineers, technicians, doctoral students and support staff. Working at CERN or at any of the 181 institutions that constitute ATLAS, the different teams work collaboratively to achieve success. Any output by any of the teams comprising ATLAS is shared with the rest of the collaboration and subjected to a strict review process before making the results public, ensuring high-quality standards.

### <sup>1849</sup> 2.3.1 Coordinate system

<sup>1850</sup> Due to its cylindrical structure, ATLAS uses a right-handed system with <sup>1851</sup> its origin at the IP where the collisions take place. On one side, there are the <sup>1852</sup> ( $x, y, z,$ ) Cartesian coordinates. The  $x$ -axis is pointing towards the centre <sup>1853</sup> of the ring circumference, the  $y$ -axis is perpendicular to the plane defined <sup>1854</sup> by the LHC ring and it points to the surface, and the  $z$ -axis is defined by <sup>1855</sup> the direction of the beam. On the other side, it is more frequent to employ <sup>1856</sup> the cylindrical coordinates  $(r, \phi, z)$  or the system defined by the azimuthal <sup>1857</sup> angle  $(\phi)$  and the pseudorapidity  $(\eta)$ :



where  $\theta$  is the polar angle<sup>4</sup>. As the polar angle approaches zero, pseudorapidity tends towards infinity. The change in pseudorapidity  $\Delta\eta$  is Lorentz invariant under boosts along the beam axis. The use of  $\eta$  is preferred over  $\theta$  because the distribution of events typically looks flat with respect to  $\eta$ . In terms of the momentum, the above equation can be expressed as:

$$\eta = -\ln \left( \frac{|\vec{p}| + p_z}{|\vec{p}| - p_z} \right)$$

<sup>1859</sup> being  $p_z$  the momentum along the beam direction. The rapidity is used <sup>1860</sup> when dealing with massive particles and it can be expressed as  $y = \frac{1}{2}\log[(E +$

---

<sup>4</sup>Defined as the angle between the particle three-momentum,  $\vec{p}$  and the positive direction of the beam axis.

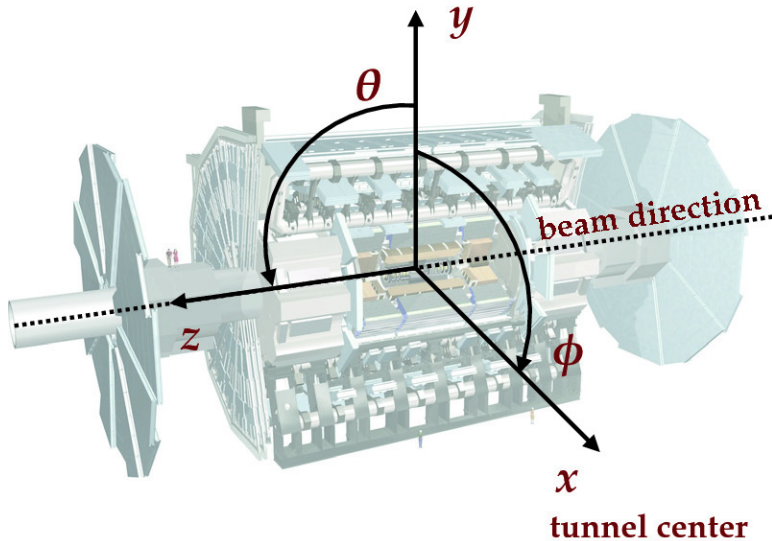


**Figure 2.17:** Coordinate system of the ATLAS detector.

1861  $p_z)(E - p_z)]$ , being  $E$  the energy projection of the momentum in the  $z$ -axis.  
 1862 Note that when the particles approach the speed of light, they are in the  
 1863 limit  $E \approx |\vec{p}|$  and the values for rapidity and pseudorapidity converge. The  
 1864 angular distance is measured in units of  $\Delta R = \sqrt{(\Delta\eta)^2 + (\Delta\phi)^2}$ , which is  
 1865 invariant under a boost along the  $z$ -axis<sup>5</sup>. Figure 2.17 shows the coordinate  
 1866 system of ATLAS for both Cartesian and cylindrical coordinates.

The transverse magnitudes such as the transverse momentum ( $p_T$ ) and transverse energy ( $E_T$ ) are defined in the  $x$ - $y$  plane. Knowing the  $p_T$ , and the  $\eta$  and  $\phi$  angles, the cartesian momentum ( $p_x, p_y, p_z$ ) can be derived from:

$$\begin{aligned} p_x &= p_T \cos(\phi) & p_y &= p_T \sin(\phi) \\ p_z &= p_T \sinh(\phi) & |\vec{p}| &= p_T \cosh(\phi) \end{aligned}$$

### 1867 2.3.2 Inner Detector

1868 The ATLAS ID [146][147][106] is the closest sub-detector to the beam  
 1869 pipe. Its layout is shown in Figures 2.18 and 2.19. The charged particles  
 1870 follow a curved trajectory inside the ID due to the magnetic field of the  
 1871 ATLAS bending magnet (see 2.3.5). The different pieces that comprise the  
 1872 ID can reconstruct the traces of these particles with great accuracy allowing,  
 1873 thus, to measure its momentum (this is done using the sagitta method  
 1874 described in Section 4.1.1). For particles coming from the IP, the geometric  
 1875 acceptance of the ID is  $|\eta| < 2.5$  for pseudorapidity and full  $\phi$  coverage in

<sup>5</sup> $\Delta\eta = \eta_2 - \eta_1$  and  $\Delta\phi = \phi_2 - \phi_1$ .

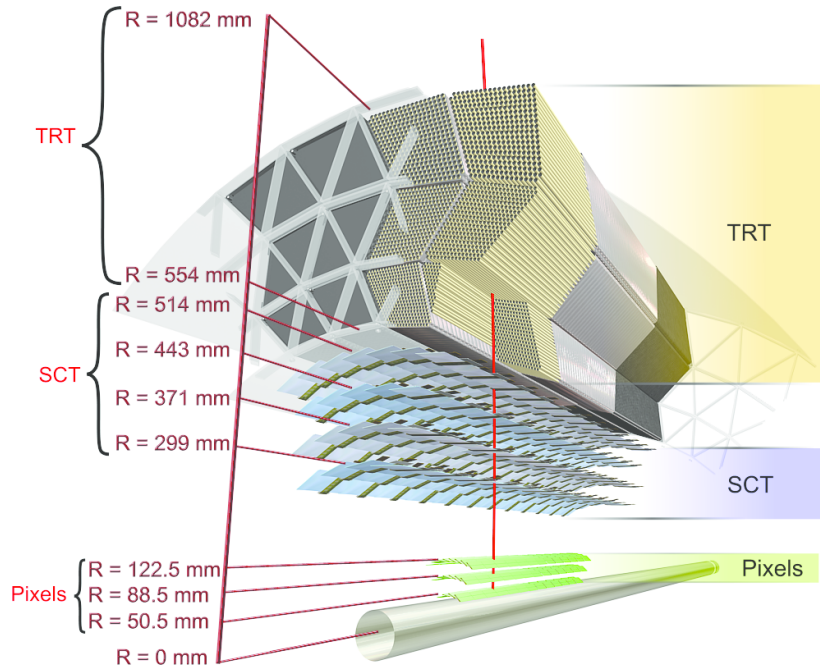


**Figure 2.18:** Barrel part of ID of the ATLAS experiment with the Pixel, SCT and TRT sub-detectors. The IBL is not shown here.

the azimuthal angle. The ID provides  $p_T$  resolution of  $\sigma_{p_T}/p_T = 0.05\%$  GeV  $\oplus 1\%$  and a transverse impact parameter resolution<sup>6</sup> of  $10 \mu\text{m}$  for particles in the central  $\eta$  region. It is designed to provide excellent momentum resolution, pattern recognition and measurements of both primary and secondary vertex for charged particles above the  $p_T$  threshold (nominally 0.5 GeV).

The ID is composed of four complementary sub-detectors: The Insertable B-Layer (IBL), the Pixel Detector, the Semiconductor Tracker (SCT) and the Transition Radiation Tracker (TRT). In the sections that follow, a description of each sub-system is provided.

Depending on the  $\eta$  that a particle has, it will interact with some elements of the detector. Figure 2.19 shows the end-cap elements transversed by two charged particles with  $\eta = 2.2$  and  $1.4$ . The track with  $\eta = 1.4$  traverses first the beryllium beam-pipe, then the three cylindrical silicon pixels and the four disks with double layers of the SCT. Finally, this particle travels across approximately 40 tubes in the TRT wheels. In contrast, the particle with  $\eta = 2.2$  encounter the first of the cylindrical silicon-pixel layers after leaving the beryllium pipe. Then, the two end-cap pixel disks and the four last disks of the end-cap SCT.

<sup>6</sup>The impact parameter determine the distance of a reconstructed track from a charged particle to the perigee (the closest point of the track to the global  $z$ -axis)

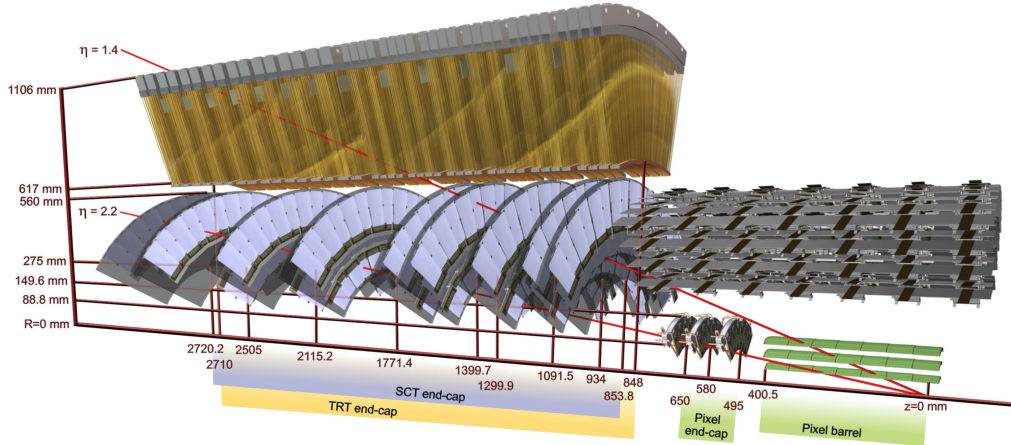


**Figure 2.19:** End-cap of the ID.

#### 1894    **Silicon semiconductors**

1895    When a charged particle traverses a doped silicon semiconductor, it creates  
 1896    a pair electron-hole by ionisation. An electric field is applied to the active  
 1897    part of the detector module so that the electron drifts in oposite direction  
 1898    of the electric field and the hole in the field direction. Then, both charges  
 1899    are collected by the p-n junctions. The silicon sensors can be shaped either  
 1900    as pixels, providing precies 2D space point, or as strips, giving a single  
 1901    dimension positioning. On the order of  $10^5$  electron-hole pairs are liberated  
 1902    when a particle crosses the silicon wafer and, with appropriate electronics,  
 1903    a clear signal is obtained in the pixel or strip in which the charged was  
 1904    collected.

#### 1905    **2.3.2.1 Insertable B-Layer**

1906    The IBL [148] is the innermost component of the ID. It is located  
 1907    between the beam pipe and the pixel detector. Added after Run-1, it  
 1908    provides the closest-to-IP measurements. This improves the robustness and  
 1909    performance of the ATLAS tracking system. It plays a fundamental role  
 1910    for  $b$ -tagging efficiency because this tagging relies on precise vertex recon-  
 1911    struction. The IBL provides redundancy in the measurements of tracks in  
 1912    order to control the fake rate arising from random combinations of clusters  
 1913    in events with a high pile-up background.

1914    With a hit resolution of  $8 \mu\text{m}$  in  $r\text{-}\phi$  and  $40 \mu\text{m}$  along  $z$ , the IBL covers  
 1915    the  $|\eta| < 2.7$  and the entire  $\phi$  range.

1916    The barrel structure if the IBL has a radius of 3.2 cm and is composed  
 1917    by 14 carbon fibre staves as it is shown in Figure 2.20. Each stave has

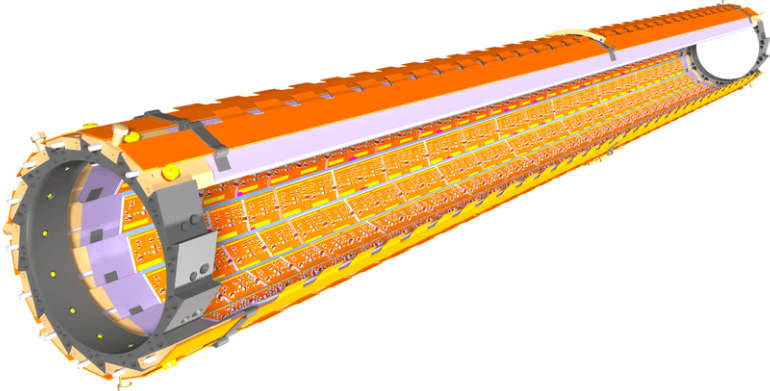


**Figure 2.20:** Schematic drawing of the ATLAS IBL Detector [148].

incorporated cooling  $\text{CO}_2$  circuits, has 32 or 16 modules and uses two types of photodetectors: ATLAS pixel planar sensors and 3D pixel sensors. The used pixels have a size of  $50 \times 400 \mu\text{m}^2$ . Due to the high luminosity of the LHC, the IBL is built with radiation-tolerant sensors.

### 2.3.2.2 Pixel Detector

The ATLAS Pixel Detector [149] consists of a strip detector in the outermost layers and a pixel detector in the region which is closer to the IBL. Along with the IBL, it aims to reconstruct the trajectories of the particles traversing it. It provides a full coverage of the azimuthal angle  $\phi$  and a pseudorapidity range of  $|\eta| < 2.5$  as well as a resolution of  $10 \mu\text{m}$  in  $r\text{-}\phi$  and  $115 \mu\text{m}$  in the  $z$ .

The Pixel Detector and the IBL combined contain  $92 \times 10^6$  pixels with its respective electronic channels, which cover an area of approximately  $1.9 \text{ m}^2$  of silicon consuming  $15 \text{ kW}$ . The barrel region consists of four concentric layers equipped with 1736 sensor modules and each of the two end-caps has three disks with 2888 modules [150]. Figure 2.22 shows the assembly view and cross section of a module of the ATLAS ID Pixel Detector. Each of these modules consists on a silicon pixel sensor bonded to the front-end electronic chips.

Hits in a pixel are read out if the signal exceeds a tunable threshold. The pulse height is measured using the Time-over-Threshold (ToT) technique.

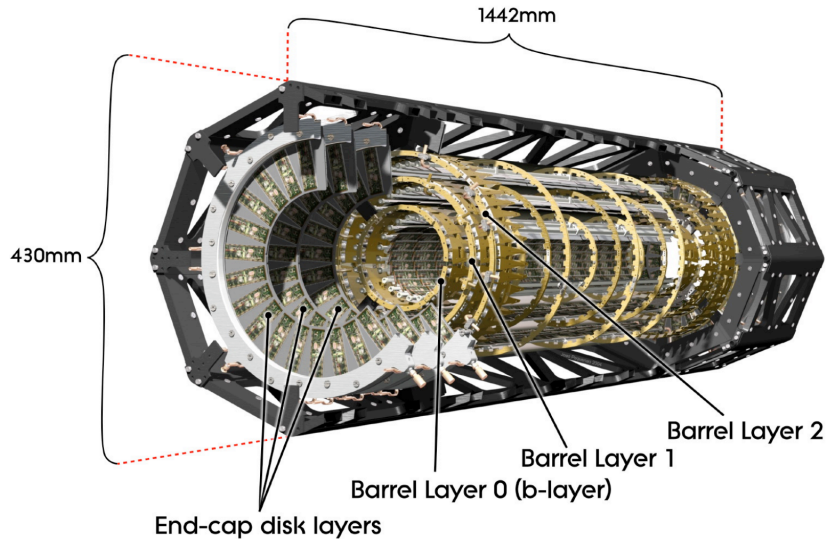


**Figure 2.21:** Schematic view of the ATLAS pixel detector consisting of individual barrel and end-cap layers [106].

### 1939 2.3.2.3 Semiconductor Tracker

1940 The SCT consists of 4088 modules tiling four coaxial cylindrical layers  
 1941 in the barrel region and two end-caps each containing nine disk layers, all  
 1942 of this surrounding the Pixel Detector and providing additional precision  
 1943 tracking. The main difference with the Pixel Detector is that the SCT uses  
 1944 microstrip sensor technology, which is very similar to that of a pixel but  
 1945 being much larger (6 cm). The reason to use microstrips instead of pixels  
 1946 is that the strips are more cost-effective than traditional pixels and a good  
 1947 spatial resolution can be obtained as well if the strips are arranged with an  
 1948 angular offset. Therefore, each SCT detector unit consists on two back-to-  
 1949 back silicon-microstrip planes with a relative angle of 40 mrad. Eight strip  
 1950 layers (i.e. four space points) are crossed by each track in the SCT providing  
 1951 valuable tracking information with resolution of  $17 \mu\text{m}$  in  $r\phi$  and  $580 \mu\text{m}$   
 1952 in the  $z$  coordinate. The SCT covers the entire  $\phi$  range and up to 2.5 in  $\eta$ .

1953 Figure 2.23 shows an exploded view of the different components of an  
 1954 SCT module, including the high thermal conductivity spine, the polyimide  
 1955 hybrids and readout chips.

### 1956 2.3.2.4 Transition Radiation Tracker

1957 The TRT is used in conjunction with the Pixel Detector and silicon micro  
 1958 strip (SCT) to extend the  $\eta$  range in which the tracks can be reconstructed to  
 1959  $|\eta| = 2$ . This part of the ID is formed by a large number of 4 mm straw tubes

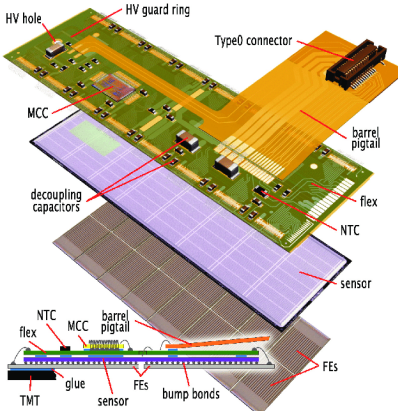


**Figure 2.22:** Pixel Detector module [149].

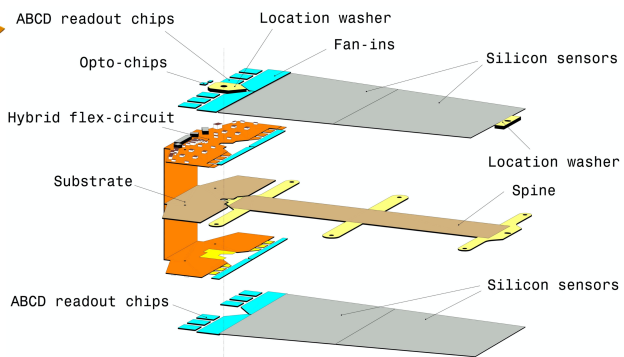


**Figure 2.23:** SCT detector module [106].

1960 filled with gas. This part of the ID relies both on the collection of primary  
1961 ionisation charge and the collection of secondary ionisation charge arising  
1962 from the transition radiation to measure the the track of charged particles.  
1963 The tube surface functions as a cathode while the wire in the center as  
1964 a cathode. When a charged particle pases through the gas in the tube, it  
1965 ionises the gas and the freed electrons drift towards the anode, generating an  
1966 electrical current. This detector provides a single hit resolution of  $170 \mu\text{m}$  in  
1967  $r\text{-}\phi$  but does not have sensitivity in  $z$ . The TRT also provides discrimination  
1968 between electrons and pions since the later generate a much smaller signal  
1969 than the former. When the electrons pass, they produce x-ray photons that  
1970 lead to strong avalanches within the tubes and, thus, a great signal.

### 1971 **2.3.3 Calorimeters**

1972 After the ID, the next layer of detectors in ATLAS correspond to the  
1973 calorimeters (Figure 2.24) [151]. Their purpose is to measure the energy  
1974 of the particles (neutral or charged), as well as to help to reconstruct the  
1975 path followed by them. Most particles initiate a shower (Section 2.3.3.1)  
1976 when they enter into the calorimeter. Part of the energy of these particles is  
1977 deposited in the device, then collected and measured by it. Most of calorim-  
1978 eters in particle physics are segmented transversely to provide information  
1979 about the direction of the particles. Based on how the particle shower devel-  
1980 ops, the longitudinal segmentation can provide information for identifying  
1981 the particle (a more detailed discussion of how particles are reconstructed  
1982 within the ATLAS detector is presented in Section ??).

1983 In general, calorimeters can be classified as sampling, when are made of  
1984 two types of materials, or homogeneous, built with just one type of material.

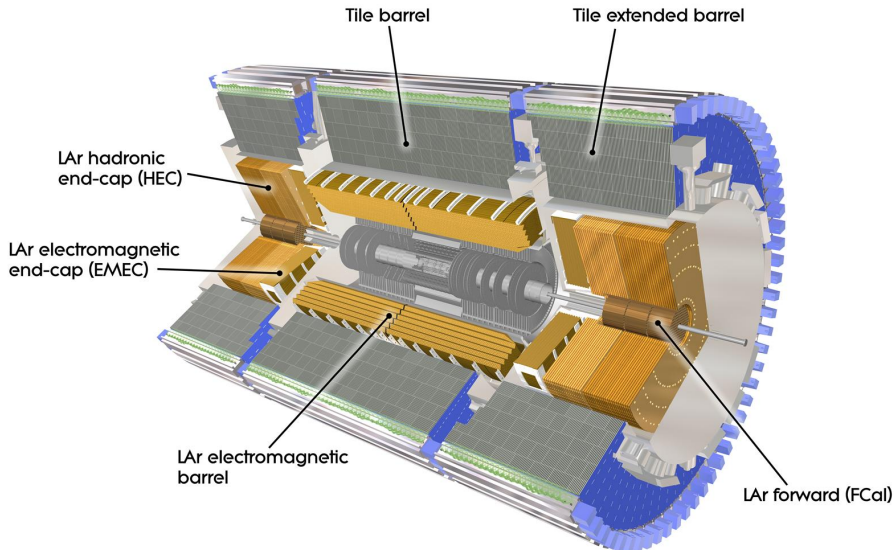


**Figure 2.24:** Computer generated image of the ATLAS calorimeter [150].

1985    ATLAS uses sampling calorimeters, which consist of alternating layers of  
 1986    different materials:

- 1987    • **Passive material:** Also known as absorber, it is a denser material to  
 1988    full stop the traversing particles. When a particle interacts with the  
 1989    passive material it produces the shower (Figures 2.25 and 2.26). For  
 1990    the absorber layers in ATLAS, lead is used for the ECAL and steel  
 1991    for the HCAL.
- 1992    • **Active material:** This material detects the particles from the shower  
 1993    originated in the absorber. The liquid Argon (LAr) is used as active  
 1994    material for ECAL and plastic scintillator for HCAL.

1995    In the homogeneous calorimeters, the material used combines the features  
 1996    of an absorber and a detector, performing both tasks.

1997    Since each type of particle interacts differently, there are two main types  
 1998    of calorimeters: the electromagnetic calorimeter (ECAL), which measures  
 1999    the energy of electrons/positrons and photons, and the hadronic calorim-  
 2000    eters (HCAL), which registers the energy of the strongly-interacting particles.  
 2001    Both classes are covered in the next sections.

## 2002    **Scintillator**

2003    The particles from the shower leave some of the molecules of the plastic

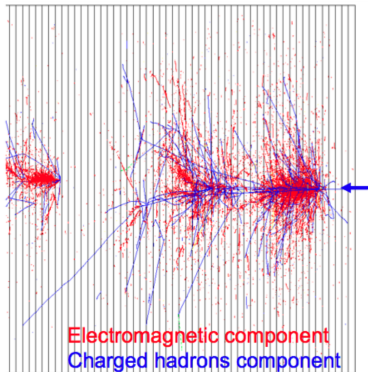


**Figure 2.25:** EM and hadronic cascades.

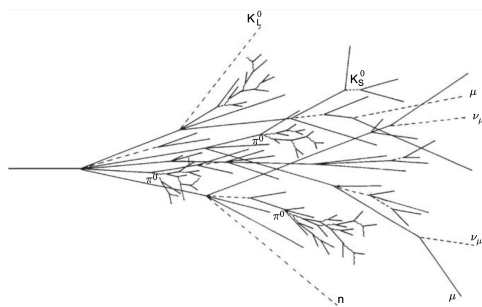


**Figure 2.26:** Sketch of a hadronic cascade [152].

2004 scintillator in an excited state. The subsequent decay of these molecules  
2005 produces the emission of photons in the ultraviolet energy region. This  
2006 light is collected by photomultiplier tubes at the edge of the tiles  
2007 and converted into a current pulse whose amplitude is proportional to the  
2008 energy deposited by transversing particle.

### 2009 **2.3.3.1 Particle showering**

2010 A particle shower is a cascade of secondary particles produced when  
2011 a high-energy particle interacts with matter. The first particle interacts  
2012 with the passive material producing a secondary particle with less energy  
2013 than the first one. The second particle does the same and, in each step,  
2014 the particles produced are less and less energetic. For a single incoming  
2015 particle, this iterative process can continue for thousands of periods [152].  
2016 An illustration of the EM and hadronic particle cascades is shown in Figure  
2017 [2.25](#).

#### 2018 **Electromagnetic shower**

2019 The electromagnetic (EM) shower is initiated by a  $e^-$ ,  $e^+$  or  $\gamma$ , these  
2020 three particles are the sole components of this type of shower. At energies  
2021 higher than 100 MeV, the EM showering is based on two main processes:  
2022 Bremsstrahlung and pair creation. The electrons lose their energy almost  
2023 exclusively by bremsstrahlung radiation, a process in which the lepton ra-  
2024 diates thousands of soft photons because of its interaction with another  
2025 charged particle. The photons lose their energy by the production of an  
2026  $e^- - e^+$  pair. At lower energy scales, other processes contribute. In the MeV

range, the Compton scattering<sup>7</sup> and photoelectric effect<sup>8</sup> are the dominant interactions for energy loss for photons, while the ionisation and excitation are for the charged particles ( $e^-$  and  $e^+$ ).

### Hadronic shower

When a hadron interacts with the passive material, this shower is initialised. Both strong and EM interactions are involved in the development of this type of shower and they present a larger variety of particle components. Therefore, the hadronic showers are significantly more complex than the EM. Figure 2.26 shows the processes leading to a hadronic cascade.

The production of neutral pions represents about a third of the energy loss of hadronic interactions. These pions decay 98.8% of times to two photons [153] that are starting the EM showers. The rest of hadronic interactions consist of the production of charged mesons, nuclear fragments and protons, soft neutrons and photons or unpredictable loss through undetectable processes.

#### 2.3.3.2 Electromagnetic calorimeter

The ECAL [151] absorbs the energy of the  $e^-$ ,  $e^+$  or a  $\gamma$  covering a pseudorapidity range of  $|\eta| < 1.475$  in the barrel. It is made of a lead absorber and LAr detector following an accordion shape, as can be seen in Figure 2.27a, where the different layers are clearly visible. The shower originated at the absorber layer ionise the LAr producing a measurable current proportional to the energy of the original particle. The LAr layer operates at 87 K.

The barrel part is split into two identical half-barrels separated by a small gap at  $z = 0$ . Each end-cap calorimeter is composed of two coaxial wheels that cover  $|\eta| < 1.475$ .

The total amount of material in the ECAL corresponds to 25-35 radiation lengths,  $X_0$ , and 2-4 nuclear interaction lengths,  $\lambda$ , over the entire  $\eta$  range. Characteristic of each material, the ration length is the mean distance over which a high-energy electron lose all but  $1/e$  of its energy by bremsstrahlung. The radiation length is the mean free path between interactions required to reduce the number of relativistic charged particles by the factor  $1/e = 0.37$  as they pass through matter.

---

<sup>7</sup>Scattering of a photon after interacting with a charged particle, usually an electron.

<sup>8</sup>Emission of photoelectrons when the EM radiation interacts with matter.

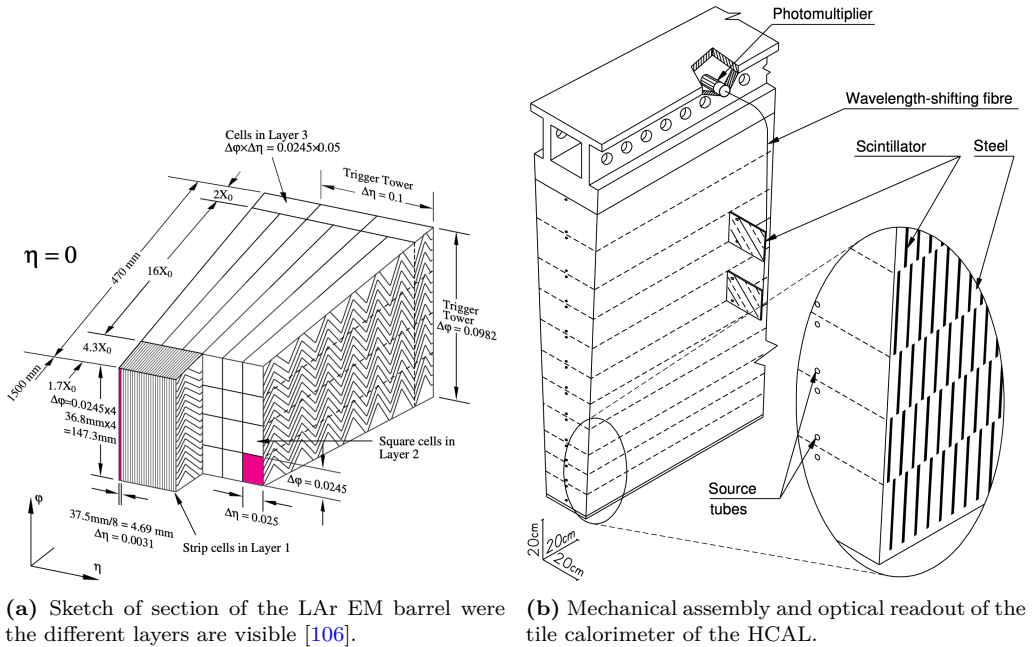


**Figure 2.27:** Sketch of a section of the ATLAS (a) ECAL and (b) HCAL [106].

The energy resolution of a calorimeter can be parametrised as:

$$\frac{\sigma_E}{E} = \frac{a}{\sqrt{e}} \oplus \frac{b}{E} \oplus c = \frac{10\%}{\sqrt{e}} \oplus \frac{170 \text{ MeV}}{E} \oplus 0.7\%$$

2060 Where  $a$  is the stochastic term,  $b$  the electronic noise and  $c$  a constant that  
2061 includes detector instabilities and increases with  $E$  [154].

### 2062 2.3.3.3 Hadronic calorimeter

2063 The ATLAS HCAL [151] is made of a sampling calorimeter of steel and  
2064 plastic scintillator tiles covering the pseudorapidity region of  $|\eta| < 1.7$  in  
2065 the barrels. The end-caps are made of copper and LAr, covering  $1.5 < |\eta| <$   
2066 3.2, and are emended in the end-caps of the ECAL. This calorimeter uses  
2067 9800 electronic channels in the barrel and 5600 in the end-cap. With 2900  
2068 tones, the HCAL is the heaviest part of the ATLAS detector. It has 420000  
2069 scintillator tiles and 9500 photomultiplier tubes [150]. All these elements are  
2070 shown in Figure 2.27b, where the tiles, the fibres and the photomultipliers  
2071 are visible.

The contribution of the electronic noise is negligible, therefore, the energy resolution for the tile calorimeter is [151]:

$$\frac{\sigma_E}{E} = \frac{5.9\%}{\sqrt{e}} \oplus 5.7\%$$

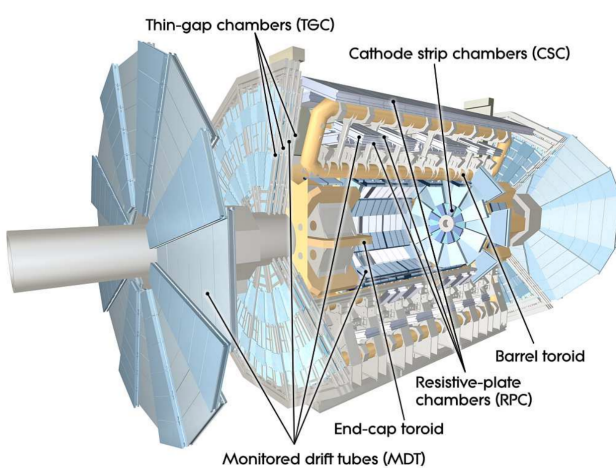


**Figure 2.28:** Conceptual layout of the MS (blue). The magnet system (yellow) is also shown [106].

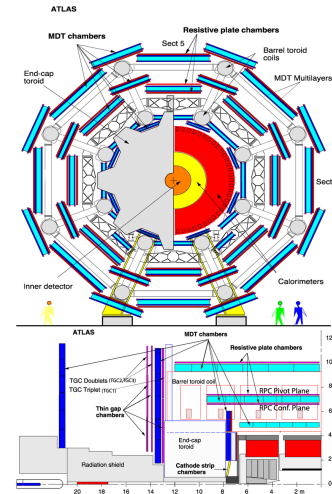


**Figure 2.29:** ATLAS Muon detectors.

### 2.3.3.4 Forward calorimeter

In addition to the ECAL and HCAL, a smaller calorimeter is placed in the end-caps surrounding the beam pipe in order to cover the forward region ( $3.1 < |\eta| < 4.9$ ), the forward calorimeter (FCAL). This coverage is required for many physics tasks such as the reconstruction of the  $E_T^{\text{miss}}$  of the forward-jet tagging.

This calorimeter is a sampling calorimeter based on LAr as active medium and copper as absorber. The thickness of the FCAL is optimised to achieve high absorption, approximately,  $10 X_0$  [154].

This detector has a resolution of:

$$\frac{\sigma_E}{E} = \frac{100\%}{\sqrt{e}} \oplus 10\%$$

### 2.3.4 Muon Spectrometer

The muons can penetrate through calorimeters and reach the last layer of the ATLAS detector, the MS [155]. Figure 2.28 shows a schematic cutaway view of the ATLAS muon system.

The MS surrounds the calorimeters and its aim is to measure the trajectories of muons to determine their direction and momentum with excellent tracking precision as well as their electric charge in a pseudorapidity coverage of  $|\eta| < 2.7$ . To bend the particle tracks after they exit the HCAL, the MS uses eight large superconducting air-core toroid magnets in  $|\eta| < 1.4$

Type	Purpose	Location	Coverage
MDT	Tracking	Barrel + end-cap	$0.0 <  \eta  < 2.7$
CSC	Tracking	End-cap layer 1	$2.0 <  \eta  < 2.7$
RPC	Trigger	Barrel	$0.0 <  \eta  < 1.0$
TGC	Trigger	End-cap	$1.0 <  \eta  < 2.4$

**Table 2.3:** ATLAS MS sub-detectors [156].

region. For the  $1.6 < |\eta| < 2.7$ , the tracks are bent by magnets inserted in the end-caps. In the transition region,  $1.4 < |\eta| < 1.6$ , the magnetic field responsible of bending the particles is provided by both the air-core toroid magnets and the smaller end-cap magnets. These fields are perpendicular to the trajectory of the muons originated in the IP. More details about the magnet systems of the MS can be found in Section 2.3.5.

The MS instrumentation is based, on one hand, on precision chambers for the coordinate measurements in the bending plane: Monitored Drift Tube chambers (MDT) and Cathode-Strip Chambers (CSC), and, on the other hand, on trigger chambers: Resistive Plate Chambers (RPC) and Thin Gap Chambers (TGC). Table 2.3 gives a summary of the MS detector components. In Figure 2.29 the distribution of the MS detectors is described.

- **Monitored Drift Tube chambers (MDTs)** [157]: The MDT chambers provide precise momentum measurements by determining with high accuracy the curve of the tracks. This part of the MS cover a pseudorapidity range of  $|\eta| < 2$ . The MDTs are designed to have stand-alone measurement capability in order to safeguard against any unanticipated background and to ensure good discovery potential in the scenario of unexpected topologies. In the barrel region, the MDTs are arranged in three cylindrical stations coaxial to the beam axis and in the end-cal, the MDTs are vertically installed in three layers. An MTD chamber consists of six layers of drift tubes (as depicted in Figure 2.30), each of them with 3 cm of diameter, filled with gas. A tube can achieve a single wire resolution of  $80 \mu\text{m}$  [156]. In the entire MDT system, there are 1 171 chambers with a total of 354 240 tubes.
- **Cathode-Strip Chambers (CSC)**: It is the innermost tracking layer of the MS. Due to its higher rate capability and time resolution, it is located close to the beam axis, where the particle fluxes are higher. This component of the muon detector system covers the  $\eta$  range  $2.0 < |\eta| < 2.7$ . It measures with precision the coordinates at

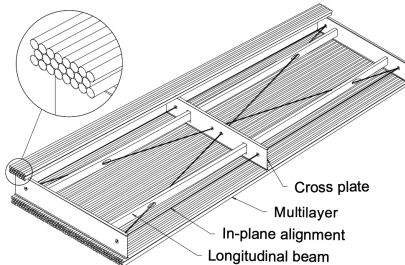


**Figure 2.30:** Schematic view of an MDT chamber.

the ends of the detector. With its 70 000 electric channel, provides a resolution around  $60 \mu\text{m}$ .

- **Resistive Plate Chambers (RPC)** [158]: This is the barrel element of the trigger system. These chambers are located on both sides of the central CSC and inside the outermost CSC station. The RPCs are gaseous detectors used for triggering and for measuring the second coordinate in the barrel region. RCPs provide a time-space resolution of  $1\text{ cm} \times 1\text{ ns}$ . The gas gap is of the order of 2 mm and the plate external surfaces are coated by thin layers of graphite painting. This part of the MS is composed of 3 800 electric channels.
- **Thin Gap Chambers (TGC)** [159]: As a first-level trigger, they have to provide high efficiency and excellent time resolution for bunch-crossing tagging in a high-background environment. The particle flux received by the TCG is higher than that of the RPC. The three TGCs are located near the middle end-cap MDT station, in the forward regions. TGCs measure the second coordinate in the non-bending direction with its circa 440 000 electrical channels.

### 2.3.5 Magnet system

The curvature in the track of the particles is fundamental to measure the transverse momentum and the charge of the particles. To bend the path of charged particles, these are immersed in a homogeneous magnetic field which is produced by the both the toroidal and solenoid magnets. The bending power is proportional to  $\int B dl$ , where  $B$  is the magnetic field component orthogonal to the charged direction.

ATLAS magnetic system is divided into three subsystems: the central solenoid magnet, the barrel toroids (BT) and the end-cap toroid (ECT).

**2147 2.3.5.1 Central solenoid magnet**

2148 The ATLAS solenoid surrounds the ID providing a 2 T magnetic at  
2149 the centre of the tracking volume. This magnet is very thin, having only  
2150 4.5 cm thickness, which minimises the interaction of the particles with the  
2151 magnet material. It is important to not use a lot of material here because,  
2152 otherwise, the interaction of the particles with the solenoid magnet would  
2153 impact negatively in the performance of the calorimeters. To achieve such  
2154 a field within a small thickness, 9 km of niobium-titanium superconductor  
2155 wires into strengthened, pure aluminium strips and cooled down to 4.5 K are  
2156 used. The central solenoid magnet has a cylindrical shape with a diameter  
2157 of 5.6 m and a length of 2.56 m, and it weights 5 tonnes.

**2158 2.3.5.2 Toroid magnets**

2159 Three large air-core toroids (one barrel and two end-caps) generate the  
2160 magnetic field in the MS. Each toroid consists of eight coils assembled with  
2161 cylindrical symmetry (see the yellow elements in Figure 2.28). The coils are  
2162 based on an aluminium stabilised Niobium-Titanium alloy (Al/NbTi/Cu)  
2163 superconductor operating at 4.5 K. The main difference between the barrel  
2164 and end-cap toroids for the cold mass is that the latter has a higher critical  
2165 current and less aluminium than the former [160].

**2166 Barrel Toroid**

2167 The Barrel Toroid magnet is the largest component of the ATLAS magnet  
2168 system. It generates a toroidal magnetic field which, as introduced in Sec-  
2169 tion 2.3.4, is almost completely perpendicular to the track of the particles.  
2170 In order to minimise the impact (i.e. reduce any interaction apart from  
2171 applying magnetic field) of the magnet system with the particles, the barrel  
2172 toroid is designed as an open and light structure. The barrel toroid coils  
2173 are housed in eight individual cryostats, with the linking elements between  
2174 them providing the overall mechanical stability. A view of the coils of the  
2175 barrel toroid in their cryostats is in Figure 2.31.

2176 The magnetic flux density delivered by this magnet is 3.9 T on the su-  
2177 perconductor. For the toroid barrel, the bending power ( $\int B dl$ ) is in the  
2178 interval 1.5 Tm to 5.5 Tm in  $0 < |\eta| < 1.4$ . It is the largest toroidal magnet  
2179 ever built (25.3 m in length), being probably the most iconic and character-  
2180 istic element of ATLAS. It weights 830 tonnes and uses more than 56 km of  
2181 superconducting wire [150].

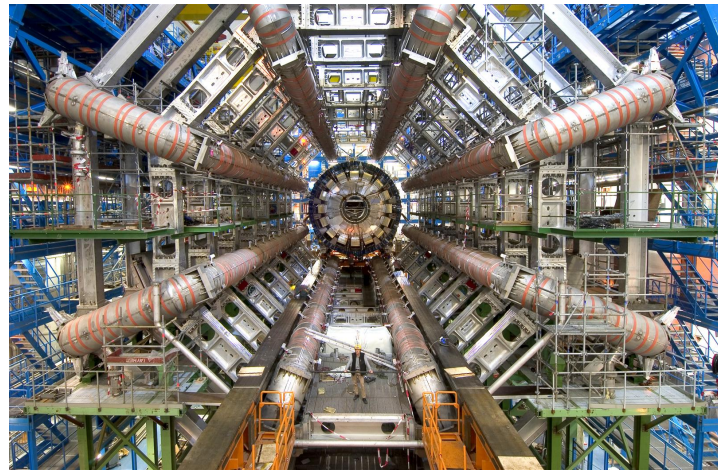


**Figure 2.31:** Very cool picture of the installation ATLAS calorimeters. The eight coils that compose the ATLAS barrel toroid magnets are already installed in the cryostats. Thus view is one of the most iconic of the ATLAS detector.

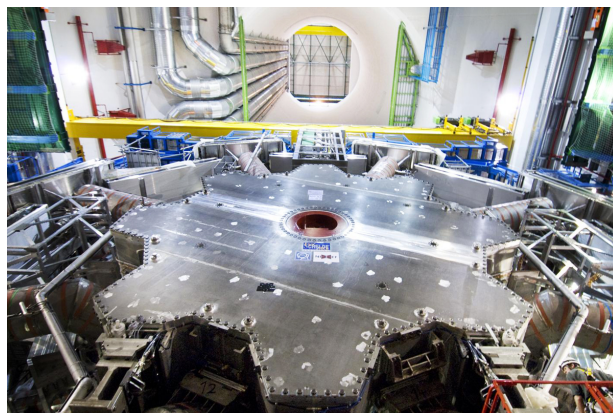


**Figure 2.32:** One of the two end-cap toroidal magnets. Each is made by eight superconducting coils with a magnetic field peaking at 4.1 T.

### 2182   **End-cap Toroid**

2183   The end-caps extend the magnetic field of the barrel toroid to the beam pipe.  
 2184   These magnets are constrained by the inner radius of the barrel toroid and  
 2185   the axial length of the experiment.

2186   As well as in the barrel toroid, it has a 4.1 T magnetic field on the  
 2187   superconductor. For the end-cap toroid, the  $\int B dl \in [4, 8]$  Tm in the  
 2188   pseudorapidity range  $1.6 < |\eta| < 2.7$  [160]. In the transition region where  
 2189   the end-cap and barrel toroids overlap ( $1.4 < |\eta| < 1.6$ ), the bending power  
 2190   is lower. Each end-cap magnet (Figure 2.32) has a diameter 10.7 m and  
 2191   weights 240 tonnes [150].

**2192 2.3.6 Trigger and Data Acquisition System**

2193     The proton bunches cross at the center of the ATLAS detector 40 million  
2194     times per second, resulting in approximately (using Run-2 mean pile-up  
2195      $\langle\mu\rangle = 33.7$ ) 1 200 million proton collisions per second. Reading out and  
2196     storing all the information from this interactions is not feasible since it has a  
2197     combined data volume of more than 60 million megabytes per second. Only  
2198     some of these events are of interest to physics studies and, consequently,  
2199     only this subset need to be saved into permanent storage for later analysis.  
2200     In order to select only interesting data, ATLAS uses a complex and highly  
2201     distributed Trigger and Data Acquisition System (TDAQ) [161] that reduces  
2202     the rate of recorded data from the initial 1 200 MHz of interactions to just  
2203     an average of 1 kHz. The reduction through the trigger is carried in two  
2204     steps: The electronic performs an initial selection and, afterwards, a large  
2205     computer farm analyses the data that pass the initial filter.

2206     The TDAQ system is an essential component of ATLAS in charge of  
2207     processing the events online, selecting the relevant ones and storing them.  
2208     To do so, the TDAQ verifies for each bunch crossing if at least one among the  
2209     hundred conditions is satisfied. These conditions, also known as “triggers”,  
2210     are based on identifying both combinations of candidate physics objects  
2211     (“signatures”) and global properties of the events [162]. Figure 2.33 shows  
2212     a diagram of the TDAQ system, in this figure can be seen the different  
2213     components as well as the detector read-out and data flow.

2214     The first-level trigger (LVL1) is a hardware-based filter performed by  
2215     ATLAS sub-detectors. The LVL1 uses the information of the Calorimeters  
2216     and the MS to select events up to the maximum-readout rate of the detector  
2217     (100 kHz) within a latency of 2.5  $\mu$ s. Additionally, the LVL1 identify the  
2218     regions of interest (RoI), which includes the position and the  $p_T$  of the  
2219     candidate objects.

2220     For each event accepted by the LVL1, the Front-End (FE) detector elec-  
2221     tronics read the detectors data and pass it to the ReadOut Drivers (ROD).  
2222     The ROD performs the initial processing and formatting and the ReadOut  
2223     Systems (ROS) buffers this data.

2224     The data from the different sub-detectors is sent from the ROS to the  
2225     software-based trigger, the so called “High Level Trigger” (HLT), when is  
2226     requested by the HLT. This system is comprised by the second-level trig-  
2227     ger (LVL2) and the Event Filter (EF or third-level), both made of several  
2228     farms of computers (about 40 000 CPU cores) interconnected by Ethernet  
2229     networks. Using modest computing power, LVL2 provides high rejection  
2230     power with fast and limited precision algorithms. With higher computing  
2231     power, the EF features lower rejection power with slower but higher preci-

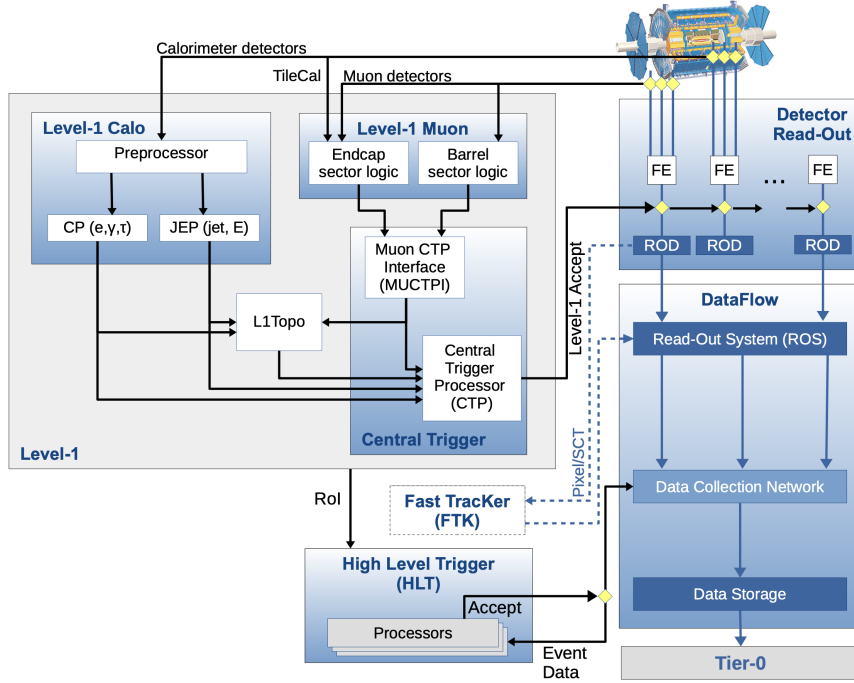


**Figure 2.33:** The ATLAS TDAQ system in Run-2.

sion algorithms [161]. This combination is a cost-effective and flexible way of implementing the HLT. The ID, which was not used by the LVL1, is of key importance for the HLT because on, one hand, the LVL2 reconstruction algorithms are specifically designed to meet strict timing requirements and, on the other hand, the track reconstruction on the EF is less time constrained. This is done by the ID's Fast TracKer (FTK) as the Figure 2.33 shows.

An average 1.2 kHz output rare for Run-2 pass the HLT (with a latency of just  $200\ \mu\text{s}$ ) and is sent by the Sub-Farm Output (SFO) to the Tier-0 facilities for permanent storage and later offline physics analysis. It is important to highlight that the decisions performed by trigger about whether or not to store an event are irrevocable. If an event does not pass the trigger requirements, it is lost forever.

### 2.3.7 ATLAS upgrade towards HL-LHC

The LHC Run-3 started on April of this year ([esto está escrito en marzo, así que habrá que ver si es verdad](#)). This is the las data-taking period of the of the collider as it was initially designed. CERN has embarked on a very ambitious project, the High Luminosity Large Hadron Collider (HL-LHC), that will dominate the accelerator-based particle physics scen-



**Figure 2.34:** Timeline for the LHC and LHC HL projects. The periods of data taking are named Runs and, between runs, there are the Long Shutdowns (LS) in which the different facilities are upgraded.

2251 ario in the years to come. The HL-LHC consists on a luminosity-enhanced  
2252 version of the LHC.

2253 Adding more particles to the bunches and focusing more the beam, would  
2254 result on a grater collision rate (of about a factor 10). This provides the  
2255 different analyses with better statistics, which eventually results in more  
2256 precise searches and measurements. A peak instantaneous luminosity of  
2257  $\mathcal{L} = 7.5 \times 10^{34} \text{ cm}^2 \text{ s}^{-1}$  is expected, this corresponds to between 140 and  
2258 200 inelastic  $pp$  collisions per bunch crossing, in contrast to the current 36.1  
2259 recorded during last year of Run-2 (Figure 2.10 shows the  $\langle\mu\rangle$  for each year  
2260 of Run-2).

2261 In contrast to the timeline in Figure 2.34, the latest update of the sched-  
2262 ule dates the Long Shutdown 3 (LS3) start in 2026 and the Run-4 start in  
2263 2029. All dates are subject to change as the unexpected events may occur  
2264 or technical/scientific reasons may lead to re-schedules.

2265 Some technologies developed to upgrade the LHC to HL-LHC are:

- 2266 • Shorter bending dipole magnets are going to be installed. The current  
2267 ones have a length of 15 m while the new are only 5.5 m, allowing  
2268 the insertion of the collimators of Figure 2.35. The new niobium-tin  
2269 dipole magnets will generate an 11 T magnetic field compared with  
2270 the current 8.3 T.

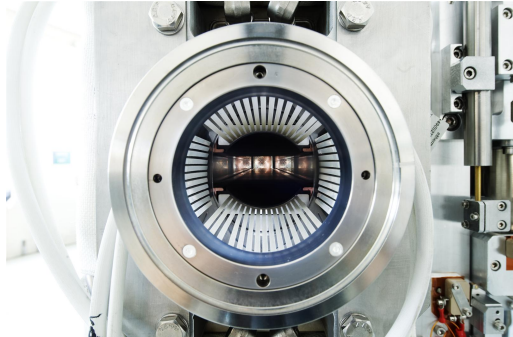


**Figure 2.35:** HL-LHC Collimator.

- 2271 • Brand new and more powerful superconducting quadrupole magnets  
2272 (up to 12 T) made of niobium and tin will substitute the current ones  
2273 (8 T). These magnets will be located at the sides of the ATLAS and  
2274 CMS detectors
- 2275 • New Beam optics. At present, as bunches cross, the protons collide  
2276 and disappear and, hence, the luminosity decreases. For the Run-4,  
2277 in order to keep the luminosity at the same level, the beam focusing  
2278 is designed to keep the collision rate constant.
- 2279 • Superconducting crab cavities for giving the bunches additional trans-  
2280 verse momentum in order to increase the probability of collisions.
- 2281 • New collimator sand injection magnets will also improve the perform-  
2282 ance of the machine.
- 2283 • Thanks to the new high-temperature superconductors, currents up to  
2284  $10^5$  Amperes will be carried over long distances.
- 2285 • New collimators that produce less electromagnetic interference with  
2286 the beam are being installed. Collimators (Figure 2.35) are important  
2287 because the machine protection is based on them. This elements of  
2288 the accelerator absorb particles that stray from the beam trajectory  
2289 and can harm the devices.
- 2290 • The accelerator chain is improved as well with the use of the linear  
2291 accelerator LINAC4 and with upgrades in the PSB, PS and PSP.

2292 Although increasing the collision rate of the beams is a crucial goal for  
2293 CERN, improving the accelerator is not enough. The current detectors have  
2294 not been designed for HL-LHC but for the LHC and, thus, cannot handle  
2295 the increased luminosity. By increasing the luminosity while keeping the  
2296 same bunch spacing, a much higher rate of collisions per bunch crossing is

2297 achieved and this implies a higher pile-up. For Run-2, the pile up peaked  
2298 around  $\mu_{max} \approx 70$  and that was already quite taxing for the system in terms  
2299 of tracking and reconstruction, and for Run-4 it may start around 140 and  
2300 increase to 200 interactions per bunch crossing.

2301 Next, the main upgrades of the ATLAS detector towards the HL-LHC  
2302 project are presented.

2303 **Inner Tracker** The elements in the ID receive a lot of radiation damage  
2304 due to the huge rate of particles hitting the detector. This radiation environment  
2305 will be even more daunting in the HL project. Therefore, the design  
2306 of ATLAS (as well as all other main detectors of LHC) has to be reviewed,  
2307 especially for the most central parts of the detector.

2308 To deal with this, ATLAS needs much more capable trackers, therefore,  
2309 the entire ID is going to be replaced with a new “inner tracker” (ITk).  
2310 This new detector consists of cylinder and end-caps equipped with silicon  
2311 detectors covering a geometrical acceptance of  $|\eta| < 4$ . This expanded  
2312 pseudorapidity range introduces many advantages in terms of object recon-  
2313 struction and pile-up mitigation by linking objects to the primary vertex  
2314 corresponding to the hard-scatter of interest. The new pixel sensors will  
2315 be placed very close to the interaction region, where the high fluencies  
2316 ( $2 \times 10^{16} n_{eq} \text{cm}^{-2}$  in the HL vs the current  $10^{15} n_{eq} \text{cm}^{-2}$ ) have to be tolerated  
2317 while maintaining a 96% efficiency of particle detection [149].

2318 As well as the ID, the ITk is divided in two subsystems mounted in  
2319 the pixel support tube: the pixel detectors and the strip detectors that  
2320 surrounds the pixels. For the strips, there are four barrel layers and six  
2321 end-cap petals and for the pixels, five layers are used.

2322 **Calorimeters** Due to radiation tolerance limits, the electronics for the  
2323 ECAL and HCAL have to be updated. The on-detector FE electronics  
2324 cannot operate with the trigger rates and latencies required for the HL-  
2325 LHC luminosities. The FCAL will remain the same as in Run-2.

2326 **Muon Spectrometer** The MS upgrades for the HL-LHC are focused on  
2327 the muon trigger chambers. The Level-0 trigger electronics of the RPC and  
2328 TCG will be upgraded and for the RPC the pseudorapidity coverage will be  
2329 significantly increased. The front-end of the MDT is going to be replaced  
2330 as well to address the trigger rate and latency requirements.

2331 **Trigger and Data Acquisition**  
 2332 **system** To reconstruct the events  
 2333 offline, they have to be recorded in  
 2334 the first place, otherwise, it makes  
 2335 no sense to have that huge  $pp$  col-  
 2336 lision rate. This is why while the  
 2337 detector hardware is being heavily  
 2338 upgraded, a lot of effort is being put  
 2339 into the trigger systems. The new  
 2340 trigger system is a multistage sys-  
 2341 tem that progressively takes more  
 2342 and more detailed information and  
 2343 each step has more time to make  
 2344 this decision. It starts with 40 MHz  
 2345 input rate ( $40^6$  input events per  
 2346 second). The triggering process  
 2347 starts by the Level-0 (Figure 2.36  
 2348 in purple) and makes very quick  
 2349 decisions ( $10\mu s$  latency), reducing  
 2350 the rate from 40 to 1 MHz. Af-  
 2351 terwards it passes to the event fil-  
 2352 ter (Figure 2.36 in orange) which  
 2353 takes the 1 MHz down to 10 kHz  
 2354 that sends to permanent storage.  
 2355 The key part is that these 10 kHz  
 2356 are really the most useful 10 kHz  
 2357 [163]. For doing so, the perfor-  
 2358 mance of the tracking is fundamen-  
 2359 tal for things like particle flow identi-  
 2360 fication,  $E_T^{\text{miss}}$  measurements, jet tag-  
 2361 ging or tau identification.

2362 .....

2363 **From ATLAS Digest: weekly news – 11 February 2022** "Con-  
 2364 cerning the High Luminosity LHC, with the new schedule, LS3 will start in  
 2365 2026 and the Run 4 would start in 2029. A new HL-LHC running param-  
 2366 eters baseline is under discussion, which leads to new projections foreseeing  
 2367 715/fb of pp data collected in Run 4. The beam energy for HL-LHC has  
 2368 also been discussed and several scenarios to reach 7 TeV per beam have been  
 2369 discussed. The high risk of warm-ups is a main concern and the decision  
 2370 will likely be postponed to the end of Run 3. Options to stay at 6.8 TeV or  
 2371 even backing off to 6.5 TeV to further avoid warm-ups are still on the table.

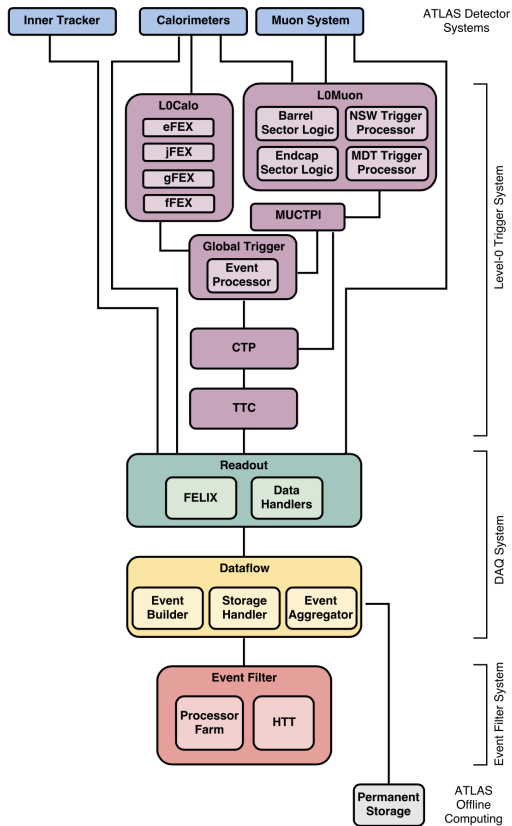


**Figure 2.36:** Design of the TDAQ Phase-II upgrade architecture, highlighting the organisation of the Upgrade Project in three main systems [163]. Direct connections between each Level-0 trigger component and the Readout system are suppressed for simplicity.

2372 Concerning the Nb3Sn inner triplets, full scale preseries prototypes are in  
2373 production."

2374 **2.4 Alignment of the inner detector**

2375 **2.4.1 Alignment requirements**

2376 **2.4.1.1 Local coordinate frame**

2377 **2.4.1.2 Track parameters**

2378 **2.4.1.3 Residuals**

2379 **2.4.2 Track based alignment**

2380 **2.4.2.1 Global  $\chi^2$  algorithm**

2381 **2.4.2.2 Weak modes**

2382 **2.4.2.3 Alignment levels and degrees of freedom**

2383 **2.4.3 Alignment results during Run-2**

2384 [Preguntar a Paolo sobre esto](#)

2385 **2.4.4 Alignment towards Run-3**

2386 [Preguntar a Paolo sobre esto](#)

2387 **2.4.4.1 Pseudo-real-time-online monitoring**

2388 **Chapter 3**

2389 **Recording data and simulating  
events in ATLAS**  
2390

2391 [164]

2392 **3.1 Data**

2393 Datasets

2394 **3.2 Monte Carlo**

2395 <https://inspirehep.net/literature/856179> In this section I  
2396 should describe the generalities of the MC generators and in the  
2397 Section4 the specifics for this analysis

2398 From ATLAS Digest: weekly news – 11 March 2022 (use  
2399 to write some comments) Reducing negative weights in Sherpa  
2400 (Frank Siegert) With the expected very large increase in size of samples  
2401 in future runs, Monte Carlo samples will not be able to scale with the accu-  
2402 mulated data, as needed for physics performance, without strong develop-  
2403 ments in several areas of the simulation. The event generation is projected  
2404 to take approximately 20% of the CPU resources and is the single largest  
2405 component in CPU consumption of the simulation. It is therefore extremely  
2406 important that strategies, that are not just to produce more since it is not  
2407 a computationally viable solution to improve on the statistical uncertainty  
2408 of the samples, be pursued. Frank discussed the importance of reducing the

2409 fraction of negative weights to improve the effective statistical uncertainty  
2410 of weighted samples in Sherpa.

2411 He described a three-fold solution he has proposed in collaboration with  
2412 Sherpa co-authors (available here) to reduce the fraction of negative weights.  
2413 The three proposed methods correspond to approximations done for (i) the  
2414 generation of events with soft emissions (S), (ii) the generation of events  
2415 with hard emissions (H) and (iii) the use of a differential K-factor for leading  
2416 order Matrix Elements with large numbers of emissions. Reducing negative  
2417 weights necessarily leads to approximations and possible biases. Frank de-  
2418 scribed in detail a comparison of the three methods. Differences are within  
2419 the systematic uncertainties of the produced samples. These methods show  
2420 that an improvement in equivalent statistics of a factor of approximately  
2421 two can be achieved. **end of ATLAS Digest**

2422 **3.2.1 MC simulations**

2423 The generation of the simulated event samples includes the effect of  
2424 multiple  $pp$  interactions per bunch crossing, as well as the effect on the  
2425 detector response due to interactions from bunch crossings before or after  
2426 the one containing the hard interaction.

2427 **3.2.1.1 Parton shower simulation**

2428 **3.2.1.2 Hadronisation simulation**

2429 **3.2.1.3 Underlying decay simulation**

2430 **3.2.1.4 Hadron decay simulation**

2431 **3.2.1.5 Pile-up simulation**

2432 **3.2.2 MC generators**

2433 **Chapter 4**

2434 **Object reconstruction and  
identification**  
2435

2436 To reconstruct the physical objects, the information of all the sub-  
2437 detectors and systems of ATLAS is employed. A detailed description of  
2438 all of them is presented in Section 2.3. After passing the trigger preselec-  
2439 tion, the raw data is analysed to build the physics objects that constitute  
2440 the subject of the physical analyses. The process of constructing this ele-  
2441 ments is known as reconstruction. Figure 2.16 illustrates how each particle  
2442 interacts with the different layers of the ATLAS detector. The reconstruc-  
2443 tioned objects are the particles tracks and vertices, the leptons, the photons,  
2444 jets (and their flavour tag) and the missing transverse momentum.

2445 **4.1 Tracking**

2446 The detection and measurement od charged particles moment is an es-  
2447 sential aspect of any large particle physics experiment. Regardless of the  
2448 medium through which a charged particle travels, it always leaves a trails  
2449 of ionised atoms and liberated electrons. By detecting this it is possible to  
2450 reconstruct the trajectory of a charged particle. ATLAS does this trough  
2451 its silicon detectors.

2452 The trajectories followed by particles are referred as “tracks”. For  
2453 charged particles, the tracks are reconstructed using, mainly, the informa-  
2454 tion of the ID and, in the case of muons, the MS. A charged particle  
2455 passing thought the ID will interact with its active sensors, the pixel detector  
2456 and SCT (Figures 2.22 and 2.23 respectively) providing a three-dimensional  
2457 measurement of space-points. While each hit in the pixel detector is directly  
2458 translated into a space-point, for the SCT two hits are needed to reconstruct

2459 one space-point. These space-points can be given by a single pixel activation  
 2460 or by several neighbouring pixels activated simultaneously. Since the  
 2461 ID is submerged in a solenoidal magnetic field, the charged particles have  
 2462 their trajectories curved by the Lorentz force, this allows to calculate its  $p_T$   
 2463 using the sagitta method. The track reconstruction is performed in two s

2464 **Highlight the importance of the alignment for the object defin-  
 2465 ition and its reconstruction. Link this section with 2.4**

2466 **4.1.1 Sagitta method**

2467 **4.2 Vertices**

2468 **4.3 Electrons and photons**

2469 **4.4 Muons**

2470 **4.5 Jets**

2471 At accelerator based detectors, quarks and gluons are detected by the  
 2472 jets of hadronic particles that they produce in the detector soon after they  
 2473 are created (remember that, as stated in Section 1.1.4, free quarks are sup-  
 2474 pressed due to color confinement). An exception to this rule are the top  
 2475 quarks, whose lifetime is smaller than the hadronisation time by two orders  
 2476 of magnitude and, hence, they are detected by its decay products. For the  
 2477 gluons and the rest of quarks, hadronisation showers (Section 2.3.3.1) take  
 2478 place and jet clustering algorithms merge the clusters and tracks produced  
 2479 by these jets to reconstruct them. In the majority of ATLAS analyses, the  
 2480 “Anti- $k_t$ ” algorithm is used [165] to analyse the data from hadronic col-  
 2481 lisions. Modelling the jet as a cone, the algorithm uses a specific choice  
 2482 of radius parameter ( $R$ ) defining the radial size of the jet. The distance  
 2483 between all pairs of objects  $i$  and  $j$  ( $d_{ij}$ ) and the distance between the  
 2484 objects and beam pipe ( $d_{iB}$ ) are used in:

$$d_{ij} = \min(k_{ti}^{2p}, k_{tj}^{2p}) \frac{\Delta_{ij}^2}{R^2}$$

$$d_{iB} = k_{ti}^{2p}$$

where

$$\Delta_{ij}^2 = (y_i - y_j)^2 - (\phi_i - \phi_j)^2$$

and  $k_{ti}$ ,  $y_i$  and  $\phi_i$  are respectively the transverse momentum, the rapidity and the azimuthal angle of object  $i$ . The parameter  $p$  accounts for the relative power of the energy versus geometrical ( $\Delta_{ij}$ ) scales. For the Anti- $k_t$ ,  $p$  is set to  $-1$ . Other clustering algorithms use different choices of  $p$  such as  $p = 0$  (Cambridge/Aachen algorithm) or  $p = 1$  (inclusive  $k_t$  algorithm).

The algorithm iterates over the topological-cluster (or, simply, top-clusters) objects of the calorimeter as it follows: First it proceeds to identify the smallest distances with among all the combinations of  $d_{ij}$  and  $d_{iB}$ . If the distance is a  $d_{iB}$ , the entity  $i$  is labeled as “jet” and removed from the list of entities. If, on the contrary, it is a  $d_{ij}$ , the objects  $i$  and  $j$  are merged together. This way, before clustering among themselves, soft components (low- $p_T$ ) tend to be merged to the hard ones (high- $p_T$ ). Then the distances are recalculated and the process repeated. This is done iteratively until all entities are assigned to a particular jet.

If a hard particle has no hard neighbours within a  $2R$  distance, all soft particles will be assigned to it, resulting in a perfectly conical jet. But if another hard particle is present in that  $2R$  distance, then there will be two hard jets and it will be impossible for both to be perfectly conical.

### Work in progress

Typically, the cone size  $R$  is selected to be 0.4 or 0.6, though the most standard used in ATLAS is 0.4. If  $R = 1$ , the jet is labeled a Large- $R$  and if  $R = 0.4$  then as Small- $R$  jet.

#### 4.5.1 Jet energy calibration and resolution

The jet calibrations and the associated uncertainties are clearly extremely important in many top analyses. This often makes them the leading experimental uncertainties in Top analyses

#### 4.5.2 Bottom quark induced jets

In general, it is impossible to determine which quark flavour was produced or even whether the jet was originated by a quark or a gluon. However, if a  $b$  quark is created, the hadronisation will produce a jet of hadrons, one of which will be a  $b$ -type hadron (B hadron). The B hadrons turn out to be relatively-long-lived particles ( $1.5 \times 10^{-12}$  s). If this larger

2517 longevity is combined with the Lorentz time-dilation that particles exper-  
2518 ience when produced in high energy collisions, it results in the B hadron  
2519 traveling on average a few mm before disintegrating.

2520 As a result, the experimental signature of a  $b$  quark is a jet of particles  
2521 emerging from the point of collision (primary vertex) and a secondary vertex  
2522 resulting from  $b$ -quark decay that is several mm away from the primary  
2523 vertex. Therefore, the capacity to resolve secondary vertices from the parent  
2524 vertex is crucial for identifying  $b$ -quark jets.

2525 **4.6 Missing transverse energy**

2526 **4.7 Overlap removal**

2527 **Chapter 5**

2528 **Probing the top-quark  
2529 polarisation in the single-top  
2530 *t*-channel production**

2531 The polarisation paper: [https://atlas-glance.cern.ch/atlas/  
2532 analysis/papers/details.php?id=13286](https://atlas-glance.cern.ch/atlas/analysis/papers/details.php?id=13286)

2533 **5.1 Introduction**

2534 Apart from the studies of the associated production of a top quark and  
2535 a Higgs boson, in this thesis is also presented a simultaneous measurement  
2536 of the three components of the top-quark and top-antiquark polarisation  
2537 vectors in *t*-channel single-top-quark production.

2538 The single-top-quark production and decay via the  $Wtb$  vertex, provides  
2539 a unique way to study the coupling between the top-quark, the  $W$  boson  
2540 and the  $b$  quarks. This vertex is studied through the measurement of the  
2541 polarisation observables for events produced in  $pp$  collisions.

2542 Importance of signal selection: In the polarisation analysis we look at an-  
2543 gular distributions. The use of a BDT or NN as it is done on the  $tHq$  studies  
2544 can introduce bias on this angular distribution. This studies are extremely  
2545 sensible to any bias introduced on the angular distributions, therefore a  
2546 count and cut method for the signal selection is the safest option.

2547 **5.2 Top quark polarisation observables**

2548 **5.3 Simulated event samples**

2549 **5.4 Object reconstruction**

2550 **5.5 Trigger requirements and event preselec-**  
2551 **tion**

2552 **5.6 Top quark reconstruction**

2553 A precise determination of the top quark 4-momentum is crucial to per-  
2554 form the polarisation measurements. If this is not done appropriately, the  
2555 angular variables can not be properly obtained and the sensibility of the  
2556 analysis is consequently reduced. The top quark is reconstructed using a  
2557 kinematic likelihood fit (KLFIT)

2558

# Chapter 6

2559

## Search for rare associate $tHq$ 2560 production

2561

### 6.1 Introduction

2562

#### Describe the strategy for the $2\ell + 1\tau_{\text{had}}$ analysis

2563 The study of the  $tHq$  production can be classified attending to the  
2564 the number of light-flavour leptons ( $\ell$ ), i.e. electrons or muons, and  
2565 hadronically-decaying tau leptons ( $\tau_{\text{had}}$ ). According to this criteria, the  
2566 channels presented in Table 6.1 have been defined. As can be seen in the  
2567 table, the study of the  $1\ell$  channel uses only the  $H \rightarrow t\bar{t}$ , which is the most  
2568 dominant decay mode for the Higgs boson with a 58% BR as is reported in  
2569 Section 1.3.3. However, for the multileptonic channels the  $H \rightarrow W^+W^-$ ,  
2570  $\rightarrow \tau^-\tau^+$  and  $\rightarrow ZZ$  are considered. These three Higgs decay channels  
2571 combined account for a total 21% BR.

#	0 $\tau_{\text{had}}$	1 $\tau_{\text{had}}$	2 $\tau_{\text{had}}$
1 $\ell$ ( $e/\mu$ )	$tHq(b\bar{b})$ $1\ell$		$tHq(WW/ZZ/\tau\tau)$ $1\ell + 2\tau_{\text{had}}$
2 $\ell$ ( $e/\mu$ )	$tHq(WW/ZZ/\tau\tau)$ $2\ell\text{SS}$	$tHq(WW/ZZ/\tau\tau)$ $2\ell + 1\tau_{\text{had}}$	
3 $\ell$ ( $e/\mu$ )	$tHq(WW/ZZ/\tau\tau)$ $3\ell$		

**Table 6.1:** Different channels for  $tHq$  production according to the presence of light-flavoured leptons and hadronically-decaying taus in the final state.

Moreover, depending on the relative charge between the light charged leptons, the  $2\ell + 1\tau_{\text{had}}$  channel is further subdivided in two sub-channels. The so-called  $2\ell \text{SS} + 1\tau_{\text{had}}$  channel is defined by the events in which the two light leptons have the same electric charge. In contrast, the one in which they have opposite electric charge is known as  $2\ell \text{OS} + 1\tau_{\text{had}}$  channel. For simplicity, through this document, these two sub-channels are usually referred just as SS and OS respectively.

The work of this thesis is focused in the  $2\ell + 1\tau_{\text{had}}$  channels. To do so, the  $2\ell \text{SS} + 1\tau_{\text{had}}$  and  $2\ell \text{OS} + 1\tau_{\text{had}}$  are treated separately since they have completely different background compositions, being the  $2\ell \text{SS} + 1\tau_{\text{had}}$  the one with the lower background contribution.

- different MVAs trained for each channel

When assuming that one of the light-flavoured leptons is originated from the Higgs-boson decay and the other one from the top-quark decay, the determination of which lepton comes from which particle is direct for the  $2\ell \text{OS} + 1\tau_{\text{had}}$  but not for the  $2\ell \text{SS} + 1\tau_{\text{had}}$ . Since knowing the origin of the light-flavoured leptons can be very useful to define variables with the power to discriminate the  $tHq$  signal from the background, tools are developed to associate these leptons to its parent particles.

- The fake estimates are being checked to see if there is anything that has to be treated differently for the two sub-channels.

## 6.2 Data and simulated events

the  $tH$  samples were done with MadGraph5\_aMC @ NLO++Pythia8+EvtGen

The underlying event is generally done with Pythia8 in ATLAS. In the  $tHq$  samples we used MadGraph5\_aMC@ NLO for the calculation of the matrix element and Pythia8 for the hadronisation and parton showering. We are also working on alternative samples with Herwig7 as parton shower generator. **While in section 3 I describe how the events and samples are generally generated and simulated, in this section I should describe what is specifically used in this analysis**

---

## 2603 6.3 Object definition and reconstruction

### 2604 6.4 Signal

2605 In this section, it is discussed how it is find what we know as signal.  
 2606 In a particular study, the “signal” is the set of events in the dataset that  
 2607 correspond to the process of interest. Therefore, in this case, the signal  
 2608 is composed by  $tHq$  production events with a  $2\ell + 1\tau_{\text{had}}$  final state. In  
 2609 contrast, the background processes are those which, a priori, look like the  
 2610 signal process but it is not.

#### 2611 6.4.1 Signal generation and validation

2612 **rivet**

#### 2613 6.4.2 Parton-level truth validation

2614 > Describe what are truth level and reconstruction level.  
 2615 > The truth information is whatever comes from the generator, the  
 2616 physics without taking into account the effects of the detector. The truth  
 2617 level does not include the effects of the interaction with matter. The truth  
 2618 also includes the parton shower and hadronisation information.  
 2619 >  $\text{truth} = \text{generator} + \text{parton shower} + \text{hadronisation}$   
 2620 > The studies I did were done at generator level  
 2621 > Particle level is part of truth information  
 2622 > Detector level = reconstruction level + calibration +  
 2623 > Creo que esto se explica bien en la tesis de florencia  
 2624 **(maybe write the calculations of BR\_tHq in the Section 6.4.2**  
 2625 **)**

#### 2626 6.4.3 Lepton assignment

2627 The two light leptons in the final state of the  $2\ell + 1\tau_{\text{had}}$  channel can  
 2628 originate either from the Higgs boson or the top quark. The ambiguities  
 2629 regarding the origin of these light-flavoured leptons, make the reconstruction  
 2630 of the top quark and Higgs boson systems extremely difficult. Nevertheless,

2631 the electric charge of these leptons could provide us useful information to  
 2632 probe their origins.

2633 To have knowledge of whether the light-flavoured leptons in the final  
 2634 state are originated from the Higgs boson or the top quark is very beneficial  
 2635 in order to both reconstruct the event and design variables at reconstruction  
 2636 level with high discriminant power. As is show in Sections 6.6.3 and 6.6.4,  
 2637 the variables using the lepton assignment information play a relevant role  
 2638 not only in the definition of the signal-enriched section but also the in  
 2639 the determination of the control regions to constrain the most important  
 2640 background processes.

2641 According to the calculations performed by combining the BR of the  
 2642 Higgs boson, the top quark and all its decay products (see Section 6.4.2),  
 2643 in the  $2\ell + 1\tau_{\text{had}}$  channel of  $tHq$  production, the  $\tau_{\text{had}}$  is produced 83.7% of  
 2644 times as a product of the Higgs-boson decay in opposition to the 16% in  
 2645 which it comes from the top-quark disintegration.

#### 2646 **Opposite-sign Leptons**

2647 In the dominant scenario ( $\tau_{\text{had}}$  from Higgs) the association of which light-  
 2648 flavoured lepton comes from the top-quark decay and which one comes  
 2649 from the Higgs-boson decay can be done directly if these two leptons have  
 2650 opposite electric charge, i.e. in the  $2\ell \text{OS} + 1\tau_{\text{had}}$  channel. Since in Higgs  
 2651 boson is neutrally charged, the sum of the charge of its decay products  
 2652 should be zero. Therefore, in the OS channel, while the light lepton with  
 2653 opposite charge to that of the  $\tau_{\text{had}}$  is the one coming from the Higgs, the  
 2654 other lepton, i.e. the one with the same charge as  $\tau_{\text{had}}$ , is the one originated  
 2655 from the top-quark decay.

#### 2656 **Same-sign Leptons**

2657 In contrast to the the  $2\ell \text{OS} + 1\tau_{\text{had}}$  channel, in the case of  $\tau_{\text{had}}$  from Higgs,  
 2658 when the two light leptons have the same electric charge (the so called  
 2659  $2\ell \text{SS} + 1\tau_{\text{had}}$ ) it is not possible to know, a priori, which of the leptons  
 2660 comes from the top-quark system and which from the Higgs-boson decay.

2661 In order to perform this association for the  $2\ell \text{SS} + 1\tau_{\text{had}}$  several methods  
 2662 relying in the truth-level information have been tested. **Describir superficialmente los métodos listados en el ítemize**

- 2664     • First method (Cyrus): Assume that the leading lepton was originated  
       2665       from the top
- 2666     • Second method (Mathias): Cut in two variables

- 2667           – Cut 1:  $m_{vis,H}(lep(t)) - m_{vis,H}(lep(H)) > 57.0 \text{ GeV}$   
 2668           – Cut 2:  $m_{pred,t}(lep(H)) - m_{pred,t}(lep(t)) > 0.0 \text{ GeV}$
- 2669       • BDT based method presented in this work

2670   **6.4.3.1 Labelling the  $2\ell \text{ SS} + 1\tau_{\text{had}}$  with the reconstruction-level**  
 2671   **and truth-level matching**

2672   Even though at reconstruction level it is not known which are the par-  
 2673   ents of the particles in the final state, at parton level this informations is  
 2674   accesible, in other words, the origin<sup>1</sup> of the light leptons is known. For a  
 2675   given event, it is possible to access to both the particle-level and parton-level  
 2676   information simultaneously. Having the parton-level leptons, whose parents  
 2677   are known, and the reconstruction level leptons, whose parents need to be  
 2678   identified, it is possible to compare them to create an association. Specific-  
 2679   ally, identify which parton-level lepton correspond to which reconstructed  
 2680   lepton. The aim of this relation is to assign the leading ( $\ell_1$ ) and sub-leading  
 2681   ( $\ell_2$ ) light leptons at reconstruction level to the the “lepton from top-quark-  
 2682   decay chain” ( $\ell_{top}$ ) and “lepton from Higgs-boson-decay chain” ( $\ell_{Higgs}$ ) at  
 2683   truth level.

2684   In order to link the reconstruction-level light leptons to the parton-level  
 2685   light leptons, a  $\Delta R < 0.01$  cone around each of the reconstructed leptons  
 2686   is built. When inside that cone there one and only one truth-level light  
 2687   lepton, there is what is called “a match”. Figure 6.1 presents the possibles  
 2688   scenarios of the association. In order to identify properly determine the  
 2689   lepton origin in an event, it is required that both leptons at reconstruction  
 2690   level have a match. There are two different cases for this. The first situation  
 2691   is that in which the leading-light lepton is  $\ell_{top}$  and the sub-leading is  $\ell_{Higgs}$ .  
 2692   For the sake of simplicity, this configuration is named Type 1 and it is  
 2693   represented in Figure 6.1a. The second double-matching combination is the  
 2694   other way around, the leading-light lepton is  $\ell_{Higgs}$  and the sub-leading is  
 2695    $\ell_{top}$ . Pictured in Figure 6.1b, this type of events are called Type 2. On  
 2696   the contrary, if only one of the two reconstructed light leptons is matched  
 2697   (Figure 6.1c), none of the leptons are classified. If a less strict criteria was  
 2698   used, it would be possible requiere only one of the two leptons matching in  
 2699   order to classify the event (the unmatched reconstruction-level lepton would  
 2700   be assigned to the unmatched parton-level lepton). The problem of the lax  
 2701   strategy is that while in cases like that on Figure 6.1c it seems clear that  
 2702   unmatched parton correspond to the unmatched reconstructed lepton, for

---

<sup>1</sup>By origin of a light lepton is meant whether it comes from the Higgs-boson-decay chain or the top-quark-decay chain.

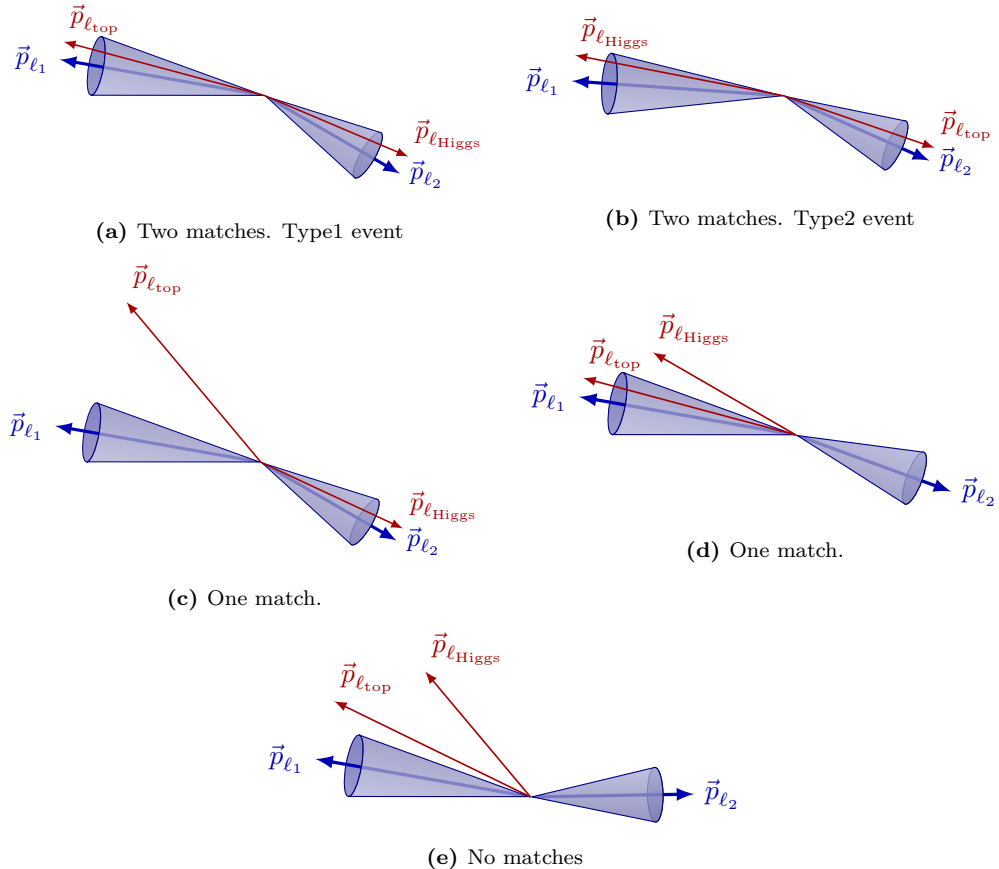


**Figure 6.1:** Association between reconstruction-level (blue) and parton-level (red) light leptons. Note that the labels  $\ell_{top}$  and  $\ell_{Higgs}$  are only available for the parton-level particles.

events such as the illustrated in Figure 6.1d the unmatched particle does not necessarily belong to the  $\ell_2$  cone. For this reason, it is mandatory that both reconstructed light leptons have a match. Finally, in the scenario in which none of the parton-level leptons fall into the cones (Figure 6.1e), no assignation takes place.

To perform this labelling, it has been required that the  $\tau_{had}$  is originated from the Higgs-boson system. This is imposed in order to guarantee that there are both a  $\ell_{top}$  and a  $\ell_{Higgs}$ . The Higgs-decay channels used for these studies are the  $H \rightarrow \tau\tau$  (one  $\tau$  decaying leptonically and the other hadronically) and the  $H \rightarrow WW$ . The  $H \rightarrow ZZ$  channel has not been included since its impact in the on the  $2\ell + 1\tau_{had}$  production when the  $\tau_{had}$  comes from the Higgs is very tiny. If the  $\tau_{had}$  is originated in the Higgs system, only a 2.0% of the events correspond to the  $H \rightarrow ZZ$  decay channel, contrasting with the 76.5% of the  $H \rightarrow \tau\tau$  and the 21.5% of the  $H \rightarrow WW$ .

2717     **Should add the fraction of events that are labeled from a) the**  
2718     **total  $2\ell + 1\tau_{\text{had}}$  sample and b) from the total  $2\ell \text{SS} + 1\tau_{\text{had}}$ .**

2719     **6.4.3.2 BDT-based method for lepton association**

- 2720     • Describe the idea of using reco-level variables to predict (on unlabelled  
2721        data) whether it is a Type1 or Type2 event by means of a BDT trained  
2722        with labeled data (isLep1fromTop)
- 2723     • Describe with a few words what a BDT is and reference appendix B.
- 2724     • Using root.TMVA - Advantages: Nowadays most of ML frameworks  
2725        (keras, pyTorch, scikit-learn, XGBoost, etc..) are based on python.  
2726        These libraries expect numpy arrays or panda data-frames as input, so  
2727        the first thing to do when using the analysis NTuples is to convert the  
2728        ROOT data-frame. An advantage of using TMVA library of ROOT  
2729        is that this data conversion is not necessary. is that
- 2730     • Describe the particularities of this gradient BDT with detail
- 2731     • One way to reap the benefits of a large training set and large test set  
2732        is to use cross validation: k-folding.
  - 2733        – Programmed in an external-to-tHqLoop script
  - 2734        – Trained only over SS signal events. In contrast to the BDT of  
2735           SR that trains over all process, this one trains only over signal  
2736           because its objective is to determine which lepton comes from  
2737           which particle in the signal events and this classification only  
2738           makes sense in signal processes.
- 2739     • Present the feature importance
  - 2740        – Present distributions of used variables and a list with the mean-  
2741           ing of this variables
  - 2742        – Present correlations between pairs of used variables. Note that  
2743           the correlation maps search for bidimensional correlations (i.e.  
2744           between pairs of two variables) and the BDT uses N-dimensional  
2745           relations. (Page 26 of the TMVA guide)
  - 2746        –
- 2747     • Discuss the negative weight strategy: Present used distributions with  
2748        'all weights' and with 'positive weights'
  - 2749        – in contrast to XGboost, ROOT.TMVA can deal with negative  
2750           weights

- 2751 • Hyperparameter optimisation
- 2752 • Present BDT response, ROC curve, ¿something else?
- 2753 • Compare to the results using other MVA methods.
- 2754 • The BDT is integrated in tHqLoop (weights.xml) ¿Where do I describe  
2755 what tHqLoop is?
- 2756 • From tHqLoop, the BDT score can be calculated for all the events  
2757 (signal or not) and then the efficiency of the lepton association can be  
2758 calculated depending on the threshold point which is chosen to define  
2759 whether the event is Type1 or Type2. Note that this efficiency is  
2760 computed only over signal events. → Table of 'efficiency vs cutpoint'

2761 **6.4.4 Top quark and Higgs boson reconstruction**

2762     **En aras de que esto es extremadamente complicado y no se**  
 2763     **logró hacer ¿tiene sentido redactar una sección?**

2764 **6.5 Background estimation**

2765     The background can be defined as everything in a subset of the data that  
 2766     simulates the signal processes without truly being a signal event. In other  
 2767     words, in this studies, everything that is not signal, is background. In this  
 2768     case, whatever that mimics the signature of an associated  $tHq$  production  
 2769     with  $2\ell + 1\tau_{\text{had}}$  final state is re referred as background.

2770     Signal (aka needle). -> Several needels Background (aka haystack) ->  
 2771     Several types of haystacks

2772     The main source of background in the  $2\ell + 1\tau_{\text{had}}$  channel is due to jets  
 2773     faking  $\tau_{\text{had}}$  **poner las figuras de oleh**

2774 **6.5.1 Fakes estimation**

2775     tau fakes are more important than light lepton fakes

2776     **This is taken from the intNote. I have to reorganise and reph-**  
 2777     **rase this information** The requirements for the objets defined in section  
 2778     (ref ref) provide significant suppression of events with jets wrongly selec-  
 2779     ted as leptons is achieved by asking electrons and muons to pass the tight

2780 requirement that combines `tightLH` ID for leptons and `medium` for muons  
2781 and `PLImprovedTight` isolation working points

2782 Similarly, the hadronic taus are required to pass the `medium` require-  
2783 ment of the RNN-based discriminator. Even so, the selected data sample  
2784 is expected to be contaminated with such type of reducible background. It  
2785 is also expected that the simulation of jets faking leptons (electron, muon,  
2786 hadronic tau) in ATLAS detector is imprecise or unreliable. Therefore, an  
2787 important step of the analysis is to estimate this background in data.

2788 **Light lepton fakes** Particles in the Feynman diagram are referred as  
2789 ‘prompt’ or ‘real’. Acceptance, quality and isolation requirements are ap-  
2790 plied to select these leptons Non-prompt leptons and non-leptonic particles  
2791 may satisfy these selection criteria, giving rise to so called ‘non-prompt and  
2792 fake’ lepton backgrounds. Fake electrons/muons will not be explicitly dis-  
2793 tinguished and are referred as fake leptons. The mis-identified lepton back-  
2794 ground arises from heavy-flavour (HF) decay leptons and electrons from  
2795  $\gamma$ -conversions. These leptons are mainly produced in  $t\bar{t}$ ,  $Z + \text{jets}$  and  $tW$   
2796 events.

2797 The estimation of the fake/non-prompt lepton background is done with  
2798 the template fit method or via the matrix method

2799 The fake and real lepton efficiencies (fake/real rates) are defined as the  
2800 probabilities of a fake or real electron or muon to pass the nominal elec-  
2801 tron/muon requirements. They are given by the tight over loose ratio

2802 - Get some ideas from here: [https://cds.cern.ch/record/1951336/  
2803 files/ATLAS-CONF-2014-058.pdf](https://cds.cern.ch/record/1951336/files/ATLAS-CONF-2014-058.pdf)

2804 **Tau fakes** In the analysis channels involving hadronic taus, all meth-  
2805 ods used for fake background estimation rely on MC-based templates.  
2806 These are splits of simulation according to a type of object mimicking the  
2807 lepton of interest. Construction of MC templates related to the electron  
2808 and muon fakes is based on `IFFTruthClassifier` tool. **Describe the**  
2809 **IFFTruthClassifier**

- 2810 • counting method  
2811 • template fit method

2812 The extracted SFs are then applied to the simulated background com-  
2813 ponent in the region with taus passing I

Process	SS	OS	SS + OS
$tHq$	0.9	1.2	2.1
$tZq$	6.2	32.9	39.1
$t\bar{t}$	47.9	2965.0	3012.9
$tW$	2.3	118.9	121.2
$W + \text{jets}$	1.9	0.5	2.4
$Z + \text{jets}$	6.7	1956.2	1962.9
diboson	8.9	121.6	130.5
$t\bar{t}W$	21.0	43.4	64.4
$t\bar{t}Z$	17.5	101.2	118.7
$t\bar{t}H$	17.8	43.2	61.0
$tWZ$	3.1	16.4	19.5
$tWH$	0.6	1.5	2.1
Other	1.9	9.3	11.2
Total	136.7	5411.3	5548.0
S/B (%)	0.6627	0.0222	0.0379
Significance	0.0771	0.0163	0.0282

**Table 6.2:** Event yields at preselection level for SS, OS and SS+OS combination.

### 2814 6.5.2 Prompt backgrounds

2815 All the processes whose signature is the same as the process of interest  
 2816 are known as prompt backgrounds as in contrast to the fake or non-prompt  
 2817 backgrounds described in Section 6.5.1.

## 2818 6.6 Event selection

### 2819 6.6.1 Preselection

2820 Preselection requirements

### 2821 6.6.2 BDT

2822 Since a BDT is going to be used for both the lepton assign-  
 2823 ment and region definition, it may be interesting to describe the  
 2824 technicalities of the BDT in an appendix

2825     Maybe, it can also be a good idea to explain the generalities of  
2826     the BDT for region definition here and then put the BDT results  
2827     into "Signal Region" and "Control Regions" section.

2828     **6.6.2.1 Performance**

2829     **6.6.2.2 Ranking of variables**

2830     **6.6.2.3 Hyperparameter optimisation**

2831     **Grid search**

2832     **Genetic algorithm**

2833     **6.6.2.4 Negative-weights strategy**

2834     **6.6.2.5 k-Folding**

2835     **6.6.3 Signal Region**

2836     **6.6.3.1 Same Sign channel**

2837     **6.6.3.2 Oposite Sign channel**

2838     **6.6.4 Control Regions**

2839     **6.6.4.1 Same Sign channel**

2840      $t\bar{t}$

2841      $t\bar{t}W$

2842      $t\bar{t}Z$

2843      $t\bar{t}H$

2844 **6.6.4.2 Oposite Sign channel**

2845  $t\bar{t}$

2846  $Z +\text{jets}$

2847 **Diboson**

2848  $tW$

## 2849 6.7 Systematic uncertainties

2850 Particle collision physics distinguish two types of uncertainties, the stat-  
2851 istical uncertainty and the systematic uncertainty. The statistical uncer-  
2852 tainty is the result of stochastic fluctuations in data and is the result of a  
2853 limited size of analysed dataset. It is fully uncorrelated between subsequent  
2854 measurements. On the other hand there are the systematic uncertainties,  
2855 which are defined as everything that is not a statistical error. These are  
2856 fully correlated between subsequent measurements and are associated with  
2857 all sort of sources such us the measurement apparatus, the assumptions  
2858 made, the model used, the MC generator and many others.

2859 While the statistical uncertainty is usually intrinsically added in the  
2860 inference method, the inclusion of the systematic uncertainties and its  
2861 propagation through the statistical analysis are not trivial.

2862 Alternative samples are produced to evaluate the systematics: - Herwig7  
2863 -> parton shower  
2864 - asdfas. -> modelling

2865

2866 **6.7.1 Theoretical uncertainties**

2867 **6.7.2 Modelling uncertainties**

2868 **6.7.3 Experimental uncertainties**

2869 **6.8 Fit results**

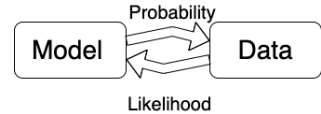
2870 **6.8.1 Likelihood fit**

2871 **Maybe I move the statistics description to an appendix** The  
2872 likelihood fit....

2873 The likelihood function is defined as the probability of observing a cer-  
2874 tain set of data ( $\vec{x}$ ) given a model or hypothesis with certain parameter  
2875 values ( $\vec{\theta}$ ). It is given by

2876

$$L(\vec{\theta}) = \mathcal{P}(\vec{x}|\vec{\theta}) = \prod_i \mathcal{P}(x_i|\vec{\theta})$$



2877 where  $i$  runs over the data points. By maximising the likelihood func-  
2878 tion, the parameters  $\vec{\theta}$  of the model that better fit the data are obtained.  
2879 These are known as estimated values. The fit is the parameter estimation  
2880 via the Likelihood maximisation,  $\vec{\theta}_{estimated} = \text{argmax}_{\vec{\theta}} L(\vec{\theta})$ .

For binned distributions the likelihood function can be written as

$$L(\vec{n}|\vec{\theta}) = \prod_{i \in bins} \mathcal{P}(n_i^{obs}|n_i^{exp}(\vec{\theta})) = \prod_{i \in bins} \mathcal{P}(n_i^{obs}|S_i^{exp}(\vec{\theta}) + B_i^{exp}(\vec{\theta}))$$

2881 Here,  $i$  runs over the bins of the histogram,  $n_i^{obs}$  and  $n_i^{exp}$  are the observed  
2882 and expected number of entries in the bin  $i$ . The predicted signal and  
2883 background entries in the bin  $i$  are  $S_i$  and  $B_i$ .

2884 Since particle physics experiments are counting experiments, the dis-  
2885 tribution follows the poissonian statistics. The Poisson distribution is a  
2886 discrete probability distribution that expresses the probability of a given  
2887 number of events occurring in a fixed interval of time or space if these  
2888 events occur with a known constant mean rate and independently of the  
2889 time since the last event

From the frequentist point of view the probability is defined as the fraction of times an event occurs, in the limit of very large number ( $N \rightarrow \infty$ )

of repeated trials

$$\mathcal{P} = \lim_{N \rightarrow \infty} \frac{\text{Number of favorable cases}}{N}$$

where  $N$  is the number of trials. Even though this infinity can be conceptually unpleasant, for LHC experiments, the amount of events is so large that this  $\mathcal{P}$  definition becomes acceptable [166].

Meanwhile, for the Bayesian (or subjective) probability expresses the degree of belief that a claim is true. Starting from a prior probability, following some observation, the probability can be modified into a posterior probability. The more information an individual receives, the more Bayesian probability is insensitive on prior probability [166].

The Bayes theorem states that considering two events  $A$  and  $B$ , the probability of  $A$  to happen given that  $B$  takes places is

$$\mathcal{P}(A|B) = \frac{\mathcal{P}(B|A)\mathcal{P}(A)}{\mathcal{P}(B)}$$

where  $\mathcal{P}(B|A)$  is the conditional probability of  $B$  given  $A$  and  $\mathcal{P}(B)$  the probability of the event  $B$  to happen. Here,  $\mathcal{P}(A)$  has the role of prior probability while  $\mathcal{P}(A|B)$  is known as posterior probability.

<sup>2901</sup> **6.8.2 Strategy**

<sup>2902</sup> **6.8.3 Fit with Asimov data**

<sup>2903</sup> **6.8.3.1 Post-fit**

<sup>2904</sup> **6.8.3.2 Pruning**

<sup>2905</sup> **6.8.3.3 Nuisance Parameters**

<sup>2906</sup> **6.8.3.4 Correlation matrix**

<sup>2907</sup> **6.8.3.5 Ranking**

<sup>2908</sup> **6.8.4 Fit to data**

<sup>2909</sup> **6.8.4.1 Post-fit**

<sup>2910</sup> **6.8.4.2 Pruning**

<sup>2911</sup> **6.8.4.3 Nuisance Parameters**

<sup>2912</sup> **6.8.4.4 Correlation matrix**

<sup>2913</sup> **6.8.4.5 Ranking**

<sup>2914</sup> **6.8.5 Results**

<sup>2915</sup> **6.8.6 Data fit**

<sup>2916</sup> **6.9 Combination results**

<sup>2917</sup> **Discuss results, compare them with CMS, future perspectives**

<sup>2918</sup> **...**

<sup>2919</sup> **6.10 Conclusions**



2920 Chapter 7

2921 Conclusion



2922 **Appendix A**

2923 **Effect of negative weights**

2924 **A.1 Negative weights uncertainties**

- 2925 • What is a weight in a MC event?
- 2926 • Why are there negatively weighted events?
- 2927 • Why are negative weights problematic?

2928 **A.2 Statistical uncertainty of negative  
2929 weights**

2930 Assume that there is a sample of  $N$  Monte Carlo simulated events. Of  
2931 these, a fraction  $x$  have negative weights and, therefore, a fraction  $(1 - x)$   
2932 has a positive weight. The effective number of events is  $(N_+ - N_-)$ , being  
2933  $N_+ = (1 - x)N$  the amount of positively weighted events and  $N_- = xN$  the  
2934 same for the negative weights.

2935 The statistical fluctuations are calculated in terms of  $x$  and the standard  
2936 deviation ( $\sigma_N = \sqrt{N}$ ). The number of positive and negative events can  
2937 fluctuate randomly between  $\pm\sigma_-$  for the later and  $\pm\sigma_+$  for the former.  
2938 Here,  $\sigma_- = \sqrt{xN} = \sqrt{x}N$  and  $\sigma_+ = \sqrt{1-x}N$

The variance ( $V = \sigma^2$ ) of the sample is then

$$V(N_+ - N_-) = xV(N) + (1 - x)V(N) = V(N)$$

and the fractional uncertainty

$$\frac{\sigma(N_+ - N_-)}{N_+ - N_-} = \frac{\sigma_N}{(1 - x)N - xN} = \frac{1}{1 - 2x} \frac{\sigma_n}{N}$$

2939 When the fraction of negative events is  $x = 0$ ,  $\frac{\sigma(N_+ - N_-)}{N_+ - N_-} = \frac{\sigma_n}{N}$  as expected.  
 2940 In contrast, if  $x = 0.5$  the fractional uncertainty is infinite, as expected.

2941 For the signal  $tHq$   $2\ell + 1\tau_{\text{had}}$  MC signal sample the fraction of negative  
 2942 weights is between 0.3 and 0.4 depending on the production used.

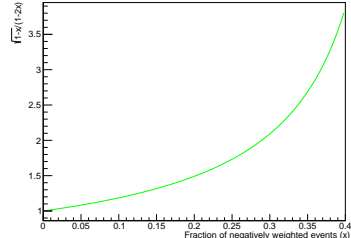
$$2943 \quad \bullet \quad x = 0.3 \rightarrow \frac{\sigma(N_+ - N_-)}{N_+ - N_-} = \frac{1}{0.2} \frac{\sigma_n}{N} = 5.0 \frac{\sigma_n}{N}$$

$$2944 \quad \bullet \quad x = 0.4 \rightarrow \frac{\sigma(N_+ - N_-)}{N_+ - N_-} = \frac{1}{0.4} \frac{\sigma_n}{N} = 2.5 \frac{\sigma_n}{N}$$

2945 The uncertainty of the effective number of events can be compared to  
 2946 that of using only the positively weighted events. If the two fractional  
 2947 uncertainties are divided:

$$\frac{\frac{\sigma(N_+ - N_-)}{N_+ - N_-}}{\frac{\sigma(N_+)}{N_x}} = \frac{\frac{1}{1-2x} \frac{\sigma_n}{N}}{\frac{1}{\sqrt{(1-x)N}}} = \frac{\sqrt{1-x} \sigma_n}{1-2x} \frac{1}{N} = \frac{\sqrt{1-x}}{1-2x}$$

2948 In the range of  $x$  values for the  $2\ell + 1\tau_{\text{had}}$  simulated signal events.



$$2949 \quad \bullet \quad x = 0.3 \rightarrow \frac{\frac{\sigma(N_+ - N_-)}{N_+ - N_-}}{\frac{\sigma(N_+)}{N_x}} = 2.09$$

$$\bullet \quad x = 0.4 \rightarrow \frac{\frac{\sigma(N_+ - N_-)}{N_+ - N_-}}{\frac{\sigma(N_+)}{N_x}} = 3.87$$

2950 In Figure A.1, several  $\Delta R$  distributions generated using all the events  
 2951 and just the positively weighted ones. As expected, the uncertainty bands  
 2952 are bigger for the 'All events' than for the 'Positive events'. These his-  
 2953 tograms were produced to verify that using only the events with positive  
 2954 weights in the training of the BDT for lepton assignment in the SS scenario  
 2955 (Section 6.4.3) was not biasing the result. The size of the error bands is  
 2956 calculated by ROOT as the square root of the quadratic sum of the weights,  
 2957 as explained below.

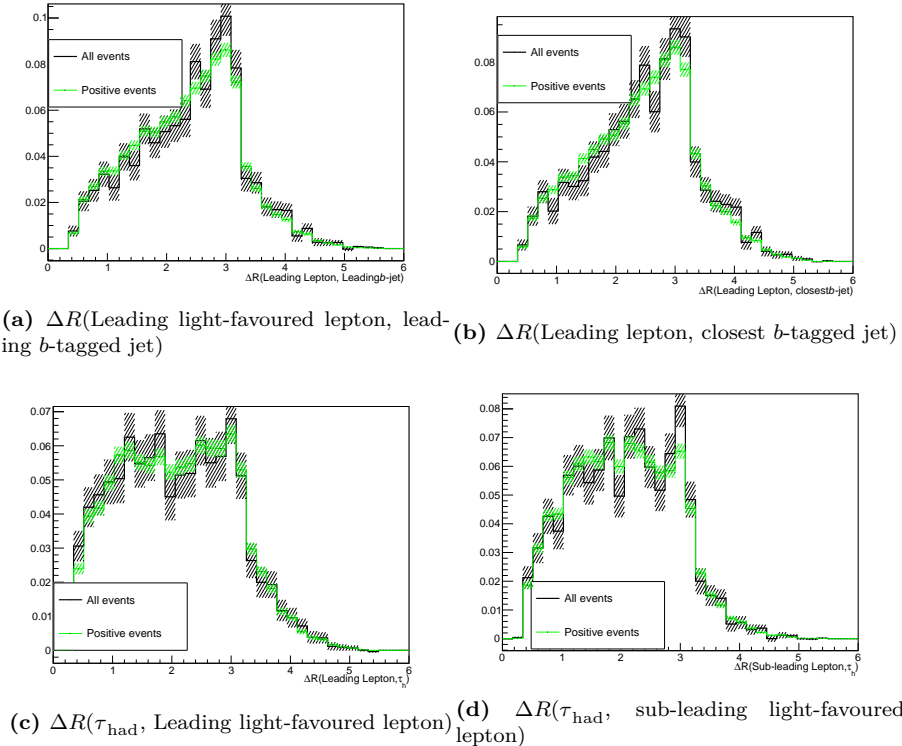


**Figure A.1:** Some normalised distributions for all the signal events in the  $2\ell \text{SS} + 1\tau_{\text{had}}$  (black) and just the positively weighted events (green). For each bin, the error band is calculated as the square root of the quadratic sum of the weights.

### 2958 A.2.1 Errors in binned histograms

If a bin of a histogram has  $n$  entries of weighted events  $w_i$  with  $i = 1, 2, \dots, n$ , the size of the bar is  $\sum_{i=1}^n w_i$ . Therefore, the error of that bar is

$$\sqrt{\sum_{i=1}^n w_i^2} \quad (\text{A.1})$$

This expression for the error of a bin in a histogram is based on error propagation and intrinsic poissonian statistics only. The variance, i.e. the error on the weighted number of events" in that bin, is given by error propagation:

$$V\left(\sum_{i=1}^n w_i\right) = \sqrt{\left(\sum_{i=1}^n w_i^2\right)^2} = \sum_{i=1}^n w_i^2 = \sum_{i=1}^n V(w_i)$$

2959 The variance of the weight  $w_i$ ,  $V(w_i)$ , is determined only by the statistical  
2960 fluctuation of the number of events considered:  $V(w_i) = w_i^2$ .

**2961 A.3 Negative weights in MVA methods**

2962 Events coming from the MC generator can be produced with (unphys-  
2963 ical) negative weights in some phase-space regions. Such occurrences are  
2964 frequently inconvenient to deal with, and whether or not they are handled ef-  
2965 fectively is dependent on the MVA method's actual implementation. Within  
2966 the ROOT TMVA library, probability and multi-dimensional probability  
2967 density estimators, as well as BDTs, are among the methods that correctly  
2968 include occurrences with negative weights. In cases where a method does  
2969 not properly treat events with negative weights, it is advisable to ignore such  
2970 events for the training but to include them in the performance evaluation  
2971 to not bias the results.

2972 **Appendix B**

2973 **Boosted Decision Trees**

2974 A boosted decision tree, typically referred just by its acronym BDT, is  
2975 a supervised<sup>1</sup> machine learning (ML) technique used for classification. The  
2976 analysis presented in this thesis uses several BDTs. Both the light lepton  
2977 origin assignment (Section 6.4.3) and the signal to background separation  
2978 (Section 6.6.2) are based on a BDT. This tool is applied in more scenarios  
2979 within within ATLAS. In the  $b$ -tagging, for instance, a BDT is trained to  
2980 discriminate  $b$ -jets from light-jets [167].

2981 **B.1 How does a BDT work?**

2982 A BDT is an ensamble of decision trees. A decision tree is a map of  
2983 possible results of related decisions. A decision tree takes a set of input  
2984 features and splits input data recursively based on those features. This  
2985 results in a tree structure that resembles that of a flow charts with a decisiion  
2986 or split at each node. The last level of the trees are the so called leaves and  
2987 each represents a class. An example of a tree can be seen on Figure B.1,  
2988 where an event is classified in one of the two categories following a set of  
2989 yes-no questions.

Boosting is a technique for turning numerous weak classifiers (trees in this case) into a powerful one. Each tree is created iteratively depending on the prior ones. The output of each tree ( $h_t(x)$ ) is given a weight ( $w_t$ ) relative to its accuracy. The ensamble output is the weighted sum

$$\hat{y}(x) = \sum_t w_t h_t(x) \quad (\text{B.1})$$

---

<sup>1</sup>Supervised learning means that the data used in the training is labeled.

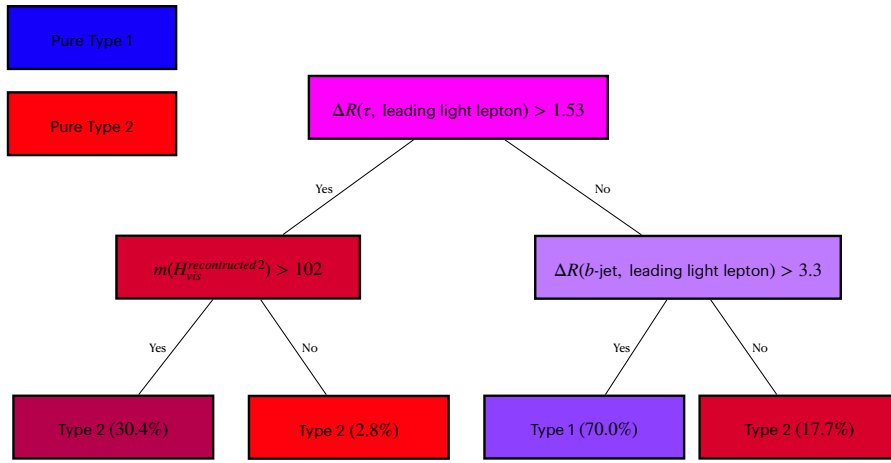


**Figure B.1:** Example of a decision tree with three nodes. This particular example corresponds to one of the trees in the BDT for the light lepton origin assignment (see Section 6.4.3). The color of the boxes represents the purity on Type 1 or Type 2 events that arrive to each node.

where  $t$  run over the trees. The goal of the boosting is to minimise an objective function

$$O(x) = \sum_i l(\hat{y}_i, y_i) + \sum_t \Omega(f_t) \quad (\text{B.2})$$

where  $l(\hat{y}_i, y_i)$  is the loss function (the distance between the truth and the prediction of the  $i^{th}$  sample) and  $\Omega(f_t)$  is the regularisation function (penalises the complexity of the  $t^{th}$  tree).

There are several types of boosting for BDTs. Some of the most common are AdaBoost, Gradient Boosting and XGBoost. The latter, which stands for “eXtreme Gradient Boosting”, is the used in this work and its details can be found in reference [168].

### 2997 B.1.1 Training

For a ML algorithm to train means to learn or determine good values for all the weights within that model. To do so, the algorithm takes the labelled data and fits the model. For instance, for the signal discrimination, the ML model takes all the MC samples, where all the events are labeled either as signal or background events. A renormalisation can take place if needed (see comment below). Apart from the data, the model also needs a set of variables that have some power to discriminate between our categories. A condition on one discriminant variable is set on each node of the BDT to split the phase space into two parts. The aim of the training is to find

3007 the optimal cut in each node so that after it the separation between the  
 3008 categories is maximised, i.e. one part is enriched in background and the  
 3009 other in signal. This is done in a loop over all discriminating variables and  
 3010 trying to test as many as possible values for each cut (the default in TMVA  
 3011 is trying 20 values for each variable). The best splitting is defined on the  
 3012 basis of the splitting index, which works as a measure of inequality because  
 3013 we want to measure the inequality between the two categories in each split  
 3014 node. A low splitting index value means a high inequality between the  
 3015 classes, i.e. high purity. The best cut is defined as the one that  
 3016 yields the highest splitting index difference between the parent node and  
 3017 the two children node (each weighted by the total number of events in  
 3018 the corresponding block). Then it is possible to keep splitting blocks until  
 3019 a stopping requirement is satisfied. A single tree is a very weak classifier  
 3020 because it is very sensitive to statistical fluctuations in the training MC  
 3021 sample.

3022 **Internal reweight of events in training sample**

3023 Sometimes, MC generators may provide event weights which may turn out  
 3024 to be extremely small or very high. To avoid artefacts, TMVA can renor-  
 3025 malise the signal and background training weights internally so that their  
 3026 respective sums of effective (weighted) events are equal. By doing this,  
 3027 the performance of the BDT can be improved since some classifiers are  
 3028 sensitive to the relative amount of each category (Type1/Type2 or sig-  
 3029 nal/background) in the training data. While for the lepton assignment  
 3030 this renormalisation does not play an important role (the amount of Type1  
 3031 and Type2 signal events is similar), for the  $tHq$  signal discrimination  
 3032 the signal sample in the training test has to be reweighted.

3033 **B.1.1.1 Loss function**

3034 **B.1.1.2 Overtraining**

3035 Let's consider a ML model  $f(x|\theta)$ , where  $x$  are the data points used as  
 3036 input and  $\theta$  the tuneable parameters of the model. The function  $f(x|\theta)$   
 3037 outputs the prediction of the model. The parameters  $\theta$  of the model are  
 3038 tuned during the training process using a training set ( $\mathcal{T}$ ). The true output  
 3039 ( $y$ ) of the elements in  $\mathcal{T}$ . When successful, the training finds the  $\theta$  that  
 3040 performs as good as possible on new, unseen, data.

For a given  $f(x|\theta)$  model, the training error,  $\text{err}(\mathcal{T})$ , is defined by [169]:

$$\text{err}(\mathcal{T}) = \frac{1}{N_t} \sum_{n=1}^{N_t} L(y_n, f(x_n|\theta)) \quad (\text{B.3})$$

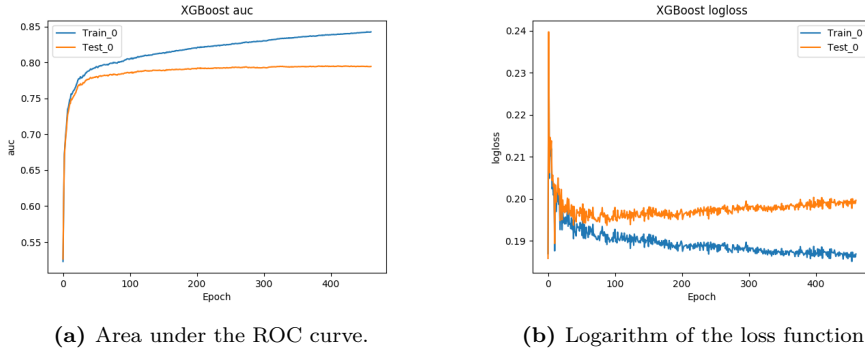


**Figure B.2:** Example of the evolution of the BDT metrics when overtraining occurs. The x-axis shows the training iteration.

3041 where  $N_t$  is the number of events used for the training and  $L$  the chosen  
 3042 loss function and  $x_n$  and  $y_n$  the points in the training set.

3043 The  $\text{err}(\mathcal{T})$  is a poor estimator of the model's performance on new, data.  
 3044 It usually decreases as the number of training cycles increases, and it can  
 3045 begin to adapt to noise in the training data. When this happens the training  
 3046 error continues to decrease but the error on the data outside of the training  
 3047 set starts increasing, jeopardising the general performance of the model.  
 3048 This effect is the so called overfitting or overtraining.

3049 Overtraining occurs when a ML model can accurately predict training  
 3050 examples but is unable to generalise<sup>2</sup> to new data. When overtraining takes  
 3051 place, the ML model has learnt the details of the training data to an extent  
 3052 in which these knowledge do not reflect the behaviour of the test sample.  
 3053 This results in poor field performance.

3054 Figure B.2 shows how an overtrained BDT evolves. In B.2a can be  
 3055 seen that as the training of the BDT continues, the ability of the model  
 3056 to classify the events in  $\mathcal{T}$  (blue) improves while for the data in the test  
 3057 sample (orange) it doesn't. This means that the model is not generalising  
 3058 properly. With the plot of the loss function (Figure B.2b) can be seen how  
 3059 the error of the test data slightly increases while for the training samples is  
 3060 strongly reduced.

3061 When tested on the training sample, overtraining results in an apparent  
 3062 improvement in classification or regression performance over the objectively  
 3063 achievable one, but an effective performance loss when measured on an  
 3064 independent test sample (even though, there is a risk that it can still happen  
 3065 even if we use separate test data). Until deployed to real unseen data, there

---

<sup>2</sup>By generalise is meant that the model recognises only those characteristics of the data that are general enough to also apply to some unseen data.

3066 is a danger that overtraining will go unnoticed. This makes of overtraining  
3067 one of the greatest dangers in ML. Other names for this phenomenon are  
3068 overfitting and type III error.

3069 Usually, this is a result of too little data or data that is too homogenous.  
3070 Overtraining arises when there are too few degrees of freedom, because too  
3071 many model parameters of an algorithm were adjusted to too few data  
3072 points. Not all MVA methods are equally sensible to overtraining. While  
3073 Fisher discriminant hardly suffers from it, BDTs usually suffer from at least  
3074 partial overtraining, owing to their large number of nodes. Nevertheless,  
3075 for the BDTs some countermeasures can be applied to preserve the ability  
3076 to generalise:

- 3077 • Never test the model on the data used for the training.
- 3078 • The number of nodes in boosted decision trees can be reduced by  
3079 removing insignificant ones (“tree pruning”). There are two types, pre-  
3080 pruning and post-pruning
  - 3081 – Pre-pruning: Refers to the early stopping of the growth of the  
3082 decision tree
  - 3083 – Post-pruning: Allows the decision tree model to grow to its full  
3084 depth, then removes the tree branches to prevent the model from  
3085 overfitting
- 3086 • Cross validation is a powerful technique to use all the data for training  
3087 at the same time that all the data for testing is employed while  
3088 avoiding overfitting. This method is based in cleverly iterating the  
3089 test and training split around and it is described in Section B.3.

### 3090 **B.1.2 Evaluation / Validation**

### 3091 **B.1.3 Application**

## 3092 **B.2 Treatment of negative weights**

## 3093 **B.3 Cross validation and $k$ -folding**

3094 Cross validation is a technique consisting in training several ML models  
3095 on different subsets of the input data and evaluated on the complementary  
3096 subset of the data. The goal cross validation is to estimate the performance

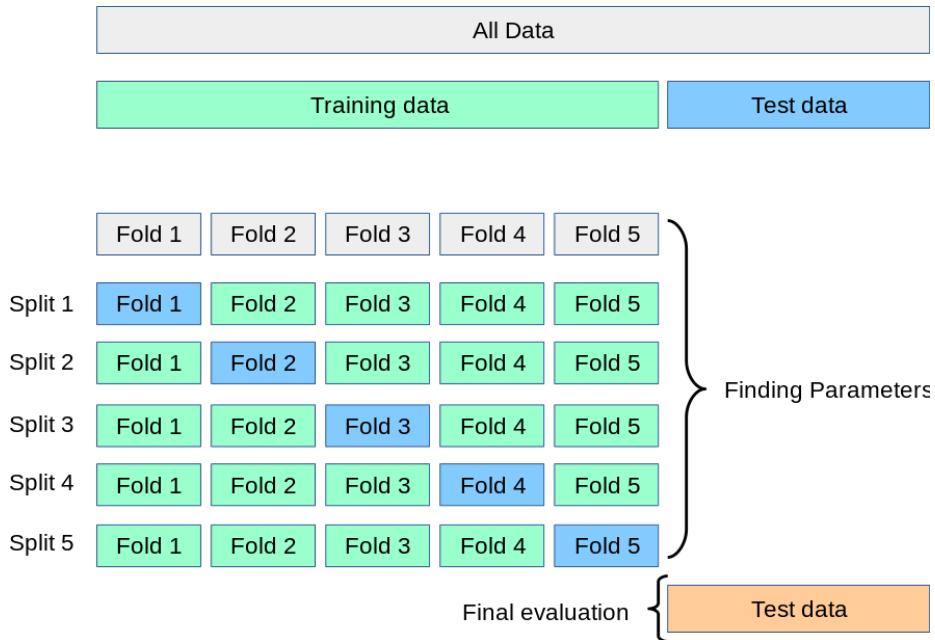


**Figure B.3:** Illustration of  $k$ -folding cross validation using 5 folds.

3097 of a machine learning model. It can identify overfitting or recognise the  
 3098 failure of the model to generalise a pattern.

3099 One particular method to do this is the  $k$ -folding. It consists on splitting  
 3100 the input data into  $k \in \mathcal{N}$  equally-sized subsets. Each of these is known  
 3101 as fold. With this procedure the ML model is trained  $k$  times. For each  
 3102 train  $k - 1$  folds are used as training set and the non-used fold is the subset  
 3103 of date where the evaluation takes place. All folds are used once as test  
 3104 sample and  $k - 1$  times in the train sample.

3105  $k$ -folding cross validation resample is of particular interest when the data  
 3106 available is limited because, by using it, all events are used in the training  
 3107 phase. It generally results in a less biased or less optimistic estimate of the  
 3108 model skill than other methods, such as a simple train/test split.

3109 Note that when the score of the model is applied, each event gets the  
 3110 score that was assigned when it was used as test event. Not doing this  
 3111 would bias the model.



<sub>3112</sub> **Abbreviations**

<sub>3113</sub>

Acronym	Meaning
AD	Antiproton Decelerator
ALICE	A Large Ion Collider Experiment
ATLAS	A Toroidal LArge AparatuS
AWAKE	Advanced Proton Driven Plasma Wakefield Acceleration Experiment
CERN	European Organization for Nuclear Research
CMS	Compact Muon Solenoid
CP	Charge conjugation Parity
CSC	Cathode-Strip Chambers
DAQ	Data Acquisition
ECAL	Electromagnetic Calorimeter
EF	Event Filter
EM	Electromagnetic
EW	Electro Weak
EWSB	Electroweak Symmetry Breaking
FASER	ForwArd Search ExpeRiment
FCAL	Forward calorimeter
FTK	Fast TracKer
GR	General Relativity
HCAL	Hadronic Calorimeter
HLT	High Level Trigger
IBL	Insertable B-Layer
IP	Interaction Point

Acronym	Meaning
IR	Insertion Regions
ISOLDE	On-Line Isotope Mass Separator
ITk	Inner Tracker
LAr	Liquid Argon
LCG	LHC Computing Grid
LEIR	Low Energy Ion Ring
LEP	Large Electron-Positron
LHC	Large Hadron Collider
LHCb	The Large Hadron Collider Beauty
LHCf	Large Hadron Collider forward
LINAC2	Linear Accelerator 2
LINAC3	Linear Accelerator 3
LINAC4	Linear Accelerator 4
3114	LO
	Leading Order
	LVL1
	Level-1 Trigger
	LVL2
	Level-2 Trigger
MATHUSLA	Massive Timing Hodoscope for Ultra Stable neutrAL pArticles
MDT	Monitored Drift Tube
MoEDAL	Monopole and exotic particle detector at the LHC
MS	Muon Spectrometer
NLO	Next-to-Leading Order
NNLO	Next-to-Next-to-Leading Order
PDF	Parton Distribution Function
PS	Proton Synchrotron
PSB	Proton Synchrotron Booster
QCD	Quantum Chromodynamics
QED	Quantum Electrodynamics
QFT	Quantum Field Theory

3115

Acronym	Meaning
RF	Radio Frequency
ROD	ReadOut Drivers
RoI	Regions of interest
ROS	ReadOut Systems
RPC	Resistive Plate Chambers
SCT	Semiconductor Tracker
SFO	Sub-Farm Output
SM	Standar Model
SPS	Super Proton Synchrotron
SSB	Spontaneus Symmetry Breakin
SSC	Superconducting Super Collider
SUSY	Supersimmetry
TGC	Thin Gap Chambers
TI	Transfer Injection

# <sup>3116</sup> Bibliography

- <sup>3117</sup> <sup>1</sup>Particle Data Group Web Page, *top-quark Mass (Direct Measurements)*,  
<sup>3118</sup> (2022) <https://pdglive.lbl.gov/DataBlock.action?node=Q007TP>  
<sup>3119</sup> (visited on 22/01/2022) (cit. on pp. v, 34).
- <sup>3120</sup> <sup>2</sup>*Measurement of the polarisation of single top quarks and antiquarks produced in the t-channel collected with the ATLAS detector at  $\sqrt{s} = 13$  TeV and bounds on the tWb dipole operator*, (2021) (2021) (cit. on p. v).
- <sup>3123</sup> <sup>3</sup>Online Etymology Dictionary, "Physics", (2022)  
<sup>3124</sup> <https://www.etymonline.com/word/physics> (visited on 20/01/2022)  
<sup>3125</sup> (cit. on p. 1).
- <sup>3126</sup> <sup>4</sup>Perseus Digital Library, "fusiko", (2022)  
<https://www.perseus.tufts.edu/hopper/text?doc=Perseus:text:1999.04.0057:entry=fusiko/s> (visited on 20/01/2022) (cit. on p. 1).
- <sup>3129</sup> <sup>5</sup>C Singer, *A Short History of Science to the Nineteenth Century*, p. 35.  
<sup>3130</sup> (Streeter Press, 2008) (cit. on p. 1).
- <sup>3131</sup> <sup>6</sup>C. C. W. Taylor et al., *The atomists, leucippus and democritus: fragments: a text and translation with a commentary*, Vol. 5  
<sup>3132</sup> (University of Toronto Press, 2010) (cit. on p. 1).
- <sup>3134</sup> <sup>7</sup>O. Leaman, *Key concepts in eastern philosophy* (Routledge, 2002)  
<sup>3135</sup> (cit. on p. 1).
- <sup>3136</sup> <sup>8</sup>A. Purcell, *Go on a particle quest at the first CERN webfest. Le premier webfest du CERN se lance à la conquête des particules*, (2012) 10 (2012)  
<sup>3137</sup> (cit. on p. 2).
- <sup>3139</sup> <sup>9</sup>A. Einstein, *The Foundation of the General Theory of Relativity*,  
<sup>3140</sup> *Annalen Phys.* **49** (1916) 769–822, edited by J.-P. Hsu and D. Fine  
<sup>3141</sup> (1916) (cit. on p. 2).
- <sup>3142</sup> <sup>10</sup>P. A. M. Dirac, *On the theory of quantum mechanics*,  
<sup>3143</sup> *Proceedings of the Royal Society of London. Series A, Containing*  
<sup>3144</sup> *Papers of a Mathematical and Physical Character* **112** (1926) 661–677  
<sup>3145</sup> (1926) (cit. on p. 3).

- <sup>3146</sup><sup>11</sup>R. Aaij et al., *Observation of a narrow pentaquark state,  $P_c(4312)^+$ , and of two-peak structure of the  $P_c(4450)^+$* ,  
<sup>3147</sup>*Phys. Rev. Lett.* **122** (2019) 222001 (2019) (cit. on p. 4).
- <sup>3149</sup><sup>12</sup>A. Pich, ‘The Standard model of electroweak interactions’,  
<sup>3150</sup>2006 European School of High-Energy Physics (2007) 1  
<sup>3151</sup>(cit. on pp. 4, 16).
- <sup>3152</sup><sup>13</sup>E. Noether, *Invariante variationsprobleme*, ger,  
<sup>3153</sup>*Nachrichten von der Gesellschaft der Wissenschaften zu Göttingen,*  
<sup>3154</sup>*Mathematisch-Physikalische Klasse* **1918** (1918) 235–257 (1918)  
<sup>3155</sup>(cit. on p. 6).
- <sup>3156</sup><sup>14</sup>C. A. Moura and F. Rossi-Torres, *Searches for Violation of CPT Symmetry and Lorentz Invariance with Astrophysical Neutrinos*,  
<sup>3157</sup>*Universe* **8** (2022) 42 (2022) (cit. on p. 9).
- <sup>3159</sup><sup>15</sup>J. S. Bell, *Time reversal in field theory*,  
<sup>3160</sup>*Proc. Roy. Soc. Lond. A* **231** (1955) 479–495 (1955) (cit. on p. 9).
- <sup>3161</sup><sup>16</sup>R. F. Streater and A. S. Wightman,  
<sup>3162</sup>*PCT, spin and statistics, and all that* (1989) (cit. on p. 9).
- <sup>3163</sup><sup>17</sup>T. D. Lee and C.-N. Yang,  
<sup>3164</sup>*Question of Parity Conservation in Weak Interactions*,  
<sup>3165</sup>*Phys. Rev.* **104** (1956) 254–258 (1956) (cit. on p. 9).
- <sup>3166</sup><sup>18</sup>C. S. Wu, E. Ambler, R. W. Hayward, D. D. Hoppes and R. P. Hudson,  
<sup>3167</sup>*Experimental Test of Parity Conservation in  $\beta$  Decay*,  
<sup>3168</sup>*Phys. Rev.* **105** (1957) 1413–1414 (1957) (cit. on p. 9).
- <sup>3169</sup><sup>19</sup>R. L. Garwin, L. M. Lederman and M. Weinrich,  
<sup>3170</sup>*Observations of the failure of conservation of parity and charge conjugation in meson decays: the magnetic moment of the free muon*,  
<sup>3171</sup>*Phys. Rev.* **105** (4 1957) 1415–1417 (1957) (cit. on p. 10).
- <sup>3173</sup><sup>20</sup>J. H. Christenson, J. W. Cronin, V. L. Fitch and R. Turlay,  
<sup>3174</sup>*Evidence for the  $2\pi$  Decay of the  $K_2^0$  Meson*,  
<sup>3175</sup>*Phys. Rev. Lett.* **13** (1964) 138–140 (1964) (cit. on p. 10).
- <sup>3176</sup><sup>21</sup>L.-L. Chau and W.-Y. Keung,  
<sup>3177</sup>*Comments on the Parametrization of the Kobayashi-Maskawa Matrix*,  
<sup>3178</sup>*Phys. Rev. Lett.* **53** (1984) 1802 (1984) (cit. on p. 11).
- <sup>3179</sup><sup>22</sup>P. A. Zyla et al., *Review of Particle Physics*,  
<sup>3180</sup>*PTEP* **2020** (2020) 083C01 (2020) (cit. on p. 12).
- <sup>3181</sup><sup>23</sup>P. Q. Hung, *The Weak Eightfold Way:  $SU(3)_W$  unification of the electroweak interactions*, (2021) (2021) (cit. on p. 11).

- <sup>3183</sup><sup>24</sup>A. M. Sirunyan et al.,  
<sup>3184</sup>*Measurement of the weak mixing angle using the forward-backward*  
<sup>3185</sup>*asymmetry of Drell-Yan events in pp collisions at 8 TeV,*  
<sup>3186</sup>*Eur. Phys. J. C* **78** (2018) 701 (2018) (cit. on p. 14).
- <sup>3187</sup><sup>25</sup>O. W. Greenberg, *Spin and Unitary Spin Independence in a Paraquark*  
<sup>3188</sup>*Model of Baryons and Mesons*, *Phys. Rev. Lett.* **13** (1964) 598–602  
<sup>3189</sup>(1964) (cit. on p. 15).
- <sup>3190</sup><sup>26</sup>D. D. Ryutov, *Using Plasma Physics to Weigh the Photon,*  
<sup>3191</sup>*Plasma Phys. Control. Fusion* **49** (2007) B429 (2007) (cit. on p. 19).
- <sup>3192</sup><sup>27</sup>F. J. Yndurain, *Limits on the mass of the gluon,*  
<sup>3193</sup>*Phys. Lett. B* **345** (1995) 524–526 (1995) (cit. on p. 19).
- <sup>3194</sup><sup>28</sup>M. Aaboud et al., *Measurement of the  $W$ -boson mass in pp collisions at*  
<sup>3195</sup> *$\sqrt{s} = 7$  TeV with the ATLAS detector,*  
<sup>3196</sup>*Eur. Phys. J. C* **78** (2018) 110, [Erratum: *Eur.Phys.J.C* 78, 898 (2018)]  
<sup>3197</sup>(2018) (cit. on p. 19).
- <sup>3198</sup><sup>29</sup>G. Abbiendi et al., *Precise determination of the  $Z$  resonance parameters*  
<sup>3199</sup>*at LEP: 'Zedometry'*, *Eur. Phys. J. C* **19** (2001) 587–651 (2001)  
<sup>3200</sup>(cit. on p. 19).
- <sup>3201</sup><sup>30</sup>J. Goldstone, A. Salam and S. Weinberg, *Broken Symmetries*,  
<sup>3202</sup>*Phys. Rev.* **127** (1962) 965–970 (1962) (cit. on p. 21).
- <sup>3203</sup><sup>31</sup>D. M. Webber et al., *Measurement of the Positive Muon Lifetime and*  
<sup>3204</sup>*Determination of the Fermi Constant to Part-per-Million Precision*,  
<sup>3205</sup>*Phys. Rev. Lett.* **106** (2011) 041803 (2011) (cit. on p. 25).
- <sup>3206</sup><sup>32</sup>M. Aker et al.,  
<sup>3207</sup>*Direct neutrino-mass measurement with sub-electronvolt sensitivity*,  
<sup>3208</sup>*Nature Phys.* **18** (2022) 160–166 (2022) (cit. on p. 27).
- <sup>3209</sup><sup>33</sup>N. Aghanim et al., *Planck 2018 results. VI. Cosmological parameters*,  
<sup>3210</sup>*Astron. Astrophys.* **641** (2020) A6, [Erratum: *Astron.Astrophys.* 652,  
<sup>3211</sup>C4 (2021)] (2020) (cit. on p. 29).
- <sup>3212</sup><sup>34</sup>V. C. Rubin and W. K. Ford Jr., *Rotation of the Andromeda Nebula*  
<sup>3213</sup>*from a Spectroscopic Survey of Emission Regions*,  
<sup>3214</sup>*Astrophys. J.* **159** (1970) 379–403 (1970) (cit. on p. 30).
- <sup>3215</sup><sup>35</sup>A. N. Taylor, S. Dye, T. J. Broadhurst, N. Benitez and E. van Kampen,  
<sup>3216</sup>*Gravitational lens magnification and the mass of abell 1689*,  
<sup>3217</sup>*Astrophys. J.* **501** (1998) 539 (1998) (cit. on pp. 30, 32).
- <sup>3218</sup><sup>36</sup>P. A. R. Ade et al., *Planck 2015 results. XIII. Cosmological parameters*,  
<sup>3219</sup>*Astron. Astrophys.* **594** (2016) A13 (2016) (cit. on p. 30).

- <sup>3220</sup><sup>37</sup>S. Amoroso et al.,  
<sup>3221</sup>*Strategy for ATLAS top quark mass measurements: 2021-2023,*  
<sup>3222</sup>tech. rep., CERN, 2020 (cit. on p. 33).
- <sup>3223</sup><sup>38</sup>M. Aaboud et al.,  
<sup>3224</sup>*Measurement of the top quark mass in the  $t\bar{t} \rightarrow \text{lepton+jets}$  channel*  
<sup>3225</sup>*from  $\sqrt{s} = 8$  TeV ATLAS data and combination with previous results,*  
<sup>3226</sup>*Eur. Phys. J. C* **79** (2019) 290 (2019) (cit. on p. 34).
- <sup>3227</sup><sup>39</sup>A. M. Sirunyan et al.,  
<sup>3228</sup>*Measurement of the Jet Mass Distribution and Top Quark Mass in*  
<sup>3229</sup>*Hadronic Decays of Boosted Top Quarks in  $pp$  Collisions at  $\sqrt{s} = \text{TeV}$ ,*  
<sup>3230</sup>*Phys. Rev. Lett.* **124** (2020) 202001 (2020) (cit. on p. 34).
- <sup>3231</sup><sup>40</sup>*Combination of CDF and D0 results on the mass of the top quark using*  
<sup>3232</sup>*up  $9.7 \text{ fb}^{-1}$  at the Tevatron,* (2016) (2016) (cit. on p. 34).
- <sup>3233</sup><sup>41</sup>M. Kobayashi and T. Maskawa,  
<sup>3234</sup>*CP Violation in the Renormalizable Theory of Weak Interaction,*  
<sup>3235</sup>*Prog. Theor. Phys.* **49** (1973) 652–657 (1973) (cit. on p. 34).
- <sup>3236</sup><sup>42</sup>J. E. Augustin et al.,  
<sup>3237</sup>*Discovery of a Narrow Resonance in  $e^+e^-$  Annihilation,*  
<sup>3238</sup>*Phys. Rev. Lett.* **33** (1974) 1406–1408 (1974) (cit. on p. 34).
- <sup>3239</sup><sup>43</sup>S. W. Herb et al., *Observation of a Dimuon Resonance at 9.5-GeV in*  
<sup>3240</sup>*400-GeV Proton-Nucleus Collisions,*  
<sup>3241</sup>*Phys. Rev. Lett.* **39** (1977) 252–255 (1977) (cit. on p. 35).
- <sup>3242</sup><sup>44</sup>F. Abe et al., *Observation of top quark production in  $\bar{p}p$  collisions,*  
<sup>3243</sup>*Phys. Rev. Lett.* **74** (1995) 2626–2631 (1995) (cit. on p. 35).
- <sup>3244</sup><sup>45</sup>S. Abachi et al., *Observation of the top quark,*  
<sup>3245</sup>*Phys. Rev. Lett.* **74** (1995) 2632–2637 (1995) (cit. on p. 35).
- <sup>3246</sup><sup>46</sup>M. Czakon and A. Ferroglio, *Top quark pair production at complete*  
<sup>3247</sup>*NLO accuracy with NNLO +NNLL corrections in QCD,*  
<sup>3248</sup>*Chinese Physics C* **44** (2020) 083104 (2020) (cit. on p. 36).
- <sup>3249</sup><sup>47</sup>P. Kant et al., *HatHor for single top-quark production: Updated*  
<sup>3250</sup>*predictions and uncertainty estimates for single top-quark production in*  
<sup>3251</sup>*hadronic collisions,* *Comput. Phys. Commun.* **191** (2015) 74–89 (2015)  
<sup>3252</sup> (cit. on p. 38).
- <sup>3253</sup><sup>48</sup>M. Aliev et al.,  
<sup>3254</sup>*HATHOR – HAdronic Top and Heavy quarks crOss section calculatoR,*  
<sup>3255</sup>*Comput. Phys. Commun.* **182** (2011) 1034–1046 (2011) (cit. on p. 38).
- <sup>3256</sup><sup>49</sup>J. A. Aguilar-Saavedra,  
<sup>3257</sup>*Single top quark production at LHC with anomalous  $Wtb$  couplings,*  
<sup>3258</sup>*Nucl. Phys. B* **804** (2008) 160–192 (2008) (cit. on p. 39).

- 3259   <sup>50</sup>J. Butterworth et al., *PDF4LHC recommendations for LHC Run II*,  
3260   *J. Phys. G* **43** (2016) 023001 (2016) (cit. on pp. 40, 76).
- 3261   <sup>51</sup>A. D. Martin, W. J. Stirling, R. S. Thorne and G. Watt,  
3262   *Parton distributions for the LHC*, *Eur. Phys. J. C* **63** (2009) 189 (2009)  
3263   (cit. on pp. 40, 77).
- 3264   <sup>52</sup>A. D. Martin, W. J. Stirling, R. S. Thorne and G. Watt,  
3265   *Uncertainties on  $\alpha_S$  in global PDF analyses and implications for*  
3266   *predicted hadronic cross sections*, *Eur. Phys. J. C* **64** (2009) 653–680  
3267   (2009) (cit. on p. 40).
- 3268   <sup>53</sup>H.-L. Lai et al., *New parton distributions for collider physics*,  
3269   *Phys. Rev. D* **82** (2010) 074024 (2010) (cit. on p. 40).
- 3270   <sup>54</sup>R. D. Ball et al., *Parton distributions with QED corrections*,  
3271   *Nucl. Phys. B* **877** (2013) 290–320 (2013) (cit. on p. 40).
- 3272   <sup>55</sup>Particle Data Group Web Page, *Higgs-boson Mass*, (2022)  
3273   <https://pdglive.lbl.gov/DataBlock.action?node=S126M> (visited  
3274   on 22/01/2022) (cit. on p. 46).
- 3275   <sup>56</sup>M. Aaboud et al., *Measurement of the Higgs boson mass in the*  
3276    *$H \rightarrow ZZ^* \rightarrow 4\ell$  and  $H \rightarrow \gamma\gamma$  channels with  $\sqrt{s} = 13$  TeV pp collisions*  
3277   *using the ATLAS detector*, *Phys. Lett. B* **784** (2018) 345–366 (2018)  
3278   (cit. on p. 46).
- 3279   <sup>57</sup>A. M. Sirunyan et al.,  
3280   *A measurement of the Higgs boson mass in the diphoton decay channel*,  
3281   *Phys. Lett. B* **805** (2020) 135425 (2020) (cit. on p. 46).
- 3282   <sup>58</sup>F. Englert and R. Brout,  
3283   *Broken symmetry and the mass of gauge vector mesons*,  
3284   *Phys. Rev. Lett.* **13** (9 1964) 321–323 (1964) (cit. on p. 46).
- 3285   <sup>59</sup>P. W. Higgs, *Broken symmetries and the masses of gauge bosons*,  
3286   *Phys. Rev. Lett.* **13** (16 1964) 508–509 (1964) (cit. on p. 46).
- 3287   <sup>60</sup>G. S. Guralnik, C. R. Hagen and T. W. B. Kibble,  
3288   *Global conservation laws and massless particles*,  
3289   *Phys. Rev. Lett.* **13** (20 1964) 585–587 (1964) (cit. on p. 46).
- 3290   <sup>61</sup>G. Aad et al., *Observation of a new particle in the search for the*  
3291   *Standard Model Higgs boson with the ATLAS detector at the LHC*,  
3292   *Phys. Lett. B* **716** (2012) 1–29 (2012) (cit. on pp. 46, 58).
- 3293   <sup>62</sup>S. Chatrchyan et al., *Observation of a New Boson at a Mass of 125*  
3294   *GeV with the CMS Experiment at the LHC*,  
3295   *Phys. Lett. B* **716** (2012) 30–61 (2012) (cit. on pp. 46, 58).

- <sup>3296</sup><sup>63</sup>T. Aaltonen et al., *Combined search for the standard model Higgs boson*  
<sup>3297</sup>*decaying to a  $b\bar{b}$  pair using the full CDF data set,*  
<sup>3298</sup>*Phys. Rev. Lett.* **109** (2012) 111802 (2012) (cit. on p. 46).
- <sup>3299</sup><sup>64</sup>V. M. Abazov et al., *Combined Search for the Standard Model Higgs*  
<sup>3300</sup>*Boson Decaying to  $b\bar{b}$  Using the D0 Run II Data Set,*  
<sup>3301</sup>*Phys. Rev. Lett.* **109** (2012) 121802 (2012) (cit. on p. 46).
- <sup>3302</sup><sup>65</sup>D. de Florian et al., *Handbook of LHC Higgs Cross Sections: 4.*  
<sup>3303</sup>*Deciphering the Nature of the Higgs Sector*, **2/2017** (2016) (2016)  
<sup>3304</sup>(cit. on pp. 48, 49).
- <sup>3305</sup><sup>66</sup>B. Mellado Garcia, P. Musella, M. Grazzini and R. Harlander,  
<sup>3306</sup>*CERN Report 4: Part I Standard Model Predictions*, (2016) (2016)  
<sup>3307</sup>(cit. on p. 49).
- <sup>3308</sup><sup>67</sup>A. Pich, *Electroweak Symmetry Breaking and the Higgs Boson*,  
<sup>3309</sup>*Acta Phys. Polon. B* **47** (2016) 151, edited by M. Praszalowicz (2016)  
<sup>3310</sup>(cit. on p. 50).
- <sup>3311</sup><sup>68</sup>M. Farina, C. Grojean, F. Maltoni, E. Salvioni and A. Thamm,  
<sup>3312</sup>*Lifting degeneracies in Higgs couplings using single top production in*  
<sup>3313</sup>*association with a Higgs boson*, *JHEP* **05** (2013) 022 (2013)  
<sup>3314</sup>(cit. on pp. 50, 51).
- <sup>3315</sup><sup>69</sup>S. Biswas, E. Gabrielli and B. Mele, *Single top and Higgs associated*  
<sup>3316</sup>*production as a probe of the  $Htt$  coupling sign at the LHC*,  
<sup>3317</sup>*JHEP* **01** (2013) 088 (2013) (cit. on p. 50).
- <sup>3318</sup><sup>70</sup>T. Appelquist and M. S. Chanowitz,  
<sup>3319</sup>*Unitarity Bound on the Scale of Fermion Mass Generation*, *Phys. Rev.*  
<sup>3320</sup>*Lett.* **59** (1987) 2405, [Erratum: *Phys.Rev.Lett.* 60, 1589 (1988)] (1987)  
<sup>3321</sup>(cit. on p. 51).
- <sup>3322</sup><sup>71</sup>M. Aaboud et al., *Observation of Higgs boson production in association*  
<sup>3323</sup>*with a top quark pair at the LHC with the ATLAS detector*,  
<sup>3324</sup>*Phys. Lett. B* **784** (2018) 173–191 (2018) (cit. on p. 51).
- <sup>3325</sup><sup>72</sup>K. Skovpen, ‘First observation of the  $t\bar{t}H$  process at CMS’,  
<sup>3326</sup>11th International Workshop on Top Quark Physics (2018)  
<sup>3327</sup>(cit. on p. 51).
- <sup>3328</sup><sup>73</sup>G. Aad et al.,  
<sup>3329</sup>*Search for  $H \rightarrow \gamma\gamma$  produced in association with top quarks and*  
<sup>3330</sup>*constraints on the Yukawa coupling between the top quark and the Higgs*  
<sup>3331</sup>*boson using data taken at 7 TeV and 8 TeV with the ATLAS detector*,  
<sup>3332</sup>*Phys. Lett. B* **740** (2015) 222–242 (2015) (cit. on p. 51).

- <sup>3333</sup><sup>74</sup>V. Khachatryan et al., *Search for the associated production of the Higgs boson with a top-quark pair,*  
<sup>3334</sup>*JHEP* **09** (2014) 087, [Erratum: *JHEP* 10, 106 (2014)] (2014)  
<sup>3335</sup>(cit. on p. 51).
- <sup>3336</sup><sup>75</sup>F. Demartin, F. Maltoni, K. Mawatari and M. Zaro,  
<sup>3337</sup>*Higgs production in association with a single top quark at the LHC,*  
<sup>3338</sup>*Eur. Phys. J. C* **75** (2015) 267 (2015) (cit. on pp. 52–54).
- <sup>3340</sup><sup>76</sup>T. M. P. Tait and C. P. Yuan, *Single top quark production as a window*  
<sup>3341</sup>*to physics beyond the standard model,* *Phys. Rev. D* **63** (2000) 014018  
<sup>3342</sup>(2000) (cit. on p. 54).
- <sup>3343</sup><sup>77</sup>S. Biswas, E. Gabrielli, F. Margaroli and B. Mele,  
<sup>3344</sup>*Direct constraints on the top-Higgs coupling from the 8 TeV LHC data,*  
<sup>3345</sup>*JHEP* **07** (2013) 073 (2013) (cit. on p. 54).
- <sup>3346</sup><sup>78</sup>V. Khachatryan et al., *Search for the associated production of a Higgs boson with a single top quark in proton-proton collisions at  $\sqrt{s} = 8$  TeV,*  
<sup>3347</sup>*JHEP* **06** (2016) 177 (2016) (cit. on p. 54).
- <sup>3349</sup><sup>79</sup>CERN Web Page, *Our Member States*, (2022)  
<sup>3350</sup>[https://home.web.cern.ch/about/who-we-are/our-](https://home.web.cern.ch/about/who-we-are/our-governance/member-states)  
<sup>3351</sup>*governance/member-states* (visited on 11/01/2022) (cit. on p. 58).
- <sup>3352</sup><sup>80</sup>T. Fazzini, G. Fidecaro, A. W. Merrison, H. Paul and A. V. Tollestrup,  
<sup>3353</sup>*Electron decay of the pion,* *Phys. Rev. Lett.* **1** (7 1958) 247–249 (1958)  
<sup>3354</sup>(cit. on p. 58).
- <sup>3355</sup><sup>81</sup>F. J. Hasert et al., *Observation of Neutrino Like Interactions Without Muon Or Electron in the Gargamelle Neutrino Experiment,*  
<sup>3356</sup>*Phys. Lett. B* **46** (1973) 138–140 (1973) (cit. on p. 58).
- <sup>3358</sup><sup>82</sup>P. M. Watkins, *Discovery of the w and 2 bosons,*  
<sup>3359</sup>*Contemporary Physics* **27** (1986) 291–324 (1986) (cit. on p. 58).
- <sup>3360</sup><sup>83</sup>D. Decamp et al.,  
<sup>3361</sup>*Determination of the Number of Light Neutrino Species,*  
<sup>3362</sup>*Phys. Lett. B* **231** (1989) 519–529 (1989) (cit. on p. 58).
- <sup>3363</sup><sup>84</sup>G. Baur et al., *Production of anti-hydrogen,*  
<sup>3364</sup>*Phys. Lett. B* **368** (1996) 251–258 (1996) (cit. on p. 58).
- <sup>3365</sup><sup>85</sup>G. D. Barr et al.,  
<sup>3366</sup>*A New measurement of direct CP violation in the neutral kaon system,*  
<sup>3367</sup>*Phys. Lett. B* **317** (1993) 233–242 (1993) (cit. on p. 58).
- <sup>3368</sup><sup>86</sup>V. Fanti et al., *A New measurement of direct CP violation in two pion decays of the neutral kaon,* *Phys. Lett. B* **465** (1999) 335–348 (1999)  
<sup>3369</sup>(cit. on p. 58).
- <sup>3370</sup>

- <sup>3371</sup><sup>87</sup>R. Aaij et al., *Observation of  $J/\psi p$  Resonances Consistent with  
3372 Pentaquark States in  $\Lambda_b^0 \rightarrow J/\psi K^- p$  Decays,*  
3373 *Phys. Rev. Lett.* **115** (2015) 072001 (2015) (cit. on p. 58).
- <sup>3374</sup><sup>88</sup>S. Maury, *The Antiproton Decelerator: AD,*  
3375 *Hyperfine Interact.* **109** (1997) 43–52 (1997) (cit. on p. 58).
- <sup>3376</sup><sup>89</sup>R. Alemany et al.,  
3377 *Summary Report of Physics Beyond Colliders at CERN,*  
3378 (2019), edited by J. Jaeckel, M. Lamont and C. Vallée (2019)  
3379 (cit. on p. 58).
- <sup>3380</sup><sup>90</sup>R. Catherall et al., *The ISOLDE facility*, *J. Phys. G* **44** (2017) 094002  
3381 (2017) (cit. on p. 58).
- <sup>3382</sup><sup>91</sup>E. Gschwendtner et al., *AWAKE, The Advanced Proton Driven Plasma  
3383 Wakefield Acceleration Experiment at CERN,*  
3384 *Nucl. Instrum. Meth. A* **829** (2016) 76–82, edited by U. Dorda et al.  
3385 (2016) (cit. on p. 58).
- <sup>3386</sup><sup>92</sup>M. Aguilar et al.,  
3387 *The Alpha Magnetic Spectrometer (AMS) on the International Space  
3388 Station. I: Results from the test flight on the space shuttle*, *Phys. Rept.*  
3389 **366** (2002) 331–405, [Erratum: *Phys.Rept.* **380**, 97–98 (2003)] (2002)  
3390 (cit. on p. 59).
- <sup>3391</sup><sup>93</sup>T. J. Berners-Lee and R. Cailliau,  
3392 *WorldWideWeb: proposal for a HyperText Project*, tech. rep.,  
3393 CERN, 1990 (cit. on p. 59).
- <sup>3394</sup><sup>94</sup>*CERN Council holds special session on the Large Hadron Collider  
3395 project*, (1991) 3 p, Issued on 19 December 1991 (1991) (cit. on p. 59).
- <sup>3396</sup><sup>95</sup>T. S. Pettersson and P Lefèvre,  
3397 *The Large Hadron Collider: conceptual design*, tech. rep., 1995  
3398 (cit. on pp. 59, 62).
- <sup>3399</sup><sup>96</sup>S. Myers,  
3400 *The LEP Collider, from design to approval and commissioning*,  
3401 John Adams' memorial lecture, Delivered at CERN, 26 Nov 1990  
3402 (CERN, Geneva, 1991) (cit. on p. 59).
- <sup>3403</sup><sup>97</sup>B. Müller, J. Schukraft and B. Wysłouch,  
3404 *First Results from Pb+Pb Collisions at the LHC*,  
3405 *Annual Review of Nuclear and Particle Science* **62** (2012) 361–386  
3406 (2012) (cit. on p. 61).
- <sup>3407</sup><sup>98</sup>CERN Web Page, *The Large Hadron Collider*, (2022)  
3408 [https://home.cern/science/accelerators/large-hadron-](https://home.cern/science/accelerators/large-hadron-collider)  
3409 *collider* (visited on 11/01/2022) (cit. on p. 61).

- 3410   <sup>99</sup>R. Steerenberg et al., ‘Operation and performance of the cern large  
3411   hadron collider during proton run 2’,  
3412   **10th international particle accelerator conference** (2019) MOPMP031  
3413   (cit. on p. 61).
- 3414   <sup>100</sup>by Rende Steerenberg and A. Schaeffer, *LHC Report: The LHC is full!*,  
3415   **(2018)** (2018) (cit. on p. 61).
- 3416   <sup>101</sup>*8th International Conference on High-Energy Accelerators*,  
3417   CERN (CERN, Geneva, 1971) (cit. on p. 61).
- 3418   <sup>102</sup>*LHC Machine*,  
3419   **JINST** **3** (2008) S08001, edited by L. Evans and P. Bryant (2008)  
3420   (cit. on pp. 61, 64).
- 3421   <sup>103</sup>*Radiofrequency cavities*, **(2012)** (2012) (cit. on p. 62).
- 3422   <sup>104</sup>K. Long et al., *Muon colliders to expand frontiers of particle physics*,  
3423   **Nature Phys.** **17** (2021) 289–292 (2021) (cit. on p. 63).
- 3424   <sup>105</sup>L Lari, H Gaillard and V Mertens,  
3425   *Scheduling the installation of the LHC injection lines*, tech. rep.,  
3426   CERN, 2004 (cit. on p. 64).
- 3427   <sup>106</sup>G. Aad et al.,  
3428   *The ATLAS Experiment at the CERN Large Hadron Collider*,  
3429   **JINST** **3** (2008) S08003 (2008) (cit. on pp. 64, 83, 87, 88, 92, 93).
- 3430   <sup>107</sup>S. Chatrchyan et al., *The CMS Experiment at the CERN LHC*,  
3431   **JINST** **3** (2008) S08004 (2008) (cit. on p. 64).
- 3432   <sup>108</sup>A. A. Alves Jr. et al., *The LHCb Detector at the LHC*,  
3433   **JINST** **3** (2008) S08005 (2008) (cit. on p. 65).
- 3434   <sup>109</sup>K. Aamodt et al., *The ALICE experiment at the CERN LHC*,  
3435   **JINST** **3** (2008) S08002 (2008) (cit. on p. 65).
- 3436   <sup>110</sup>O. Adriani et al.,  
3437   *The LHCf detector at the CERN Large Hadron Collider*,  
3438   **JINST** **3** (2008) S08006 (2008) (cit. on p. 66).
- 3439   <sup>111</sup>O. Adriani et al.,  
3440   *Technical design report of the LHCf experiment: Measurement of*  
3441   *photons and neutral pions in the very forward region of LHC* (2006)  
3442   (cit. on p. 66).
- 3443   <sup>112</sup>C. Alpigiani et al., *A Letter of Intent for MATHUSLA: A Dedicated*  
3444   *Displaced Vertex Detector above ATLAS or CMS.*, (2018) (2018)  
3445   (cit. on p. 67).

- <sup>3446</sup><sup>113</sup>J. H. Yoo, *The milliQan Experiment: Search for milli-charged Particles*  
<sup>3447</sup>at the LHC, PoS ICHEP2018 (2018) 520. 4 p, proceeding for ICHEP  
<sup>3448</sup>2018 SEOUL, International Conference on High Energy Physics, 4-11  
<sup>3449</sup>July 2018, SEOUL, KOREA (2018) (cit. on p. 67).
- <sup>3450</sup><sup>114</sup>A. Ball et al., *Search for millicharged particles in proton-proton*  
<sup>3451</sup>*collisions at  $\sqrt{s} = 13$  TeV*, Phys. Rev. D **102** (2020) 032002 (2020)  
<sup>3452</sup>(cit. on p. 67).
- <sup>3453</sup><sup>115</sup>V. A. Mitsou, *The MoEDAL experiment at the LHC: status and results*,  
<sup>3454</sup>J. Phys. Conf. Ser. **873** (2017) 012010, edited by B. Grzadkowski,  
<sup>3455</sup>J. Kalinowski and M. Krawczyk (2017) (cit. on p. 67).
- <sup>3456</sup><sup>116</sup>G. Anelli et al.,  
<sup>3457</sup>*The TOTEM experiment at the CERN Large Hadron Collider*,  
<sup>3458</sup>JINST **3** (2008) S08007 (2008) (cit. on p. 67).
- <sup>3459</sup><sup>117</sup>A. Ariga et al., *Technical Proposal for FASeR: ForwArd SeArch*  
<sup>3460</sup>*ExpeRiment at the LHC*, (2018) (2018) (cit. on p. 67).
- <sup>3461</sup><sup>118</sup>A. Ariga et al.,  
<sup>3462</sup>*Letter of Intent for FASeR: ForwArd SeArch ExpeRiment at the LHC*,  
<sup>3463</sup>(2018) (2018) (cit. on p. 67).
- <sup>3464</sup><sup>119</sup>*LHC computing Grid. Technical design report*,  
<sup>3465</sup>(2005), edited by I. Bird et al. (2005) (cit. on p. 67).
- <sup>3466</sup><sup>120</sup>WLCG Web Page, *Resources*, (2022)  
<sup>3467</sup><https://wlcg-public.web.cern.ch/resources> (visited on  
<sup>3468</sup>31/01/2022) (cit. on p. 68).
- <sup>3469</sup><sup>121</sup>*ATLAS computing: Technical design report*,  
<sup>3470</sup>(2005), edited by G. Duckeck et al. (2005) (cit. on p. 67).
- <sup>3471</sup><sup>122</sup>WLCG Web Page, *Tier centres*, (2022)  
<sup>3472</sup><https://wlcg-public.web.cern.ch/tier-centres> (visited on  
<sup>3473</sup>31/01/2022) (cit. on pp. 68, 69).
- <sup>3474</sup><sup>123</sup>W. Herr and B Muratori, *Concept of luminosity*, (2006) (2006)  
<sup>3475</sup>(cit. on pp. 70, 71).
- <sup>3476</sup><sup>124</sup>A. Hoecker, ‘Physics at the LHC Run-2 and Beyond’,  
<sup>3477</sup>2016 European School of High-Energy Physics (2016)  
<sup>3478</sup>(cit. on pp. 71, 72, 79).
- <sup>3479</sup><sup>125</sup>M. Aaboud et al., *Luminosity determination in pp collisions at  $\sqrt{s} = 8$*   
<sup>3480</sup>*TeV using the ATLAS detector at the LHC*,  
<sup>3481</sup>Eur. Phys. J. C **76** (2016) 653 (2016) (cit. on p. 71).
- <sup>3482</sup><sup>126</sup>G. Aad et al., *ATLAS data quality operations and performance for*  
<sup>3483</sup>*2015–2018 data-taking*, JINST **15** (2020) P04003 (2020) (cit. on p. 72).

- 3484 <sup>127</sup>*Luminosity determination in pp collisions at  $\sqrt{s} = 13$  TeV using the*  
3485 *ATLAS detector at the LHC*, tech. rep., CERN, 2019 (cit. on p. 72).
- 3486 <sup>128</sup>F. S. Cafagna, *Latest results for Proton-proton Cross Section*  
3487 *Measurements with the TOTEM experiment at LHC*,  
3488 PoS **ICRC2019** (2021) 207 (2021) (cit. on p. 75).
- 3489 <sup>129</sup>Particle Data Group Web Page,  
3490 *Data files and plots of cross-sections and related quantities for hadrons*,  
3491 (2022) <https://pdg.lbl.gov/2021/hadronic-xsections/> (visited on  
3492 08/02/2022) (cit. on p. 76).
- 3493 <sup>130</sup>*Shrek*, 2001 (cit. on p. 81).
- 3494 <sup>131</sup>*CERN Council holds special session on the Large Hadron Collider*  
3495 *project*, (1991) 3 p, Issued on 19 December 1991 (1991) (cit. on p. 79).
- 3496 <sup>132</sup>*ATLAS: technical proposal for a general-purpose pp experiment at the*  
3497 *Large Hadron Collider at CERN*, LHC technical proposal  
3498 (CERN, Geneva, 1994) (cit. on p. 80).
- 3499 <sup>133</sup>A. collaboration, ‘First 2.36 TeV Collision Events recorded by the
- 3500 *ATLAS experiment*, December 8th and 14th, 2009’, 2009 (cit. on p. 80).
- 3501 <sup>134</sup>G. Aad et al., *Measurements of the Higgs boson production and decay*  
3502 *rates and constraints on its couplings from a combined ATLAS and*  
3503 *CMS analysis of the LHC pp collision data at  $\sqrt{s} = 7$  and 8 TeV*,  
3504 JHEP **08** (2016) 045 (2016) (cit. on p. 80).
- 3505 <sup>135</sup>G. Aad et al., *Measurement of the top quark-pair production cross*  
3506 *section with ATLAS in pp collisions at  $\sqrt{s} = 7$  TeV*,  
3507 Eur. Phys. J. C **71** (2011) 1577 (2011) (cit. on p. 80).
- 3508 <sup>136</sup>G. Aad et al., *Evidence for Electroweak Production of  $W^\pm W^\pm jj$  in pp*  
3509 *Collisions at  $\sqrt{s} = 8$  TeV with the ATLAS Detector*,  
3510 Phys. Rev. Lett. **113** (2014) 141803 (2014) (cit. on p. 80).
- 3511 <sup>137</sup>M. Aaboud et al., *Evidence for light-by-light scattering in heavy-ion*  
3512 *collisions with the ATLAS detector at the LHC*,  
3513 Nature Phys. **13** (2017) 852–858 (2017) (cit. on p. 80).
- 3514 <sup>138</sup>M. Aaboud et al., *Search for the standard model Higgs boson produced*  
3515 *in association with top quarks and decaying into a  $b\bar{b}$  pair in pp*  
3516 *collisions at  $\sqrt{s} = 13$  TeV with the ATLAS detector*,  
3517 Phys. Rev. D **97** (2018) 072016 (2018) (cit. on p. 80).
- 3518 <sup>139</sup>M. Aaboud et al., *Observation of  $H \rightarrow b\bar{b}$  decays and VH production*  
3519 *with the ATLAS detector*, Phys. Lett. B **786** (2018) 59–86 (2018)  
3520 (cit. on p. 80).
- 3521 <sup>140</sup>S. Amoroso, *Precision measurements at the LHC*, tech. rep.,  
3522 CERN, 2020 (cit. on p. 80).

- <sup>3523</sup><sup>141</sup>H. Pacey, *EW SUSY Production at the LHC*, tech. rep., CERN, 2021  
<sup>3524</sup>(cit. on p. 80).

<sup>3525</sup><sup>142</sup>S. Das Bakshi, J. Chakrabortty, C. Englert, M. Spannowsky and  
<sup>3526</sup>P. Stylianou, *CP Violation at atlas in effective field theory*,  
<sup>3527</sup>*Phys. Rev. D* **103** (5 2021) 055008 (2021) (cit. on p. 80).

<sup>3528</sup><sup>143</sup>B. T. Carlson, *Dark Matter searches with the ATLAS detector*, (2020)  
<sup>3529</sup>(2020) (cit. on p. 82).

<sup>3530</sup><sup>144</sup>J. L. Pinfold, *ATLAS and astroparticle physics*, *Nucl. Phys. B Proc.*  
<sup>3531</sup>*Suppl.* **175-176** (2008) 25–32, edited by K. S. Cheng et al. (2008)  
<sup>3532</sup>(cit. on p. 82).

<sup>3533</sup><sup>145</sup>N. D. Brett et al., *Discovery Reach for Black Hole Production*, (2009)  
<sup>3534</sup>(2009) (cit. on p. 82).

<sup>3535</sup><sup>146</sup>*ATLAS inner detector: Technical Design Report*, 1,  
<sup>3536</sup>Technical design report. ATLAS (CERN, Geneva, 1997) (cit. on p. 83).

<sup>3537</sup><sup>147</sup>G. Aad et al.,  
<sup>3538</sup>*The ATLAS Inner Detector commissioning and calibration*,  
<sup>3539</sup>*Eur. Phys. J. C* **70** (2010) 787–821 (2010) (cit. on p. 83).

<sup>3540</sup><sup>148</sup>M Capeans et al., *ATLAS Insertable B-Layer Technical Design Report*,  
<sup>3541</sup>tech. rep., 2010 (cit. on pp. 85, 86).

<sup>3542</sup><sup>149</sup>*Technical Design Report for the ATLAS Inner Tracker Pixel Detector*,  
<sup>3543</sup>tech. rep., CERN, 2017 (cit. on pp. 86, 88, 102).

<sup>3544</sup><sup>150</sup>ATLAS Experiment Web Page, *Detector and Technology*, (2022)  
<sup>3545</sup><https://atlas.cern/discover/detector> (visited on 02/02/2022)  
<sup>3546</sup>(cit. on pp. 86, 89, 92, 96, 97).

<sup>3547</sup><sup>151</sup>F. Cavallari, *Performance of calorimeters at the LHC*,  
<sup>3548</sup>*Journal of Physics: Conference Series* **293** (2011) 012001 (2011)  
<sup>3549</sup>(cit. on pp. 88, 91, 92).

<sup>3550</sup><sup>152</sup>C. Grupen and B. Shwartz, ‘Calorimetry’, *Particle detectors*, 2nd ed.,  
<sup>3551</sup>Cambridge Monographs on Particle Physics, Nuclear Physics and  
<sup>3552</sup>Cosmology (Cambridge University Press, 2008) 230–272 (cit. on p. 90).

<sup>3553</sup><sup>153</sup>Particle Data Group Web Page,  $\pi^0$  Decay Modes, (2022)  
<sup>3554</sup><https://pdglive.lbl.gov/DataBlock.action?node=Q007TP> (visited  
<sup>3555</sup>on 02/02/2022) (cit. on p. 91).

<sup>3556</sup><sup>154</sup>A. Tarek Abouelfadl Mohamed, ‘The lhc and the atlas experiment’,  
<sup>3557</sup>*Measurement of higgs boson production cross sections in the diphoton*  
<sup>3558</sup>*channel: with the full atlas run-2 data and constraints on anomalous*  
<sup>3559</sup>*higgs boson interactions*  
(Springer International Publishing, Cham, 2020) 61 (cit. on pp. 92, 93).

- 3561 <sup>155</sup> *ATLAS muon spectrometer: Technical design report*, (1997) (1997)  
3562 (cit. on p. 93).
- 3563 <sup>156</sup> K. Ishii, *The ATLAS muon spectrometer*, PoS **HEP2001** (2001) 253,  
3564 edited by D. o. Horváth, P. Lévai and A. Patkós (2001) (cit. on p. 94).
- 3565 <sup>157</sup> M Livan, *Monitored drift tubes in ATLAS*, tech. rep., CERN, 1996  
3566 (cit. on p. 94).
- 3567 <sup>158</sup> G. Cattani, *The resistive plate chambers of the ATLAS experiment:*  
3568 *performance studies*,  
3569 *Journal of Physics: Conference Series* **280** (2011) 012001 (2011)  
3570 (cit. on p. 95).
- 3571 <sup>159</sup> K. Nagai, *Thin gap chambers in ATLAS*, Nucl. Instrum. Meth. A **384**  
3572 (1996) 219–221, edited by F. Ferroni and P. Schlein (1996)  
3573 (cit. on p. 95).
- 3574 <sup>160</sup> *ATLAS magnet system: Technical Design Report*, 1,  
3575 Technical design report. ATLAS (CERN, Geneva, 1997)  
3576 (cit. on pp. 96, 97).
- 3577 <sup>161</sup> *ATLAS high-level trigger, data acquisition and controls: Technical*  
3578 *design report*, (2003) (2003) (cit. on pp. 98, 99).
- 3579 <sup>162</sup> G. Aad et al., *Performance of the ATLAS Trigger System in 2010*,  
3580 *Eur. Phys. J. C* **72** (2012) 1849 (2012) (cit. on p. 98).
- 3581 <sup>163</sup> *Technical Design Report for the Phase-II Upgrade of the ATLAS TDAQ*  
3582 *System*, tech. rep., CERN, 2017 (cit. on p. 103).
- 3583 <sup>164</sup> G. Aad et al., *The ATLAS Simulation Infrastructure*,  
3584 *Eur. Phys. J. C* **70** (2010) 823–874 (2010) (cit. on p. 105).
- 3585 <sup>165</sup> P. Mato, *GAUDI-Architecture design document*, (1998) (1998)  
3586 (cit. on p. 108).
- 3587 <sup>166</sup> L. Lista, ‘Practical Statistics for Particle Physicists’,  
3588 *2016 European School of High-Energy Physics* (2017) 213  
3589 (cit. on p. 126).
- 3590 <sup>167</sup> I. Connelly, *Performance and calibration of b-tagging with the ATLAS*  
3591 *experiment at LHC Run-2*, EPJ Web Conf. **164** (2017) 07025, edited by  
3592 L. Bravina, Y. Foka and S. Kabana (2017) (cit. on p. 135).
- 3593 <sup>168</sup> T. Chen and C. Guestrin, ‘XGBoost’,  
3594 *Proceedings of the 22nd ACM SIGKDD international conference on*  
3595 *knowledge discovery and data mining* (2016) (cit. on p. 136).

- 3596   <sup>169</sup>J Zimmermann,  
3597   *Statistical learning methods: basics, control and performance*,  
3598   Nuclear Instruments and Methods in Physics Research Section A:  
3599   Accelerators, Spectrometers, Detectors and Associated Equipment **559**  
3600   (2006) 106–114 (2006) (cit. on p. 137).

<sup>3601</sup> **Summary of the results**



3602 **Recerca de la producció**  
3603 **associada de bosó de Higgs i**  
3604 **un quark top amb dos leptons i**  
3605 **tau hadrònic a l'estat final**

3606 **1 Marc teòric**

3607 **1.1 El Model Estàndard**

3608 Maybe, I could translate this for the SM summary:  
3609 <https://www.quantamagazine.org/a-new-map-of-the-standard-model->  
3610 [of-particle-physics-20201022/](https://www.quantamagazine.org/a-new-map-of-the-standard-model-of-particle-physics-20201022/)

3611 **1.2 La física del quark top**

3612 **1.3 La física del bosó de Higgs**

3613 **2 Dispositiu experimental**

3614 El treball desenvolupat al doctorat s'emmarca dins del detector ATLAS,  
3615 que opera registrant les dades de les col·lisions del gran col·lisionador  
3616 d'hadrons (LHC). El nom ATLAS prové de l'acronim angles d'un aparell  
3617 toroidal del LHC.

3618 Aquestes eines pertanyen al centre europeu de recerca en física de  
3619 partícules, popularment conegut com a CERN.

3620 **3 L'experiment ATLAS del LHC al CERN**

3621 **3.1 El gran col·lisionador d'hadrons**

3622 **3.2 El detector ATLAS**

3623 **4 Mesura de la polarització del quark top al  
3624 canal-*t***

3625 Mesura d'observables sensibles a la polarització del quark top

3626 **4.1 Selecció d'esdeveniments**

3627 **4.2 Estimació del fons**

3628 **4.3 Fonts d'incertesa**

3629 **4.4 Resultats**

3630 **5 Recerca de processos  $tH$  amb un estat fi-  
3631 nal  $2\ell + 1\tau_{\text{had}}$**

3632 **5.1 Selecció d'esdeveniments**

3633 **5.2 Estimació del fons**

3634 **5.3 Fonts d'incertesa**

3635 **5.4 Resultats**

3636 **6 Conclusions**

3637



# 3638 Contraportada

3639      The discovery of a Higgs boson by the ATLAS and CMS experiments  
3640 in 2012 opened a new field for exploration in the realm of particle physics.  
3641 In order to better understand the Standard Model (SM) of particle physics,  
3642 it is imperative to study the Yukawa coupling between this new particle  
3643 and the rest of the SM components. Among these, of prominent interest is  
3644 the coupling of the Higgs boson to the top quark ( $y_t$ ), which is the most  
3645 massive fundamental particle and, consequently, the one with the strongest  
3646 coupling to the Higgs

3647      The direct measurement of  $y_t$  is only possible at LHC via two associated  
3648 Higgs productions; with a pair of top quarks ( $t\bar{t}H$ ) and with single-top  
3649 quark ( $tHq$ ). While the  $t\bar{t}H$  permits a model-independent determination of  
3650 the magnitude of  $y_t$ , the only way of directly measuring its sign is through  
3651 the  $tHq$  production. This is due to the fact that the two leading-order  
3652 Feynman diagrams for  $tHq$  production interfere with each other depending  
3653 on  $y_t$  sign. Current experimental constraints on  $y_t$  favour the SM predictions,  
3654 even though an opposite sign with respect to the SM expectations is not  
3655 completely excluded yet.

3656      In this work it is presented a search for the production of a Higgs boson in  
3657 association with a single-top quark in a final state with two light-floavoured-  
3658 charged leptons and one hadronically decaying tau lepton (named  $2\ell + 1\tau_{\text{had}}$   
3659 channel). This analysis uses an integrated luminosity of  $139 \text{ fb}^{-1}$  of proton-  
3660 proton collision data at centre-of-mass energy of  $13 \text{ TeV}$  collected by ATLAS  
3661 during LHC Run 2.

3662      This search is exceptionally challenging due to the extremely small cross  
3663 section of the  $tHq$  process ( $70 \text{ fb}^{-1}$ ) in general and, more particularly, the  
3664 the  $2\ell + 1\tau_{\text{had}}$  final-state channel, which only accounts for a 3.5% of the  
3665 total  $tHq$  production.

3666      Because of this, the separation of the  $tHq$  signal events from background  
3667 events is done by means of machine-learning (ML) techniques using boosted-  
3668 decision trees (BDT) to define both signal and control regions. The most  
3669 most relevant background processes are those related to top-pairs produc-

3670 tion (such as  $t\bar{t}$ ,  $t\bar{t}H$ ,  $t\bar{t}Z$  and  $t\bar{t}W$ ),  $Z$ -boson plus jets and single-top  
3671 processes.

3672 Significant suppression of the background events with jets wrongly selected  
3673 as leptons is achieved by demanding electrons and muons to pass strict  
3674 isolation requirements. Simultaneously, hadronic-tau leptons are demanded  
3675 to pass the requirement of the recurrent-neural-network-based discriminator  
3676 to reduce misidentifications from jets.

3677 The reconstruction of the events is also enhanced by similar ML methods  
3678 since in the scenario in which the light-flavour leptons have the same sign,  
3679 in principle, it is not possible to determine which lepton is originated from  
3680 the Higgs boson and which from the top quark.

3681 The possible observation of an excess of signal events with respect to  
3682 the SM predictions, would be a clear evidence of new physics in terms of  
3683  $\mathcal{CP}$ -violating  $y_t$  coupling.

3684 Additionally, the contribution to the single-top-quark polarisation first  
3685 measurement is presented as well. In this other analysis the components of  
3686 the full polarisation vector of the top quark are measured taking advantage  
3687 of the peculiarities of the single-top-quark decay. Benefitting from the fact  
3688 that the top quark lifetime is smaller than the depolarisation timescale, the  
3689 decay products preserve the spin information of the top quark. Via angular  
3690 distributions, it is measured in the top-quark rest frame.